Shock and Vibration

Vibration Signal Detection and Feature Extraction based on Entropy

Lead Guest Editor: Yuxing Li
Guest Editors: Nabil Neggaz and Xiao Chen

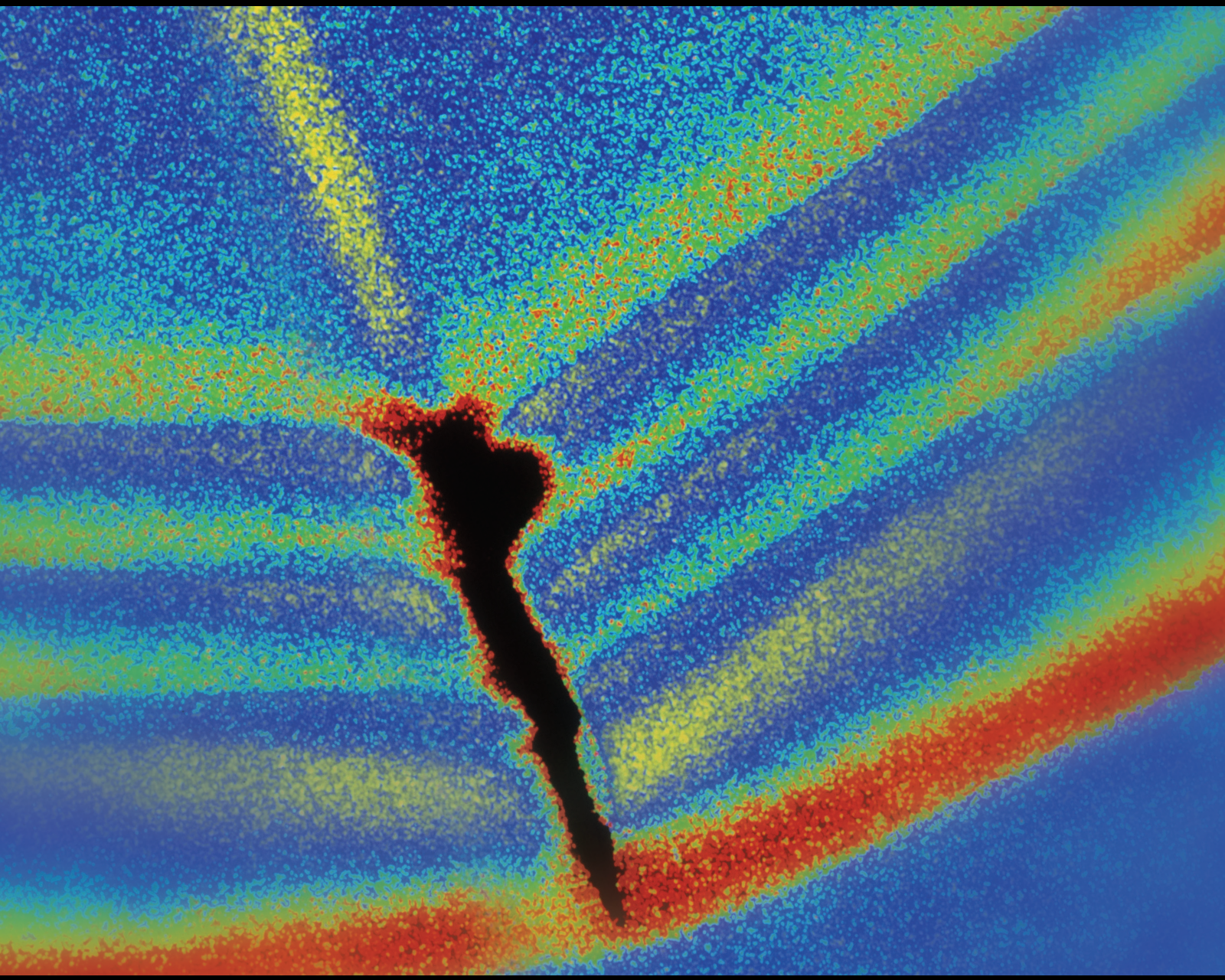

Vibration Signal Detection and Feature Extraction based on Entropy

Shock and Vibration

Vibration Signal Detection and Feature Extraction based on Entropy

Lead Guest Editor: Yuxing Li
Guest Editors: Nabil Neggaz and Xiao Chen

Chief Editor

Associate Editors

Academic Editors

Contents

Retracted: Precision Analysis of Noncircular Gears Based on CNC Machining Technology under Cloud Computing Platform
Shock and Vibration
Retraction (1 page), Article ID 9891849, Volume 2024 (2024)

Retracted: Analysis and Design of Cooperative Control Solutions for Electrical Systems of Laser CNC Machines
Shock and Vibration
Retraction (1 page), Article ID 9791575, Volume 2024 (2024)

Retracted: Research on the Bolt Positioning System Based on Multieye Vision Industrial Robots
Shock and Vibration
Retraction (1 page), Article ID 9768621, Volume 2024 (2024)

Retracted: High-Resolution Direction of Arrival Estimation of Underwater Multitargets Using Swarming Intelligence of Flower Pollination Heuristics
Shock and Vibration
Retraction (1 page), Article ID 9753919, Volume 2024 (2024)

Retracted: Effect of Rotating Magnetic Field on Hydrogen Production from Electrolytic Water
Shock and Vibration
Retraction (1 page), Article ID 9790625, Volume 2023 (2023)

[Retracted] Effect of Rotating Magnetic Field on Hydrogen Production from Electrolytic Water
Hao Guo and Sangyoung Kim
Research Article (11 pages), Article ID 9085721, Volume 2022 (2022)

[Retracted] Research on the Bolt Positioning System Based on Multieye Vision Industrial Robots
Jun Kong, Qiang Li, Yi Yin, Cen Li, and Wei Luo
Research Article (11 pages), Article ID 7563199, Volume 2022 (2022)

An Enhanced Gated Recurrent Unit-Based Adaptive Fault Diagnosis of Rotating Machinery
Zhen Li, Saleem Riaz, Muhammad Waqas, and Munira Batool
Research Article (13 pages), Article ID 4648311, Volume 2022 (2022)

[Retracted] Analysis and Design of Cooperative Control Solutions for Electrical Systems of Laser CNC Machines
Shufeng Shao
Research Article (14 pages), Article ID 1423767, Volume 2022 (2022)

[Retracted] High-Resolution Direction of Arrival Estimation of Underwater Multitargets Using Swarming Intelligence of Flower Pollination Heuristics
Nauman Ahmed, Huigang Wang, Shanshan Tu, Norah A.M. Alsaif, Muhammad Asif Zahoor Raja, Muhammad Kashif, Ammar Armghan, Yasser S. Abdalla, Wasiq Ali, and Farman Ali
Research Article (16 pages), Article ID 5876874, Volume 2022 (2022)

[Retracted] Precision Analysis of Noncircular Gears Based on CNC Machining Technology under Cloud Computing Platform
JianQing Dai, Wei Xu, and FenFen OuYang
Research Article (12 pages), Article ID 1359084, Volume 2022 (2022)

Single Feature Extraction Method of Bearing Fault Signals Based on Slope Entropy
Erna Shi
Research Article (9 pages), Article ID 6808641, Volume 2022 (2022)

Feature Extraction of Ship-Radiated Noise Based on Hierarchical Dispersion Entropy
Leilei Xiao
Research Article (10 pages), Article ID 3238461, Volume 2022 (2022)

Rotating Machinery Fault Diagnosis Using HHO-RSSD and RCGmvMAAPE
Ning Zhang
Research Article (34 pages), Article ID 6266671, Volume 2022 (2022)

Hindawi
Shock and Vibration
Volume 2024, Article ID 9891849, 1 page
https://doi.org/10.1155/2024/9891849

Retraction

Retracted: Precision Analysis of Noncircular Gears Based on CNC Machining Technology under Cloud Computing Platform

Shock and Vibration

Received 23 January 2024; Accepted 23 January 2024; Published 24 January 2024

This article has been retracted by Hindawi following an investigation undertaken by the publisher [1]. This investigation has uncovered evidence of one or more of the following indicators of systematic manipulation of the publication process:

(1) Discrepancies in scope

(2) Discrepancies in the description of the research reported

(3) Discrepancies between the availability of data and the research described

(4) Inappropriate citations

(5) Incoherent, meaningless and/or irrelevant content included in the article

(6) Manipulated or compromised peer review

The presence of these indicators undermines our confidence in the integrity of the article's content and we cannot, therefore, vouch for its reliability. Please note that this notice is intended solely to alert readers that the content of this article is unreliable. We have not investigated whether authors were aware of or involved in the systematic manipulation of the publication process.

Wiley and Hindawi regrets that the usual quality checks did not identify these issues before publication and have since put additional measures in place to safeguard research integrity.

We wish to credit our own Research Integrity and Research Publishing teams and anonymous and named external researchers and research integrity experts for contributing to this investigation.

The corresponding author, as the representative of all authors, has been given the opportunity to register their agreement or disagreement to this retraction. We have kept a record of any response received.

References

[1] J. Dai, W. Xu, and F. OuYang, "Precision Analysis of Noncircular Gears Based on CNC Machining Technology under Cloud Computing Platform," *Shock and Vibration*, vol. 2022, Article ID 1359084, 12 pages, 2022.

Hindawi
Shock and Vibration
Volume 2024, Article ID 9791575, 1 page
https://doi.org/10.1155/2024/9791575

Retraction

Retracted: Analysis and Design of Cooperative Control Solutions for Electrical Systems of Laser CNC Machines

Shock and Vibration

Received 23 January 2024; Accepted 23 January 2024; Published 24 January 2024

This article has been retracted by Hindawi following an investigation undertaken by the publisher [1]. This investigation has uncovered evidence of one or more of the following indicators of systematic manipulation of the publication process:

(1) Discrepancies in scope

(2) Discrepancies in the description of the research reported

(3) Discrepancies between the availability of data and the research described

(4) Inappropriate citations

(5) Incoherent, meaningless and/or irrelevant content included in the article

(6) Manipulated or compromised peer review

The presence of these indicators undermines our confidence in the integrity of the article's content and we cannot, therefore, vouch for its reliability. Please note that this notice is intended solely to alert readers that the content of this article is unreliable. We have not investigated whether authors were aware of or involved in the systematic manipulation of the publication process.

Wiley and Hindawi regrets that the usual quality checks did not identify these issues before publication and have since put additional measures in place to safeguard research integrity.

We wish to credit our own Research Integrity and Research Publishing teams and anonymous and named external researchers and research integrity experts for contributing to this investigation.

The corresponding author, as the representative of all authors, has been given the opportunity to register their agreement or disagreement to this retraction. We have kept a record of any response received.

References

[1] S. Shao, "Analysis and Design of Cooperative Control Solutions for Electrical Systems of Laser CNC Machines," *Shock and Vibration*, vol. 2022, Article ID 1423767, 14 pages, 2022.

Hindawi
Shock and Vibration
Volume 2024, Article ID 9768621, 1 page
https://doi.org/10.1155/2024/9768621

Retraction

Retracted: Research on the Bolt Positioning System Based on Multieye Vision Industrial Robots

Shock and Vibration

Received 23 January 2024; Accepted 23 January 2024; Published 24 January 2024

This article has been retracted by Hindawi following an investigation undertaken by the publisher [1]. This investigation has uncovered evidence of one or more of the following indicators of systematic manipulation of the publication process:

(1) Discrepancies in scope

(2) Discrepancies in the description of the research reported

(3) Discrepancies between the availability of data and the research described

(4) Inappropriate citations

(5) Incoherent, meaningless and/or irrelevant content included in the article

(6) Manipulated or compromised peer review

The presence of these indicators undermines our confidence in the integrity of the article's content and we cannot, therefore, vouch for its reliability. Please note that this notice is intended solely to alert readers that the content of this article is unreliable. We have not investigated whether authors were aware of or involved in the systematic manipulation of the publication process.

Wiley and Hindawi regrets that the usual quality checks did not identify these issues before publication and have since put additional measures in place to safeguard research integrity.

We wish to credit our own Research Integrity and Research Publishing teams and anonymous and named external researchers and research integrity experts for contributing to this investigation.

The corresponding author, as the representative of all authors, has been given the opportunity to register their agreement or disagreement to this retraction. We have kept a record of any response received.

References

[1] J. Kong, Q. Li, Y. Yin, C. Li, and W. Luo, "Research on the Bolt Positioning System Based on Multieye Vision Industrial Robots," *Shock and Vibration*, vol. 2022, Article ID 7563199, 11 pages, 2022.

Hindawi
Shock and Vibration
Volume 2024, Article ID 9753919, 1 page
https://doi.org/10.1155/2024/9753919

Retraction

Retracted: High-Resolution Direction of Arrival Estimation of Underwater Multitargets Using Swarming Intelligence of Flower Pollination Heuristics

Shock and Vibration

Received 23 January 2024; Accepted 23 January 2024; Published 24 January 2024

This article has been retracted by Hindawi following an investigation undertaken by the publisher [1]. This investigation has uncovered evidence of one or more of the following indicators of systematic manipulation of the publication process:

(1) Discrepancies in scope

(2) Discrepancies in the description of the research reported

(3) Discrepancies between the availability of data and the research described

(4) Inappropriate citations

(5) Incoherent, meaningless and/or irrelevant content included in the article

(6) Manipulated or compromised peer review

The presence of these indicators undermines our confidence in the integrity of the article's content and we cannot, therefore, vouch for its reliability. Please note that this notice is intended solely to alert readers that the content of this article is unreliable. We have not investigated whether authors were aware of or involved in the systematic manipulation of the publication process.

Wiley and Hindawi regrets that the usual quality checks did not identify these issues before publication and have since put additional measures in place to safeguard research integrity.

We wish to credit our own Research Integrity and Research Publishing teams and anonymous and named external researchers and research integrity experts for contributing to this investigation.

The corresponding author, as the representative of all authors, has been given the opportunity to register their agreement or disagreement to this retraction. We have kept a record of any response received.

References

[1] N. Ahmed, H. Wang, S. Tu et al., "High-Resolution Direction of Arrival Estimation of Underwater Multitargets Using Swarming Intelligence of Flower Pollination Heuristics," *Shock and Vibration*, vol. 2022, Article ID 5876874, 16 pages, 2022.

Hindawi
Shock and Vibration
Volume 2023, Article ID 9790625, 1 page
https://doi.org/10.1155/2023/9790625

Retraction

Retracted: Effect of Rotating Magnetic Field on Hydrogen Production from Electrolytic Water

Shock and Vibration

Received 29 August 2023; Accepted 29 August 2023; Published 30 August 2023

This article has been retracted by Hindawi following an investigation undertaken by the publisher [1]. This investigation has uncovered evidence of one or more of the following indicators of systematic manipulation of the publication process:

(1) Discrepancies in scope

(2) Discrepancies in the description of the research reported

(3) Discrepancies between the availability of data and the research described

(4) Inappropriate citations

(5) Incoherent, meaningless and/or irrelevant content included in the article

(6) Peer-review manipulation

The presence of these indicators undermines our confidence in the integrity of the article's content and we cannot, therefore, vouch for its reliability. Please note that this notice is intended solely to alert readers that the content of this article is unreliable. We have not investigated whether authors were aware of or involved in the systematic manipulation of the publication process.

Wiley and Hindawi regrets that the usual quality checks did not identify these issues before publication and have since put additional measures in place to safeguard research integrity.

We wish to credit our own Research Integrity and Research Publishing teams and anonymous and named external researchers and research integrity experts for contributing to this investigation.

The corresponding author, as the representative of all authors, has been given the opportunity to register their agreement or disagreement to this retraction. We have kept a record of any response received.

References

[1] H. Guo and S. Kim, "Effect of Rotating Magnetic Field on Hydrogen Production from Electrolytic Water," *Shock and Vibration*, vol. 2022, Article ID 9085721, 11 pages, 2022.

Hindawi
Shock and Vibration
Volume 2023, Article ID 9790625, 1 page
https://doi.org/10.1155/2023/9790625

Retraction

Retracted: Effect of Rotating Magnetic Field on Hydrogen Production from Electrolytic Water

Shock and Vibration

Received 29 August 2023; Accepted 29 August 2023; Published 30 August 2023

This article has been retracted by Hindawi following an investigation undertaken by the publisher [1]. This investigation has uncovered evidence of one or more of the following indicators of systematic manipulation of the publication process:

(1) Discrepancies in scope

(2) Discrepancies in the description of the research reported

(3) Discrepancies between the availability of data and the research described

(4) Inappropriate citations

(5) Incoherent, meaningless and/or irrelevant content included in the article

(6) Peer-review manipulation

The presence of these indicators undermines our confidence in the integrity of the article's content and we cannot, therefore, vouch for its reliability. Please note that this notice is intended solely to alert readers that the content of this article is unreliable. We have not investigated whether authors were aware of or involved in the systematic manipulation of the publication process.

Wiley and Hindawi regrets that the usual quality checks did not identify these issues before publication and have since put additional measures in place to safeguard research integrity.

We wish to credit our own Research Integrity and Research Publishing teams and anonymous and named external researchers and research integrity experts for contributing to this investigation.

The corresponding author, as the representative of all authors, has been given the opportunity to register their agreement or disagreement to this retraction. We have kept a record of any response received.

References

[1] H. Guo and S. Kim, "Effect of Rotating Magnetic Field on Hydrogen Production from Electrolytic Water," *Shock and Vibration*, vol. 2022, Article ID 9085721, 11 pages, 2022.

Hindawi
Shock and Vibration
Volume 2022, Article ID 9085721, 11 pages
https://doi.org/10.1155/2022/9085721

Research Article

Effect of Rotating Magnetic Field on Hydrogen Production from Electrolytic Water

Hao Guo[1] **and Sangyoung Kim**[2]

[1]*Jilin Business and Technology College, Changchun, China*
[2]*South Korea National Kunsan University, Gunsan, Republic of Korea*

Correspondence should be addressed to Sangyoung Kim; 662526@stu.ahu.edu.cn

Received 17 June 2022; Accepted 15 July 2022; Published 2 September 2022

Academic Editor: Yuxing Li

In order to reveal the influence of magnetic field on electrochemical machining, a research method of the influence of rotating magnetic field on hydrogen production from electrolytic water is proposed in this paper. Firstly, taking pure water as electrolyte, this paper selects rigid SPCE water molecular model, constructs the molecular dynamics model under the action of magnetic field, and simulates it. In this paper, the thermodynamics, electric power principle, and electrolytic reaction of hydrogen production from electrolytic water are analyzed, and the working processes of alkaline electrolytic cell, solid oxide electrolytic cell, and solid polymer electrolytic cell are analyzed. Based on solid polymer electrolytic cell, the effects of membrane electrode performance, diffusion layer material, contact electrode plate, electrolytic temperature, and electrolyte types on hydrogen production are analyzed. The experimental results show that the heteroions in the lake electrolyte significantly affect the performance of the membrane electrode, and the number of heteroions in the electrolyte should be controlled during the experiment. The hydrogen production capacity and energy efficiency ratio of the unit are basically not affected by different water flow dispersion. When dilute sulfuric acid electrolyte is selected in the experiment, the concentration should be 0.1%–0.2%; After the proton exchange membrane enters the stable period after the activation period, with the increase of the electrolysis time of tap water, (24 h) the membrane electrode will weaken the catalyst activity and reduce the electrolysis efficiency in the electrolysis process. Furthermore, the correctness of rotating magnetic field on hydrogen production from electrolytic water is verified.

1. Introduction

Developing sustainable energy strategies and solving future energy problems have become the consensus of all countries. Among them, the important thing is to use sustainable fuels or energy instead of traditional energy such as oil, natural gas, and coal, change the energy structure based on limited fossil fuels, and strive to move towards a sustainable and sustainable energy structure [1]. Hydrogen energy is an efficient, clean, and environment-friendly energy. The development of hydrogen energy in China has important strategic significance. Hydrogen storage, especially in the form of compounds, is rich in water on Earth. By integrating hydrogen into the current energy system, we can solve the problems of fuel resistance, waste emission, and waste, meet the high energy demand of modern society, reduce previous energy resources, and deal with the serious environmental problems caused by fossil fuel combustion. Hydrogen is the lowest density gas on Earth. Under standard conditions, the density of hydrogen is 0.0899 g/L, which is 1/14 of the air quality. Hydrogen is the lightest and most common element in nature [2]. Under normal temperature, the nature of hydrogen is very stable, it is not easy to dissolve in water, and it is not easy to have chemical reaction with other substances. Under some conditions, such as adsorption on metals such as handlebars or platinum, hydrogen has a strong effect and is easy to explode when touching flame. Hydrogen energy has high energy density. When it is used as a fuel carrier to provide energy, it does not produce air pollutants and can realize carbon-free emission [3, 4].

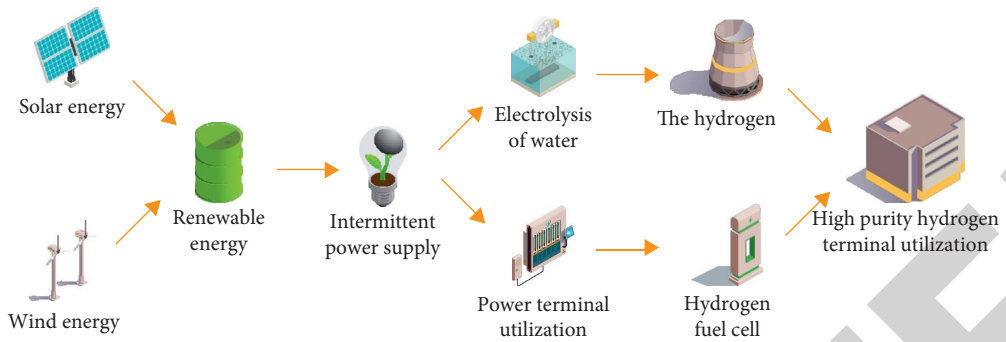

Figure 1: Distributed continuous clean energy supply system with hydrogen production from electrolytic water as the medium.

In order to improve the accuracy of ECM, compound ECM is proposed, which includes laser assisted electrochemical spraying technology and magnetic field assisted ECM technology. Magnetic field assisted electrochemical machining technology is proposed based on the principle of the interaction between magnetic field and electric field. Because adding an external magnetic field is equivalent to adding Lorentz force, at this time, Lorentz force can change the physical characteristics of charged particles in electrolyte, such as velocity and position. Secondly, there is always an electric field in the electrochemical machining process. At this time, the external magnetic field and electric field interact to improve the machining accuracy by changing the movement direction and trajectory of ions. According to the current experimental research results, through the magnetic circuit design, magnetic field assisted electrochemical machining can effectively reduce stray corrosion, improve surface roughness, shape and position accuracy, and improve the material removal rate. However, this technology is only studied from the perspective of technology, and the research object is also for specific shape workpieces or workpiece materials, so the research results have great limitations. Moreover, this technology faces some shortcomings, such as lack of micromechanism research and difficulty to control precision. Therefore, based on the microbasic theoretical research of this technology, this subject plans to build the microstructure model of electrolyte under the condition of magnetic field, study the influence of microdiffusion characteristics of electrolyte under the action of magnetic field by using molecular dynamics simulation technology, reveal the microbehavior mechanism of electrolyte in magnetic field assisted electrochemical machining, and finally verify and modify the model through experimental methods to provide theoretical basis and process scheme for magnetic field assisted electrochemical machining technology [5, 6]. In the conceptual distributed clean energy production, conversion, storage, and community use system shown in Figure 1, hydrogen produced by electrolytic water can play an important role as an energy storage medium in the system.

2. Literature Review

The advantages of ECM are that it can process difficult materials, no cathode loss, high machining efficiency, and no residual stress on the machined surface. Because the machining process of ECM corrodes material ions, it has the ability of precision machining. However, due to many influencing factors, including electrochemical reaction, flow field, and electric field, it is difficult to control effectively and the machining accuracy is not easy to control. Therefore, more and more experimental studies tend to composite field assisted electrochemical machining technology. PR and others applied the rotating magnetic assisted ultrasonic electrochemical finishing technology and obtained that this technology helps to reduce the processing time and make the workpiece surface smooth and bright [7]. Koponen and others used the electrochemical machining technology embedded in magnetic circuit to improve the ability of centralized etching and effectively reduce stray corrosion. Water is the raw material of hydrogen production from electrolytic water. Because it is colorless and pollution-free in the process of production, its development prospect will be wider and wider with the development of science and technology and the treatment of air. Hydrogen production from electrolytic water originates from alkaline electrolytic cell. The technology is relatively simple and the cost of hydrogen production is low, but the efficiency of hydrogen production is low and the purity of hydrogen is not high. At the same time, there are safety problems in alkaline electrolyte. The current research mainly focuses on the integration of electrode and membrane, ensuring the close connection between anode and cathode, replacing toxic cotton, and improving the activity of electrocatalyst to reduce the reaction overpotential [8]. The diaphragm of the electrolytic cell is made of polyimide membrane to separate the high concentration of alkali and acid in the electrolytic cell. Proost proposed the hydrogen production method of acid-base amphoteric electrolytic water by membrane method. This method improves the electrochemical reaction activity, reduces the overpotential of hydrogen evolution, and reduces the energy consumption of hydrogen production [9]. Based on the battery theory, the step-by-step method of electrode reaction, that is, the highly reversible charging and discharging process of secondary battery electrode, is used to realize the cache of ions and electrons. Wang and others proposed to split the electrolytic water process into separate steps of hydrogen and oxygen production, so as to realize the production of hydrogen and oxygen without membrane [10]. Koponen and others

pointed out that the calcite type oxide material can greatly reduce the traditional fuel reaction activity range by reducing the polarity resistance of the material, greatly improve the catalytic activity of oxygen at medium and low temperature, and guide the electrode electrolytic gas to the full electrode interface. The material also has excellent oxygen mobility, low coefficient of thermal expansion, abnormal catalytic activity, higher antioxidant substances, and higher resistance [11]. Horikoshi and others systematically summarized the research progress of disulfide key based hydrogen evolution catalysts, compared pure disulfide key, base electrocatalyst and self-supporting electrocatalyst, and analyzed the two ways of active site regulation and improving conductivity. It shows that the disulfide key has great potential as an electrocatalyst for hydrogen evolution under acidic conditions [12].

Based on this research, a study on the effect of rotating magnetic field on hydrogen production from electrolytic water is proposed in this paper. This topic plans to build the potential energy model of electrolyte in ECM under the action of external magnetic field, that is, adding electrostatic field and different magnetic field strength to the potential energy model. The electrolyte adopts pure aqueous solution and NaCl solution with mass fraction of 3.5%. The molecular dynamics simulation method is used to analyze the influence of the microdiffusion characteristics of the electrolyte under the action of external magnetic field and complete the calculation of the properties of the electrolyte under the action of magnetic field. Finally, the experimental verification is carried out through macroexperiment (i.e., infrared spectroscopy technology), so as to provide theoretical basis and process scheme for magnetic field assisted electrochemical machining technology.

3. Research Methods

3.1. Basic Theory of Hydrogen Production from Electrolytic Water. Hydrogen is a renewable and clean energy, which can be widely used in all walks of life as industrial raw materials and energy carriers. Therefore, low-cost and efficient hydrogen production technology from electrolytic water is extremely important and has a very broad market prospect and research value.

3.1.1. Hydrogen Production Raw Materials. Thermodynamic principles: hydrogen production by electrolyzing water is powered by electric energy to electrolyze water molecules into hydrogen and oxygen at the anode and cathode of the device. The reaction equations are as follows:

$$\text{Anodic reaction}: \cdot H_2O - 2e \longrightarrow O_2 + H^+, \quad (1)$$

$$\text{Cathodic reaction}: \cdot 2H^+ + 2e \longrightarrow H_2. \quad (2)$$

If the electrolytic cell works at a certain temperature and pressure, the energy required for the reaction of electrolytic water is determined by baking ΔH. The Gibbs-free energy ΔG is equivalent to the necessary heat Q and the external electric energy. The heat Q is equal to the product of the temperature T in the reaction process and the direct change ΔS before and after the reaction. Then the thermodynamic equation can be expressed as follows:

$$\Delta G = \Delta H - Q = \Delta H - T^* \Delta S, \quad (3)$$

where, at 298.15 K and 1 atm, the enthalpy change ΔH is 285.84 kJ/mol, the entropy change ΔS is 163.1 J/mol, the free energy ΔG is 237.2 1 kJ/mol, and the unit of process temperature T is kelvin K.

The external power supply provides power for the electrolytic reaction. The minimum voltage required for the electrolytic reaction of water molecules in the electrolytic cell is the equilibrium potential Vrev. The relationship between Gibbs-free energy ΔG and the equilibrium potential Vre is shown in the following:

$$\begin{aligned} \text{Vrev} &= \frac{\Delta G}{z * F} \\ &= 226.21 \times \frac{102\,(J/\text{mol})}{2 \times 95376} \\ &= 1.218V, \end{aligned} \quad (4)$$

where Z is the number of electrons required for each mole of hydrogen produced by the reaction and F is Faraday constant, 95374 C/mol.

If the phase state of water changes from liquid to gas due to the change of temperature in the electrolytic reaction, the heat Q required in the phase state transformation process is provided by electric energy. At 298.15 K, 1 atm, for the electrolytic cell with phase change process, the minimum voltage required for electrolytic reaction is recorded as thermal neutral electrolytic voltage Vtn, as shown in the following:

$$\begin{aligned} \text{Vtn} &= V\Delta H \\ &= \frac{\Delta H}{(z * F)} \\ &= +\frac{274.73\,(kJ/\text{mol})}{2 \times 95376} \\ &= 1.371V. \end{aligned} \quad (5)$$

3.1.2. Principles of Electricity. The completion of electrolytic reaction requires electric energy from external power supply. When the generation rate of hydrogen in the cell increases or the electrolytic current increases, the cell voltage V_{cell} of the cell will also increase. Moreover, due to the electrolytic cell device and equipment, the electrolytic cell has the contact resistance between various components and the activation resistance generated by the energy barrier in the electron migration process during the electrolytic reaction between the anode and the cathode electrodes. Due to the different transmission dispersion of electrolyte in the electrolytic reaction, the concentration at the interface of two electrodes and in the solvent is inconsistent, and the resulting

concentration polarization will affect the actual voltage, so that the voltage value of the cell in the electrolytic process is greater than the voltage value required for water electrolysis in theory [13, 14]. The relationship of various voltage values in the electrolytic cell is shown in the following:

$$V\text{cell} = V\text{rev} + V\text{ohm} + V\text{act} + V\text{con}, \tag{6}$$

where V_{rev} is equilibrium voltage of electrolytic cell reaction, unit: V; V_{ohm} is contact resistance voltage of electrolytic cell, unit: V; V_{act} is activated overpotential of electrolytic cell, unit: V; and V_{con} is concentration overpotential of electrolytic cell, unit: V.

Theoretically, the concentration overpotential V_{con} is often small in the electrolytic cell and is much smaller than the contact resistance voltage V_{ohm} and the activation overpotential V_{act}.

When studying the energy efficiency of the electrolytic cell, the current efficiency of the electrolytic cell can be calculated by comparing the output of hydrogen per unit time with the electrolytic current per unit time. Ideally, according to Faraday's law, the generation rate of hydrogen should be in direct proportion to the input electrolytic current [15]. Therefore, under a certain electrolytic current, the hydrogen generation rate f_{H2} (unit: m^3/h) of the electrolytic cell can be shown in the following:

$$f_{H_2} = \left(\eta_F \times N_{\text{cell}} \times \frac{\text{Icell}}{z \times F}\right) \times \left(21.31 \times \frac{3500}{1000}\right), \tag{7}$$

where η_g is current efficiency of electrolytic cell; N_{cell} is number of electrolytic cells, unit: piece; and I_{cell} is input current of electrolytic cell, unit: a.

Considering the actual influencing factors, the electric energy consumed by the actual electrolytic reaction of the electrolytic cell is compared with the electric energy consumed by the electrolytic reaction in the ideal state, which is recorded as the electrolytic efficiency of the actual electrolytic cell. The formula is expressed as

$$\eta_E = \frac{C_F}{C_E}, \tag{8}$$

where η_g is overall electrolytic efficiency of electrolytic cell; C_F is electric energy required to produce hydrogen per unit time when the electrolytic cell reacts; and C_E is electric energy consumed by hydrogen production per unit time in the actual electrolysis process.

3.1.3. Type of Electrolytic Cell. Hydrogen production from electrolytic water starts from alkaline electrolysis technology. The hydrogen production equipment from electrolytic water in front of mouth mainly includes alkaline electrolytic cell, polymer film electrolytic cell, and solid oxide electrolytic cell. Hydrogen production by alkaline electrolytic cell is the longest and most mature technology. Hydrogen production from solid oxide is still in the research and development stage because the electrolysis process requires high temperature conditions and relatively harsh application conditions. Hydrogen production by solid polymer electrolysis has attracted more and more attention because of its compact structure, small volume, and high adaptability to electrolysis conditions [16].

3.2. Effect of Magnetic Field on Water Electrolysis Process. In industrial electrolytic cells, the electrode layout and electrode form are generally optimized, or the flow of electrolyte is mechanically driven to accelerate mass transfer and discharge of gaseous products, so as to reduce ohmic voltage drop and electrode overpotential. In recent years, with the demand of industrial application and the in-depth development of relevant scientific research, more and more new methods have garnered increasing attention. The most significant methods include the use of catalysts to reduce the activation energy of hydrogen electrolysis reaction and the methods of external energy field, such as ultrasonic oscillation and hypergravity field. It has been found that the effect of magnetic field outside the electrolytic cell can significantly affect the mass transfer process and change the movement of gas-phase products, resulting in the reduction of electrode potential. The provision of static magnetic field does not require additional energy input. NdFeB permanent magnet can produce a strong enough magnetic field to meet the requirements. At the same time, the magnetic field device is cheaper and easier to use than electrocatalyst. In the process of water electrolysis, different electrode forms, magnetic fields, and different electrode layout can introduce different forms of electromagnetic forces into the electrolyte, mainly manifested in MHD (magnetohydrodynamic) and micro-MHD (micro-magneto-hydrodynamic) effects driven by Lorentz force [17].

3.2.1. Simulation of Bubble Growth Behavior on Electrode Surface. The formation of bubbles on the electrode surface will have a direct impact on the whole electrochemical reaction process, whether it is the gas-phase product or side reaction product we want to obtain by electrolysis. Bubble growth is a mass transfer process through the phase interface. Simulating its evolution behavior from the single bubble scale can help us deeply understand the gas-liquid mass transfer process on the electrode surface and the influence of bubble formation on the local flow field and concentration field. The bubble core initially growing on the electrode surface carries out interphase mass transfer driven by the concentration difference inside and outside the gas-liquid interface. In this process, it involves the control of the electrochemical reaction rate of hydrogen on the electrode surface, the transmission of hydrogen components in the liquid phase, and a reasonable mass transfer rate model at the gas-liquid interface. With the growth of bubbles, bubbles are subject to the combined action of two forces that inhibit their detachment and promote their detachment. When bubbles grow in acidic environment, their contact angle changes constantly, so the simulation of bubble growth needs to provide reasonable contact angle change input as boundary conditions. For the simulation of single bubble growth, VOF method and gas-liquid mass transfer rate model are used to compile the changes of electrode surface

electrochemical reaction rate, interfacial mass transfer rate, and dynamic contact angle into fluent computing platform through UDF. The mass transfer model and bubble evolution behavior are compared with the experimental results [18–20]. For the observation of bubble behavior and the influence of magnetic field on electrode potential difference, the experiment is carried out on the same experimental platform. The experimental platform includes the experimental section composed of permanent magnet and electrolytic cell, power control system, and bubble behavior recording system. Different electrolytic cells and electrodes are used for different experiments, and the layout direction of magnetic field, electrolytic cell, and electrode needs to be changed. The experimental system is shown in Figure 2.

3.3. Molecular Dynamics Simulation of the Effect of Magnetic Field on the Microstructure of Electrolyte in Electrochemical Machining. According to the results of molecular dynamics simulation, a trajectory related to the velocity and position of particles in the simulation system can be obtained, and various physical quantities can be extracted through this trajectory. In the third chapter, the influence of magnetic field on the microdiffusion characteristics of water molecules and ions in pure aqueous solution and NaC1 solution in ECM is obtained by using this simulation method. It is pointed out that the effect of external magnetic field has a certain influence on its diffusion coefficient. This chapter attempts to further explain this phenomenon by using the influence of law of magnetic field on the radial distribution function of electrolyte and the number of hydrated ions in ECM [21, 22].

3.3.1. Simulation Results and Discussion of Radial Distribution Function of Magnetic Field on Electrolyte in ECM. Radial distribution function (RDF), also known as pair correlation function, can be defined as the average number density of molecules in the volume element with a distance of $r + \delta r$ from the central ion. Therefore, the radial distribution function describes the aggregation characteristics of molecules or ions in the solution, so we can understand the structure of the liquid. Then the expression of the function is as follows:

$$g(r) = \frac{1}{\rho 4\pi r^2 \delta r} \frac{\sum_{T=1}^{T} \sum_{j=1}^{t} \Delta N(r \longrightarrow r + \delta t)}{N \times T}, \quad (9)$$

where N is number of molecules in the system and T is total number of simulated steps.

3.3.2. Effect of Magnetic Field Intensity on Radial Distribution Function of Pure Water. In ECM, the radial distribution functions $g_{O-H}(r)$ and $g_{O-O}(r)$ of pure water under the action of magnetic field are shown in Figures 3 and 4. In $g_{O-H}(r)$, the first peak represents the hydrogen oxygen covalent bond within water molecules in pure aqueous solution, while the second peak represents the hydrogen bond between water molecules in pure aqueous solution. It can be seen from the figure that when $R < 1.55a$, $g_{O-H}(r) = 0$, indicating that the distance between water molecules in the simulation system should be 1.55 larger. When $r = 5.75$ A, $g_{O-H}(r) = 1$, indicating that when the distance between two water molecules is greater than 5.75, it has the same properties as a uniform liquid [23, 24].

In Figure 4, the main peak represents the nearest distance between two water molecules. The secondary peak represents the distance between two water molecules connected to the same water molecule through hydrogen bond. It can be seen from the figure that the nearest distance between two water molecules is 3.35 A. Under the action of magnetic field, the first peak of the two diagrams of $g_{O-H}(r)$ and $g_{O-O}(r)$ is obviously large, which leads to the increase of the number of water molecules in the first coordination ring, the enhancement of structural stability, and the decrease of the diffusion coefficient of water molecules in the solution. However, the first peak position does not change, indicating that the nearest distance between the two water molecules to form hydrogen bond has little effect on the external field.

3.3.3. Effect of Magnetic Field Intensity on Radial Distribution Function of 3.5% NaC1 Solution. Analyze the radial distribution function between ions and water molecules in NaC1 solution with mass fraction of 3.5% under the action of magnetic field (0 T and 5 T), as shown in Figures 5 and 6. The maximum peak of the radial distribution function appears at $r = 2.25$ A and $r = 2.7$ A, which indicates that it is most likely to present other molecules or atoms near molecules $r = 2.25$ A and $r = 2.7$ A. When $r < 1.9$ A, the radial distribution function is zero, indicating that the nearest distance between two atoms should be greater than 1.9 A. The first peak value of $g_{Na-o}(r)$ is obviously greater than $g_{Cl-H}(r)$ under the action of magnetic field or no magnetic field, indicating that sodium ions have strong hydration ability. However, under the action of magnetic field, the first peak value of radial distribution function curve between ions and water molecules decreases, indicating that the interaction between ions and water molecules decreases and the number of ion hydration decreases; this is because the mobility of ions is enhanced, the number of hydrogen bonds between water molecules in the solution is reduced, the action is weakened, and the relatively stable structure of water molecules is destroyed [25].

The radial distribution function $g_{Na-Cl}(r)$ of sodium ion and chloride ion in the solution is shown in Figure 7. When the magnetic field intensity is 5 T, the first peak value of $g_{Na-Cl}(r)$ is at the same position as that without external magnetic field; that is, both are at $r = 2.7$ A. Under the action of magnetic field, the first peak value of radial distribution function $g_{Na-Cl}(r)$ of electrolyte increases, which is because the mobility of ions is increased under the stirring of Lorentz force, the possibility of ions appearing around them is increased, and the interaction with water molecules is weakened. The second peak decreased significantly, which means that the interaction between ions and water molecules in the solution is weakened.

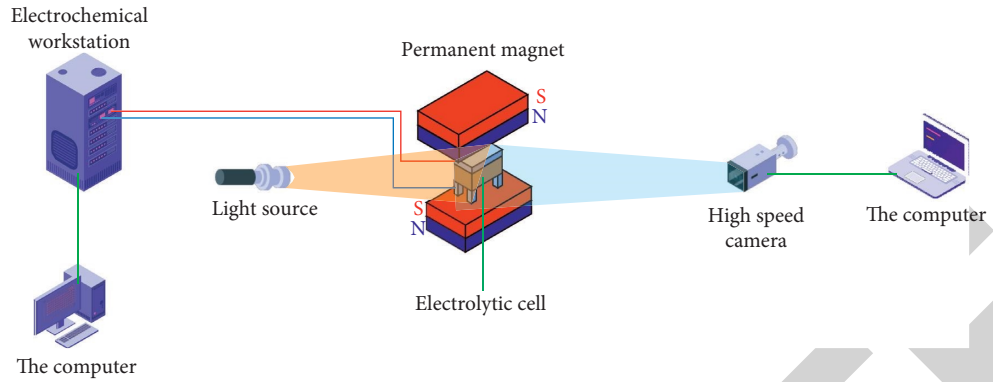

Figure 2: Experimental system diagram.

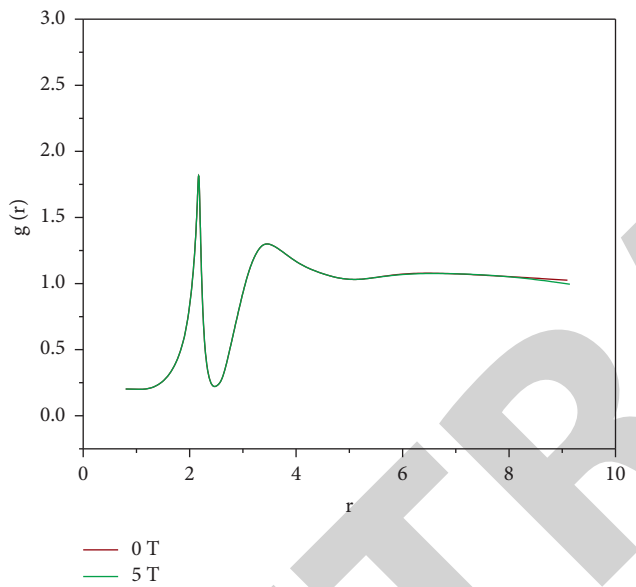

Figure 3: Effect of magnetic field on microstructure of pure water $g_{O-H}(r)$.

3.4. Ion Hydration Number. In fact, the number of ions in the hydration solution can be calculated by simulating the number of ions in the water around NaC1, which is the first number of ions in the hydration solution. Integrating the radial distribution function of sodium ion oxygen to the first peak and valley, the hydrate number of the first hydration circle of ions can be calculated, and the expression is as follows:

$$n = \rho_\omega \int_0^r g_{io}(r) 4\pi r^2 \mathrm{d}r, \tag{10}$$

where n is the hydration number, ρ_ω is the density of the solution, and R is the first minimum value of $g_{io}(r)$; the hydration number of sodium ions without and with magnetic field is obtained from formula (10), as shown in Table 1.

It is found that the number of sodium ions hydrated decreases under the action of magnetic field. This is because the Lorentz force has a stirring effect on the ions in the solution, which increases the probability of collision between ions, weakens the interaction with water molecules, reduces the number of hydrogen bonds formed between water molecules, qualitatively destroys the stability of water molecules, and then increases its diffusion coefficient.

4. Result Discussion

4.1. Comparative Analysis of Tap Water and Lake Water. It can be seen from Figure 8 that the hydrogen production amount is in direct proportion to the current, and the water quality does not affect the linear growth relationship between the hydrogen production amount and the current during the electrolysis process. After standing, the lake water is full of miscellaneous ions. Although the amount of hydrogen production increases linearly, it is significantly lower than that of tap water, and the increase of temperature has little effect on the difference of hydrogen production between them. Therefore, the amount of miscellaneous ions affects the hydrogen production rate of the electrolytic cell.

4.2. Influence Analysis of Acid Solution at Different Temperatures. The same set of electrolytic device is used in the experiment. The dilute sulfuric acid solution with the concentration of 0.5% is used as the electrolyte. The input current of the system is changed to 0.13 A–0.9 A. the electrolyte temperature is adjusted and set through the constant temperature water bath. The electrolyte temperature is set to 30°C = 40°C and 50°C, respectively. The average value of the three groups is taken, and the voltage and electrolytic water loss rate of the device are recorded.

It can be seen from Figure 9 that, under the working condition of 0.5% dilute sulfuric acid, when the electrolysis temperature is 30°C, 40°C, and 50°C, there is basically no difference in the hydrogen production capacity of the electrolytic cell. Changing the temperature of acid electrolyte has little effect on hydrogen production.

It can be seen from Figure 10 that the energy efficiency ratio of the same concentration of sulfuric acid at different temperatures varies greatly. When the current is in the range of 0.13 A–0.5 A, the influence of temperature on the energy efficiency ratio is obvious. The energy efficiency ratio at 40°C and 50°C is high, and the energy efficiency ratio at 30°C is the lowest. In the current region of 0.6aA0.9 A, the influence of

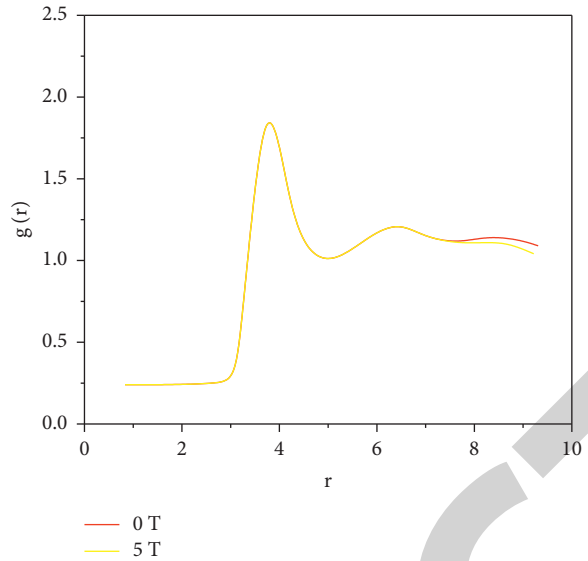

Figure 4: Effect of magnetic field on microstructure of pure water $g_{O-O}(r)$.

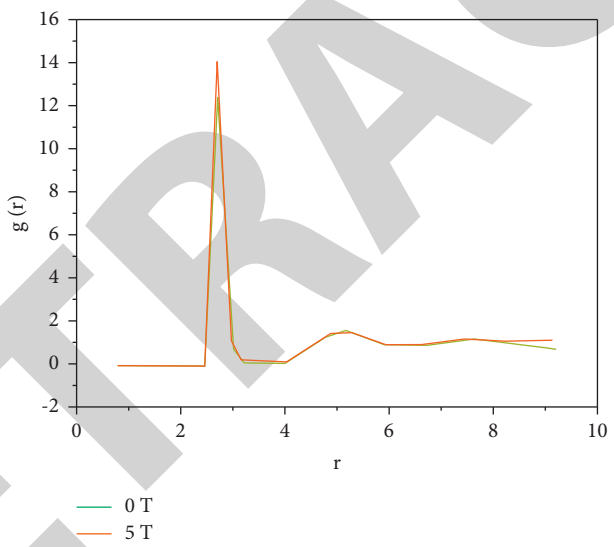

Figure 5: Effect of magnetic field on microstructure of 3.5% NaCl solution $g_{Na-o}(r)$.

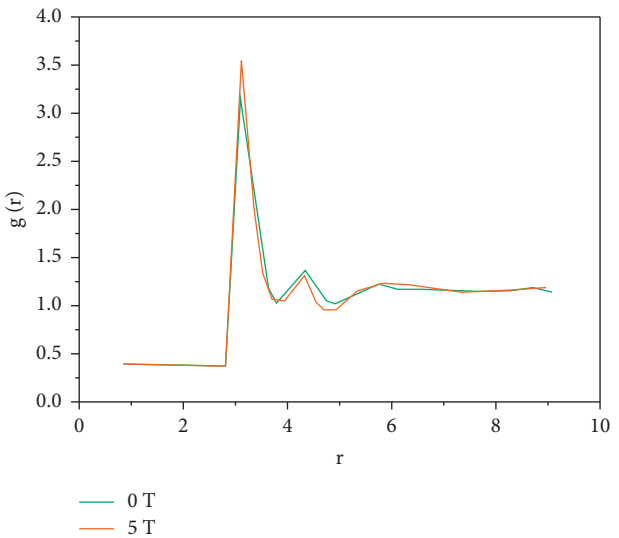

Figure 6: Effect of magnetic field on microstructure of 3.5% NaCl solution $g_{Cl-H}(r)$.

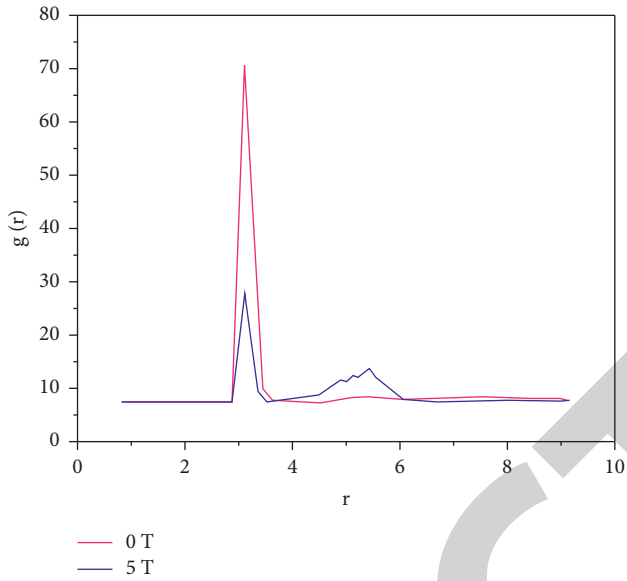

Figure 7: Effect of magnetic field on microstructure of 3.5% NaC1 solution $g_{\mathrm{Na-Cl}}(r)$.

Table 1: Ion hydration number of salt ion pairs in solution.

Magnetic field intensity (T)	0	5
Ion hydration number	6.54	6.34

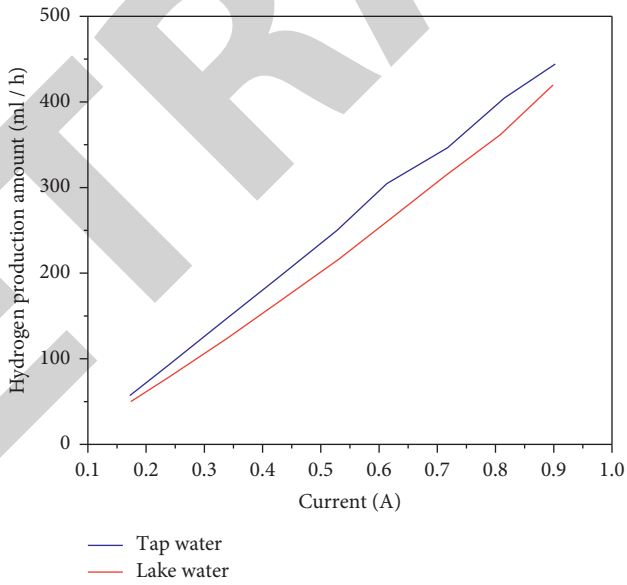

Figure 8: Variation of hydrogen production from electrolytic water with tap water and lake water.

temperature on the energy efficiency ratio is not obvious, and the energy efficiency ratio corresponding to the three temperatures has little difference. In conclusion, under low electrolytic current, the increase of temperature is conducive to hydrogen production reaction, and the hydrogen production rate of electrolytic cell is improved, but, under high electrolytic current, the influence of temperature on hydrogen production rate is weakened. In the experiment, the increase of acid and electrolyte temperature should not be considered, and the corrosion of electrolyte at room temperature should not be considered.

By controlling the electrolyte temperature, membrane electrode, diffusion layer, and contact electrode plate, the hydrogen production capacity of high-purity water and 1% acid solution is large, but the energy efficiency ratio is low. When the concentration is 0.1%–0.5%, there is basically no

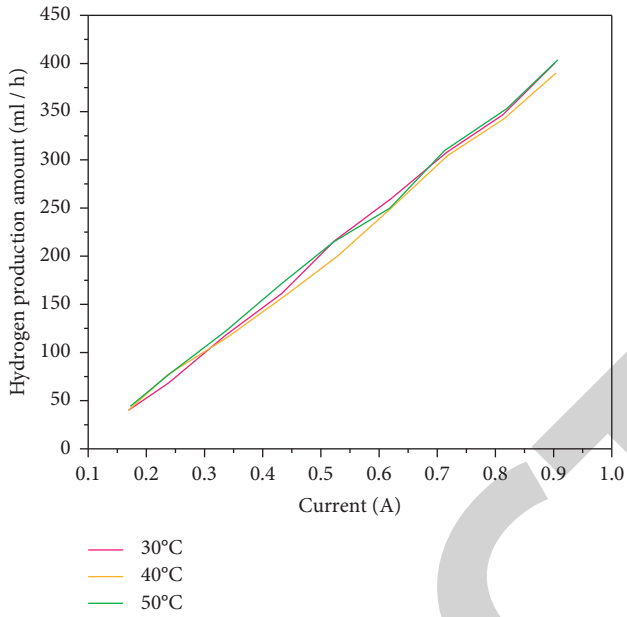

Figure 9: Variation of hydrogen production from electrolytic water with temperature under the condition of 0.5% dilute sulfuric acid.

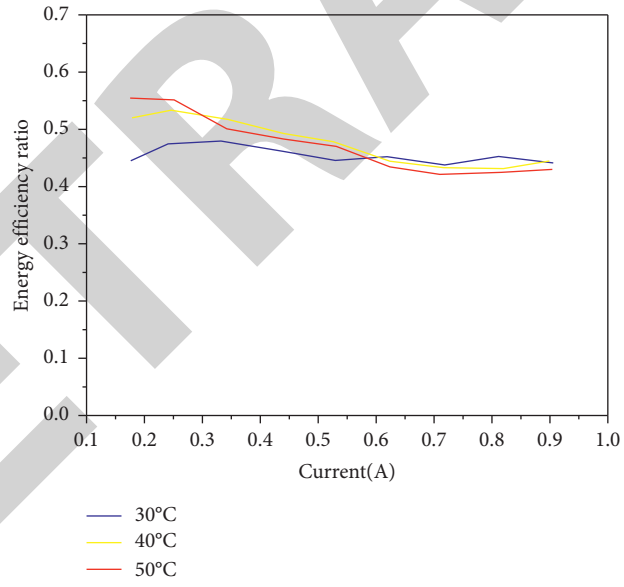

Figure 10: Variation of energy efficiency ratio of electrolytic water with temperature under the working condition of 0.5% dilute sulfuric acid.

difference in hydrogen production, but the difference in energy efficiency ratio is large. The increase of acid temperature has little effect on hydrogen production and energy efficiency ratio. Comprehensively, the concentration of acid electrolyte in the experiment should be 0.1%–0.2%, and it is more suitable at room temperature.

5. Conclusion

This paper mainly focuses on the generation and movement of hydrogen bubbles in the process of water electrolysis, and the driving mechanism of external magnetic field for gas products. Through experiments and numerical simulation,

the effects of different scale magnetic convection on the growth behavior of single bubble and the distribution of gas products are revealed. It involves many aspects, such as electrochemical reaction kinetics, gas-liquid two-phase flow, interphase mass transfer, and bubble dynamics. In this paper, the microchannel membrane SPE electrolytic water hydrogen production system is used, and the influencing factors of electrolytic water hydrogen production are analyzed and studied by using the method of controlling variables. The influencing factors of electrolytic water hydrogen production are analyzed and studied by changing the electrolytic current, electrolytic temperature, material of contact electrode plate and channel slot width, material of diffusion layer, water flow confusion, electrolyte type, and concentration of dilute sulfuric acid of the experimental system. The following conclusions are drawn.

Electrolyte solution: the hydrogen production rate and energy efficiency ratio of lake water are lower than those of tap water. The heteroions in lake water electrolyte significantly affect the performance of membrane electrode, so the number of heteroions in electrolyte should be controlled during the experiment. When dilute sulfuric acid is used as acid electrolyte, considering the factors of hydrogen production and energy efficiency ratio, the optimal concentration is 0.1%–0.2%. When the electrolysis temperature is 30°C–50°C, the temperature rise has a positive impact on the hydrogen production efficiency under the current of 0.13 a–0.5 a, and the hydrogen production efficiency under the current of 0.6 a–0.9 A is not obvious. The simulation results show that the diffusion coefficient of water molecules in pure water decreases with the increase of magnetic field intensity. This is because the combination of external magnetic field and electric field makes many water molecules combine through hydrogen bonds to form different forms of water molecular chains or rings and then form a hydrogen bond grid composed of many water molecules, making the structure of water molecules more compact. Therefore, the diffusion coefficient of water molecules in pure water decreases with the increase of magnetic field intensity.

As hot clean energy, hydrogen is of great significance for new energy vehicles and oxyhydrogen fuel cells to study the influencing factors of hydrogen production from electrolytic water. In this paper, some influencing factors of electrolytic water device are experimentally studied. There are still many factors to be deeply studied in SPE electrolytic water hydrogen production system.

Data Availability

The labeled data set used to support the findings of this study is available from the corresponding author upon request.

Conflicts of Interest

The author declares that there are no conflicts of interest.

Acknowledgments

This work was supported by the Basic Science Research Program through the National Research Foundation of Korea (NRF) funded by the Ministry of Education (2019R1I1A3A0106276412).

References

[1] I. O. Baibars, M. G. Abd El-Moghny, A. S. Mogoda, and M. S. El-Deab, "Microporous film of ternary ni/co/fe alloy for superior electrolytic hydrogen production in alkaline medium," *Journal of the Electrochemical Society*, vol. 168, no. 5, Article ID 054509, 2021.

[2] Z. Zhao, L. Liu, L. Min, W. Zhang, and Y. Wang, "A facile method to realize oxygen reduction at the hydrogen evolution cathode of an electrolytic cell for energy-efficient electrooxidation," *Materials*, vol. 14, no. 11, pp. 2841–2847, 2021.

[3] X. Zhang, F. Jia, and S. Song, "Recent advances in structural engineering of molybdenum disulfide for electrocatalytic hydrogen evolution reaction," *Chemical Engineering Journal*, vol. 405, pp. 127013–127016, 2021.

[4] R. Guo, Y. Li, and M. Lv, "Nonlinear predictive filter based fault diagnosis of oxygen generation system by using electrolytic water in space station," *Acta Astronautica*, vol. 168, pp. 230–241, 2020.

[5] C. Chen, Q. Bai, J. Liu, Z. Wang, and K. Cen, "Characteristics and anode reaction of organic wastewater-assisted coal electrolysis for hydrogen production," *International Journal of Hydrogen Energy*, vol. 45, no. 41, pp. 20894–20903, 2020.

[6] L. Wu, M. Zhang, Z. Wen, and S. Ci, "V8c7 decorating cop nanosheets-assembled microspheres as trifunctional catalysts toward energy-saving electrolytic hydrogen production," *Chemical Engineering Journal*, vol. 399, no. 3, pp. 125728–125734, 2020.

[7] A. Pr, A. Sy, and B. Ls, "A review on cobalt phosphate-based materials as emerging catalysts for water splitting - sciencedirect," *Ceramics International*, vol. 47, no. 12, pp. 16385–16401, 2021.

[8] J. Koponen, V. Ruuskanen, M. Hehemann et al., "Effect of power quality on the design of proton exchange membrane water electrolysis systems," *Applied Energy*, vol. 279, no. 21, pp. 115791–115798, 2020.

[9] J. Proost, "Critical assessment of the production scale required for fossil parity of green electrolytic hydrogen," *International Journal of Hydrogen Energy*, vol. 45, no. 35, pp. 17067–17075, 2020.

[10] Z. Wang, H. Wang, S. Ji, X. Wang, B. G. Pollet, and R. Wang, "Multidimensional regulation of ni_3s_2@co(oh)_2 catalyst with high performance for wind energy electrolytic water," *Journal of Power Sources*, vol. 446, pp. 227348.1–227348.7, 2020.

[11] J. Koponen, A. Poluektov, V. Ruuskanen, A. Kosonen, M. Niemelä, and J. Ahola, "Comparison of thyristor and insulated-gate bipolar transistor -based power supply topologies in industrial water electrolysis applications," *Journal of Power Sources*, vol. 491, no. 33, pp. 229443–229449, 2021.

[12] S. Horikoshi, L. Takahashi, K. Sueishi, H. Tanizawa, and N. Serpone, "Microwave-driven hydrogen production (mdhp) from water and activated carbons (acs). application to wastewaters and seawater," *RSC Advances*, vol. 11, no. 50, pp. 31590–31600, 2021.

[13] G. De Dominici and B. Gabriel, "Analytical study of overvoltages in alkaline electrolysis and their parametric dependencies through a multi-physical model," *International Journal of Energy Research*, vol. 46, no. 3, pp. 3295–3323, 2022.

[14] S. A. Haider, M. Sajid, and S. Iqbal, "Forecasting hydrogen production potential in islamabad from solar energy using

Hindawi
Shock and Vibration
Volume 2024, Article ID 9768621, 1 page
https://doi.org/10.1155/2024/9768621

Retraction

Retracted: Research on the Bolt Positioning System Based on Multieye Vision Industrial Robots

Shock and Vibration

Received 23 January 2024; Accepted 23 January 2024; Published 24 January 2024

This article has been retracted by Hindawi following an investigation undertaken by the publisher [1]. This investigation has uncovered evidence of one or more of the following indicators of systematic manipulation of the publication process:

(1) Discrepancies in scope

(2) Discrepancies in the description of the research reported

(3) Discrepancies between the availability of data and the research described

(4) Inappropriate citations

(5) Incoherent, meaningless and/or irrelevant content included in the article

(6) Manipulated or compromised peer review

The presence of these indicators undermines our confidence in the integrity of the article's content and we cannot, therefore, vouch for its reliability. Please note that this notice is intended solely to alert readers that the content of this article is unreliable. We have not investigated whether authors were aware of or involved in the systematic manipulation of the publication process.

Wiley and Hindawi regrets that the usual quality checks did not identify these issues before publication and have since put additional measures in place to safeguard research integrity.

We wish to credit our own Research Integrity and Research Publishing teams and anonymous and named external researchers and research integrity experts for contributing to this investigation.

The corresponding author, as the representative of all authors, has been given the opportunity to register their agreement or disagreement to this retraction. We have kept a record of any response received.

References

[1] J. Kong, Q. Li, Y. Yin, C. Li, and W. Luo, "Research on the Bolt Positioning System Based on Multieye Vision Industrial Robots," *Shock and Vibration*, vol. 2022, Article ID 7563199, 11 pages, 2022.

Hindawi
Shock and Vibration
Volume 2022, Article ID 7563199, 11 pages
https://doi.org/10.1155/2022/7563199

Research Article

Research on the Bolt Positioning System Based on Multieye Vision Industrial Robots

Jun Kong, Qiang Li, Yi Yin, Cen Li, and Wei Luo

School of Mechanical, Electronic and Control Engineering, Beijing Jiaotong University, Beijing 100044, China

Correspondence should be addressed to Qiang Li; bjjdjdxy@163.com

Received 25 June 2022; Revised 15 July 2022; Accepted 19 July 2022; Published 24 August 2022

Academic Editor: Yuxing Li

In order to improve the accuracy of bolt positioning for industrial robots, this paper studies the bolt positioning system of industrial robots combined with multieye vision technology. This paper introduces three reconstruction algorithms ART, SIRT, and SART from the perspective of theory and implementation. Moreover, the projection matrix calculated with 0, 1 weighting, length weighting, and linear interpolation weighting is used for three reconstruction algorithms to carry out reconstruction experiments. In addition, this paper combines the actual working conditions of bolt positioning to construct the system of this paper and conducts system simulation research combined with the working conditions of the robot. The research shows that the bolt positioning system based on the multieye vision industrial robot proposed in this paper has a good performance in bolt positioning.

1. Introduction

Robots are mechanical devices that perform work automatically. It can either obey human commands, run preprogrammed programs, or act according to principles and programs formulated with artificial intelligence technology. Moreover, its task is to assist or replace human work in production, construction, and other works.

Literature [1] developed a bolt-fastening system for automotive engine end covers. The system takes the robot as the core, adopts an intelligent robot, and is equipped with a corresponding tightening mechanism, jacking mechanism, and pressing mechanism to ensure that the production qualification rate reaches more than 99%. At the same time, it can be applied to the tightening of bolts at other types of end caps, with high flexibility. . A bolt replacement robot for replacing the isolation switch on the high-voltage line of the power station is designed. The robot is equipped with a vision sensor, a four-axis mobile platform, and an end effector [2]. Through visual positioning, the bolts that need to be replaced can be found on the isolation plate, and mechanical disassembly and replacement of new bolts can be performed at the end. This design replaces manual work on high-voltage wires using robot operation, improves efficiency, reduces the danger of manual high-altitude work, and improves the automatic maintenance level of the power station [3]. A wind turbine tower connecting bolt inspection robot is designed, which improves the working condition of manual tightening of the connecting bolts of the wind turbine tower. Its structure consists of three parts: a circumferential motion mechanism, an adaptive mechanism, and a three-point clamping mechanism. The mechanism consists of an electric push rod and a clamp, which drives a torque wrench for maintenance [4]. This design solves the maintenance problem of wind turbines and greatly reduces maintenance costs; a bolt-tightening robot for tightening bolts has been developed. The robot is a high-power robot equipped with a 170 F gasoline engine, an electromagnetic clutch, coupling, energy storage body, reversing mechanism, etc. [5], built a control system for the robot, and completed the actual test. This design improves the work efficiency of rail fastening in railway maintenance work. Many excellent results have been achieved in the research of bolt assembly robots, but there are few types of research on light-load

vision-guided robots in production lines. At the same time, further research and development are needed for the flexible adaptive structure in the process of helical motion. Research design.

Literature [6] proposes a stereo vision ranging system integrated into a humanoid robot. The system uses the image processing library OpenCV and OpenGL to design a corresponding automatic recognition software system according to the requirements of automatic feature recognition and detection of corresponding points and uses OpenGL. Open Graphics Library shows the 3D model obtained from the reconstruction. It was finally used in the actual test of the robot and got good results, which improved the work efficiency. Literature [7] developed and tested a vision-guided grasping system for Phalaenopsis tissue culture seedlings. The system applies a binocular stereo vision algorithm to calculate the 3D coordinates of the grasping point and uses an image processing algorithm that locates the grasping point to determine the appropriate grasping point on the root. Meanwhile, his research team developed and tested a device suitable for gripping Phalaenopsis tissue culture seedlings. Finally, the binocular vision localization algorithm is integrated with the robotic grasper to construct an automatic grasping system. The experimental results show that the automatic grasping system has a success rate of 78.2% in grasping the seedlings in the proper position. The welding seam tracking and feedback technology of the welding robot are researched, and computer vision is used to identify and find the position of the welding crease and then weld the position of the crease. The system is a binocular system based on two CCD cameras. The cameras are installed on opposite sides of the outer hollow shaft to capture images of the welding seam [8]. At the same time, the electromagnetic air valve and two cylinders are used to work with the welding device. The research solves the problem of weld positioning accuracy during mechanical welding and improves the level of welding automation [9].

For the production line where the robot base and the RV reducer are connected, a binocular vision guidance scheme for assembly is designed. The scheme uses HALCON for binocular vision processing and camera calibration at the same time. Through median filtering, adaptive K-means segmentation of lab color space, template matching based on image pyramid, subpixel edge detection, and so on, the collected images are contour fitted, and the coordinates of feature points of threaded holes are obtained [10]. Finally, guide the robot to assemble; after completing the algorithm development, use VisualStudio to design control software and finally complete the research and development of the entire assembly system.

Literature [11] designed and developed a part recognition and detection system under the binocular camera and used the system to combine with an industrial robot to complete the actual grasping measurement. In this system, the contour of the part edge is identified by the improved Canny algorithm, and the feature point extraction and stereo matching are carried out by using the scale-invariant feature conversion method; the mathematical model of the pose detection system is established by using the stereo vision 3D reconstruction method. The coordinates of the parts on the worktable are obtained, and the parts are grasped through the control of programmed software. This research plays a very important role in the field of automatic loading and unloading of industrial robots [12]. In-depth research on the visual guidance technology of the bolt tightening robot was carried out, and the design of binocular software was completed on the VisualStudio platform; the three parts of the binocular target, image correction, bolt feature point extraction, and pose measurement were completed [13]. In the process of feature extraction, image preprocessing, dynamic threshold segmentation, Minkowski addition and expansion, Minkowski subtraction and erosion, subpixel precision contour, and rammer edge fitting are adopted, and finally, the six corner coordinates of the bolt are extracted to guide the robot to grasp [14].

In this paper, multi-eye vision technology is used to study the bolt positioning system of industrial robots to improve the bolt positioning effect of industrial robots.

2. Basic Principles of Binocular Vision Imaging

2.1. Physical Basis of Binocular Vision Imaging. Robotic vision light is a high-energy electromagnetic wave with a certain energy and penetrating ability, which can penetrate some substances (such as human tissue) that visible light cannot pass through, as shown in Figure 1. Generally, visible light has a longer wavelength, and when a photon hits an object, part of it is reflected and most of it is absorbed, while the wavelength of the robot's vision light is extremely short, and the photon contains high energy. The penetration of the robot's visual light is related to information such as the equivalent atomic number and density of the irradiated material, and the transmittance of the robot's visual light is stronger for the material with a lower atomic number and vice versa. The transmission of robot vision light is an important basis for binocular vision imaging.

A beam of robotic vision rays injected into a homogeneous material is considered, as shown in Figure 2(a). Considering Beer's theorem, we have

$$I = I_0 \exp(-\mu \Delta x) \Rightarrow \mu \Delta x = \ln\left(\frac{I}{I_0}\right). \quad (1)$$

It can be seen from formula (1) that the object with a high μ value causes more attenuation of the robot's visual photons than the object with a low μ value. For example, the μ of bone is higher than that of soft tissue, indicating that it is more difficult for robotic vision photons to penetrate bone than soft tissue. On the other hand, the μ value of air is almost 0, indicating that the input and output of X rays hardly change on the path through the air.

When the material scanned by the X-ray is inhomogeneous, the medium distributed along path 1 can be discretized into several continuous small blocks. When these small pieces are small enough, the medium inside the small pieces can be considered to be homogeneous and have the same attenuation coefficient. The thickness of each discrete

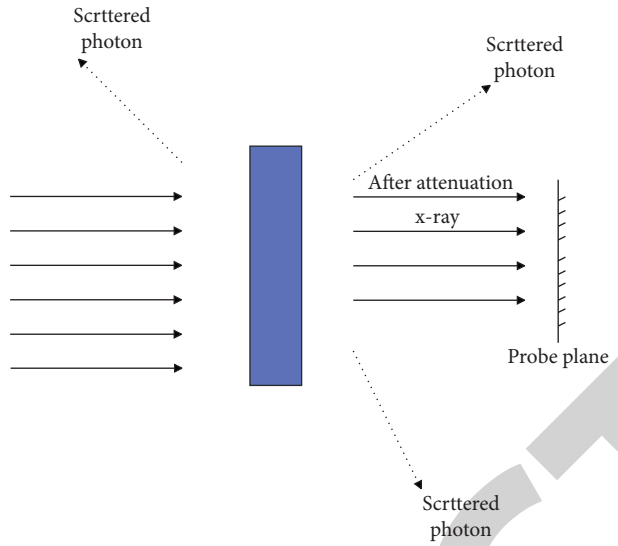

Figure 1: Schematic diagram of the material that transmits light to the robot vision.

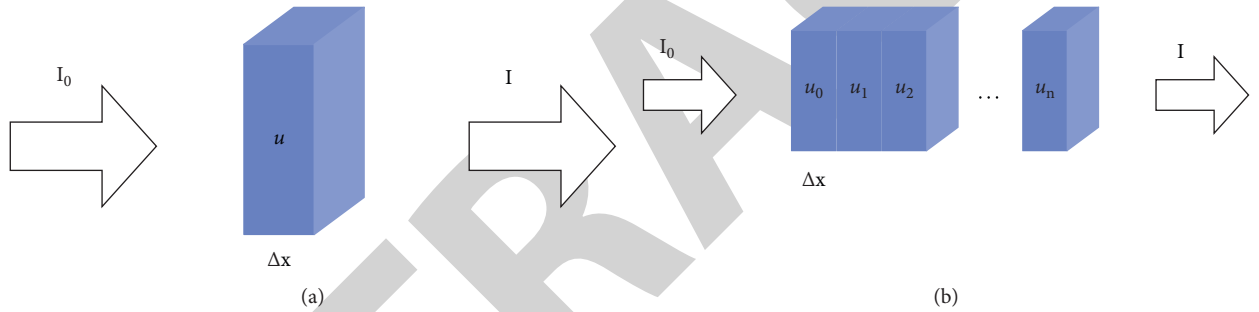

Figure 2: Schematic diagram of visual light passing through. (a) Schematic diagram of robot vision light passing through homogeneous material. (b) Schematic diagram of the robot's vision of light passing through inhomogeneous materials.

small block is assumed to be Δx, and the attenuation coefficients of each discrete small block are $\mu_0, \mu_1, \mu_2, \mu_3, \ldots, \mu_n$, respectively, as shown in Figure 2.

The ray intensity of the robot vision light after passing through the first small block is I_1, and the ray intensity after passing through the second block is $I_2 \ldots$.

The final transmission intensity is I_n, then there are

$$I_1 = I_0 \exp(-\mu_1 \Delta x), \tag{2}$$

$$I_2 = I_1 \exp(-\mu_2 \Delta x). \tag{3}$$

Substituting formulas (2) into (3), we get

$$I_2 = I_0 \exp(-(\mu_1 + \mu_2)\Delta x). \tag{4}$$

It continues to accumulate attenuation values along the propagation direction of the robot's vision light until the final transmission intensity I_n of the robot's vision light when it leaves the illuminated object, as shown in the following equation:

$$I_n = I_0 \exp(-(\mu_1 + \mu_2 + \cdots + \mu_n)\Delta x). \tag{5}$$

We take the positive exponent of formula (5) and express it in summed form, we get

$$p = \sum_{i=1}^{n} \mu_i \Delta x = \ln\left(\frac{I_0}{I_n}\right). \tag{6}$$

p in formula (6) is the projection. If the incident intensity I_0 and outgoing intensity I_n of the X ray are known, a linear formula with $\mu_i\,(i = 1, 2, \ldots, n)$ as the last known is obtained according to formula (6). When $\Delta x \longrightarrow 0$, formula (6) can represent the summation of continuous variation, and its integral form is

$$p = \ln\left(\frac{I_0}{I_n}\right) = \int_L \mu(l). \tag{7}$$

In formula (7), $\mu(l)$ is a continuous function of the decay rate with respect to path l. The process of finding the attenuation coefficient function $\mu(l)$ by projection is called back projection. If the two-dimensional density function $f(x, y)$ is used to describe the attenuation rate of the two-dimensional plane, then the problem of binocular vision

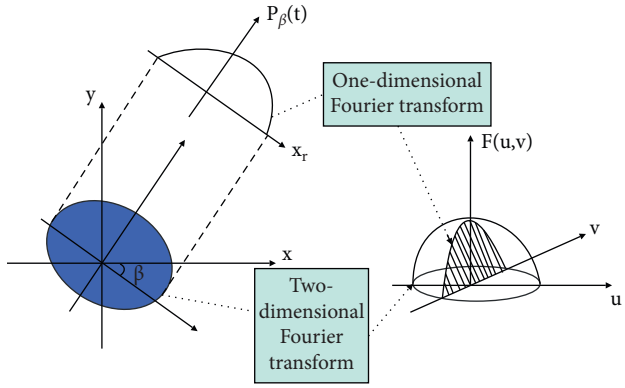

Figure 3: Schematic diagram of the central slice theorem.

imaging can be expressed as the measured linear integral of an object is given, and the decay rate at each point is calculated to produce two-dimensional density data.

2.2. Analytical Reconstruction Algorithm. Two-dimensional Radon transform is a projection transform of straight line integral, and it can be defined in many forms. This paper takes the most commonly used case as an example.

We assume that in the plane area R^2, any point (x, y) can be represented by polar coordinates (ρ, θ), ρ represents the distance from the line to the origin, θ represents the angle between the straight line l and the positive y-axis, and the function $f(x, y)$ is the image to be reconstructed. We assume that any straight line $l \in R^2$, then the two-dimensional Radon transform of the function $f(x, y)$ is defined as

$$\begin{aligned} p &= \int_l f(x, y)\mathrm{d}l = \int_l \widehat{f}(r, \theta)\mathrm{d}l \\ &= \int_{-\infty}^{+\infty} \widehat{f}\left(\sqrt{L^2 + l^2}, \phi + \tan^{-1}\frac{l}{L}\right)\mathrm{d}l. \end{aligned} \tag{8}$$

The formula of the straight line can be expressed as $\rho = x\cos\beta + y\sin\beta$ in polar coordinates, then formula (8) can be further expressed as

$$\begin{aligned} p &= \int_{-\infty}^{+\infty} f(x, y)\mathrm{d}l \\ &= \int_{-\infty}^{+\infty}\int_{-\infty}^{+\infty} f(x, y)\delta(x\cos\beta + y\sin\beta - \rho)\mathrm{d}x\mathrm{d}y. \end{aligned} \tag{9}$$

Among them, (x, y) represents the position of the reconstructed pixel in the Cartesian coordinate system, and $\delta(x)$ represents the sampling function. This process is the integration of the image in a straight line. According to the previous physical principle of the X-ray, we can abstract the attenuation process of the X-ray into this integration process, and the projection value of the X-ray is the value of the Radon transform at angle β. If the projection is performed at multiple angles, the Radon value of each angle can be obtained, and the two-dimensional image $f(x, y)$ of the original plane can be reconstructed by performing the Radon inverse transformation on these obtained Radon values.

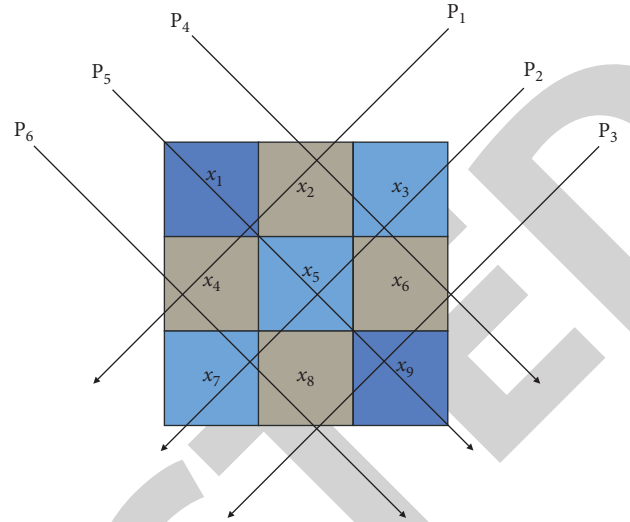

Figure 4: Schematic diagram of discretized image projection.

The formula for the two-dimensional inverse Radon transform is

$$f(x, y) = \widehat{f}(r, \theta) = \frac{1}{2\pi^2}\int_0^{\pi}\int_{-\infty}^{+\infty}\frac{1}{r\cos(\theta - \beta) - \rho}\frac{\partial p}{\partial \rho}\mathrm{d}\rho\mathrm{d}\beta. \tag{10}$$

Three-dimensional Radon transform is a generalization of two-dimensional, extending the line integral in two-dimensional to an area integral, each area integral corresponds to a point in Radon space. This point is the intersection of the plane with the normal to the plane through the origin. The three-dimensional Radon transform space is composed of all transform values.

Figure 3 shows the Fourier reconstruction method, which is also the derivation basis of the commonly used filtered back projection (FBP) reconstruction algorithm. As can be seen from the figure, one-dimensional Fourier transform is first performed for each projection data:

$$f(x, y) = \int_{-\infty}^{+\infty} P_\beta(t)\mathrm{e}^{-j2\pi\omega t}\mathrm{d}t. \tag{11}$$

$P_\beta(t)$ in formula (11) is to calculate the projection of $f(x, y)$ on the β direction according to the Radon transform:

$$P_\beta(t) = \int_{-\infty}^{+\infty}\int_{-\infty}^{+\infty} f(x, y)\delta(x\cos\beta + y\sin\beta - \rho)\mathrm{d}x\mathrm{d}y. \tag{12}$$

2.3. Iterative Reconstruction Algorithm. The filtered back projection (FBP) algorithm has certain limitations in practical application. For example, it requires that the projection data must be completely and uniformly distributed, the formula of the filtered back projection is continuous, and the image must be discretized during implementation. In this case, an iterative algorithm is a good choice.

The biggest difference between the concept of the iterative reconstruction algorithm and the analytical reconstruction algorithm is that the former discretizes continuous

images $f(r, \theta)$. The algorithm divides the entire image area into $J = n \times n$ finite number of pixels, which are represented by $\widetilde{f}(r, \theta)$. Figure 4 shows the process of reconstructing the image after the ray is discretized:

Among them, $x_1, x_2, \ldots, x_9$ represent the corresponding pixel values. It can be seen from the figure that the sum of the rays is

$$\begin{aligned} p_1 &= w_{11}x_1 + w_{12}x_2 + \cdots + w_{19}x_9, \\ p_2 &= w_{21}x_1 + w_{22}x_2 + \cdots + w_{29}x_9, \\ p_3 &= w_{31}x_1 + w_{32}x_2 + \cdots + w_{39}x_9, \\ &\cdots \\ p_6 &= w_{61}x_1 + w_{62}x_2 + \cdots + w_{69}x_9. \end{aligned} \tag{13}$$

Formula (13) can be expressed in a more compact form:

$$p_i = \sum_{j=1}^{9} w_{ij}x_j \quad i = 1, 2, \ldots, 6. \tag{14}$$

Alternatively, it can be expressed in matrix representation:

$$\mathbf{p} = \mathbf{W}\mathbf{x}. \tag{15}$$

In formula (15), $\mathbf{p} = [p_1, p_2, \ldots, p_6]^T$, $\mathbf{x} = [x_1, x_2, \ldots, x_9]^T$, W is the matrix of 6×9. Formulas (13) to (15) are derived from the special case of 9 pixels and 6 rays. We then generalize it to the general case and assume the general case of J pixels and I rays. At this time, $\mathbf{x}$ is the J-dimensional vector, which is called the image vector, I is the I-dimensional vector, which is called the measurement vector, and $\mathbf{W}$ is the $I \times J$ matrix, which is called the projection matrix.

The task of iterative reconstruction is to find $\mathbf{x}$ according to the measured $\mathbf{p}$, and the known projection matrix $\mathbf{W}$ ($\mathbf{W}$) can be determined according to the system geometry, focal spot shape, detector response, and other physical parameters of the binocular vision system). w_{ij} in (13 to (15) represents the weighting factor of i-ray to j pixel, and there are many ways to calculate the weighting factor. In the simplest case, the weighting factor is set to 0 or 1 according to whether the ray passes through the pixel, as shown in the following formula:

$$w_{ij} = \begin{cases} 1, & I - \text{ray passes through } j - \text{pixel}, \\ 0, & \text{other}. \end{cases} \tag{16}$$

The ray can also be regarded as having a certain width, and the width is assumed to be τ (usually taking the pixel width δ). This thick line covers a part of the area of the pixel, and the ratio of the coverage area to the area of the pixel is the weighting factor of the pixel to the projection of the ray. For example, the gray value of the j pixel is x_i, the area of the overlapping area between the i ray and the j pixel is Δs, and the ratio of it to the pixel area δ_2 is $w_{ij} = \Delta s/\delta_2$, which is the weighting factor of the i ray to the j pixel.

With the above foundation, the reconstruction problem of the binocular visual image can be transformed into a linear formula-solving process. The most intuitive way is to find the inverse matrix W^{-1} of matrix W, so as to get

$$\mathbf{x} = W^{-1}\mathbf{p}. \tag{17}$$

The second solution is to accumulate all the ray values passing through the j pixel to get the j pixel value:

$$x_i = \sum_{i=1}^{I} w_{ij}p_i, \quad j = 1, 2, \ldots, J. \tag{18}$$

It can be written as a matrix problem as

$$\mathbf{x} = \mathbf{W}^T\mathbf{p}. \tag{19}$$

Formula (19) is the form of back-projection reconstruction in the case of discrete pixels, and artifacts are very serious when using this reconstruction formula. However, formula (19) helps us understand the iterative reconstruction algorithm. So far, the main problems encountered by iterative reconstruction may be (1) generally, the number of pixels and the number of rays are extremely large, and it is difficult to directly find $\mathbf{W}^{-1}$. Even if $\mathbf{W}^{-1}$ is stored as a sparse matrix, it still requires a large amount of calculation; (2) in some cases, the number of projections is much smaller than the number of pixels, and the linear formula system may have an infinite number of solutions; (3) in the actual acquisition process, it may be affected by factors such as physical deviation or projection noise, and the reconstruction result cannot be obtained. Therefore, it is necessary to introduce an error value and estimate a set of solutions to make it optimal under a certain optimal criterion. Therefore, formula (15) can be modified as follows:

$$\mathbf{p} = \mathbf{W}\mathbf{x} + \mathbf{e}. \tag{20}$$

Here, e is the error vector, which can be measurement deviation and additional noise, such as detector electronics noise. According to the principle of numerical calculation and optimization, the estimation process can be implemented iteratively, which generally includes the following steps: (1) the image is discrete and initialized; (2) selection of iterative methods; (3) selection of optimal criteria. The iterative methods are as described above, mainly including classical iterations (such as ART, SIRT, and others) and statistical-based iterations (such as EM, MAP, and others). Step 3 also has more options: least squares criterion, maximum uniformity and smoothing criterion, maximum entropy criterion, and Bayesian criterion.

2.4. Evaluation Criteria for Reconstruction Algorithms. When using simulated data for testing, since the exact parameters of the simulated data are known, the reconstructed data can be accurately numerically compared with the original data to make an objective evaluation of the reconstruction quality. A commonly used simulation data model is the Shepp. LogaJl standard head model, which is

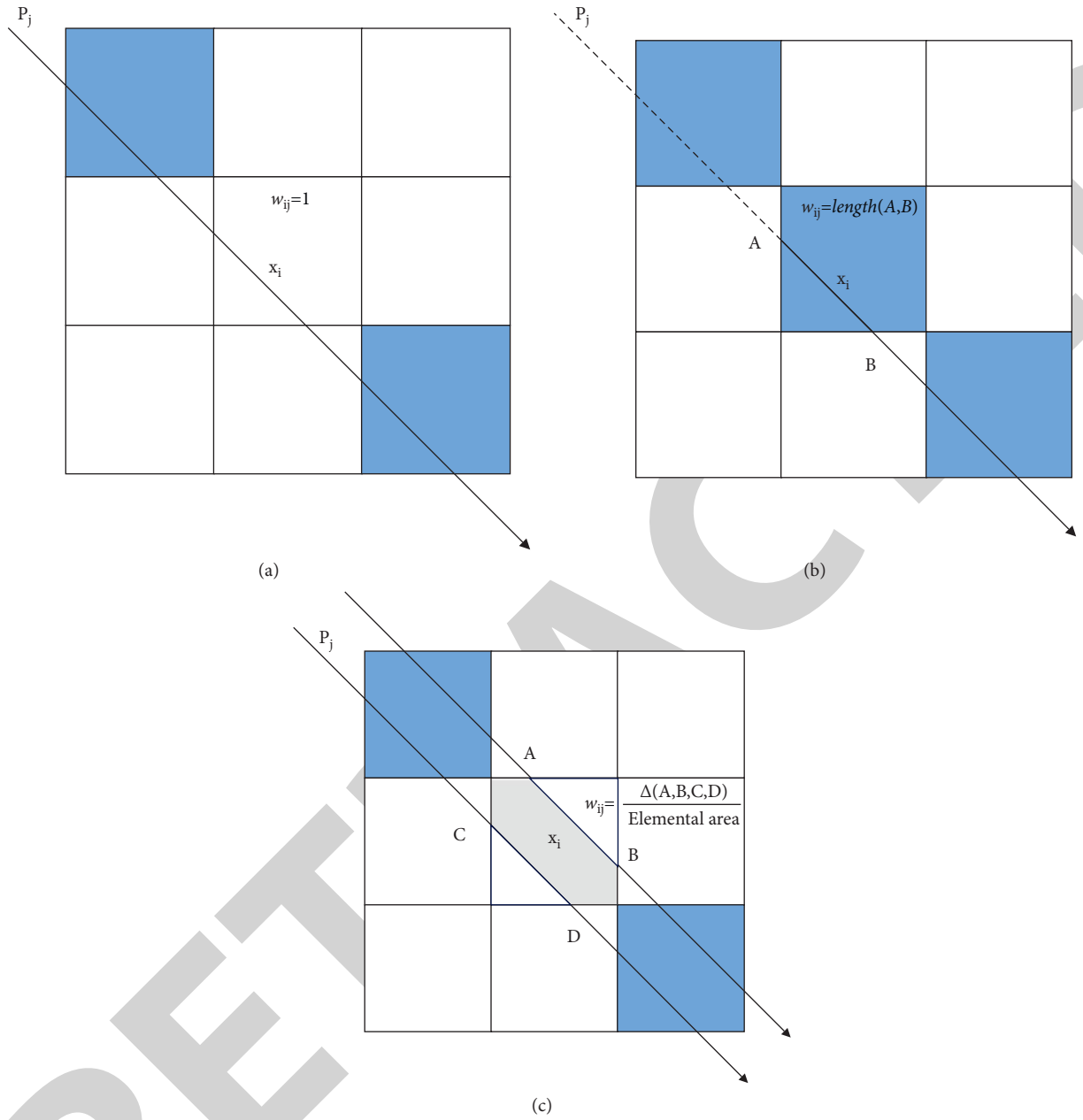

Figure 5: Three basic projection matrix calculation methods. (a) Projection matrix based on 0, 1. (b) Length-based projection matrix. (c) Area-based projection matrix.

composed of many ellipses with different sizes and densities. Common image numerical evaluation criteria are

(1) The measured value ε of the image similarity coefficient is as follows:

$$\varepsilon = \frac{\sum_{i=1}^{N}\left(x_i - \overline{x}\right)\left(x_i^* - \overline{x^*}\right)}{\left[\sum_{i=1}^{N}\left(x_i - \overline{x}\right)^2 \sum_{i=1}^{N}\left(x_i^* - \overline{x^*}\right)^2\right]^{1/2}}. \tag{21}$$

(2) The normalized RMS distance measurement d is as follows:

$$d = \left[\frac{\sum_{i=1}^{N}\left(x_i - x_i^*\right)^2}{\sum_{i=1}^{N}\left(x_i - \overline{x}\right)^2}\right]^{1/2}. \tag{22}$$

(3) The normalized mean absolute distance measurement r is

$$r = \frac{\sum_{i=1}^{N}\left|x_i - x_i^*\right|}{\sum_{i=1}^{N} x_i}. \tag{23}$$

(4) The image signal-to-noise ratio (SNR) is

$$\text{snr} = 10 \times \lg\left(\frac{\sum_{i=1}^{N} x_i^2}{\sum_{i=1}^{N} \left(x_i - x_i'\right)^2}\right). \tag{24}$$

Among them, N is the number of pixels in the reconstructed image; x_i is the gray value of the x_{i} pixel in the model image; x_i^* is the gray value of the x_{i} pixel in the reconstructed image; $\overline{x}$ is the average gray value in the model image; $\overline{x^*}$ is the average gray value in the reconstructed image.

The four measurements above highlight different aspects of image quality. The image similarity coefficient ε reflects the similarity between the reconstructed image and the simulated image. The larger the ε is, the more similar the two images are, and when ε is 1, the two images are identical. The normalized RMS distance measurement value d is more sensitive to reflect the error of the local situation, and if there is a large deviation of individual pixels, it will lead to a large d. The normalized mean absolute distance measurement value r is more sensitive to reflect the small error situation of most points. Contrary to d, it emphasizes the importance of more small errors rather than a small number of large errors. The signal-to-noise ratio (SNR) measures the ratio of the image signal to the noise signal, often expressed in decibels.

2.5. Calculation of Projection Matrix. The exact projection matrix plays a decisive role in reconstructing an image. Among all the methods for calculating projection matrices, the simplest model is the 0,1 model, as shown in Figure 5(a). We assume that the projection matrix entry w_{ij} is 1 when the ray p_j passes through the pixel, x_i, and 0 otherwise. Figure 5(b) shows the projection matrix calculation based on length weighting. The value of the projection matrix entry w_{ij} is the value of the length of the ray p_j intercepted by the pixel x_i. Figure 5(c) shows the projection matrix calculation based on area weighting. In this model, the ray is regarded as having a certain width, and the value of the projection matrix item w_{ij} is the ratio of the area covered by the ray p_j of the pixel x_i to the pixel area. In practical applications, the internal attenuation of objects is continuous, and the attenuation values inside the discrete pixel cells are not completely equal. Therefore, the reconstructed image is only a discretized approximation of the real image, and the reconstructed image may be grainy. In theory, we can reconstruct a continuous description of the original image by using interpolation methods.

As shown in Figure 6, a ray p_i is injected into the reconstruction area and is sampled at equal intervals, and the center of the interpolation kernel function $h(u, v)$ is placed on the sampling point. All reconstructed pixels in the range of the revalued kernel are accumulated and appropriately weighted with the revalued kernel. Figure 6 shows that the sampled value s_{ik} at the point $(X(s_{ik}), Y(s_{ik}))$ is calculated from the adjacent pixel values. The value of s_{ik} is calculated by formula (6):

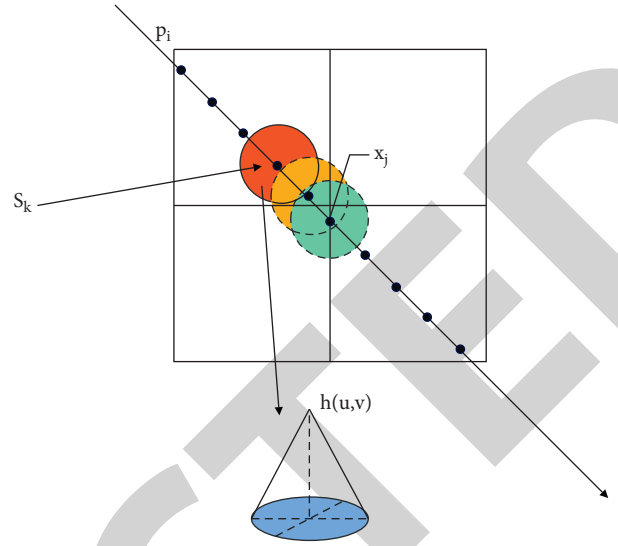

Figure 6: Schematic diagram of the calculation of the sampling value s_{ik} at the point $(X(s_{ik}), Y(s_{ik}))$.

$$s_{ik} = \sum_i h\left(X(s_{ik}) - X(x_i), Y(s_{ik}) - Y\left(x_j\right)\right) \times x_i. \tag{25}$$

$$s_{ik} = \sum_j h\left(X(s_{ik}) - X\left(x_j\right), Y(s_{ik}) - Y\left(x_j\right)\right) \times x_j. \tag{26}$$

The value of the projected pixel value p_i corresponding to the ray p_i is the accumulation of all the sampling values s_{ik} along the ray:

$$p_i = \sum_k \sum_j h\left(X(s_{ik}) - X\left(x_j\right), Y(s_{ik}) - Y\left(x_j\right)\right) \times x_j. \tag{27}$$

Formula (26) is a discrete approximation of formula (27):

$$p_i = \int \left(\sum_j h\left(X(s_{ik}) - X\left(x_j\right), Y(s_{ik}) - Y\left(x_j\right)\right) \times x_j \right) \mathrm{d}s_i. \tag{28}$$

Formula (27) is rearranged, and we get

$$p_i = \sum_j x_j \int h\left(X(s_{ik}) - X\left(x_j\right), Y(s_{ik}) - Y\left(x_j\right)\right) \mathrm{d}s_i. \tag{29}$$

Formula (28) is shown in Figure 7. Similar to formula (14), a projected pixel value p_i is calculated as follows:

$$p_i = \sum_k x_j \cdot w_{ij}. \tag{30}$$

Therefore, the weights are calculated by integrating the value kernel along the ray:

$$w_{ij} = \int h\left(X(s_{ik}) - X\left(x_j\right), Y(s_{ik}) - Y\left(x_j\right)\right) \mathrm{d}s_i. \tag{31}$$

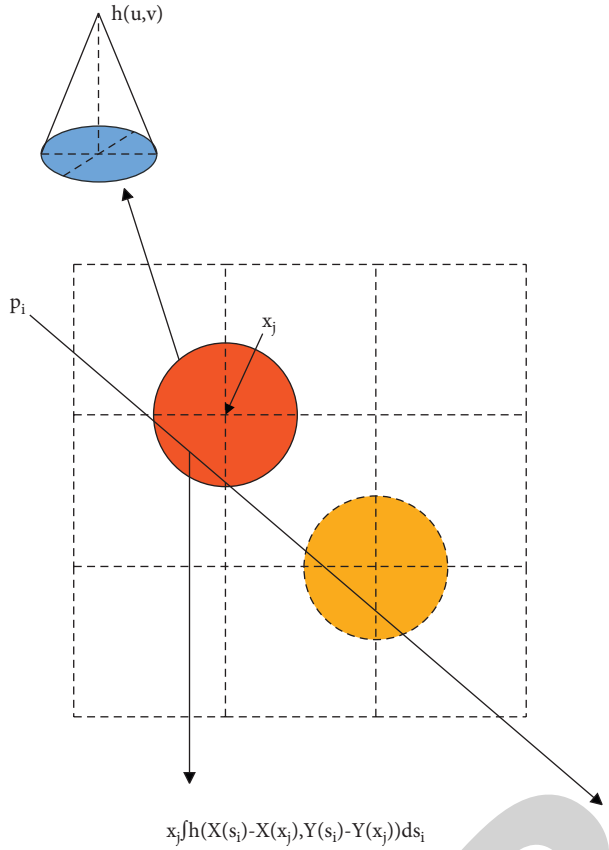

Figure 7: Schematic diagram of interpolation calculation of pixel x_j and ray p_i.

2.6. Algebraic Reconstruction Method (ART). The algebraic reconstruction algorithm (ART) is proposed to solve the problem of 3D object reconstruction. ART can be written as a linear geometry problem with $\mathbf{Wx} = \mathbf{p}$. Here, $\mathbf{x}$ is an unknown ($N \times 1$-dimensional) column vector to hold all $N = n^3$ voxels in the reconstruction region of size $n \times n \times n$. $\mathbf{p}$ is an R-dimensional column vector, and R is obtained by multiplying the number of pixels of each projection R_m by the number of projections M in the set of total projected images P_ψ, that is, $R = R_m \times M$. P_ψ refers to the set of all projected images during one scan. W is a $R \times N$ projection matrix, and the element w_{ij} in $\mathbf{W}$ represents the influence of the voxel v_j on the ray r_i. $\mathbf{Wx} = \mathbf{p}$ can be written in the form of a linear system of formulas in formula (13). As mentioned above, it is very difficult to solve this linear system of formulas directly. So, here we introduce Kaczmarz's method of solving this system of linear formulas.

The expression for the update process of the reconstruction region x is shown in formula (31):

$$x_j^{k+1} = x_j^k + \lambda \frac{p_i - \sum_{n=1}^{N} w_{in} x_n^k}{\sum_{n=1}^{N} w_{in}^2} w_{ij}. \quad (32)$$

λ in formula (31) is a relaxation factor whose value range is in the (0,1] interval. But in general, if the λ value is too close to 0, it will lead to overoptimization. The algorithm calculates the formulas in formula (18) in sequence. After completion, some reconstructed pixels may not necessarily meet the convergence conditions, and the next iteration can be performed in the same way. Figure 8 shows the geometric process of the Kaczmarz method. The two straight lines in the figure can be expressed as two linear formulas, and the process shown in the figure is the solution process.

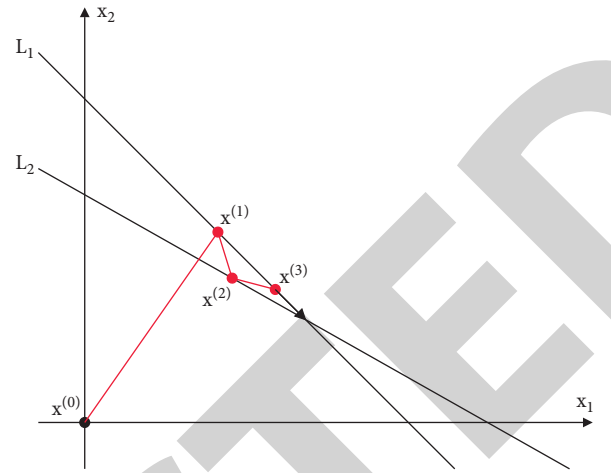

Figure 8: Schematic diagram of the solution process of the Kaczmarz method.

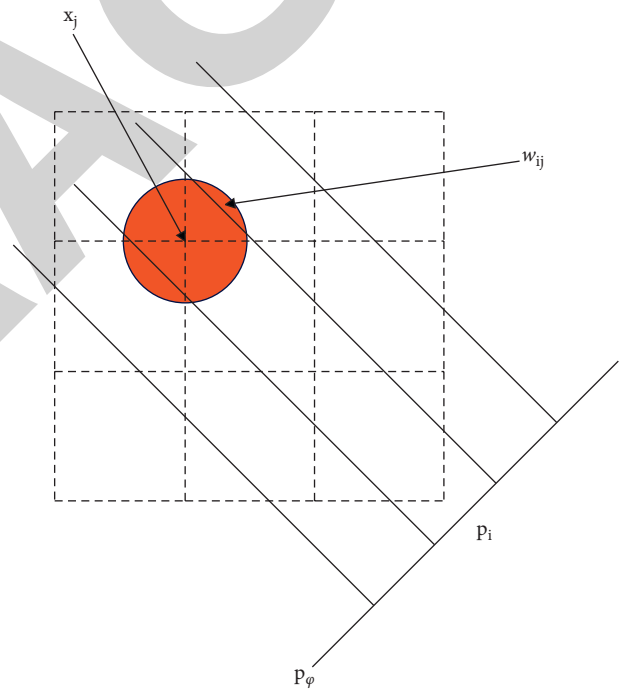

Figure 9: Schematic diagram of SART projection matrix calculation.

2.7. Combined Reconstruction Method (SIRT). The joint iteration method (SIRT) was proposed by Gilbert shortly after ART was proposed, and it is a parallel computing form of the ART algorithm. In this method, all the pixels of a certain

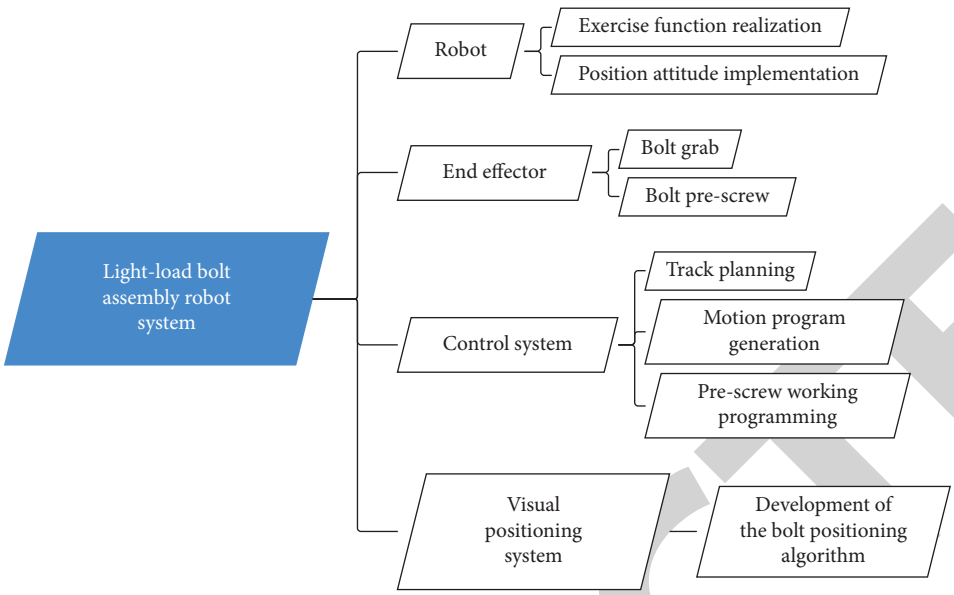

Figure 10: Robot system scheme composition.

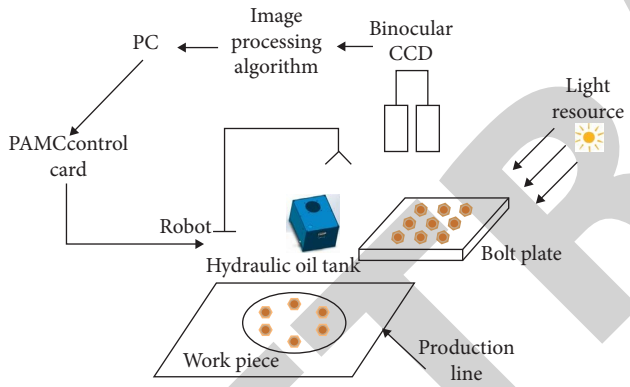

Figure 11: Schematic diagram of the workflow of the robot.

projection p are calculated first, and then the voxels of the entire reconstruction area are updated. Before the updated value is added to the voxel value, it needs to be weighted and normalized with the weighted value.

As shown in formula (19), if w is a nonsingular matrix, its least squares solution is

$$\mathbf{x} = \left(\mathbf{W}^T\mathbf{W}\right)^{-1}\mathbf{W}^T\mathbf{p}. \tag{33}$$

Among them, $\mathbf{W}^T\mathbf{p}$ represents the back-projection operation of $\mathbf{p}$. If $(\mathbf{W}^T\mathbf{W})^{-1}$ is viewed as a two-dimensional filter, formula (32) is the aforementioned two-dimensional filtered back-projection. Formula (32) can be transformed into

$$\mathbf{x} = \mathbf{W}^T\left(\mathbf{W}\mathbf{W}^T\right)^{-1}\mathbf{p}. \tag{34}$$

In formula (33), $(\mathbf{W}\mathbf{W}^T)^{-1}$ is a one-dimensional ρ filter, which filters $\mathbf{p}$. Formula (33) is solved iteratively:

Table 1: Statistical table of the accuracy of bolt positioning based on multivision industrial robots.

Num	Accuracy (%)
1	98.6
2	97.8
3	97.4
4	99.2
5	99.5
6	97.9
7	97.2
8	99.7
9	97.2
10	97.9
11	98.0
12	99.1
13	98.9
14	100.0
15	97.2
16	97.3
17	99.5
18	98.6
19	98.5
20	98.7
21	99.4
22	98.0
23	98.9
24	97.1
25	98.1
26	97.7
27	97.8
28	98.9
29	97.8
30	97.9
31	99.9
32	99.9
33	98.3
34	98.8
35	98.1
36	98.2

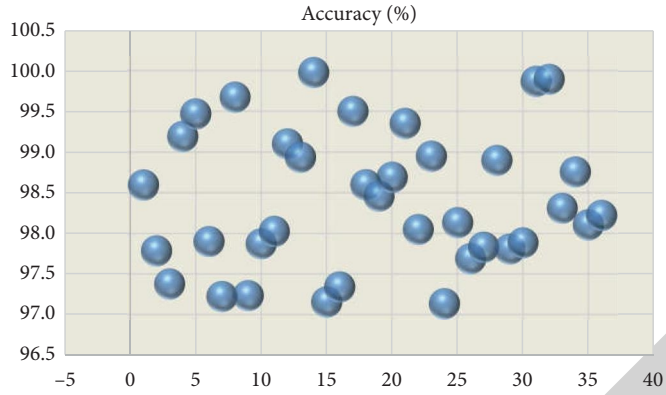

Figure 12: Statistical diagram of the accuracy of bolt positioning based on multieye vision industrial robots.

$$\begin{cases} \mathbf{x}^0 = \mathbf{W}^T\mathbf{p}, \\ \mathbf{x}^{k+1} = \mathbf{x}^k + \lambda^k\left(\mathbf{W}^T\mathbf{p} - \mathbf{W}^T\mathbf{W}\mathbf{x}^k\right) \\ = \mathbf{x}^k + \lambda^k\mathbf{W}^T\left(\mathbf{p} - \mathbf{W}\mathbf{x}^k\right). \end{cases} \tag{35}$$

In formula (34), the projection value $\mathbf{p}$ is used as the initial value of the back projection. At the $k+1$-th iteration, the algorithm uses the k-th iteration result $\mathbf{x}^k$ to add the correction value to obtain $\mathbf{x}^{k+1}$, which is the back projection $\mathbf{W}^T(\mathbf{p} - \mathbf{W}\mathbf{x}^k)$ of the correction value and the kth-estimated error vector. Thus, the correction value for each voxel is the sum of the error values for all rays passing through that voxel, not just one ray. Therefore, the correction process of SIRT is called a point-by-point correction. This is the biggest difference from the ART algorithm and the fundamental reason why the SIRT algorithm can suppress noise; some random errors are averaged out by the common contribution of all rays passing through the voxel. In order to facilitate the iterative calculation, SIRT can also be rewritten as

$$x_j^{k+1} = x_j^k + \lambda \sum_{p_i \in P_\varphi} \left(p_i - \sum_{n=1}^{N} w_{in} x_n^k \right) w_{ij}. \tag{36}$$

2.8. Joint Algebraic Reconstruction Method (SART). The SART algorithm does not correct each pixel (each ray) of the projected image, but it first calculates the projected image of the entire reconstructed area (denoted as P_φ at the angle φ). Each pixel value in P_φ contributes to the corrected value of each voxel, and the updated value of each voxel is obtained by accumulating these contributions on each voxel. If the correction terms are simply added, the noise that may exist in the projected image will be added to the reconstructed image to produce artifacts, so weighting needs to be performed when updating. Figure 9 is a schematic diagram of the SART projection matrix calculation.

The way SART updates the reconstruction area $\mathbf{x}$ can be expressed in the following form:

$$x_j^{k+1} = x_j^k + \frac{\sum_{p_i \in P_\varphi} \left(\lambda\left(\left(p_i - \sum_{n=1}^{N} w_{\text{in}} x_n^k \right) / \sum_{n=1}^{N} w_{\text{in}} \right) \right) w_{ij}}{\sum_{p_i \in P_\varphi} w_{ij}}. \tag{37}$$

There are two significant differences between formulas (36) and (31) : 1. The correction term for a particular voxel x_j is calculated by calculating the adjacent pixels p_i in the projected image and weighting the influence of the pixel p_i on each voxel by the coefficient w_{ij}. 2. Although the ART method guided by Kaczmarz's method requires the sum of squared weights, the idea of SART regards ART as the inverse process of volume rendering.

3. Bolt Positioning of Industrial Robots Based on Multieye Vision

The whole scheme is centered on the robot, with the end effector with grasping and prescrewing functions. The control system is responsible for the implementation of trajectory motion, grasping, and prescrewing, and the vision system realizes the positioning of parts. The whole scheme is shown in Figure 10.

Common robot types include Cartesian robots, cylindrical coordinate robots, articulated robots, SCARA robots, spherical robots, and so on, as shown in Figure 11. The articulated six-degree-of-freedom robot is the most common one and plays an important role in industrial production. The SCARA plane articulated robot has the least interference in space and has the optimal structural solution.

Based on the above, the effect of the bolt positioning system based on the multivision industrial robot proposed in this paper is verified, and the bolt positioning accuracy is calculated. A total of 36 groups were marked with 1000 bolts in each group, and the test results were obtained as shown in Table 1 and Figure 12.

From the above research, it can be seen that the bolt positioning system based on the multieye vision industrial robot proposed in this paper has a good performance in bolt positioning.

Hindawi
Shock and Vibration
Volume 2022, Article ID 4648311, 13 pages
https://doi.org/10.1155/2022/4648311

Research Article

An Enhanced Gated Recurrent Unit-Based Adaptive Fault Diagnosis of Rotating Machinery

Zhen Li,[1] Saleem Riaz,[2] Muhammad Waqas,[3] and Munira Batool[4]

[1]*Department of Automotive Engineering, Sichuan Vocational and Technical College Communications, Chengdu City, Sichuan Province 611130, China*
[2]*Sool of Automation, Northwestern Polytechnical University, Shaanxi, Xi'an, China*
[3]*School of Electrical Engineering, Beijing University of Technology, No. 100 Ping Le Yuan, Beijing 100124, China*
[4]*Department of Electrical Engineering, University of Engineering and Technology, Taxila, Pakistan*

Correspondence should be addressed to Munira Batool; munira.batool@uettaxila.edu.pk

Received 14 May 2022; Revised 1 July 2022; Accepted 8 July 2022; Published 8 August 2022

Academic Editor: Xiaoxi Ding

As the most basic component of rotating machinery, rolling bearing frequently works in harsh environments and complex working conditions, and its health status affects seriously the working efficiency. The health statuses of rolling bearing can not only reduce equipment maintenance costs but also contribute to reducing major accidents. Based on this, an adaptive diagnosis method that combines deep gated recurrent unit (DGRU) with wavelet packet decomposition (WPD) and extreme learning machine (ELM) is proposed for rolling bearing. Firstly, WPD is utilized to eliminate the noise of data. Secondly, DGRU is designed to extract the representative features of denoised data. Finally, ELM is utilized to output the diagnosis results. Massive results prove that the superiority and robustness of our approach outperform existing popular methods. Additionally, the proposed method can also achieve powerful antinoise ability.

1. Introduction

The health state of rotating parts directly affects the operation reliability of the whole mechanical system [1–3]. Once the rotating parts fail, it will cause serious accidents. Machinery and equipment are widely used in various industrial scenarios and electrified transmission systems, and sometimes, this equipment may run under unfavorable conditions, such as high temperature, high humidity, and high load environment, which will eventually lead to equipment failure and cause high maintenance of high maintenance cost, serious property loss, and safety hazards. The faults of mechanical equipment can usually be attributed to different types of faults, including driving inverter faults, stator faults, rotor faults, and bearing failures. According to statistics, bearing faults are the most common types of faults, and the incidence of failure reaches 30% to 40% [4–6]. Since bearing is the most vulnerable parts of mechanical equipment, the diagnosis of accurate bearing faults has been a study of engineers and scientists in the past few decades. Therefore, an effective rotating machinery condition monitoring and fault identification system are established to ensure the safe operation of equipment and personnel safety. As the most basic component, bearings frequently work in harsh environments and complex working conditions, and its health status affects seriously the working efficiency [7–10]. The health statuses of rolling bearing can not only reduce equipment maintenance costs but also contribute to reducing major accidents [11, 12].

Fault diagnosis methods based on deep learning are booming. This method is based on data-driven methods and integrates feature learning and intelligent recognition. Compared with traditional methods, it gets signal preprocessing and expert knowledge, especially when analyzing massive monitoring data. Bearing fault diagnosis has long been a hot topic of research [13–15]. Deep learning methods have made lots of achievements on the advent of avoiding extracting manually features [16–19]. However, most of

these models can exhibit excellent performance under the premise that the data have the same data distribution. Unfortunately, it is difficult or even unrealistic to meet the premise when considering complicated operating conditions, the degradation of equipment performance [20–23]. The diagnosis performance of most deep learning models will be greatly reduced when the premise is not accessible. Some researchers try to use fine-tuning algorithm or retraining model strategy to tackle the above issue, but a few labeled target data still need to be provided. Collecting labeled data requires lots of expenses or is even impossible in actual scenarios. Hence, it is very necessary to explore some promising methods that can apply the knowledge from relevant areas to solve problems. The generative adversarial network (GAN) was innovatively designed by Goodfellow et al., which utilizes the adversary between generators and discriminators for generating data with the same distribution as the raw. However, the adversarial mechanism renders the model challenging to be in equilibrium. Hence, many scholars have offered research solutions for further improving the GAN model. Radford et al. [24] proposed deep convolutional generative adversarial networks (DCGANs) fusing CNN with GAN, which avoids the GAN model to converge the learned data distribution to the same one.

Unlike DAE, DBN, CNN, and GAN, RNN is still in its infancy in diagnosis field. The main reason is conventional RNN that has an unignored problem-gradient vanishing [25]. Gated recurrent unit (GRU) can solve this problem [26]. GRU, as the newest variant of RNN, has achieved huge success in fault diagnosis issues [27, 28]. Thus, in this paper, GRU-based network is developed to effectively solve problems. However, the vibration signals are always contaminated by the noise that heavily influence the diagnosis performance of network [29]. Thus, wavelet packet decomposition (WPD) that has been recognized as an effective vibration signals denoising method is used for eliminating the noise of vibration signals [30–34].

An adaptive diagnosis method that combines deep gated recurrent unit (DGRU) with wavelet packet decomposition (WPD) and extreme learning machine (ELM) is proposed for rolling bearing. Firstly, WPD is utilized to eliminate the noise of data. Secondly, DGRU is designed to extract the representative features of denoised data. Finally, ELM is utilized to output the diagnosis results. Massive results prove that the superiority and robustness of our method outperform existing popular methods. Additionally, the proposed method can also achieve powerful antinoise ability.

The specific arrangements of this paper are as follows: Section 2 describes basic theoretical knowledge. A concrete introduction of our method is given in Section 3. Section 4 analyzes the effectiveness. Conclusions are generalized in Section 5.

2. The Brief Theory of Gated Recurrent Unit

Similar to long short-term memory neural network (LSTM), gated recurrent unit (GRU) is also a method proposed to solve the problem, but it is simpler than LSTM [25, 26]. GRU uses an update gate and a reset gate. These two gates together determine the output of GRU [35]. The specific structure is shown in Figure 1.

$$\begin{aligned} z_t &= \sigma\left(E_z X_t + F_z Y_{t-1}\right), \\ r_t &= \sigma\left(E_r X_t + F_r Y_{t-1}\right), \\ H_t &= \tanh\left(E x_t + F\left(r_t Y_{t-1}\right)\right), \\ Y_t &= \left(1 - z_t\right) Y_{t-1} + z_t H_t, \end{aligned} \tag{1}$$

where σ and tanh denote the sigmoid and tangent activation functions. E_z, E_r, E, F_z, F_z, and F are the weight matrices and element-wise multiplications. y_t is an activation at time t, and h_t means a candidate activation.

3. The Proposed Method

Rotating machinery is applied to many fields. Rolling bearing is a necessary component to ensure the normal operation of rotating machinery. It has a direct impact on the accuracy and reliability of rotating machinery equipment. Therefore, rolling bearing faults are one of the most common reasons for rotating mechanical failures. Due to the long-term operation of rotating machinery under harsh and complex conditions, it is inevitable that faults will occur. Therefore, the state of machinery must be monitored in time to diagnose faults as soon as possible. One of the four key tasks is to find out whether the rotation of the machine is abnormal or not, and to predict the severity of the rotation of the machine. Due to the higher requirements for high performance, safety, and reliability, fault diagnosis of rotating machinery becomes not only more and more important but also more and more difficult. Therefore, in recent decades, rotating machinery fault diagnosis has received more and more attention and considerable development. This paper develops a new rotating machinery fault diagnosis method that combines a deep gated recurrent unit (DGRU) with wavelet packet decomposition (WPD) and extreme learning machine (ELM) to identify locomotive bearing fault conditions.

3.1. Wavelet Packet Decomposition Denosing. WPD is generally used to deal with nonstationary signals. It can analyze both time domain and frequency domain, and analyze the characteristics of signals locally. Wavelet transform decomposition mainly focuses on low-frequency signals and cannot decompose high-frequency signals containing a large amount of detailed information, such as rolling bearing vibration signals, remote sensing images, seismic signals, and biomedical signals. WPD is based on the idea of multiresolution analysis, that is, the signal can be decomposed and reconstructed in different frequency bands under the wavelet basis, which is suitable for dealing with discontinuous and nonstationary signals. WPD makes up for the shortcomings of wavelet transform. It can solve the signal energy from different decomposition scales. The multilevel division of frequency band can decompose not only low-frequency signals but also high-frequency signals, making the division of signals more precise. The signal decomposition process reflects the relationship between the

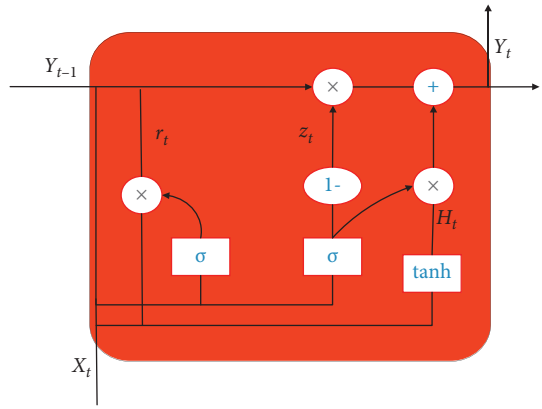

Figure 1: Structure of GRU.

wide-band signal and the fine band signal. The nonstationary vibration signal can approach the fault characteristic frequency of the system through WPD to obtain the instantaneous signal containing stationary signal components. The decomposition algorithm principle is to calculate the average and the difference between the first number and the average, and the system fault can be detected by analyzing the energy distribution in different frequency bands; WPD has neither redundancy nor omission. The vibration signals often contain noise that greatly influences the diagnosis accuracy. Thus, it is essential to eliminate the noise firstly. WPD is viewed as an effective method for vibration signal denoising [31]. WPD splits into two branches, low and high frequencies at all decomposition processes [36]. The three-layer binary trees of WPD are shown in Figure 2. The steps of signals denoising using WPD is illustrated in Table 1.

3.2. Deep Gated Recurrent Unit Construction. The operating conditions of mechanical equipment are changing, and the data label information of the training set data under most of the working conditions is unknown, and it is difficult to effectively train intelligent identification models. However, the training process of the above methods uses a small amount of labeling data, so it cannot be used to solve the problem of health status recognition under the case of unknown label information. Rotating machinery plays a vital role in the application of coal industry. Due to the long-term operation of rotating machinery under harsh and complex conditions, it is inevitable that faults will occur. Therefore, the state of machinery must be monitored in time to diagnose faults as soon as possible. One of the four key tasks is to find out whether the rotation of the machine is abnormal or not, and to predict the severity of the rotation of the machine. Due to the higher requirements for high performance, safety, and reliability, fault diagnosis of rotating machinery becomes not only more and more important but also more and more difficult. Therefore, in recent decades, rotating machinery fault diagnosis has received more and more attention and considerable development.

The health state of rotating parts such as bearings and gears directly affect the operation reliability of the whole mechanical system. Once the rotating parts fail, it will cause serious safety accidents and huge economic losses. Therefore, the establishment of an effective rotating machinery condition monitoring and fault identification system is of great significance to ensure the safe operation of equipment and personnel safety. Signal processing technology is an important subject of rotating machinery fault diagnosis, which has been widely used in various industrial fields. In addition, due to more and more attention, artificial intelligence technology has also been applied to rotating machinery fault diagnosis. Based on this, the illustration of DGRU is presented in Figure 3. $X(s)$ means the denoised data processed by WPD. $Y(s)$ and $Z(s)$ represent the extracted first-layer and second-layer features.

$$\sigma(t) = \frac{1}{1 + e^{-t}}. \tag{2}$$

The loss function is cross-entropy loss function that estimates the difference between the predicted label and actual label.

$$L(x, y) = -\sum_{i=1}^{N} y_i \log_2 x_i, \tag{3}$$

where x_i denotes the actual label and y_i is the predicted label.

3.3. Extreme Learning Machine Classification. ELM is the result of improving the algorithm [37]. The structure is shown in Figure 4. x and t are the input vectors and output labels respectively, (W, b) are the weights and bias of input layer and hidden layer, β is the value of the implication layer and the output layer. The difference from the BP neural network trained by gradient descent is that the weights generated during the training of the limit learning machine, and there is no need to adjust after generation. The specific calculation formulas are shown in equations (4), (5), and (6), the hidden layer vector h_i $(i = 1, 2, \ldots, n)$, where n is the number of input samples. T is the matrix composed of sample label vector, and H^+ is the generalized inverse matrix of H. Based on the principle of the least square method, the whole process does not need feedback iterative adjustment.

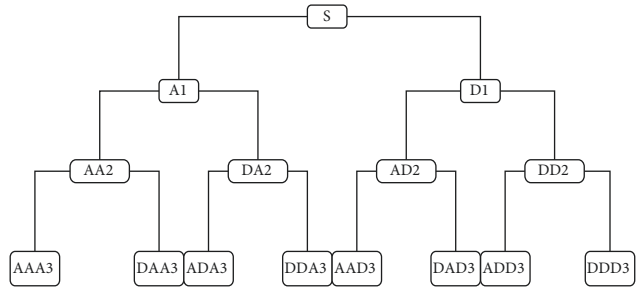

Figure 2: Three-layer binary trees WPD.

Table 1: The steps of signals denoising using WPD.

Steps	Detailed description
A. Signal decomposition	Select the wavelet function to decompose the noisy signals. Therefore, the wavelet packet coefficients at each level are obtained.
B. Thresholding	A threshold rule is used to decompose the coefficients to eliminate most of noisy coefficients
C. Signal reconstruction	The inverse WPD of each scale is performed by using the obtained approximate coefficients and the detailed coefficients of denoising.

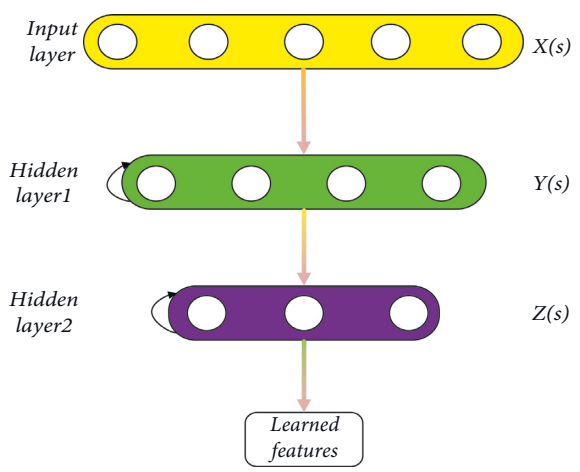

Figure 3: Structure of DGRU.

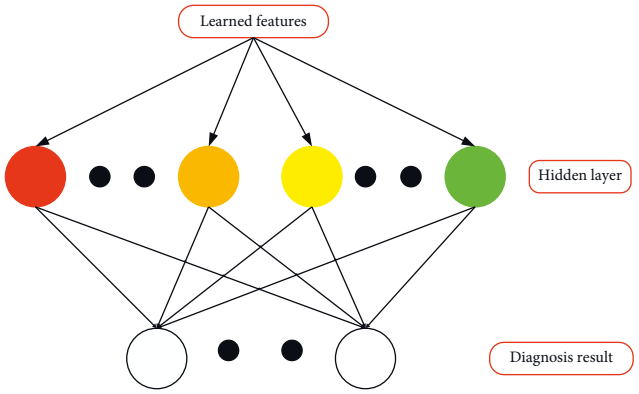

Figure 4: The basic framework.

$$H = \begin{bmatrix} F(\beta_1, \gamma_1, y_1) & \cdots & F(\beta_K, \gamma_K, y_1) \\ \vdots & \vdots & \vdots \\ F(\beta_1, \gamma_1, y_M) & \cdots & F(\beta_K, \gamma_K, y_M) \end{bmatrix}_{M \times K}, \quad (4)$$

$$\beta = \begin{bmatrix} \alpha_1 \\ \vdots \\ \alpha_K \end{bmatrix}_{K \times N}, \text{ and } T = \begin{bmatrix} t_1 \\ \vdots \\ t_M \end{bmatrix}_{M \times N}. \quad (5)$$

Known from Reference [38], β can be represented by

$$\beta = H^{+}T, \quad (6)$$

where H^{+} is the Moore–Penrose generalized inverse of H.

3.4. General Steps. The health state of rotating parts directly affects the operation reliability of the whole mechanical system. Once the rotating parts fail, it will cause serious accidents. Therefore, the establishment of an effective rotating machinery condition monitoring and fault identification system is to ensure the safe operation of equipment and personnel safety. An adaptive diagnosis method that combines DGRU with WPD and ELM is proposed. The updating process of our method is described in Figure 5 with the following three steps.

(i) Step 1: measure data from rotating machinery

(ii) Step 2: eliminate the noise of vibration signals by using WPD

(iii) Step 3: divide the denoised signals into trained and tested samples

(iv) Step 4: DGRU with ELM is constructed to diagnose railway locomotive bearing faults

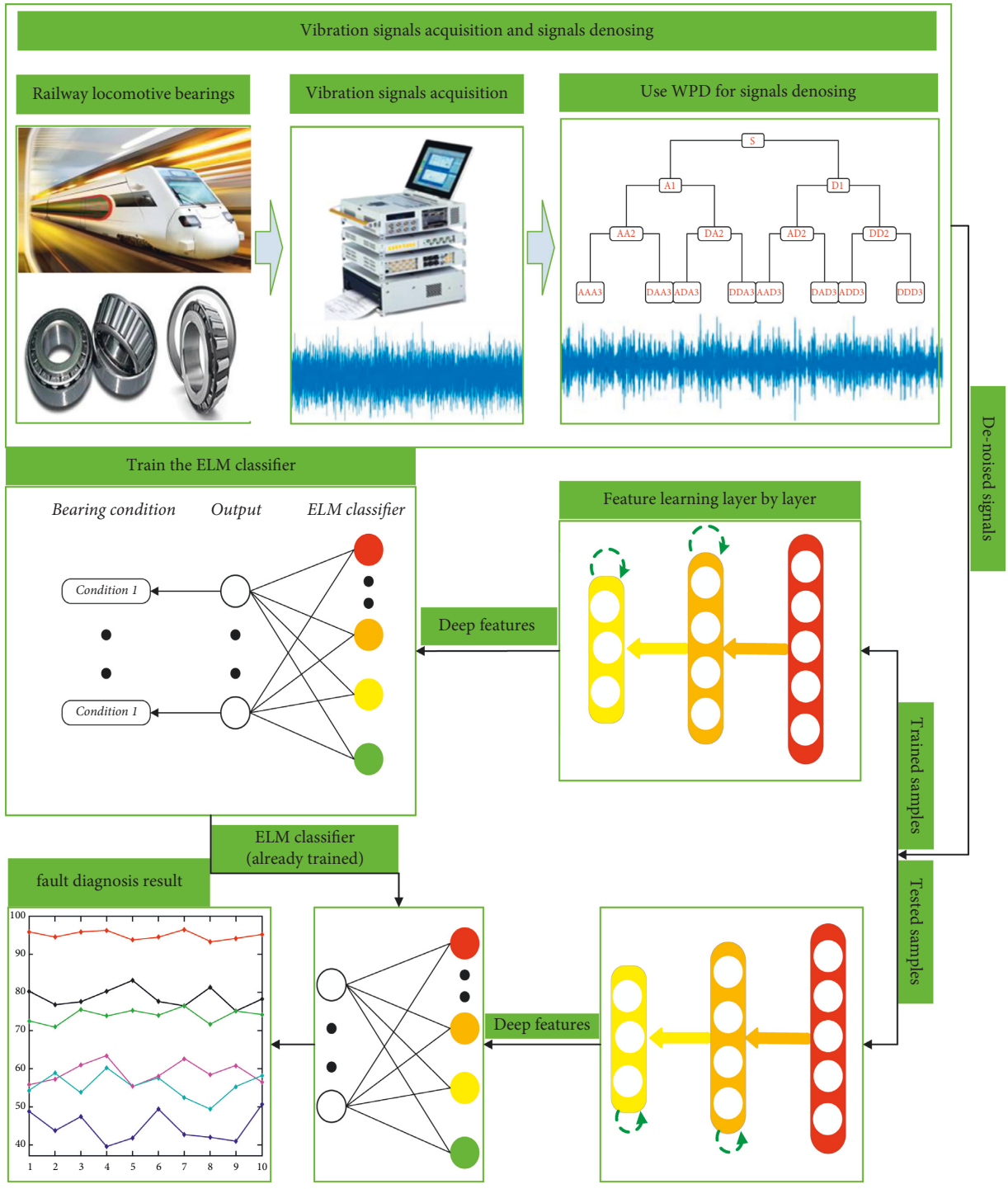

Figure 5: The framework of our approach.

(v) Step 5: the constructed model is used for learning the trained-samples features and verified by the tested-samples features

(vi) Step 6: output the diagnosis result.

4. Experimental Verification

4.1. Experimental Data Description. Because rotating machinery under harsh and complex conditions, it is inevitable that faults will occur. Therefore, the state of machinery must be monitored in time to diagnose faults as soon as possible. One of the four key tasks is to find out whether the rotation of the machine is abnormal or not, and to predict the severity of the rotation of the machine. Due to the higher requirements for high performance, safety, and reliability, fault diagnosis of rotating machinery becomes not only more and more important but also more and more difficult.

In this section, a representative simulating high-speed bearings dataset is selected to validate the feasibility of the proposed method. Various indicators are adopted to prove the effectiveness of data augmentation. Simulated fault diagnosis experiments are conducted separately with other approaches to corroborate the superiority of the algorithm in this paper. The simulated high-speed bearing dataset is applied to the laboratory dataset. The dataset is provided by railway locomotive bearing. According to different health conditions and three damage levels, 9 health categories with 12.8 kHz sampling frequency are obtained to form the dataset. The experimental platform presented in Figures 6 and 7 represents the specific faults of rolling bearings.

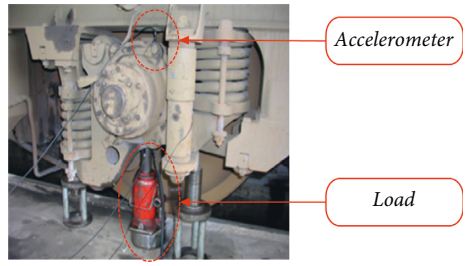

Figure 6: Experimental locomotive bearing device.

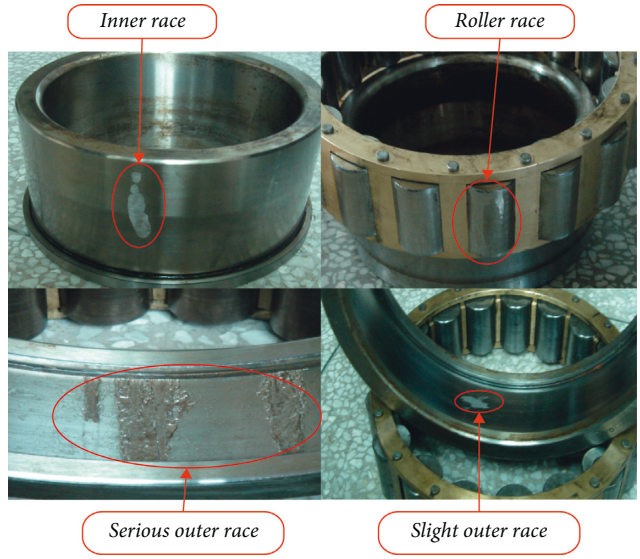

Figure 7: Four types of rolling bearing faults.

4.2. Compared with Traditional Methods. To evaluate the effectiveness of our approach for noisy signals, the collected data are added white Gaussian noise (WGN) in this part as shown in Figure 8. The noisy signals are described as

$$V(s) = v(s) + k \times n(s), \tag{7}$$

where $V(s)$ represents the noisy signals, $v(s)$ is the collected vibration signals, $n(s)$ is the WGN, and k is the coefficient. Larger k means heavier noise.

In this part, k is 0.4 and then we obtain the noisy signals. Then, the noisy signals are one input. The denoised signals that are processed by WPD are another input. Figure 9 describes the noisy data and the denoised data of each condition, each condition contains 8,192 data points. There are two important points to be explained: (1) For the proposed method and DGRU with SVM classifier, the only input is the noisy signals. (2) SVM and ANN both have two inputs, the noisy signals and the denoised signals.

To demonstrate the superiority of our, six methods are considered as the comparison methods. More details about these methods are provided as follows. As in this article, the optimization algorithm is the Adam algorithm. The learning rate is 0.0002 in all experiments. The relevant parameters of these methods are determined by relevant literature and experiments so that these methods could achieve the best recognition performance for different diagnosis tasks. These results are depicted in Figure 10. The confusion matrix is illustrated in Figure 11. Table 2 shows the results per method in all tasks.

It is obviously observed from Table 3 that the average accuracy of the proposed method is 94.98%, which is obviously higher than the other five methods, which are 78.64%, 55.47%, 73.95%, 44.61%, and 58.85%, respectively. The standard deviation is only 1.10, obviously lower than the other five methods which are 2.35, 3.28, 2.25, 3.96, and 3.22. The results present that: (1) Comparing all the methods, we can clearly observe that DGRU, SVM, and ANN are all sensitive about the noise. (2) Comparing Method 1 with Method 2, it can be known that the denoised signals could make much better diagnosis accuracy. It also proves the necessity and effectiveness of the noisy signals processed by WPD. (3) By comparing Method 1, Method 4, and Method 6, it can be seen that the proposed method has much more accurate and robust performance than SVM and ANN. The main reason is that the deep architecture has a more powerful ability to learn functions. Therefore, it can automatically learn more appropriate internal error characteristics from the inputs and provide more reliable conclusions.

4.3. The Antinoise Ability of the Proposed Method. This part is mainly to research the influence of different noisy signals and the antinoise ability of the proposed method. To avoid the chance of result, each condition runs 5 times. The description of each condition and the average accuracy is shown in Table 4. The noisy signals represent the signals contain noise; the denoised signals represent the noisy signals processed by WPD. The concrete diagnosis result of each trail is shown in Figure 12.

The average accuracy and standard deviation of each condition are shown in Table 4. It can be known that for the DGRU with ELM classifier, the denoised signals could lead to much better accuracy and robust performance than the noisy signals. With more noise of the vibration signals, the diagnosis accuracy becomes lower and more and more unstable. No matter how powerful the denoising method is, the denoised signals could not be better than the normal vibration signals. It also can be found that with the increase of noise, the result of WPD dealing with noisy signals is also getting worse. However,

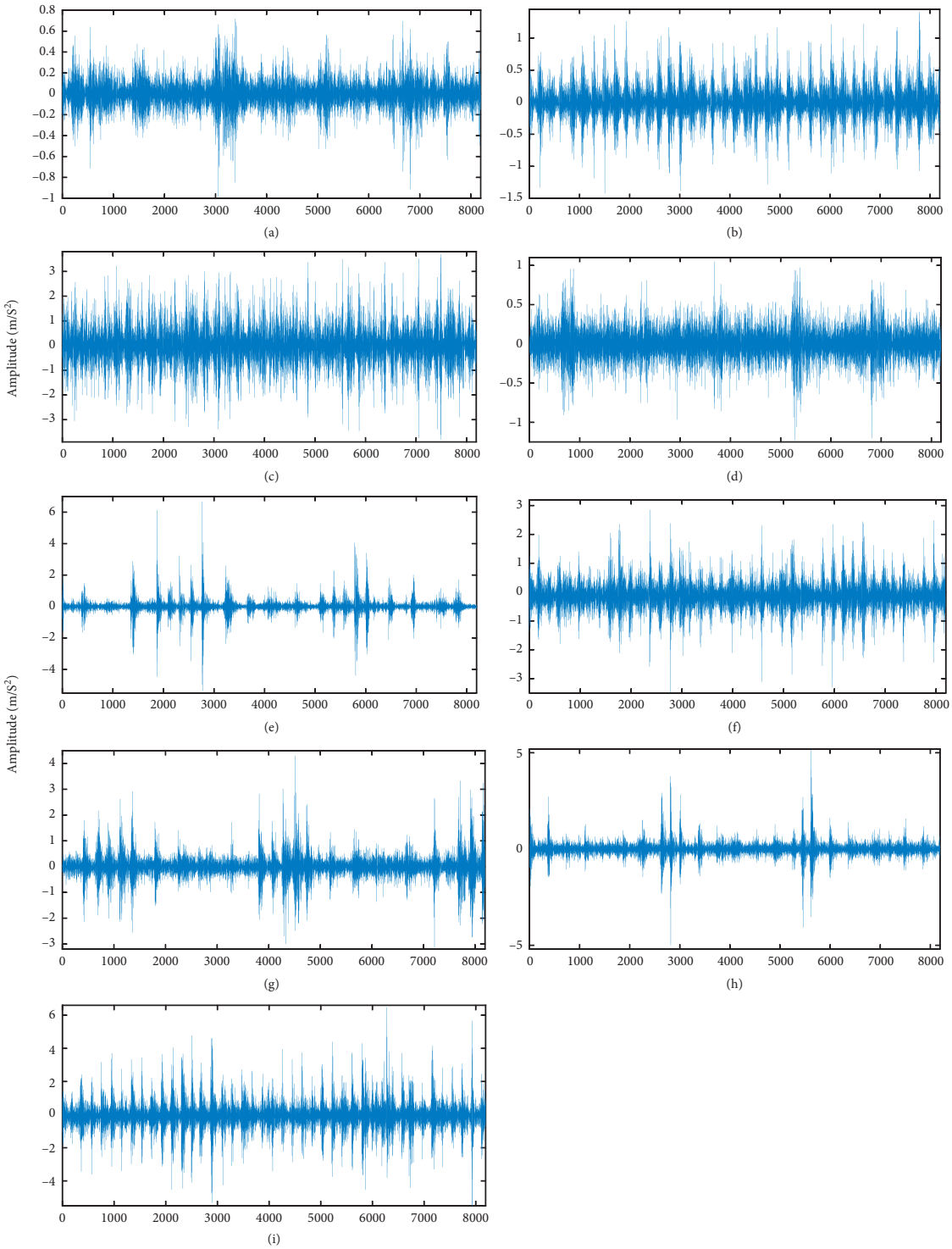

Figure 8: The collected vibration signals of the nine conditions.

the diagnosis result is also higher than 90%. According to the above-mentioned and diagnosis results, it can be confirmed that the proposed method has a powerful antinoise ability.

The classifiers with the identical parameters are employed for the same purpose. Ablation experiments are required for the CNN classifier to ensure that it is resistant to engineering noise interference. The settings and results of the ablation

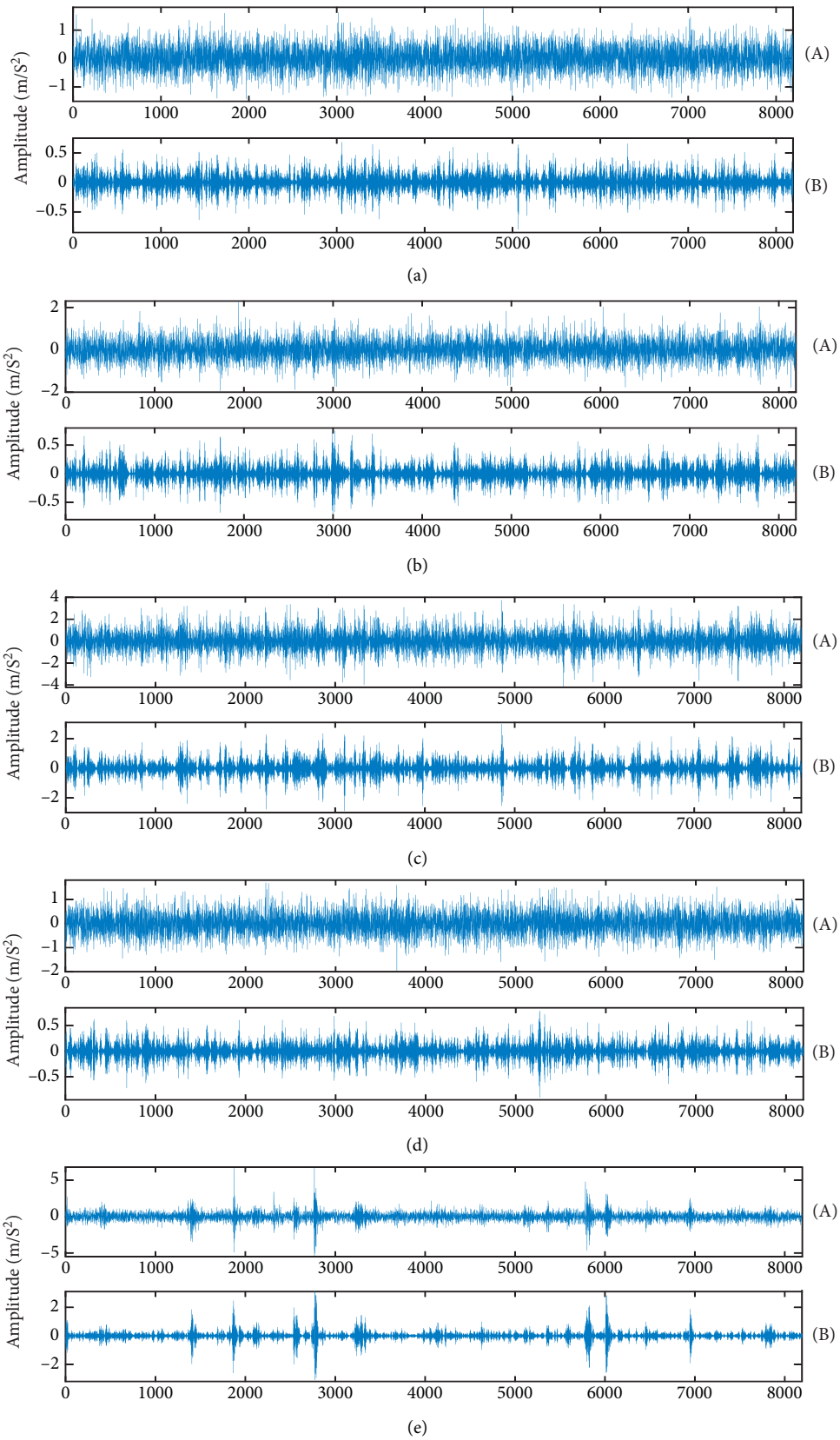

Figure 9: Continued.

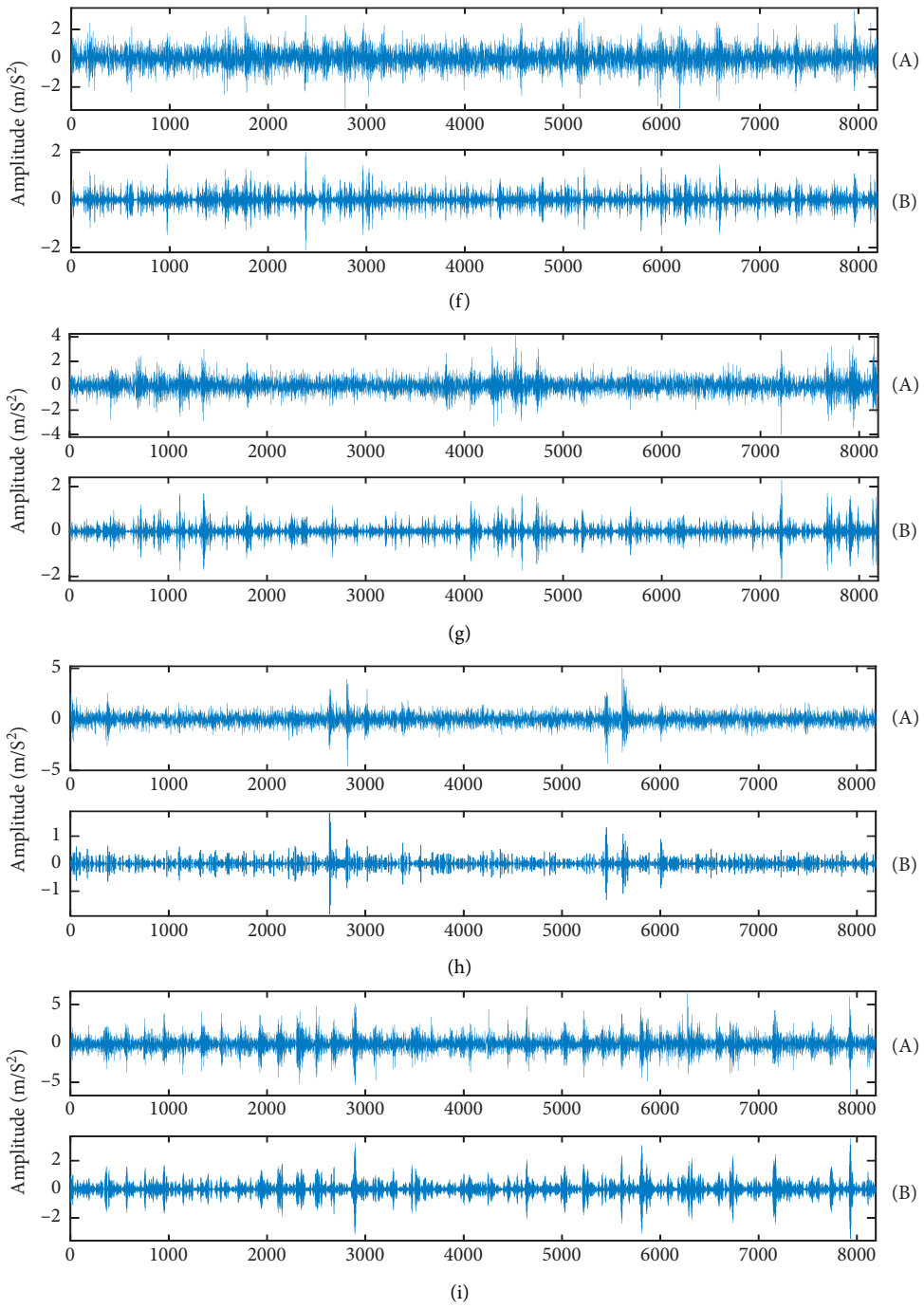

Figure 9: The noisy signals and the denoised signals of the nine conditions. (A) Noisy signals. (B) Denoised signals.

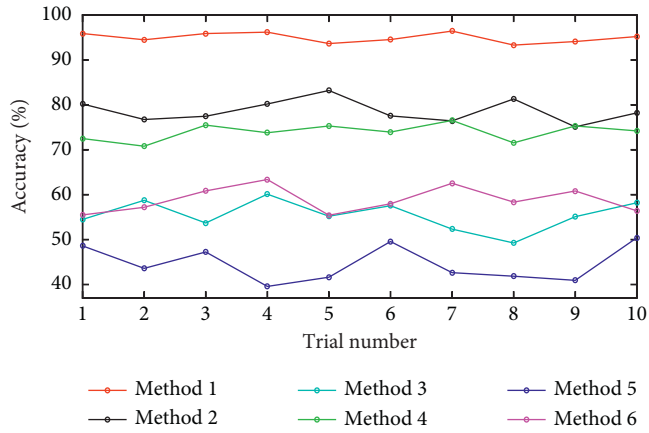

Figure 10: Diagnosis results of the 10 trials.

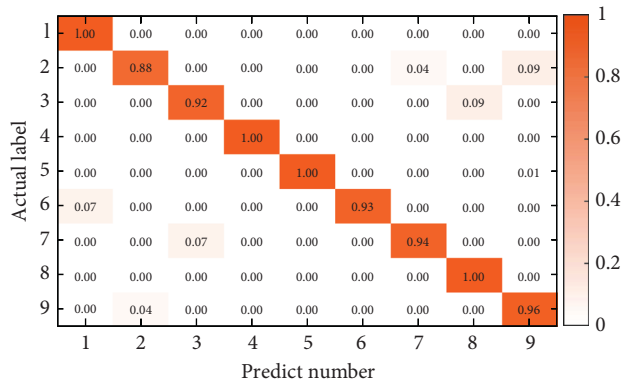

Figure 11: The confusion matrix using the proposed method (the first trial).

Table 2: Comparison of methodologies.

Method	Description	Inputs
1	Suggested technique	Noisy signals
2	DGRU + ELM classifier	Noisy signals
3	SVM	Noisy signals
4	SVM	Denoised signals
5	ANN	Noisy signals
6	ANN	Denoised signals

Table 3: The concrete classification accuracy and standard deviation per method.

Method	Average accuracy (%)	Standard deviation
1	94.98	**1.10**
2	78.64	2.35
3	55.47	3.28
4	73.95	2.25
5	44.61	3.96
6	58.85	3.22

Table 4: Average accuracy and standard deviation of each condition.

Condition	k	Inputs	Average accuracy (%)	Standard deviation
1	0	Collected signals	96.69	1.47
2	0.2	Noisy signals	82.46	2.45
3		Denoised signals	92.39	1.17
4	0.4	Noisy signals	79.57	2.57
5		Denoised signals	95.03	1.10
6	0.6	Noisy signals	74.15	2.93
7		Denoised signals	91.93	1.10
8	0.8	Noisy signals	67.80	6.31
9		Denoised signals	90.36	1.25

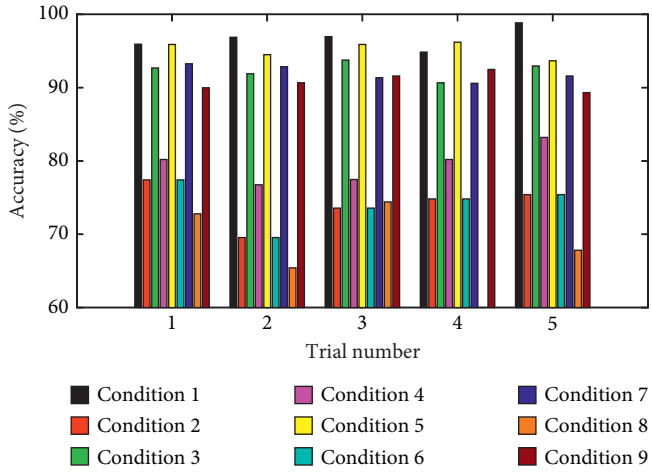

Figure 12: Diagnosis accuracy of the 5 trials.

Table 5: The framework of CNN for ablation experiment.

Parameter profile	Framework A	Framework B	Framework C	Framework D
Input	1024	1024	1024	1024
Convolution	32, 3, 1, same	32, 5, 1, same	32, 3, 2, same	48, 3, 1, same
Maxpooling	2	2	—	2
Convolution	64, 3, 1, same	64, 5, 1, same	64, 3, 2, same	96, 3, 1, same
Maxpooling	2	2	—	2
Convolution	128, 3, 1, same	128, 5, 1, same	128, 3, 2, same	192, 3, 1, same
Maxpooling	2	2	—	2
Fully connection	1024	1024	1024	1024
Fully connection	9	9	9	9
Keep_prob	0.9	0.9	0.9	0.9
Learning rate	0.1	0.1	0.1	0.1
Accuracy	95.18% ± **1.64**	94.22% ± 1.84	93.16% ± 1.86	92.52% ± 1.98

experiments are listed in Table 5. CNNs with different frameworks and parameters are adopted to fault diagnose on the dataset to select the best CNN diagnostic model. From Table 5, it is clear that framework A is more robust for better fault diagnosis compared to other structures. Accordingly, an alternative ablation experiment is conducted on the key parameters of CNN with framework A as the basis.

5. Conclusion

In this paper, an adaptive diagnosis method that combines deep gated recurrent unit (DGRU) with wavelet packet decomposition (WPD) and extreme learning machine (ELM) is proposed for rolling bearing. Firstly, WPD is utilized to eliminate the noise of data. Secondly, DGRU is designed to extract the representative features of denoised data. Finally, ELM is utilized to output the diagnosis results. Massive experimental results prove that the superiority and robustness of the proposed method outperform existing popular methods. Additionally, the proposed method can also achieve powerful antinoise ability.

In conclusion, we will further improve our model to deal with the challenge of transfer experimental data knowledge to diagnose practical engineering equipment faults in future research [39].

Data Availability

The data used to support the findings of this study are available from the corresponding author upon request.

Conflicts of Interest

The authors declare that they have no conflicts of interest.

Authors' Contributions

All the authors equally contributed in the manuscript for "conceptualization, validation, formal analysis, investigation, and resources." All authors have read and agreed to the published version of the manuscript.

References

[1] J. Li, Z. Meng, P. Zuozhou, C. Lixiao, and F. Fengjie, "Multi-source feature extraction of rolling bearing compression measurement signal based on independent component analysis," *Measurement*, vol. 172, Article ID 108908, 2021.

[2] H. G. Yang, H. B. Lin, and K. Ding, "Sliding window denoising K-Singular Value Decomposition and its application on rolling bearing impact fault diagnosis," *Sound and Vibration*, vol. 421, pp. 205–219, 2018.

[3] K. Zhao, H. K. Jiang, C. Q. Liu, Y. F. Wang, and K. Zhu, "A new data generation approach with modified Wasserstein auto-encoder for rotating machinery fault diagnosis with limited fault data," *Knowledge-Based Systems*, vol. 238, Article ID 107892, 2022.

[4] W. H. Li, S. H. Zhang, and S. Rakheja, "Feature denoising and nearest–farthest distance preserving projection for machine fault diagnosis," *IEEE Transactions on Industrial Informatics*, vol. 12, no. 1, pp. 393–404, 2016.

[5] S. B. Wang, I. Selesnick, G. G. Cai, Y. N. Feng, X. Sui, and X. F. Chen, "Nonconvex sparse regularization and convex optimization for bearing fault diagnosis," *IEEE Transactions on Industrial Electronics*, vol. 65, no. 9, pp. 7332–7342, 2018.

[6] Z. Y. Wang, C. Lu, and B. Zhou, "Fault diagnosis for rotary machinery with selective ensemble neural networks," *Mechanical Systems and Signal Processing*, vol. 113, pp. 112–130, 2018.

[7] J. Y. Jiao, M. Zhao, J. Lin, and J. Zhao, "A multivariate encoder information based convolutional neural network for intelligent fault diagnosis of planetary gearboxes," *Knowledge-Based Systems*, vol. 160, pp. 237–250, 2018.

[8] Z. H. An, S. M. Li, J. R. Wang, and X. X. Jiang, "A Novel Bearing Intelligent Fault Diagnosis Framework under Time-Varying Working Conditions Using Recurrent Neural Network," *ISA Transactions*, vol. 100, pp. 155–170, 2019.

[9] J. R. Wang, S. M. Li, Z. H. An, X. X. Jiang, W. W. Qian, and S. S. Ji, "Batch-normalized deep neural networks for achieving fast intelligent fault diagnosis of machines," *Neurocomputing*, vol. 329, pp. 53–65, 2019.

[10] K. Zhao, H. K. Jiang, K. B. Wang, and Z. Y. Pei, "Joint distribution adaptation network with adversarial learning for rolling bearing fault diagnosis," *Knowledge-Based Systems*, vol. 222, Article ID 106974, 2021.

[11] X. J. Guo, L. Chen, and C. Q. Shen, "Hierarchical adaptive deep convolution neural network and its application to bearing fault diagnosis," *Measurement*, vol. 93, pp. 490–502, 2016.

[12] M. D. Sun, H. Wang, P. Liu, S. D. Huang, and P. Fan, "A sparse stacked denoising autoencoder with optimized transfer learning applied to the fault diagnosis of rolling bearings," *Measurement*, vol. 146, pp. 305–314, 2019.

[13] S. Y. Shao, S. McAleer, R. Q. Yan, and P. Baldi, "Highly accurate machine fault diagnosis using deep transfer learning," *IEEE Transactions on Industrial Informatics*, vol. 15, no. 4, pp. 2446–2455, 2018.

[14] Z. H. Wu, H. K. Jiang, K. Zhao, and X. Q. Li, "An adaptive deep transfer learning method for bearing fault diagnosis," *Measurement*, vol. 151, Article ID 107227, 2020.

[15] X. A. Yan and M. P. Jia, "A novel optimized SVM classification algorithm with multi-domain feature and its application to fault diagnosis of rolling bearing," *Neurocomputing*, vol. 313, pp. 47–64, 2018.

[16] J. X. Ma, F. Y. Xu, K. Huang, and R. Huang, "GNAR-GARCH model and its application in feature extraction for rolling bearing fault diagnosis," *Mechanical Systems and Signal Processing*, vol. 93, pp. 175–203, 2017.

[17] K. Zhao, H. K. Jiang, Z. H. Wu, and T. F. Lu, "A novel transfer learning fault diagnosis method based on Manifold Embedded Distribution Alignment with a little labeled data," *Journal of Intelligent Manufacturing*, vol. 33, no. 1, pp. 151–165, 2020.

[18] Y. Zhu, X. D. Wu, P. P. Li, Y. H. Zhang, and X. G. Hu, "Transfer learning with deep manifold regularized auto-encoders," *Neurocomputing*, vol. 369, pp. 145–154, 2019.

[19] Z. F. Kang, B. Yang, Z. S. Li, and P. Wang, "OTLAMC: an online transfer learning algorithm for multi-class classification," *Knowledge-Based Systems*, vol. 176, pp. 133–146, July 2019.

[20] X. Li, X. D. Jia, W. Zhang, H. Ma, and X. Li, "Intelligent Cross-Machine Fault Diagnosis Approach with Deep Auto-Encoder and Domain Adaptation," *Neurocomputing*, vol. 383, pp. 235–247, 2019.

[21] L. Wen, L. Gao, and X. Y. Li, "A new deep transfer learning based on sparse auto-encoder for fault diagnosis," *IEEE Transactions on Systems, Man, and Cybernetics: Systems*, vol. 49, no. 1, pp. 136–144, 2019.

[22] L. Guo, Y. G. Lei, S. B. Xing, T. Yan, and N. P. Li, "Deep convolutional transfer learning network: a new method for intelligent fault diagnosis of machines with unlabeled data," *IEEE Transactions on Industrial Electronics*, vol. 66, no. 9, pp. 7316–7325, 2018.

[23] D. Y. Xiao, Y. X. Huang, L. J. Zhao, C. Q. Qin, H. T. Shi, and C. L. Liu, "Domain adaptive motor fault diagnosis using deep transfer learning," *IEEE Access*, vol. 7, Article ID 80937, 2019.

[24] X. X. Wang, H. B. He, and L. S. Li, "Hierarchical deep domain adaptation approach for fault diagnosis of power plant thermal system," *IEEE Transactions on Industrial Informatics*, vol. 15, no. 9, pp. 5139–5148, 2019.

[25] B. Yang, Y. G. Lei, F. Jia, and S. B. Xing, "An intelligent fault diagnosis approach based on transfer learning from laboratory bearings to locomotive bearings," *Mechanical Systems and Signal Processing*, vol. 122, pp. 692–706, 2019.

[26] T. Han, C. Liu, W. G. Yang, and D. X. Jiang, "Learning transferable features in deep convolutional neural networks for diagnosing unseen machine conditions," *ISA Transactions*, vol. 93, pp. 341–353, October 2019.

[27] J. D. Wang, Y. Q. Chen, S. J. Hao, W. J. Feng, and Z. Q. Shen, "Balanced distribution adaptation for transfer learning," in *Proceedings of the 2017 IEEE International Conference on Data Mining*, pp. 1129–1134, New Orleans, LA, USA, November 2017.

[28] B. D. Shai, B. John, C. Koby, and P. Fernando, "Analysis of representations for domain adaptation," *Advances in Neural Information Processing Systems 19*, in *Proceedings of the Twentieth Annual Conference on Neural Information Processing Systems*, Vancouver, Canada, December 2006.

[29] R. Zhao, D. Z. Wang, R. Q. Yan, K. Z. Mao, F. Shen, and J. J. Wang, "Machine health monitoring using local feature-based gated recurrent unit networks," *IEEE Transactions on Industrial Electronics*, vol. 65, no. 2, pp. 1539–1548, 2018.

[30] K. Saito, K. Watanabe, Y. Ushiku, and T. Harada, "Maximum classifier discrepancy for unsupervised domain adaptation," in *Proceedings of the 2018 IEEE/CVF Conference on Computer Vision and Pattern Recognition*, pp. 3723–3732, Salt Lake City, AL, USA, June 2018.

[31] H. D. Shao, J. S. Cheng, H. K. Jiang, Y. Yang, and Z. T. Wu, "Enhanced Deep Gated Recurrent Unit and Complex Wavelet Packet Energy Moment Entropy for Early Fault Prognosis of Bearing," *Knowledge.-Based System*, vol. 188, Article ID 105022, 2019.

[32] H. K. Jiang, X. Q. Li, H. Shao, and K. Zhao, "Intelligent fault diagnosis of rolling bearings using an improved deep recurrent neural network," *Measurement. Science. Technology*.vol. 29, no. 6, Article ID 65107, 2018.

[33] K. Zhao, H. K. Jiang, X. Q. Li, and R. X. Wang, "An optimal deep sparse autoencoder with gated recurrent unit for rolling bearing fault diagnosis," *Measurement. Science. Technology*.vol. 31, no. 1, Article ID 15005, 2019.

[34] K. A. Loparo, "Case Western Reserve University Bearing Data Center Website," 2012, http://csegroups.case.edu/bearingdatacenter/home.

[35] S. J. Pan, I. W. Tsang, J. T. Kwok, and Q. Yang, "Domain adaptation via transfer component analysis," *IEEE Transactions on Neural Networks*, vol. 22, no. 2, pp. 199–210, 2011.

[36] M. S. Long, J. M. Wang, G. G. Ding, J. G. Sun, and P. S. Yu, "Transfer Feature Learning with Joint Distribution Adaptation," in *Proceedings of the 2013 IEEE International Conference on Computer Vision*, pp. 2200–2207, Sydney, Australia, December 2013.

[37] Ke Zhao, H. Jiang, and Z. Wu, "Transfer residual convolutional neural network for rotating machine fault diagnosis under different working conditions," in *Proceedings of the 2021 12th International Conference on Mechanical and Aerospace Engineering (ICMAE)*, pp. 477–483, IEEE, Athens, Greece, July 2021.

[38] Y. Ganin, E. Ustinova, H. Ajakan et al., "Domain-adversarial training of neural networks," *Journal of Machine Learning Research*, vol. 17, no. 59, pp. 1–35, 2016.

[39] W. Zhang, J. Chen, S. Riaz, N. Zheng, and L. Li, "Research on distributed cooperative control strategy of microgrid hybrid energy storage based on adaptive event triggering," *CMES-Computer Modeling in Engineering & Sciences*, vol. 132, no. 2, pp. 585–604, 2022.

Hindawi
Shock and Vibration
Volume 2024, Article ID 9791575, 1 page
https://doi.org/10.1155/2024/9791575

Retraction

Retracted: Analysis and Design of Cooperative Control Solutions for Electrical Systems of Laser CNC Machines

Shock and Vibration

Received 23 January 2024; Accepted 23 January 2024; Published 24 January 2024

This article has been retracted by Hindawi following an investigation undertaken by the publisher [1]. This investigation has uncovered evidence of one or more of the following indicators of systematic manipulation of the publication process:

(1) Discrepancies in scope

(2) Discrepancies in the description of the research reported

(3) Discrepancies between the availability of data and the research described

(4) Inappropriate citations

(5) Incoherent, meaningless and/or irrelevant content included in the article

(6) Manipulated or compromised peer review

The presence of these indicators undermines our confidence in the integrity of the article's content and we cannot, therefore, vouch for its reliability. Please note that this notice is intended solely to alert readers that the content of this article is unreliable. We have not investigated whether authors were aware of or involved in the systematic manipulation of the publication process.

Wiley and Hindawi regrets that the usual quality checks did not identify these issues before publication and have since put additional measures in place to safeguard research integrity.

We wish to credit our own Research Integrity and Research Publishing teams and anonymous and named external researchers and research integrity experts for contributing to this investigation.

The corresponding author, as the representative of all authors, has been given the opportunity to register their agreement or disagreement to this retraction. We have kept a record of any response received.

References

[1] S. Shao, "Analysis and Design of Cooperative Control Solutions for Electrical Systems of Laser CNC Machines," *Shock and Vibration*, vol. 2022, Article ID 1423767, 14 pages, 2022.

Hindawi
Shock and Vibration
Volume 2022, Article ID 1423767, 14 pages
https://doi.org/10.1155/2022/1423767

Research Article

Analysis and Design of Cooperative Control Solutions for Electrical Systems of Laser CNC Machines

Shufeng Shao

Zhejiang Industry Polytechnic College, Shaoxing 312000, China

Correspondence should be addressed to Shufeng Shao; shaoshufeng1015@126.com

Received 17 May 2022; Revised 18 June 2022; Accepted 21 June 2022; Published 1 July 2022

Academic Editor: Yuxing Li

In order to further improve the collaborative control efficiency of the electrical system of the laser CNC machine tool, an electrical system based on the ultrafast laser CNC machine tool is proposed. The design of the collaborative control scheme is discussed from three aspects: the overall control scheme design, hardware structure design, and control software implementation of the electrical system of the laser numerical control machine tool. The experimental results show that the length of the metal sheet processed by the electrical system of the laser CNC machine tool is 5.3 cm and the width is about 3.6 cm, and the actual processing aperture size will also change according to the set number of variable radius turns, and more precise processing can be enabled in the online test. The research results show that this electrical collaborative control system scheme has strong practicability and feasibility. With the help of system upgrades and optimization, the efficient integration of laser processing technology and numerical control technology can be better achieved. It should be noted that the machining process of the machine tool is also required to make in-depth improvements, which can maximize the operating efficiency and machining accuracy of the electrical system of the CNC machine tool. The laser CNC machine tool researched and developed in this paper verifies the rationality and feasibility of the collaborative control scheme through practical experiments, which can meet the processing requirements and realize the integration of laser processing technology and numerical control technology. High machining efficiency and machining accuracy.

1. Introduction

Computer engineering has gradually replaced modern work tools, and office equipment has never been adapted to current work needs. While the development of computer technology and its application in the field of the machinery industry have changed the traditional processing methods, the work efficiency of the equipment has been further improved by integrating computer technology, automated control systems, and CNC machine tool technology. Compared with traditional CNC machine tool technology, with the improvement of computer technology, on the basis of the full integration of automation control technology, computer technology, and CNC machine tool technology, laser CNC machine tools integrate optical, mechanical, electrical, detection, and other technologies into one. Based on the integration of laser processing and CNC machine tools, compared with traditional CNC machine tools, laser CNC machine tools have many advantages and characteristics of traditional CNC machine tools and laser manufacturing machine tools and can better replace the work of traditional props. The machining speed of the tool is faster, the surface deformation of the machined workpiece is smaller, and a wider variety of complex workpieces can be machined. On the basis of synthesizing a variety of technologies, laser CNC machine tool technology has higher processing efficiency, greatly improved processing accuracy, and a higher degree of automation. Based on these characteristics, a control system for CNC machine tools based on ultrafast laser is proposed, which can better realize the coordinated control of the electrical system of CNC machine tools.

2. Literature Review

Macmammah et al. said that the application range of CNC machine tools in the industry is constantly expanding, and it has many advantages compared with ordinary machine tools, but at present, CNC machine tools cannot completely replace ordinary machine tools, nor can they be the most economical way to solve all problems in the machining process [1]. Klausen et al. said that CNC machine tools are mainly suitable for processing complex shapes and high precision requirements while producing parts with small batches but many varieties [2]. Singh and Kedia said that a large number of CNC machine tools are needed to support their production in the automobile manufacturing industry, machinery industry, and military industry [3]. Singh et al. said that CNC machine tools, as the working machine of equipment manufacturing, are the mainstay of a country's industrial development [4]. Lee and others said that due to the continuous advancement of industrial modernization, the requirements of modern manufacturing for CNC machine tools have long been no longer focused on simple automated processing but have put forward more advanced processing accuracy, processing speed, and processing technology for high demands [5]. Lan et al. stated that from the perspective of these needs, high-end CNC machine tools would be a good choice, but the actual processing of high-end CNC machine tools is only used to complete the processing process and for the similarity processing of microholes. While precision cutting requires precision, it is difficult for high-end CNC machine tools to meet the requirements [6]. At this time, it is necessary to find a more suitable processing method and processing technology, and laser processing is the best choice for this kind of processing. Compared with traditional machine tool processing, laser processing has the following advantages: Lui et al. said that laser processing has high production efficiency, reliable workpiece processing quality, and processing accuracy that can reach the order of microns [7]. During the laser processing, there is no contact with the workpiece to be processed, which will not bring about "tool" wear, and at the same time, there is no direct impact on the workpiece, so there is no mechanical deformation; it is suitable for the processing of some metals and nonmetals, especially for high hardness and processing of materials with high brittleness and high melting point; Gupta and Paliwal said that the beam guidance and focusing of the laser are simple in the processing process, which can easily realize the transformation of all directions, which is very suitable for the processing of complex workpieces with the numerical control system [8]. As can be seen from the advantages of laser processing, laser processing is a very simple process. Zahedmanesh et al. said that the combination of laser processing and CNC machine tools and the use of lasers to convert the machine tools into laser CNC machine tools for operation is not only the function of CNC machine tools but also the quality of laser processing [9]. Therefore, laser CNC machine tools will have the advantages of CNC machine tools and laser processing at the same time. For precision processing such as microhole processing, it can not only achieve a high degree of automation of processing but also achieve higher processing accuracy and processing efficiency. Sanjareh et al. said that although the current applications of laser CNC machine tools in China's processing industry are mostly special-purpose mid-to-low-end machine tools, mainly used for laser cutting, cladding, heat treatment, laser welding, etc. with the development of laser processing technology and the continuous improvement of CNC machine tools and the deepening of technical research, laser CNC machine tools will have a wide range of applications [10]. Laser CNC machine tools combine the advantages of CNC machine tools and laser processing, are necessary to improve the efficiency of the processing process, and are an important part of the development and adjustment of CNC machine tools. At present, the development of laser CNC machine tools is still in its infancy, but it has been widely used in production. It can be seen that laser CNC machine tools can be improved. The next step in the research of laser CNC machine tools will only focus on the integration of CNC machine tools and laser processing equipment in the processing process to improve the process and make tool making and setting easy so that the advantages of CNC machine tools and laser processing can be effectively utilized to implement manufacturing innovation. The electrical system of the CNC machine tool is shown in Figure 1.

3. Methods

In the CNC machining system, the processing of the corners of the motion segment is the key issue to improve the smoothness of the motion trajectory. The problem includes two aspects: first, the determination of the corner speed. The smoothness of the motion is significantly reduced; secondly, the smoothness of the trajectory at the corner is improved. Under the condition of ensuring the trajectory error, a motion segment with smooth characteristics is added to the corner to satisfy the better trajectory smoothness [11]. In order to solve the above problems, this chapter has carried out research on the transition technology at the corner of the motion segment. The basic idea is shown in Figure 2.

The technical introduction is shown in Figure 3.

Set points, $Pi-1$, Pi, $Pi+1$, are the endpoint positions of the two motion segments of sequential processing, as shown in

$$\overline{Q_0Q_1Q_2}. \tag{1}$$

It is the transition arc that is tangent to the two line segments at the same time, wherein $Q0$ and $Q2$ are the tangent points of the transition arc and the adjacent motion segments $Pi-1Pi$ and $PiPi+1$, respectively, and $Q1$ is the midpoint of the transition arc. The geometric relationship between the transition arc and the two adjacent motion segments is analytically represented, as shown in Figure 4.

In the figure, ΔQ_0OQ_2 is easily known as an isosceles triangle according to the knowledge of plane geometry. According to the basic properties of the tangent, it can be concluded that $\Delta Q_0P_iQ_2$ is also an isosceles triangle. Therefore, the corner point P_i of the two motion segments

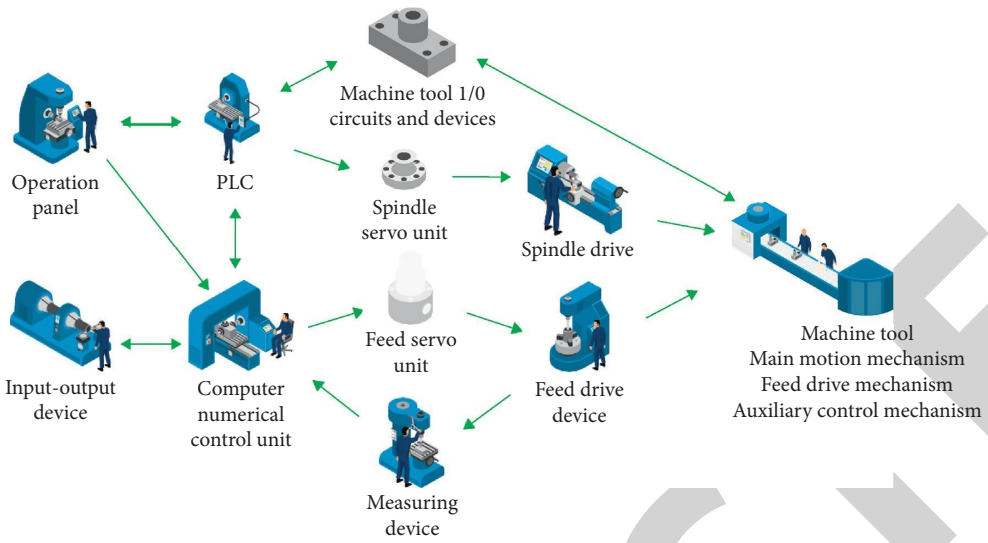

Figure 1: Cooperative control of the electrical system of the laser CNC machine tool.

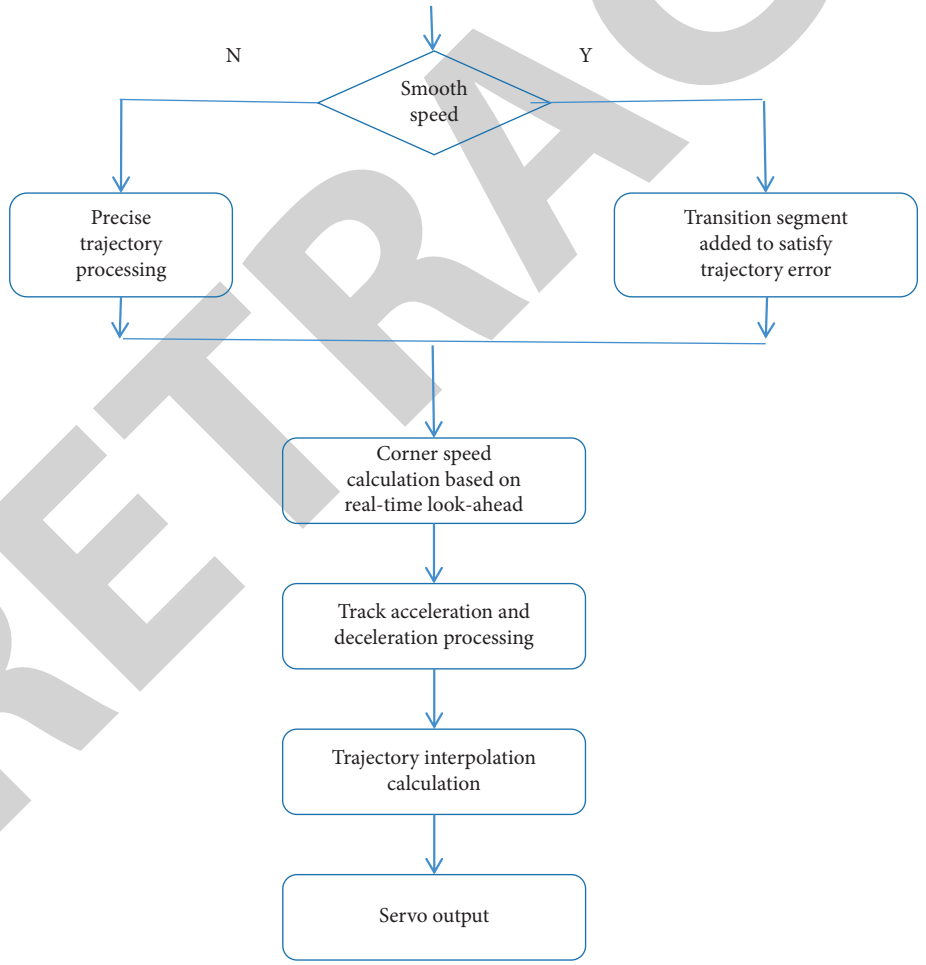

Figure 2: Transition processing flow at the corner of the motion segment.

and the starting point $Q0$ and the end of the transition arc of the points $Q2$ are equidistant, and the above distance is defined here as the transition distance, that is, the distance from P_i to the starting point Q0 and the ending point $Q2$. Assuming that the lengths of two adjacent motion segments $Pi-1Pi$ and $PiPi+1$ are represented as Si and $Si+1$,

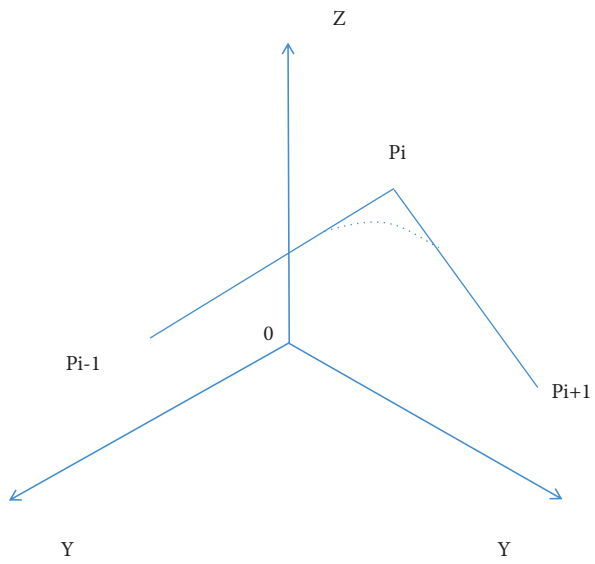

Figure 3: Schematic diagram of arc transition.

respectively, and the included angle between the two motion segments is α, according to the knowledge of plane geometry, the following relationship can be obtained as follows:

$$\begin{cases} \phi = \alpha, \\ \dfrac{r}{e+r} = \cos\dfrac{\phi}{2}, \\ \dfrac{l}{e+r}\sin\dfrac{\phi}{2}. \end{cases} \tag{2}$$

It can be further deduced through the above formula relationship. According to the angle α between adjacent motion segments and the contour error determined by the machining accuracy, the transition distance l between the two motion segments and the radius r of the transition arc are, respectively, related to α and α. The relationship of e is shown in formulas (3) and (4):

$$l = \frac{\sin(\alpha/2)}{1-\cos(\alpha/2)}, \tag{3}$$

$$r = \frac{\cos\ (\alpha/2)}{1-\cos(\alpha/2)}e. \tag{4}$$

When the transition arc is used to achieve a smooth transition between adjacent motion segments, there is a fitting error between the actual path and the original path. First, considering the requirements of contour error after fitting the motion segment, according to the geometric relationship between the contour error, the angle between the two motion segments, and the length of the motion segment, the radius of the transition arc and the start and end points of the transition arc are determined. Second, it is necessary to consider that the feed rate on the transition arc must meet the maximum acceleration performance of the machine tool, and the maximum feed rate of the transition arc is determined by the maximum acceleration.

3.1. Determine the Transition Arc Radius, Start Point, and End Point. In order to meet the requirements of contour machining accuracy, the requirements of contour error must be met first when determining the radius, starting point, and end point of the transition arc. Therefore, the maximum contour error E_m needs to be used as a constraint to determine other parameters of the transition arc. Substituting E_m into equations (3) and (4), the transition distance l_c that satisfies the maximum contour error can be obtained

$$l_c = \frac{\sin(\alpha/2)}{1-\cos(\alpha/2)}E_m. \tag{5}$$

Since the above formula is obtained according to the geometric relationship, for the motion segment under normal circumstances, E_m is much smaller than the length of the motion segment, so the transition distance l_c under the constraint of E_m must be smaller than the length of the adjacent motion segment. Taking any three adjacent motion segments to form 2 corner points, the situation in the figure may occur because the middle motion segment is the upper transition distance, as shown in Figure 5.

That is, the two transition arcs before and after do not intersect, which means that the radius of the transition is too large, and the transition distance does not satisfy the connection relationship, so not only the contour error but also the length of the motion segment itself determine the radius of the transition arc and the transition distance and other parameters [12, 13]. In order to ensure that two adjacent transition arcs can intersect, it must be ensured that the transition distance on each motion segment cannot exceed half the length of the motion segment

$$l_s = \min\left(\frac{S_i}{2}, \frac{S_{i+1}}{2}\right). \tag{6}$$

Consider the case of $l_c \le l_s$, in which the transition distance can satisfy the constraint condition of the length of the motion segment, and the parameters of the transition arc are completely determined by the maximum contour error, as shown in formulas (7)–(9):

$$r = \frac{\cos(\alpha/2)}{1-\cos(\alpha/2)}E_m, \tag{7}$$

$$Q_0 = \frac{l_c}{S_i}P_{i+1} + \frac{S_i - l_c}{S_i}P_i, \tag{8}$$

$$Q_2 = \frac{S_{i+1} - l_c}{S_{i+1}}P_i + \frac{l_c}{S_{i+1}}P_{i+1}. \tag{9}$$

When considering the case of $l_c > l_s$, in this case, the transition distance cannot meet the constraint condition of the length of the motion segment. According to the aforementioned method, the problem of overlapping transition distances will occur. Therefore, in this case, the parameters of the transition arc should first consider the motion segment and the constraints of its own length, as shown in formula (10)–(12):

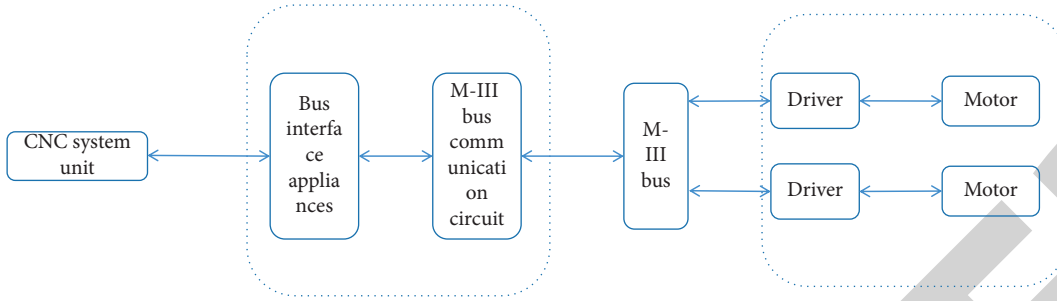

Figure 4: Arc transition coordinate system.

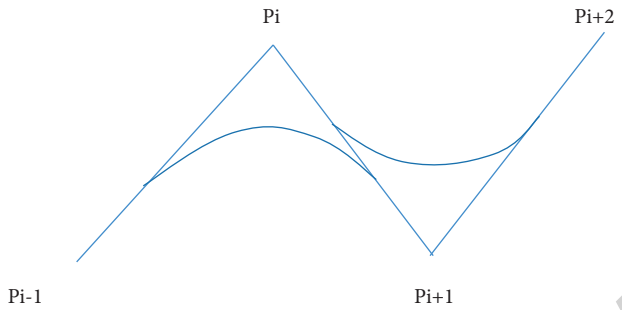

Figure 5: Schematic diagram of transition distance overlap.

$$r = \frac{\cos(\alpha/2)}{\sin(\alpha/2)} l_s, \tag{10}$$

$$Q_0 = \frac{l_c}{S_i} P_{i-1} + \frac{S_i - l_c}{S_i} P_i, \tag{11}$$

$$Q_2 = \frac{S_{i+1} - l_c}{S_{i+1}} P_i + \frac{l_c}{S_{i+1}} P_{i+1}. \tag{12}$$

3.2. Determination of the Maximum Feed Rate of the Transition Arc Segment. From the centripetal acceleration formula, the constraint relationship between the maximum feed rate v_m and the maximum acceleration of the machine tool is a_m, and the radius r of the transition arc is shown in

$$v_m = \sqrt{a_m r}. \tag{13}$$

Therefore, in order to ensure that the transition arc processing can meet both the requirements of the machining accuracy and the acceleration and deceleration performance of the machine tool, the maximum speed of the transition arc segment processing should be selected from the maximum processing speed set by the workpiece program and the speed constrained by the maximum acceleration of the machine tool. The smaller value in v_m is

$$v = \min(F, v_m). \tag{14}$$

In order to meet the feed rate when processing the transition arc segment, before the transition arc segment, the feed rate is planned based on the forward-looking algorithm, so that the feed rate of the starting point of the transition arc is v, and the transition arc is guaranteed. The speed remains constant during the processing.

$Pi-1$, Pi, and $Pi+1$ are the endpoints of adjacent arc segments and straight-line segments, and the arc $\overline{Q_0Q_1Q_2}$ is the transition curve inserted between the program segments. It can be divided into two cases as shown in the figure, and the processing method is similar, as shown in Figure 6.

Similar to the transition processing between two straight-line segments, the length of Pi from the tangent point between the transition arc and the two adjacent program segments is called the transition distance. The distance e between Pi and the transition arc vertex is the shortest distance from Pi to the transition arc $\overline{Q_0Q_1Q_2}$, which is called the contour error, as shown in Figure 7.

Assume that the central angle of the transition arc is ϕ, the error between the transition arc and the original trajectory is e, the distance between Pi and $O1$ is h, and the length between Pi and the tangent point is d:

$$\begin{cases} \theta = \dfrac{\pi - \phi}{2}, \\ h = \dfrac{e}{1 - \sin\theta}, \\ d = h \cdot \cos\theta. \end{cases} \tag{15}$$

Considering the limitation of the length of the motion segment itself, the transition distance on each line segment does not exceed half of its own length, as shown in

$$l_s = \min\left(\frac{S_i}{2}, \frac{S_{i+1}}{2}, d\right). \tag{16}$$

And the radius is determined after trimming as shown in

$$R_1 = l_s \cdot \tan\theta. \tag{17}$$

And the processing of the transition arc needs to meet the normal acceleration requirements. Let the radius that meets the requirements be $R2$, the processing speed that meets the process requirements is v, and the normal acceleration is an

$$R_2 = \frac{v^2}{a_n}. \tag{18}$$

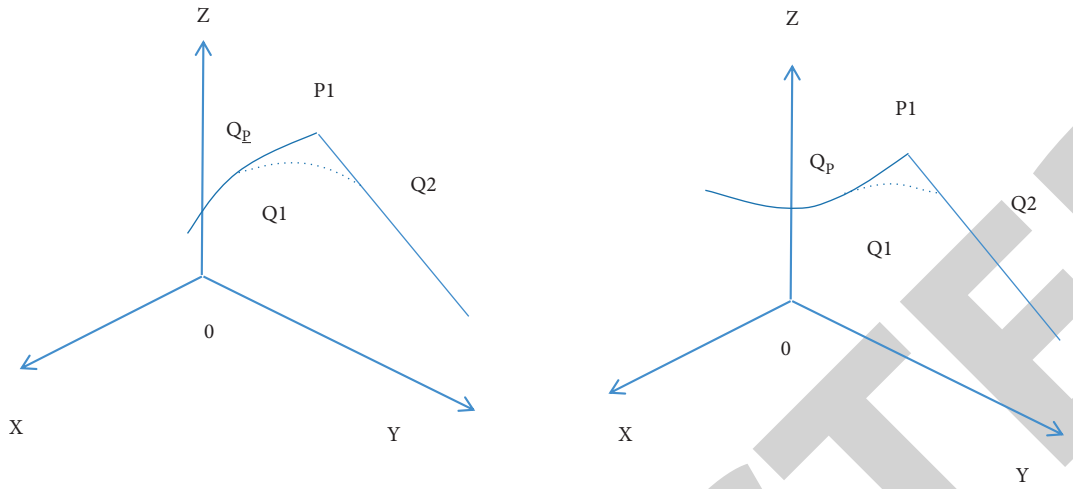

Figure 6: Schematic diagram of the transition between the arc and straight line.

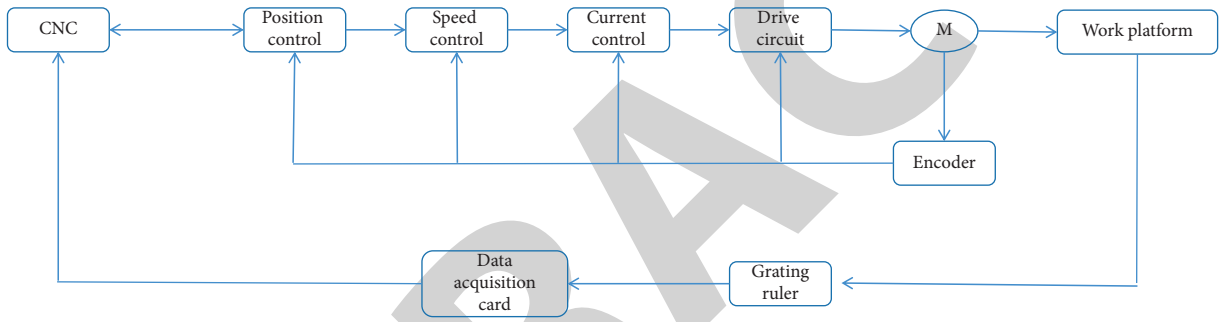

Figure 7: Arc and straight-line transition coordinate system.

The radius R satisfying the above constraints is

$$R = \min\{R_1, R_2\}. \tag{19}$$

The transition length $l1$ of the straight-line segment satisfying the constraints is shown in

$$l_1 = \frac{R}{\tan\theta}. \tag{20}$$

Let $\overline{O_2O_1}, \overline{O_1P}$ be a unitized vector, and the transition length of the arc segment that satisfies the constraints is shown in

$$l_2 = \arccos\left(\overline{O_2O_1} \cdot \overline{O_1P}\right). \tag{21}$$

Machining speed and precision are the key factors that affect the machining performance of CNC machine tools. The two restrict each other, and the optimal effect of the two cannot be obtained at the same time. Usually, the machining speed is maximized under the condition of ensuring the machining accuracy. From this point of view, the machining accuracy has a decisive effect on the machining speed, and the machining accuracy depends on the ability of the controller's trajectory to follow. Therefore, factors such as the accuracy of acceleration and deceleration of each axis of the machine tool, as well as the sudden change of feed rate and feed rate, have resulted in the reduction of the precision of CNC machine tools.

In the CNC system in the form of front acceleration and deceleration, since the theoretical trajectory error is zero, the machining accuracy is relatively high. The sudden change of feed is the main factor of machining error [14, 15]. Therefore, in this form of acceleration and deceleration, in order to minimize the machining error, the feed rate must be adjusted smoothly, and the axis speed must be limited within the allowable value range. In order to adjust the change of feed smoothly, it is necessary to ensure sufficient acceleration value of each axis, so as to maximize the acceleration and deceleration performance of CNC machine tools. When two shorter program segments are connected one after the other, since the length of the two programs is too short, the acceleration distance required by the commanded speed cannot be reached, and the obtained speed curve shows a special shape similar to the sawtooth. Therefore, it is necessary to comprehensively consider the commanded speed and the length of subsequent blocks to minimize the fluctuation of the feed speed.

4. Experiments and Analysis

Laser CNC machine tools not only include processing equipment but also monitoring and testing equipment. At the same time, because the laser processing equipment is different from the tools of general machine tools, its

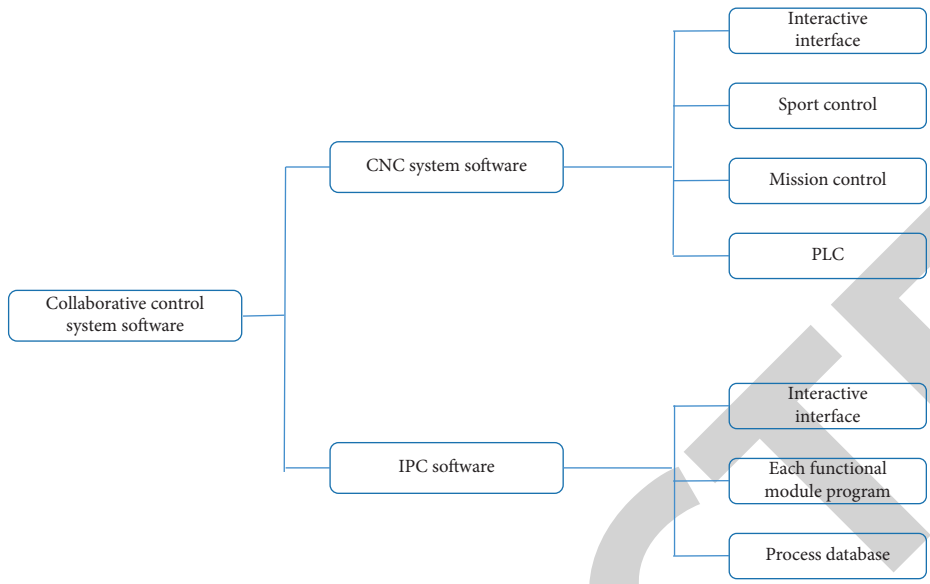

Figure 8: Overall design structure diagram of collaborative control system software.

composition includes laser, light guide system, and monitoring system. Therefore, compared with the general CNC machine tool processing technology, the operation mechanism of the laser CNC machine tool will include additional processing technology [16]. In response to this problem, according to the research on the control system of the laser numerical control machine tool in Figure 7, the actual operation process can be divided into different functions according to the different operations, which can be obtained from the processing process which is independent, as shown in Figure 8.

According to the above processing flow, it can be seen that the software modules included in the actual demand functions of the collaborative control system software design include three-dimensional measurement, focal length measurement, process database, laser and processing head adjustment, terminal monitoring, pointing monitoring, and power monitoring [17]. According to the processing flow, it can be seen that the collaborative control system software needs the coordination and cooperation of various functional modules in the specific processing process, so the design of the entire control system is also designed in accordance with the collaborative control scheme. According to the hardware structure of the machine control system, software integration can be divided into two parts by function: industrial computer control software and numerical control system software. All software design architecture of the integrated control system is shown in [18]. The CNC system part of the control system software adopts the open-source existing CNC system, which was approved as the Linux system platform at that time, realizes the functions of task control, motion control, and PLC through the software, and provides a human-computer interaction interface for display processing. information. In the actual processing process, the numerical control system is mainly responsible for realizing the axis motion control and focal length measurement module, the communication between the industrial computer and the numerical control system is realized through the serial port, and the coordinated control system can directly send the control to the numerical control system through the industrial computer to control the movement of the machine tool axis. The command is then handed over to the CNC system to complete. Therefore, the development environment of other functional modules has nothing to do with the operating environment of the CNC system. The computer software industry is developed and used by *Qt*. *Qt* is a cross-platform C++ GUI application development framework that supports Linux, Mac OS X, Windows, Linux, Android, and other platforms. It can design GUI services as well as non-GUI services such as console tools and servers. *Qt* is not only easy to connect but also allows the latest component programming. With *Qt*, you can create an application that does not change the code and can be used on multiple platforms, which reduces the installation time of the application. This topic chooses *Qt*4 to realize the development of industrial computer software man-machine interface and processing auxiliary module software, and the development tool chooses *Qt* Creator. *Qt* Creator is a lightweight integrated development environment (IDE) that supports the cross-platform operation and supports multiple operating systems [19].

In order to achieve higher benefits and reduce research costs, the CNC system part of the collaborative control system of this project adopts the GJ430 system developed by High Precision CNC Intelligent Technology Co., Ltd., which avoids the redevelopment of CNC system software. Therefore, the main task of collaborative control system software development is to complete the development of other specific functional modules based on the industrial computer platform on the basis of the existing CNC system and to realize the entire CNC machine tool electrical system in the processing process through the operation of these functional modules. According to the analysis of the laser CNC machine tool processing process and the overall design

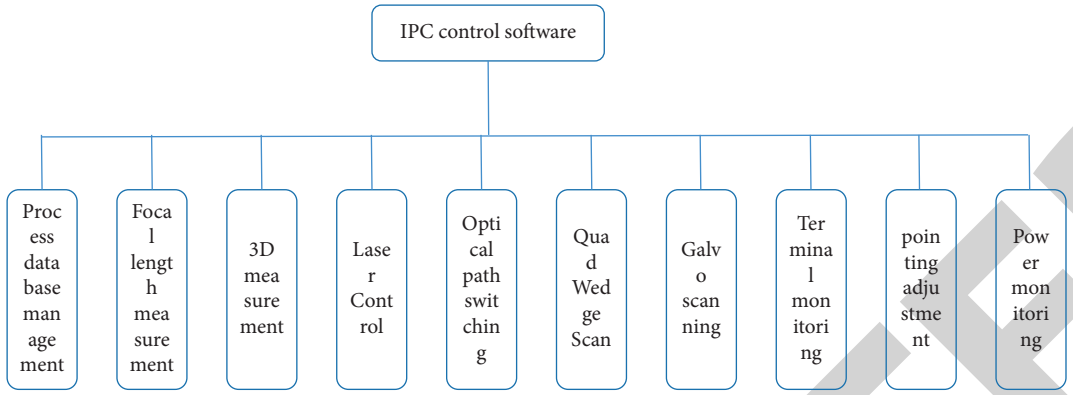

Figure 9: Structure diagram of IPC software module.

Table 1: Process database parameter table.

Serial number	Parameter	Type of data	Unit	Scope
1	Hole serial number	Unsigned int	—	1~1 0000
2	*X* coordinate	Float	mm	0~1 000.000
3	*y* coordinate	Float	mm	0~450.000
4	*Z* coordinate	Float	mm	0~500.000
5	*A* coordinate	Float	deg	−95.000~95.000
6	*C* coordinate	Float	deg	0~359.999
7	Feed rate	Unsigned int	mm/min	0~2000
8	Single layer feed	Float	mm	0~1.00

planning of the collaborative control system software, the functional module structure diagram of the industrial computer software is shown in Figure 9.

The following introduces the realization of the main functional modules in the process of IPC control software processing.

The process database is used to store the processing parameters. According to the processing requirements, the processing parameters, data types, units, and values in the process database are shown in Table 1.

Among them, the serial numbers 2 to 6 in the parameter table of the process database are the coordinate parameters of the hole-making machine tool; the serial numbers 7 to 10 are the *Z*-axis feed process parameters for the helical scanning; the serial number 11 is the laser output power value during hole making (when the actual setting is ready, the output power value is converted into a percentage for display); serial numbers 12 to 17 are the parameters of the four-beam beam scanning module when making holes; serial number 18 is the process identification, which is used to mark the scanning track of the four-beam wedge scanning head during laser hole making, including helix line scan (ID: 0), circle scan (ID: 1), and selection processing (ID: 2) methods, which can be defined or modified according to the configuration file. Each vertex of the special-shaped hole in the selected processing method is determined by separate software. The interface is defined in polar coordinates, and the center point of the polar coordinate system is concentric with the center of the circular hole nested in the special-shaped hole. Among them, the coordinates of the hole-making machine tool from 2 to 6 are the parameters obtained automatically by the 3D detection auxiliary positioning module, and the other parameters are obtained by the operator manually editing the data table [20–22].

The function of the 3D measurement module is to realize the auxiliary positioning of the workpiece processed by the machine tool, determine the accurate representation of the workpiece in the machine tool coordinate system, and save the final measured processing position information to the database. It can be seen from Chapter 2 that there are two main methods for the 3D measurement module, one is line laser scanning assisted positioning, and the other is point laser six-point assisted positioning [23, 24]. The software realization of the three-dimensional measurement module of this subject adopts the method of point laser six-point auxiliary positioning. The working flow chart of the 3D measurement module using the point laser six-point assisted positioning measurement method is shown in Figure 10.

According to the workflow of the 3D measurement module, it can be known that the function realization of the 3D measurement module needs to be completed through the cooperation of the numerical control system and the 3D measurement software. The 3D measurement software is provided with a supporting executable program by the 3D measurement equipment provider. The executable program runs on the industrial computer. The industrial computer communicates with the 3D measurement equipment through the RS232 serial port. Therefore, the 3D measurement software realizes the control of the 3D measurement equipment through this connection and acquisition of measurement data. During the execution of the 3D measurement module, the CNC system mainly obtains the axis

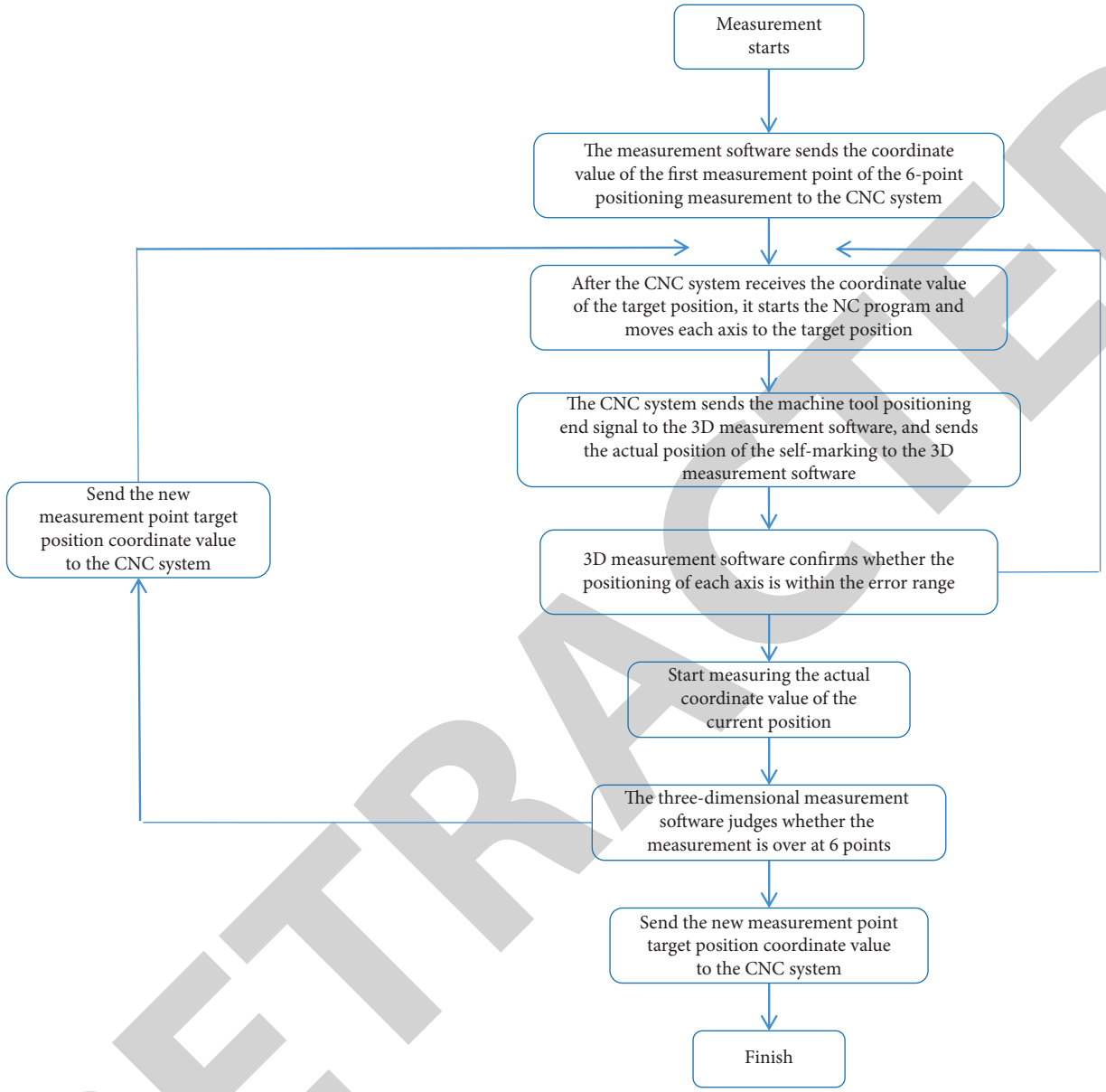

Figure 10: Workflow of the 3D measurement module.

position information and sends the axis position information to the 3D measurement software of the industrial computer and at the same time moves the machine tool coordinate axis to the target position according to the command of the industrial computer [25, 26].

The main purpose of focal length measurement is to ensure that the focus of the laser beam falls on the center of the workpiece during processing. The realization is based only on the input data of the measuring sensors and the axis movements of the CNC system. The computer focal length measurement module includes a comprehensive axis display, measurement axis measurement, and measurement results. The function of the data table is similar to the function of the data table in the database module process, and the data in the database can be selected for analysis [27–29]. The workflow of focal length measurement is shown in Figure 11.

The focal length measurement function of the industrial computer software makes it possible to measure the focal length of all the machined holes directly from the human-machine interface during specific operations, save the measurement results in the process database, and directly load the process database during processing to obtain the processing parameters and speed up processing [30].

The Modbus protocol adopts a master-slave communication method and is a question-and-answer communication protocol. A communication station can connect one or more slave communication stations through an interconnection line. Among them, the master station of the station gives the address of the slave station, starts to ask the

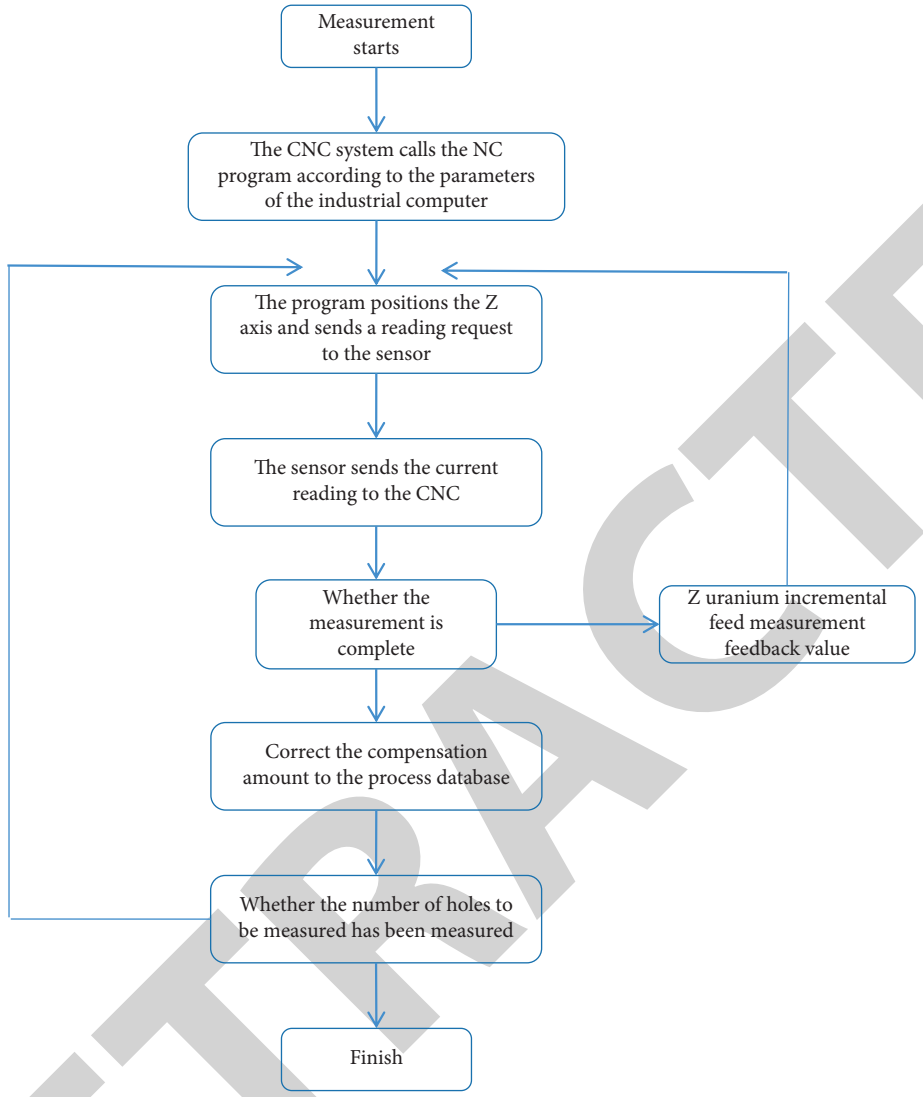

Figure 11: Flow chart of focal length measurement.

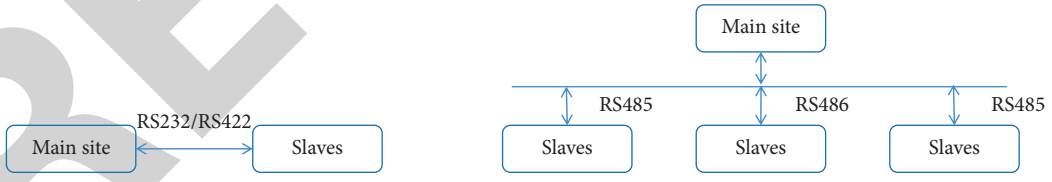

Figure 12: Comparison of Modbus protocol point-to-point communication and multipoint communication.

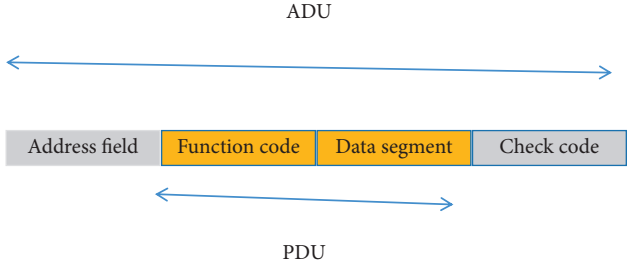

Figure 13: Modbus general frame format.

slave station, sends information, and so on. The slave receives the information sent by the master and sends a response to the master. Figure 12 shows the comparison of the connection mode between the point-to-point communication and the multipoint communication mode of the Modbus protocol using the serial port [31].

The general frame format structure of the Modbus protocol is shown in Figure 13.

The Modbus protocol consists of 4 types of registers and multiple function numbers, each function representing a different function of data in different registered entities. The

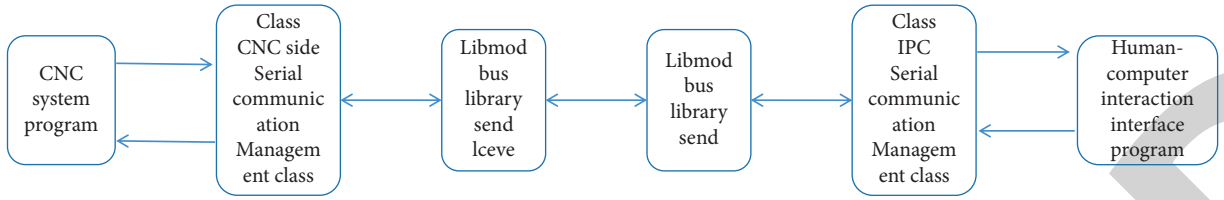

Figure 14: The realization process of communication between a CNC system and an industrial computer.

master-slave command response process according to the general statement of the Modbus model is as follows: the master sends a command according to the slave product created in the initial command and requests to read or write the record in the registration area. This time, after each slave device receives the statement, it compares the device address in the statement with its own address. If similar, it will accept the post and respond accordingly. If it is different, it discards the message frame and continues to wait for the command from the master [32].

In using this software, in order to facilitate the communication between computerized business and digital management, two types of communication based on computerized and digital business were developed. At the same time, the serial communication control class of the CNC terminal also provides a connection for receiving CNC system information and sending commands to the CNC system. The software implementation process of the communication between the CNC system and the industrial computer is shown in Figure 14.

After completing the absent initialization and the files required for Modbus communication, the communication class of the CNC terminal starts to patrol the serial port to check whether the Modbus frame is issued by the owner and whether the frame file is available. Then, it will receive the frame data and store it in the specified array, parse the data in the array to get data such as function code and offset address, and then determine what to do according to the function code. These operations include reading CNC system parameters and retrieval, and providing CNC system commands so that the CNC system can complete corresponding tasks according to the commands and responses. Figure 15 shows the flow chart of serial communication on the CNC system side.

Since the computer can be used as a proprietary device, the computer only needs to determine the slave address of the received data when sending the actual data. The serial communication class on the computer side sets the Modbus communication address of the CNC system through macro definitions. Each function module of the software provides the communication function with the CNC system and encapsulates the parameters and user operation commands obtained from the interface [33].

The kinematic model of the ultrafast laser CNC machine tool needs to verify the algorithm of the control strategy of the rotary axis, so it is necessary to simulate the tool attitude and attitude error of the three interpolation methods, respectively. The attitude error corresponding to the improved vector interpolation method is the smallest., the linear

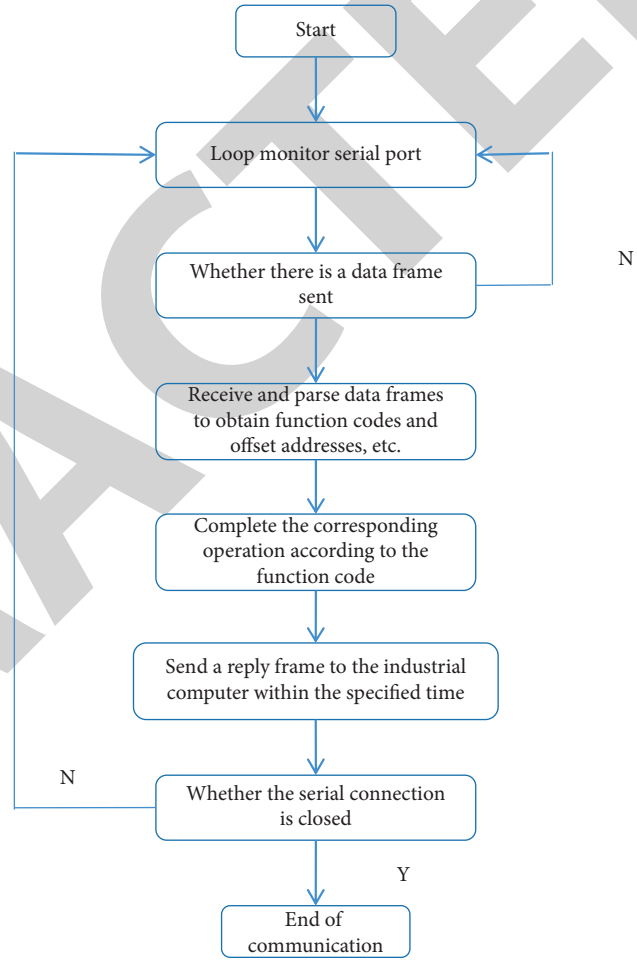

Figure 15: Flowchart of serial communication on the CNC system side.

interpolation mode is the largest, and the error is 44°, which meets the requirements of the system error, as shown in Figure 16.

As can be seen from Figure 16, during the interpolation process of vector interpolation, the speed of the C-axis will change drastically at the singular point, far exceeding the maximum acceleration performance of the machine tool. The linear interpolation method produces a larger tool attitude error. The advantages are proposed in this research.

In the interpolation process, the speed change is relatively gentle and meets the requirements of machining accuracy.

It is important to note that when assembling a Modbus frame, the internal computer industry determines the

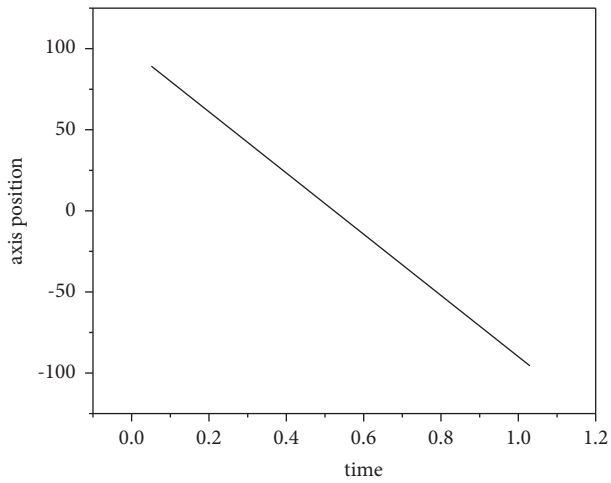

Figure 16: Schematic diagram of AC axis position curve.

location in the Modbus frame based on the type of operations registered and invoked. In the above rule, since the final call is to record multiple registry functions, the base functions are assembled in Modbus. When framing, the job number is set to 16 (multiple names assigned). The software application process of other functions and control signal communication in the computer software industry is similar to the communication process using the optical modification process and will not be explained one by one.

5. Conclusion

The combination of CNC technology and laser processing technology is a new direction for the development of CNC machine tools in the future. Through laser processing, CNC machine tools can further improve the power addition accuracy and processing efficiency and make it possible for CNC machine tools to complete finer processing. The research results show that this electrical collaborative control system scheme has strong practicability and feasibility. With the help of system upgrades and optimization, the efficient integration of laser processing technology and numerical control technology can be better achieved. It should be noted that the machining process of the machine tool is also required. In-depth improvements should be made, which can maximize the operating efficiency and machining accuracy of the electrical system of the CNC machine tool. Although CNC technology and laser technology are still relatively mature at present, there are still many problems in the development of more general laser CNC machine tools, and further exploration and research are needed. Compared with general machine tools, the research and development of laser CNC machine tools are still in the preliminary stage. There is no relatively unified manufacturing standard. More research and development are carried out to meet specific processing needs. The experience and results will provide a certain reference for further in-depth research and development in the future.

This research focuses on the research and implementation of electrical system cooperative control in ultrafast laser CNC machine tools, mainly from three aspects:

(1) Research and design of the overall control scheme. By analyzing the equipment composition and functions of the laser CNC machine tools, combined with the processing requirements and the control relationship between the equipment, in order to better meet the processing requirements, a collaborative control scheme for the electrical system of the machine tool based on the industrial computer is proposed, and this collaborative control scheme is used as a guide for machine tool hardware structure design and software design.

(2) Hardware structure design, based on the control relationship between laser numerical control machine tool equipment analyzed in the first part and the proposed collaborative control scheme to complete the overall hardware structure design of the machine tool, and introduce the hardware structure design of the numerical control system and collaborative control unit in detail, and finally complete the machine tool equipment intercommunication design.

(3) The software management department was informed. As the basis for the hardware components of the machine tool, an integrated control unit integrated with the computer was developed, including the main control unit. The integrated control system consists of two parts: the industrial computer control software and the digital control system. Among them, the CNC system software is famous for controlling the movement of the machine tool axis, and the industrial computer software is used for real-time operation and comprehensive control. Finally, the realization of the main function modules of the control system software and the software realization of the communication between the numerical control system and the industrial computer are introduced in detail.

The laser CNC machine tool researched and developed verifies the rationality and feasibility of the collaborative control scheme through practical experiments, which can meet the processing requirements and realize the integration of laser processing technology and numerical control technology. There are high machining efficiency and machining accuracy. In general, although the machine tools studied in this topic are highly specialized, they still have certain reference value for future related research. The main development trend of the laser industry in the future is as follows: ultrafast laser will become the future development trend of the laser industry, the industry will continue to develop in the direction of high precision, and the industry will continue to develop in the direction of flexibility. The laser processing control system is the brain of the laser processing equipment. With the continuous development of the laser processing equipment, the performance requirements of the laser processing control system are increasing day by day. In the future, the application of the laser processing control system will develop in the direction of high precision.

Data Availability

The labeled data set used to support the findings of this study is available from the corresponding author upon request.

Conflicts of Interest

The author declares that there are no conflicts of interest.

Acknowledgments

This work was supported by the Zhejiang Industry Polytechnic College.

References

[1] M. Macmammah, J. Atuchukwu, C. I. Obinwa, and C. E. Agbaraji, "Robust compensating function scheme for adequate electrical power system stabilization," *Journal of Scientific Research and Reports*, vol. 27, no. 4, pp. 80–91, 2021.

[2] K. Klausen, C. Meissen, T. I. Fossen, M. Arcak, and T. A. Johansen, "Cooperative control for multirotors transporting an unknown suspended load under environmental disturbances," *IEEE Transactions on Control Systems Technology*, vol. 28, no. 2, pp. 653–660, 2020.

[3] J. Singh and D. Kedia, "Spectral efficient precoding design for multi-cell large mu-mimo system," *IETE Journal of Research*, vol. 66, no. 5, pp. 1–16, 2020.

[4] A. Singh, H. Ahuja, V. S. Bhadoria, and S. Singh, "Control implementation of squirrel cage induction generator based wind energy conversion system," *Journal of Scientific & Industrial Research*, vol. 79, no. 4, pp. 306–311, 2020.

[5] H. Lee, J. Kim, C. Lee, and J. Kim, "Novel cooperative controller design of heterogeneous energy storages for economic applications in electric railway systems," *Journal of Electrical Engineering & Technology*, vol. 15, no. 2, pp. 979–987, 2020.

[6] Y. H. Lan, B. Wu, and Y. P. Luo, "Finite difference based iterative learning control with initial state learning for fractional order linear systems," *International Journal of Control, Automation and Systems*, vol. 20, no. 2, pp. 452–460, 2022.

[7] D. G. Lui, A. Petrillo, and S. Santini, "Leader tracking control for heterogeneous uncertain nonlinear multi-agent systems via a distributed robust adaptive pid strategy," *Nonlinear Dynamics*, vol. 108, no. 1, pp. 363–378, 2022.

[8] N. P. Gupta and P. Paliwal, "Design and operation of smart hybrid microgrid," *International Journal of Emerging Electric Power Systems*, vol. 22, no. 6, pp. 729–744, 2021.

[9] A. Zahedmanesh, K. M. Muttaqi, and D. Sutanto, "A cooperative energy management in a virtual energy hub of an electric transportation system powered by pv generation and energy storage," *IEEE Transactions on Transportation Electrification*, vol. 7, no. 3, p. 1, 2021.

[10] M. B. Sanjareh, M. H. Nazari, and S. H. Hosseinian, "A novel strategy for frequency control of islanded greenhouse with cooperative usage of bess and led lighting loads," *Electrical Engineering*, vol. 103, no. 1, pp. 265–277, 2020.

[11] M. Liu, C. Wei, and L. Xu, "Development of cooperative controller for dual-motor independent drive electric tractor," *Mathematical Problems in Engineering*, vol. 2020, Article ID 4826904, 12 pages, 2020.

[12] J. Duan, H. Xu, W. Liu, J. C. Peng, and H. Jiang, "Zero-sum game based cooperative control for onboard pulsed power load accommodation," *IEEE Transactions on Industrial Informatics*, vol. 16, no. 1, pp. 238–247, 2020.

[13] T. B. Avraham, G. Sharon, Y. Zarai, and M. Margaliot, "Dynamical systems with a cyclic sign variation diminishing property," *IEEE Transactions on Automatic Control*, vol. 65, no. 3, pp. 941–954, 2020.

[14] S. Kim, "Cooperative game based traffic control scheme for the dual-channel can platform," *IEEE Access*, vol. 9, no. 99, p. 1, 2021.

[15] S. Mahmoud, "An overview of high impedance differential scheme, design, protection and simulation for a 132 kv double bus bar single breaker system," *International Journal of Engineering and Technical Research*, vol. 09, no. 3, pp. 163–168, 2020.

[16] S. R. Shakirov, A. G. Kvashnin, and A. V. Pisarev, "Research and development of mathematical models of elements of a gas-air flow for improvement of automatic control system of organic waste processing plant," *Mekhatronika, Avtomatizatsiya, Upravlenie*, vol. 21, no. 10, pp. 575–583, 2020.

[17] Z. Dong, Y. Liu, H. Wang, and T. Qin, "Method of cooperative formation control for underactuated usvs based on nonlinear backstepping and cascade system theory," *Polish Maritime Research*, vol. 28, no. 1, pp. 149–162, 2021.

[18] J. K. Arun and S. L. Stuwart, "Cyclic interleaving scheme for an ifdma system," *Annals of Telecommunications*, vol. 75, no. 5-6, pp. 241–252, 2020.

[19] R. R, "Design and implementation of imc-wpt system with efficient control management strategy for vehicle to grid application," *Journal of Advanced Research in Dynamical and Control Systems*, vol. 12, no. SP7, pp. 1775–1781, 2020.

[20] X. Huang, F. Zhao, Z. Sun, Z. Zhu, and X. Mei, "A Novel Condition Monitoring Signal Analysis Method of Numerical Control Machine Tools in Varying Duty Operation," *IEEE Access*, vol. 8, no. 99, p. 1, 2020.

[21] N. Hidman, G. Sardina, D. Maggiolo, H. Ström, and S. Sasic, "Numerical frameworks for laser-induced cavitation: is interface supersaturation a plausible primary nucleation mechanism?" *Crystal Growth & Design*, vol. 20, no. 11, pp. 7276–7290, 2020.

[22] J. Wang, C. Cheng, and H. Li, "A novel approach to separate geometric error of the rotary axis of multi-axis machine tool using laser tracker," *International Journal of Precision Engineering and Manufacturing*, vol. 21, no. 6, pp. 983–993, 2020.

[23] A. A. Gribkov, P. M. Pivkin, and A. A. Zelenskii, "State industrial policy and the machine-tool industry," *Russian Engineering Research*, vol. 41, no. 4, pp. 342–346, 2021.

[24] H. Yang, Z. Wang, T. Zhang, and F. Du, "A review on vibration analysis and control of machine tool feed drive systems," *International Journal of Advanced Manufacturing Technology*, vol. 107, no. 1-2, pp. 1–23, 2020.

[25] L. Luo, Z. X. Yang, L. Tang, and K. Zhang, "An elm-embedded deep learning based intelligent recognition system for computer numeric control machine tools," *IEEE Access*, vol. 8, no. 99, p. 1, 2020.

[26] B. Li, T. Wang, and P. Wang, "An analytical and optimal corner smoothing method for cnc machine tools along linear segments," *Journal of Mechanical Science and Technology*, vol. 36, no. 4, pp. 1959–1973, 2022.

[27] T. M. Volkova, E. N. Nerush, and I. Y. Kostyukov, "Using machine-learning methods for analysing the results of numerical simulation of laser-plasma acceleration of electrons," *Quantum Electronics*, vol. 51, no. 9, pp. 854–860, 2021.

[28] F. E. Bock, J. Herrnring, M. Froend, J. Enz, and B. Kashaev, "Experimental and numerical thermo-mechanical analysis of

Hindawi
Shock and Vibration
Volume 2024, Article ID 9753919, 1 page
https://doi.org/10.1155/2024/9753919

Retraction

Retracted: High-Resolution Direction of Arrival Estimation of Underwater Multitargets Using Swarming Intelligence of Flower Pollination Heuristics

Shock and Vibration

Received 23 January 2024; Accepted 23 January 2024; Published 24 January 2024

This article has been retracted by Hindawi following an investigation undertaken by the publisher [1]. This investigation has uncovered evidence of one or more of the following indicators of systematic manipulation of the publication process:

(1) Discrepancies in scope

(2) Discrepancies in the description of the research reported

(3) Discrepancies between the availability of data and the research described

(4) Inappropriate citations

(5) Incoherent, meaningless and/or irrelevant content included in the article

(6) Manipulated or compromised peer review

The presence of these indicators undermines our confidence in the integrity of the article's content and we cannot, therefore, vouch for its reliability. Please note that this notice is intended solely to alert readers that the content of this article is unreliable. We have not investigated whether authors were aware of or involved in the systematic manipulation of the publication process.

Wiley and Hindawi regrets that the usual quality checks did not identify these issues before publication and have since put additional measures in place to safeguard research integrity.

We wish to credit our own Research Integrity and Research Publishing teams and anonymous and named external researchers and research integrity experts for contributing to this investigation.

The corresponding author, as the representative of all authors, has been given the opportunity to register their agreement or disagreement to this retraction. We have kept a record of any response received.

References

[1] N. Ahmed, H. Wang, S. Tu et al., "High-Resolution Direction of Arrival Estimation of Underwater Multitargets Using Swarming Intelligence of Flower Pollination Heuristics," *Shock and Vibration*, vol. 2022, Article ID 5876874, 16 pages, 2022.

Hindawi
Shock and Vibration
Volume 2022, Article ID 5876874, 16 pages
https://doi.org/10.1155/2022/5876874

Research Article

High-Resolution Direction of Arrival Estimation of Underwater Multitargets Using Swarming Intelligence of Flower Pollination Heuristics

Nauman Ahmed,[1] **Huigang Wang**,[1] **Shanshan Tu**,[2] **Norah A.M. Alsaif**,[3] **Muhammad Asif Zahoor Raja**,[4] **Muhammad Kashif**,[5] **Ammar Armghan**,[6] **Yasser S. Abdalla**,[7,8] **Wasiq Ali**,[5] **and Farman Ali**[8,9]

[1]*School of Marine Science and Technology Northwestern Polytechnical University, Xian, Shaanxi, China*
[2]*Engineering Research Center of Intelligent Perception and Autonomous Control, Faculty of Information Technology, Beijing University of Technology, Beijing 100124, China*
[3]*Department of Physics, College of Science, Princess Nourah bint Abdulrahman University, P. O. Box 84428, Riyadh 11671, Saudi Arabia*
[4]*Future Technology Research Center, National Yunlin University of Science and Technology, 123 University Road, Section 3, Douliou, Yunlin 64002, Taiwan*
[5]*Department of Electrical and Computer Engineering, COMSATS University Islamabad Attock Campus, Islamabad, Pakistan*
[6]*Department of Electrical Engineering, College of Engineering, Jouf University, Sakaka 72388, Saudi Arabia*
[7]*Department of Computer Engineering and Networks, College of Computer and Information Sciences, Jouf University, Sakakah, Saudi Arabia*
[8]*Faculty of Technology and Education, Suez University, Suez, Egypt*
[9]*Department of Electrical Engineering, Qurtuba University of Science and IT, Dera Ismail Khan 29050, Pakistan*

Correspondence should be addressed to Nauman Ahmed; nauman@mail.nwpu.edu.cn, Shanshan Tu; sstu@bjut.edu.cn, and Farman Ali; drfarmanali.optics@qurtuba.edu.pk

Received 6 January 2022; Revised 19 April 2022; Accepted 21 April 2022; Published 30 June 2022

Academic Editor: Yuxing Li

Developing the parameter estimation, particularly direction of arrival (DOA), utilizing the swarming intelligence-based flower pollination algorithm (FPA) is considered an optimistic solution. Therefore, in this paper, the features of FPA are applied for viable DOA in the case of several robust underwater scenarios. Moreover, acoustic waves impinging from the far-field multitarget are evaluated using the different number of hydrophones of uniform linear array (ULA). The measuring parameters like robustness against noise and element quantity, estimation accuracy, computation complexity, various numbers of hydrophones, variability analysis, frequency distribution and cumulative distribution function of root mean square error (RMSE), and resolution ability are applied for analyzing the performance of the proposed model with additive white Gaussian noise (AWGN). For this purpose, particle swarm optimization (PSO), minimum variance distortion-less response (MVDR), multiple signal classification (MUSIC), and estimation of signal parameter via rotational invariance technique (ESPRIT) standard counterparts are employed along with Crammer–Rao bound (CRB) to improve the worth of the proposed setup further. The proposed scheme for estimating the DOA generates efficient outcomes compared to the state-of-the-art algorithms over the Monte Carlo simulations.

1. Introduction

Swarming intelligence of evolutionary algorithms is a significant development in signal processing for direction of arrival (DOA) estimation of underwater multitargets [1, 2]. For solving such problems, subspace-based methods were used like multiple signal classification (MUSIC) [3]. If used in a constraint environment like assuming incoherent

sources, with a specified number of snapshots and high SNR signals, these methods give good results. But due to these limitations, it can only be applied to very few scenarios and problems. Parametric methods like maximum likelihood (ML) [4, 5] are also used to address such issues, but they are computationally complex, which impedes the fertility of application. Previously, most of the published research validated the performance of DOA estimators using asymptotic assumptions, which requires either a high signal-to-noise ratio or a more significant number of samples, which are not specific in many real-life problems [6, 7]. DOA estimator accuracy is dependent on the signal power and the rate of transmission, which are beyond the control of the system designer [8]. Therefore, such systems operate in a low SNR, estimating accurate angular localization, a challenging task [9]. New intelligent optimization algorithms have been proposed recently for estimation of DOA like genetic algorithm (GA) [9], differential evolution (DE) method [8], particle swarm optimization (PSO), seeker optimization algorithm (SOA), sine cosine algorithm (SCA), invasive weed optimization (IWO) [10], and squirrel search algorithm (SSA) [11]. In [12], GA is proposed with accurate and reliable results for the estimation of the parameters of DOA problems, and the performances of the GA, ML, and MUSIC algorithm have been compared with different variants of SNR, computational cost, and the number of snapshots. The detection probability is modeled in [13], through the active sonar equation for probability hypothesis density (PHD) and cardinalized PHD (CPHD). Novel complexity measure is proposed in [14] for improving permutation entropy (PE) and analyzing the time series. Similarly, missing amplitude information and single scale problem in PE are addressed in [15] through refined composite multiscale reverse weighted PE (RCMRWE). A modified version of the GA is applied to the nonlinear and highly nonlinear function to estimate the parameters of DOA as presented in [16]. In [17, 18], PSO algorithm and pattern search algorithm were developed to estimate the parameters of the multimodal function. In [19], the PSO ML estimator shows very healthy and reliable results as compared to conventional parameter estimation techniques for DOA. Using the ant colony optimization (ACO) by extending the pheromone, DOA parameters are estimated in [20], with outstanding results and low computational complexity. In [21], the artificial bee colony (ABC) algorithm is used to achieve higher statistical performance. A high degree of freedom for DOA is studied in [22] using Cuckoo search algorithm. The analytical model was discussed for the proposed approach in terms of fitness function, SNR, and cumulative distributive function. In [23], the authors have proposed adaptive FPA mechanism in order to localize the nodes in wireless sensor networks. Back in 2019, a Squirrel Search Algorithm (SSA) was proposed, which is a novel numerical optimization algorithm. It focuses on the foraging and gliding behavior of flying squirrels to determine their efficient way of locomotion. Gliding is a powerful technique used by small mammals for traveling long distances. The present work mathematically models this behavior to realize the process of optimization. These features may be helpful to improve convergence and reduce the number of iterations of the SSA algorithm to determine the ML DOA estimate [24].

In this study, optimization strength of nature-inspired heuristics of flower pollination algorithm (FPA) is exploited for possible DOA estimation in case of different scenarios of the underwater environment using a uniform linear array (ULA) of hydrophones for influencing acoustic waves from far-field multitargets. The high resolution for close space targets is achieved using fewer snapshots viably with FPA by investigating the global minima of the highly nonlinear cost function of ULA with multiple local minima. Performance analysis is conducted for different number of targets employing estimation accuracy, robustness against noise, and number of hydrophones in the presence of additive white Gaussian measurement noise, and comparative studies with MVDR, MUSIC, Root MUSIC, and ESPRIT counterparts along with Crammer–Rao bound analysis reveals the worth of the scheme for estimating DOA parameters, which are further endorsed from the results of Monte Carlo simulations.

The rest of the paper is arranged as follows: Section 2 defines the mathematical model for ULA. The conventional beamforming (CBF) algorithm, MVDR, MUSIC, Root MUSIC, and ESPRIT are explained with their procedure for the DOA problem in Section 3. Performance analysis of algorithms concerning RMSE is illustrated in Section 4. Finally, Section 5 explains the main contributions of the proposed study.

2. Mathematical Model

In this study, the ULA of hydrophones is used for 1D-DOA estimation. So, according to the characteristics of ULA, the impinged plane waves from the far-field region are phase-shifted versions of consecutive hydrophones as explained in Figure 1. The angle of arrival [25, 26] can be denoted as

$$\theta = [\theta_1, \theta_2, \theta_3, \ldots, \theta_D]. \tag{1}$$

Here, θ_D is the associated angle to the D^{th} acoustic source.

$$\begin{aligned} \mathbf{z}(t) &= [z_1(t), z_2(t), \ldots, z_W(t)], \\ \mathbf{g}(\theta_i) &= \left[1, e^{(-jkd\sin(\theta_i))}, e^{(-jk2d\sin(\theta_i))}, \ldots, e^{-jk(W-1)d\sin(\theta_i)}\right]^T, \\ \mathbf{G}(\theta) &= [\mathbf{g}(\theta_1), \mathbf{g}(\theta_2), \ldots, \mathbf{g}(\theta_D)]. \end{aligned} \tag{2}$$

Here, $k = 2\pi/\lambda$, while λ is the wave length. $\mathbf{z}(\mathbf{t})$ is the hydrophone's output vector with dimension $W \times 1$ and can be known as array response.

$$\mathbf{z}(\mathbf{t}) = \mathbf{G}(\theta)\mathbf{y}(t) + \mathbf{v}(t). \tag{3}$$

The steering matrix G of dimension $W \times D$ comprises the time delay entities of signals for each hydrophone. Here, $\mathbf{v}(\mathbf{t})$ is additive white Gaussian noise of zero mean with a dimension of $W \times 1$. The covariance matrix [27, 28] is defined as

$$\mathbf{R} = E\left[\mathbf{z}(t)\mathbf{z}^H(t)\right]. \tag{4}$$

The previous equation can be written when a finite number of snapshots are available:

$$\mathbf{R} = \frac{1}{K}\sum_{n=1}^{K}\mathbf{z}(n)\mathbf{z}^H(n), \tag{5}$$

where $E[.]$ and $[.]^H$ are ensemble average and Hermitian operators, respectively. So the correlation matrix [29, 30] can be written as

$$\mathbf{R} = \mathbf{G}\mathbf{R}_s\mathbf{G}^H + \sigma^2\mathbf{I}_D. \tag{6}$$

where $\mathbf{R}_y$ is the correlation associated with signal and $\sigma^2\mathbf{I}_D$ is the noise correlation matrix.

3. DOA Estimation

Generally, DOA estimation algorithms are divided into two categories, i.e., CBF techniques and subspace-based techniques. In this work, the performance analysis has been taken for both the CBF and subspace-based algorithms under varying noise levels for different acoustic sources.

3.1. Particle Swarm Optimization. The heuristics of PSO was proposed by Kennedy and Eberhart having motivation from the pool of birds congregating for food in a random manner [31]. The idea of seeking food is a heuristic approach because all the birds have the information of distance but are not familiar with the explicit location of food. They seek the food by exchanging their search information via crossover and kid production method. The PSO is introduced for the pool of applications almost in every walk of engineering [32, 33]. In this work, PSO performs searching via a swarm of particles that updates recursively. To approach the optimal solution, each particle (DOAs) moves in the direction to its previously best ($p$best) position and the global best ($g$best) position in the swarm.

$$\begin{aligned}\mathbf{v}_i(n+1) = {} & \boldsymbol{\omega}\mathbf{v}_\mathbf{i}(\mathbf{n}) + \mathbf{c}_1\mathbf{r}_1\left(\boldsymbol{\theta}_\mathbf{i}(\mathbf{n}) - \boldsymbol{\theta}_\mathbf{pbest}\right) \\ & + \mathbf{c}_2\mathbf{r}_2\left(\boldsymbol{\theta}_\mathbf{i}(\mathbf{n}) - \boldsymbol{\theta}_\mathbf{gbest}\right).\end{aligned} \tag{7}$$

$$\boldsymbol{\theta}_i(n+1) = \boldsymbol{\theta}_i(n) + \mathbf{v}_i(n+1). \tag{8}$$

Here, $\theta_{p\text{best}}$ and $\theta_{g\text{best}}$ can be calculated as

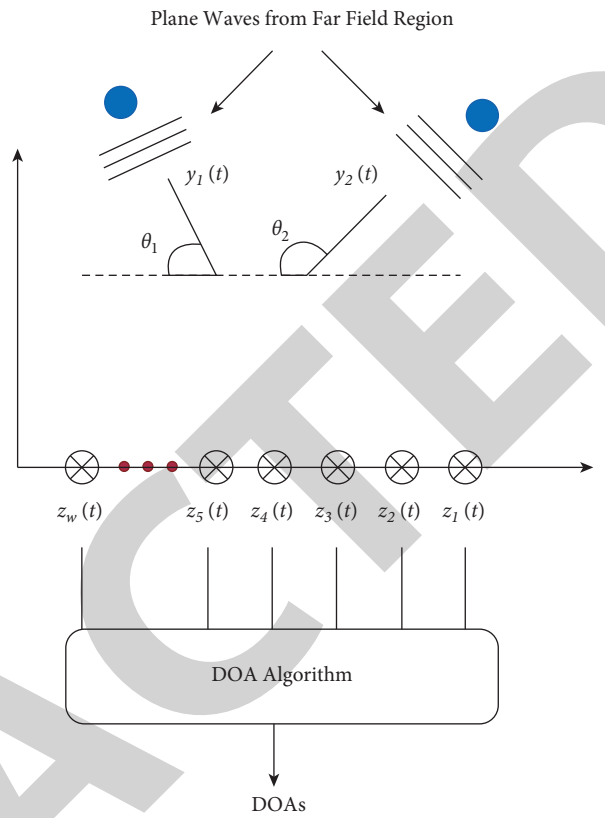

Figure 1: DOA estimation model.

$$\begin{aligned}\boldsymbol{\theta}_{p\text{best}}(i) &= \text{argmin}_{i=1,\ldots,K} f\left(\theta_n(i)\right), \\ \boldsymbol{\theta}_{g\text{best}}(i) &= \text{argmin}_{n=1,\ldots,N} f\left(\theta_n(i)\right).\end{aligned} \tag{9}$$

Here, i denotes the particle index, n is the current iteration number, and $f(\theta_n(i))$ is the fitness function that can be defined as

$$f(\theta_e) = \left|\mathbf{z}\boldsymbol{\theta}_\mathbf{e}(\mathbf{t}) - \mathbf{z}\boldsymbol{\theta}_\mathbf{a}(\mathbf{t})\right|^2. \tag{10}$$

And, the parameters ω, c_1, c_2, r_1, and r_2 are inertia weight, two positive constants, and two random parameters within [0, 1], respectively. The velocity v and positions (DOAs) of particles are updated with equations (9) and (10).

3.2. Basis Principle of FPA. The features of pollination scheme, flower reliability, and behavior of the pollinator can be analyzed efficiently by the following principles:

(1) The global pollination scheme consists of cross-pollination and biotic methods, while pollinators perform levy flights with pollen (global optimization)

(2) The local pollination mechanism consists of self-pollination and abiotic methods (local optimization) [34]

(3) A switch probability $p \epsilon [0, 1]$ is designed to control global pollination and local pollination schemes

Figure 2: Flow chart of FPA.

In the complete pollination process, the local pollination scheme can experience a large quantity of fraction p. Its reason can be environmental factors like wind and physical proximity. Generally, many flowers can grow on a plant, and pollen gametes from each flower can be released in billions. However, here we suppose that every plant has the ability to harvest only one flower and only one pollen gamete can be produced from each flower. Therefore, plant, flower, and pollen gamete are easy to identify for finding the solution to a problem. The above assumption develops the most straightforward way that solution can be equal to a pollen gamete and a flower. In future research, especially for multiobjective optimization problems, different numbers of flowers can be associated with each plant and multiple pollen gametes can be assigned to each flower. A flower-based algorithm, known as flower pollination algorithm (FPA), can

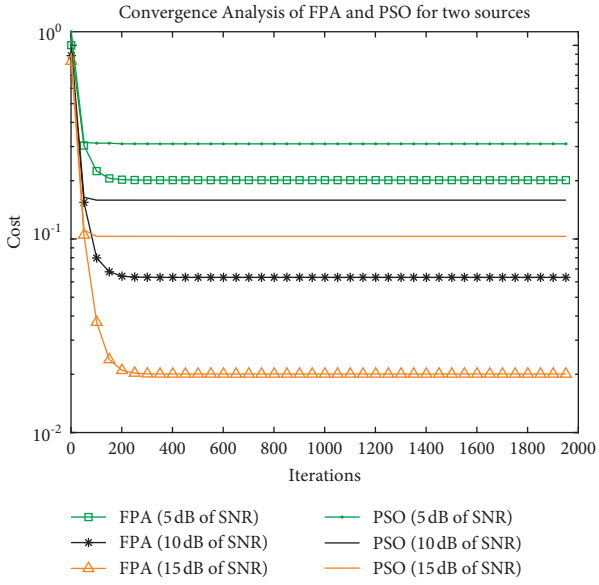

Figure 3: Convergence analysis of FPA for two sources.

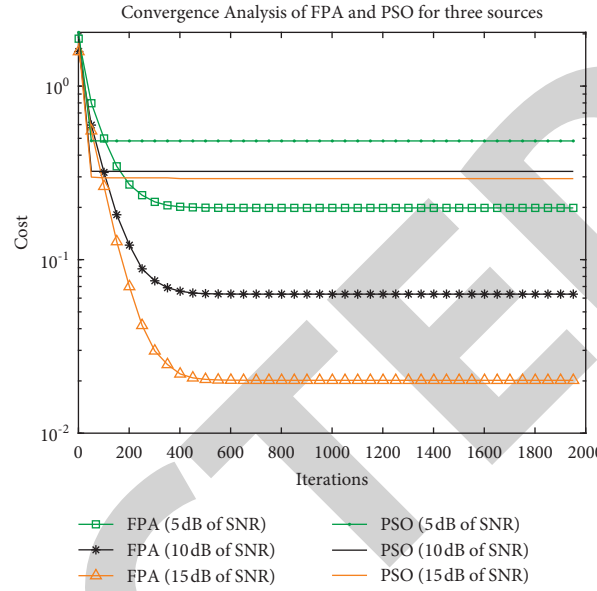

Figure 4: Convergence analysis of FPA for three sources.

be designed from the above principles and arguments. Global pollination and local pollination are two major stages of this algorithm [35]. In the phase of global pollination, insects work as pollinators for carrying flower pollens over long distances because of their capability to move and fly for a more extended range. In this way, fittest reproduction and pollination can be ensured. Flower reliability phenomena and the first rule of global pollination step can be mathematically [36, 37] described as

$$\theta_i(n+1) = \theta_i(n) + L\left(\theta_i(n) - \theta_{\text{best}}\right). \tag{11}$$

Here, pollen i is represented by $\theta_i(n)$ at iteration n, while at current iteration, the best value among all values is denoted by θ_{best}. Pollination strength is shown with parameter L, which represents step size. Levy flight mechanism can be used accurately to analyze the property of insects to travel over long distances using many steps. Thus, from Levy distribution, we develop $L > 0$. In the end, the best result can be referred to as the best approximated angle.

$$L = \lambda\Gamma(\lambda)\sin\left(\frac{\pi\lambda}{2}\right)\left(\pi.s^{(1+\lambda)}\right)^{-1}. \tag{12}$$

The standard gamma function is represented by $\Gamma(\lambda)$ with $\lambda = 1.5$, and s consists of Gaussian distributions U and V described as

$$s = U.|V|^{-1/\lambda}, \tag{13}$$

where $U \sim N(0, \sigma^2)$ and $V \sim N(0, 1)$, and σ^2 can be computed as

$$\sigma^2 = \left\{\frac{\Gamma(1+\lambda)}{\lambda\Gamma[(1+\lambda)/2]}.\frac{\sin(\pi\lambda/2)}{2^{(\lambda-1)/2}}\right\}^{1/\lambda}. \tag{14}$$

Local pollination step and flower reliability phenomena can be written as

$$\theta_i(n+1) = \theta_i(n) + \varepsilon\left(\theta_j(n) - \theta_k(n)\right). \tag{15}$$

Two arbitrary pollens produced from unlike flowers of the similar plant are denoted with $\theta_j(n)$ and $\theta_k(n)$ in the above mathematical model. This behavior shows the reliability of a flower in a limited community. Mathematically, these solutions are selected from the same population with a random walk of ϵ drawn from a uniform distribution in [0, 1]. Many of the flower pollination processes happen at both global and local levels. Practically local flower pollens pollinate the nearby flowers and flower patches or those not so from them. Thus, using this property, a switch or proximity probability p_s (Rule 3) is developed to shift among global mutual pollination and complete local pollination. By applying switch probability, $p_s = 0.5$ can be used as starting value, and after this, a suitable range of parameters can be developed. The literature shows that $p_s = 0.8$ is appropriate for many practical applications.

3.3. DOA Estimation Using FPA. The general goal of DOA estimation is a continuous optimization that is used to find the θ_{best} which satisfies

$$f\left(\theta_{\text{best}}\right) = \min_{\theta \epsilon S} f(\theta), \tag{16}$$

where $S \epsilon R^D$ and $f(\theta)$ comprise the cost values of the corresponding solution θ. The cost function of DOA estimation can be defined as

$$f(\theta) = \left|z_e(\theta) - z\left(\theta_a\right)\right|^2, \tag{17}$$

where $z_e(\theta)$ is the estimated (approximated using optimized parameters) array output and $z(\theta_a)$ is the actual array out. Therefore, the actual goal of the optimizer is to compute the associated argument for the minimum cost of the cost function as shown in Figure 2. Hence, the population of N individuals will be used to solve the optimization problem

Table 1: Estimation accuracy for two sources.

SNR = 5 dB, snapshots = 20, hydrophones = 8, $d = \lambda/2$							
Algorithms		FPA	ESPRIT	RMUSIC	MUSIC	MVDR	PSO
$\theta_1 = 30$	Mean	30.005	29.680	26.125	31.980	32.036	33.549
	Variance	0.0162	5.490	347.70	1.932	0.869	33.549
$\theta_1 = 35$	Mean	34.953	35.693	35.246	32.993	33.036	278.68
	Variance	0.008	12.373	33.661	1.960	0.869	476.42

Table 2: Estimation accuracy for three sources.

SNR = 5 dB, snapshots = 20, hydrophones = 8, $d = \lambda/2$							
Algorithms		FPA	ESPRIT	RMUSIC	MUSIC	MVDR	PSO
$\theta_1 = 30$	Mean	29.999	29.099	11.961	38.710	39.666	37.447
	Variance	0.0188	46.4054	854.4187	55.3792	46.2022	439.3751
$\theta_2 = 40$	Mean	39.998	39.792	38.310	41.033	41.153	47.041
	Variance	0.0205	14.4508	47.6986	53.7322	44.8432	345.3394
$\theta_1 = 50$	Mean	50.007	50.686	48.330	42.483	42.920	51.160
	Variance	0.0295	14.3758	19.3924	51.7431	40.6736	138.6291

Table 3: Estimation accuracy for four sources.

SNR = 5 dB, snapshots = 20, sydrophones = 8, $d = \lambda/2$							
Algorithms		FPA	ESPRIT	RMUSIC	MUSIC	MVDR	PSO
$\theta_1 = 10$	Mean	10.798	6.754	−23.206	21.393	23.207	9.859
	Variance	63.4	137.7	753.8	98.5	97.0	1224.0
$\theta_2 = 20$	Mean	20.248	18.989	14.247	24.713	25.583	41.079
	Variance	16.3	18.9	58.3	102.3	94.3	1032.8
$\theta_3 = 30$	Mean	30.001	30.628	25.541	28.473	27.853	39.7725
	Variance	0.0204	21.7581	69.7347	93.6560	89.8585	550.2132
$\theta_4 = 40$	Mean	39.995	41.852	37.238	31.137	29.893	47.3674
	Variance	0.0274	29.1674	35.1613	75.3313	78.6620	391.5863

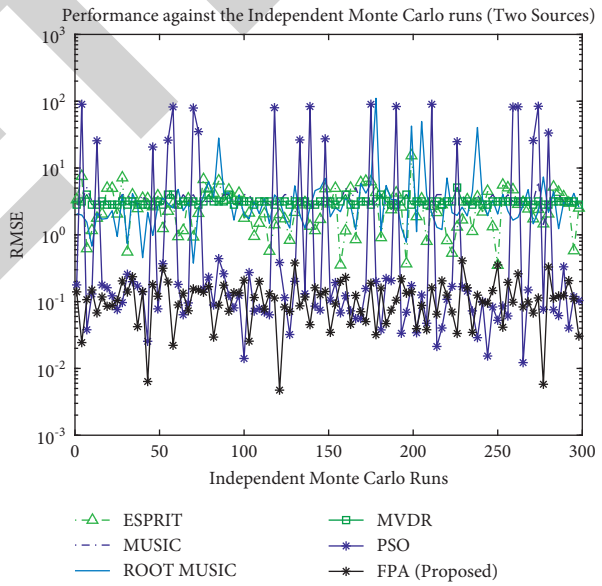

Figure 5: Performance against independent Monte Carlo runs for two sources with 5 dB of SNR.

having T iterations (trials). The set of D-dimensional vectors (total N vectors) for i iteration can be denoted as

$$\theta_1(i), \theta_2(i), \theta_3(i), \ldots, \theta_N(i). \quad (18)$$

Hence, the best solution at iteration i can be found as

$$\theta_{\text{best}}(i) = \text{argmin}_{n=1,\ldots,N} f(\theta_n(i)). \quad (19)$$

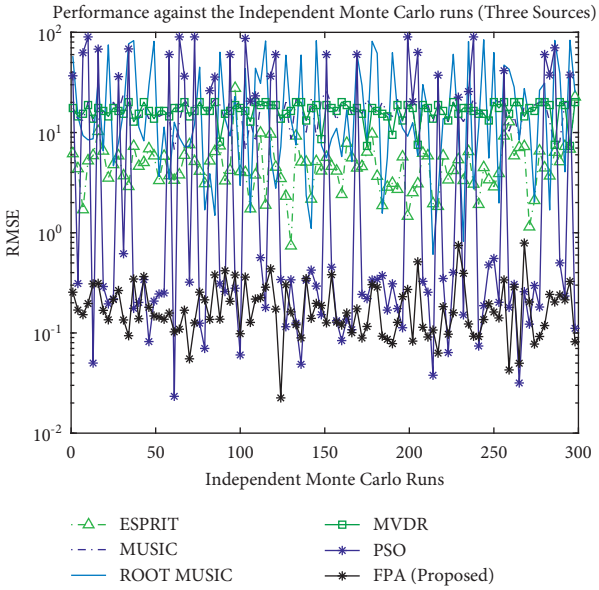

Figure 6: Performance against independent Monte Carlo runs for three sources with 5 dB of SNR.

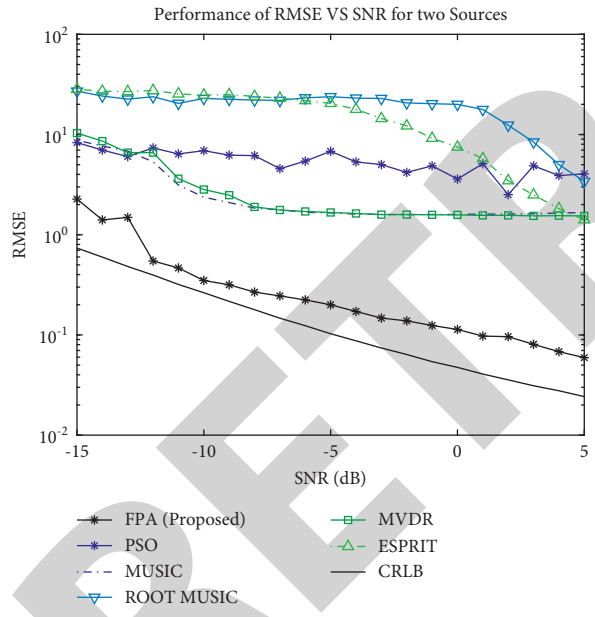

Figure 7: Performance of RMSE vs SNR for two sources.

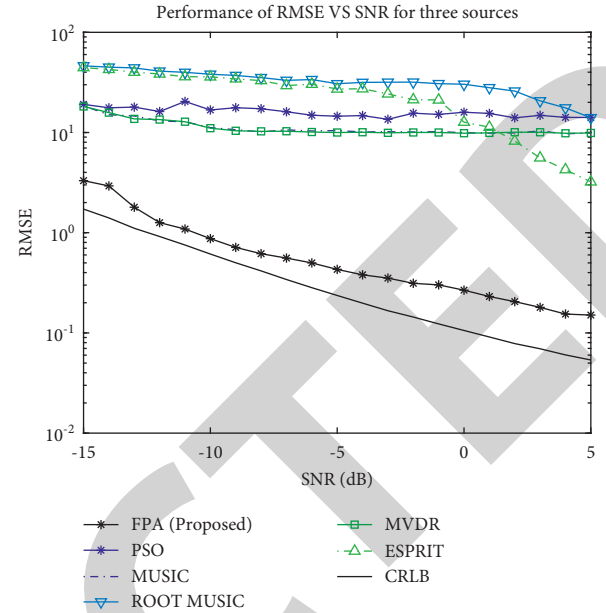

Figure 8: Performance of RMSE vs SNR for three sources.

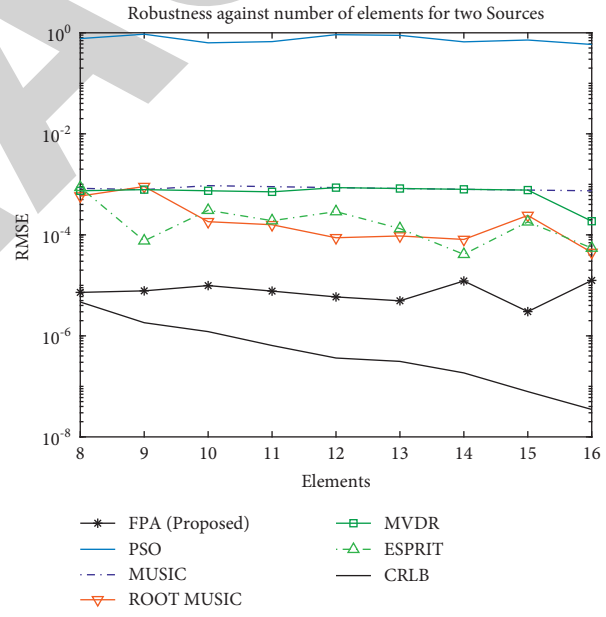

Figure 9: Robustness against the number of elements for two sources of 5 dB of SNR.

4. Experimental Results and Comparison

In this section, numerous simulations have been carried out to analyze the performance of the FPA against the state-of-the-art algorithms. The performance has been studied in terms of estimation accuracy, convergence analysis, robustness against noise, and the robustness against the number of hydrophones used in the array. The conditions for FPAs are also depicted in this section. The measures of performance illustrate the comprehensive analysis of FPAs as explained in the following areas.

4.1. Convergence Analysis. In this section, we examined the performance of FPA and PSO in terms of convergence. The performance is analyzed for two and three sources with the varying noise level. Figures 3 and 4 show that the FPA converged towards the minimum cost as compared to that of PSO.

4.2. Estimation Accuracy. The estimation accuracy of MVDR, MUSIC, Root MUSIC, ESPRIT, PSO, and FPA is examined here by taking signal sources with different positions and different noise levels. The noise is assumed to be

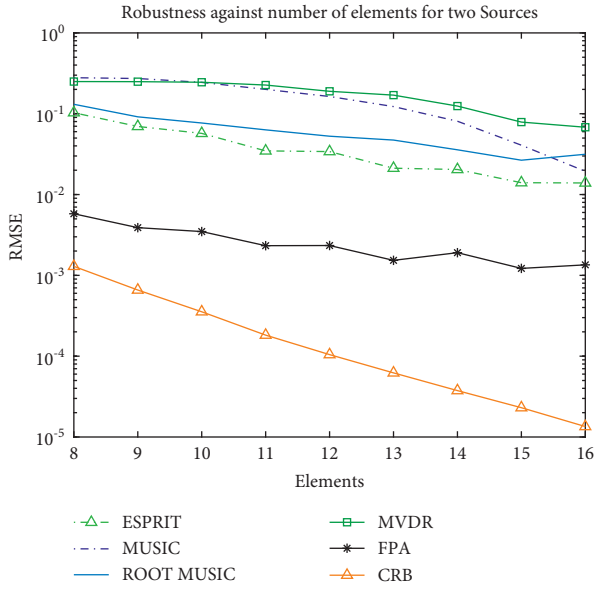

Figure 10: Robustness against the number of elements for two sources of 10 dB of SNR.

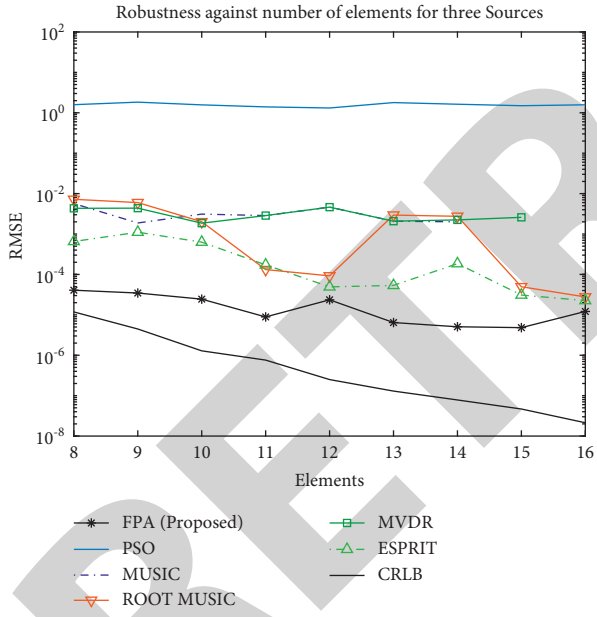

Figure 11: Robustness against the number of elements for three sources of 5 dB of SNR.

additive white Gaussian with zero means. The statistical measures of the mean and variance have been calculated from 300 independent Monte Carlo simulations as discussed in the tables for each algorithm. It can be seen from Tables 1–3 that the best performance is for FPAs in all different noise levels and in all two cases of Monte Carlo simulations (mean, variance).

4.3. Performance against the Independent Monte Carlo Runs. The performance metrics are analyzed by calculating RMSE that is defined as follows:

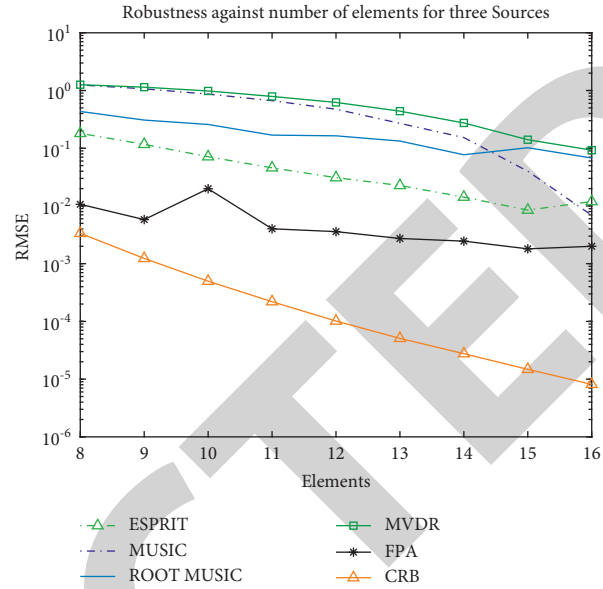

Figure 12: Robustness against the number of elements for three sources of 10 dB of SNR.

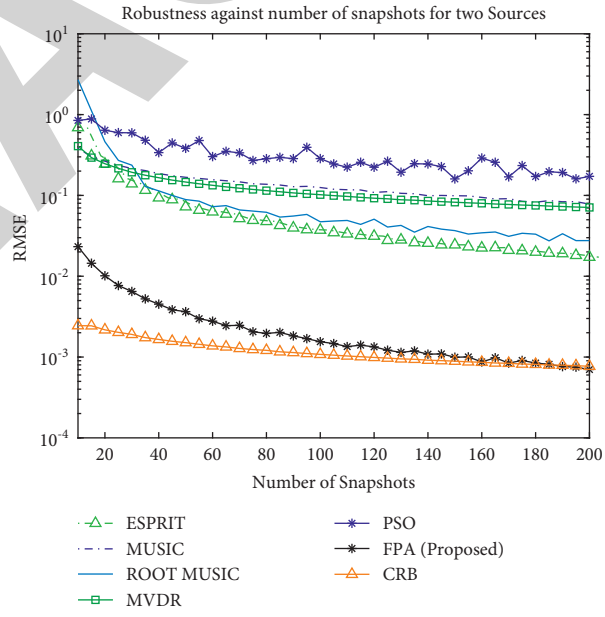

Figure 13: Robustness against snapshots for two sources.

$$\text{RMSE} = \sqrt{\sum_{K}\sum_{i=1}^{D}\frac{1}{\text{KD}}\left(\theta_{i(a)} - \theta_{i(e)}\right)^2}. \tag{20}$$

Here, $\theta_{i(a)}$ is the actual DOA and $\theta_{i(e)}$ is the estimated DOA.

In this section, the performance has been analyzed against the independent Monte Carlo runs. The simulation results show that the oscillations of the maximum and minimum of RMSE describe the best and worst performance of the algorithm. Hence, the reliability of the FPA outperforms that of the MVDR, MUSIC, RMUSIC, and ESPRIT and PSO algorithm for independent Monte Carlo runs as shown in Figures 5 and 6.

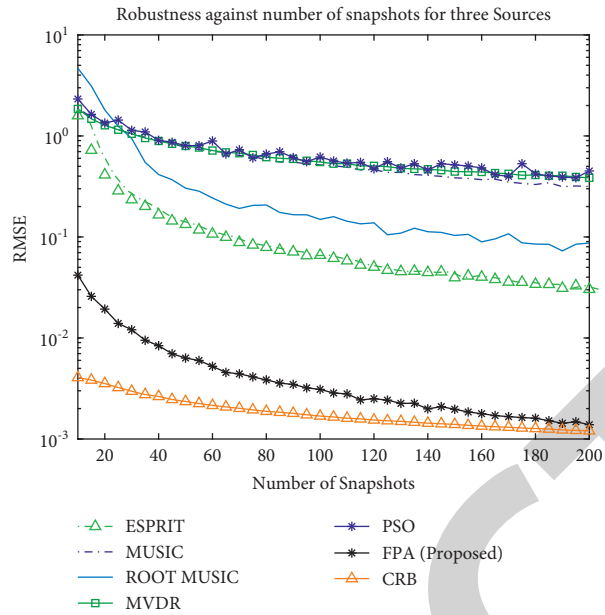

Figure 14: Robustness against snapshots for three sources.

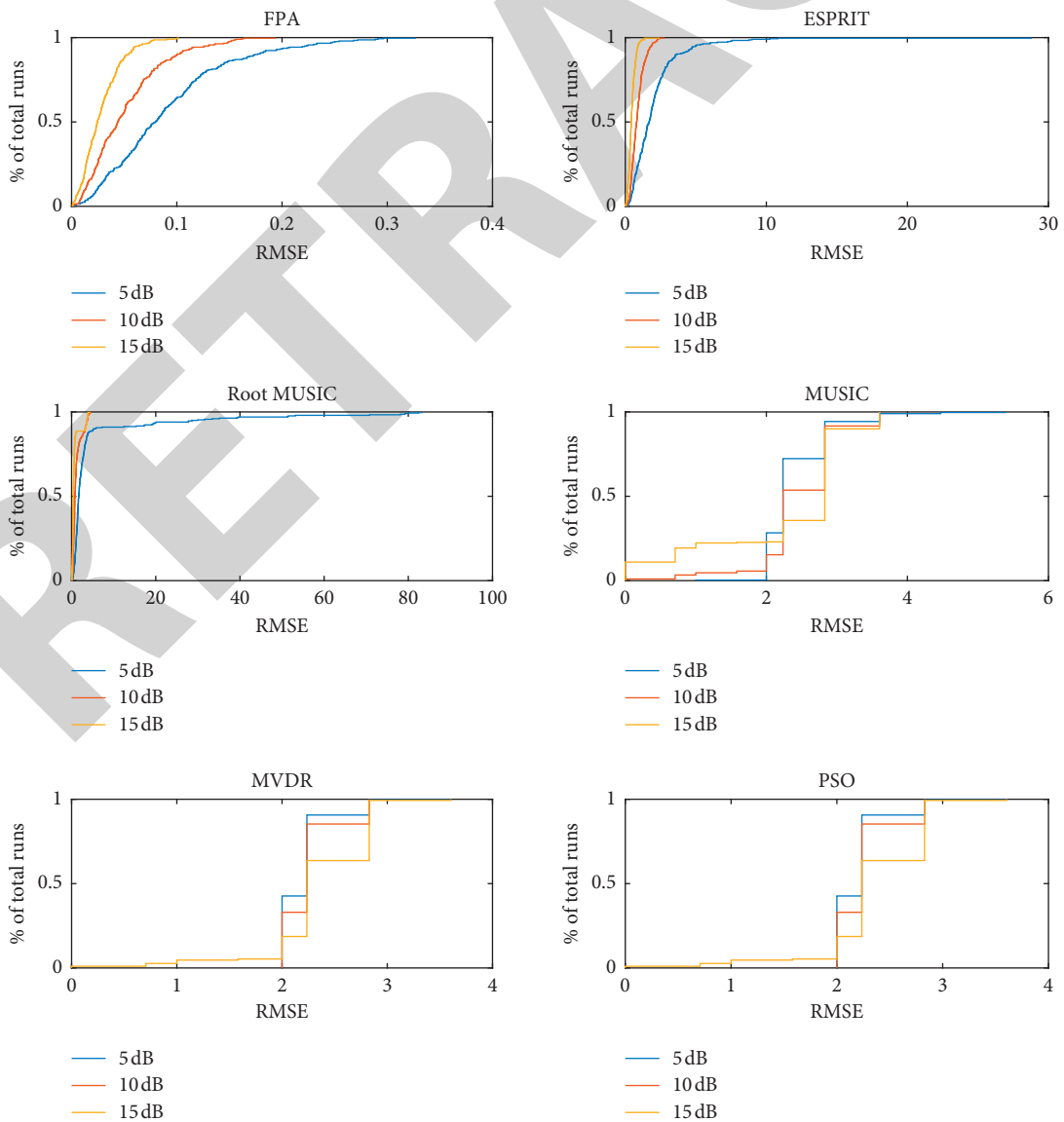

Figure 15: CDF of RMSE for two sources.

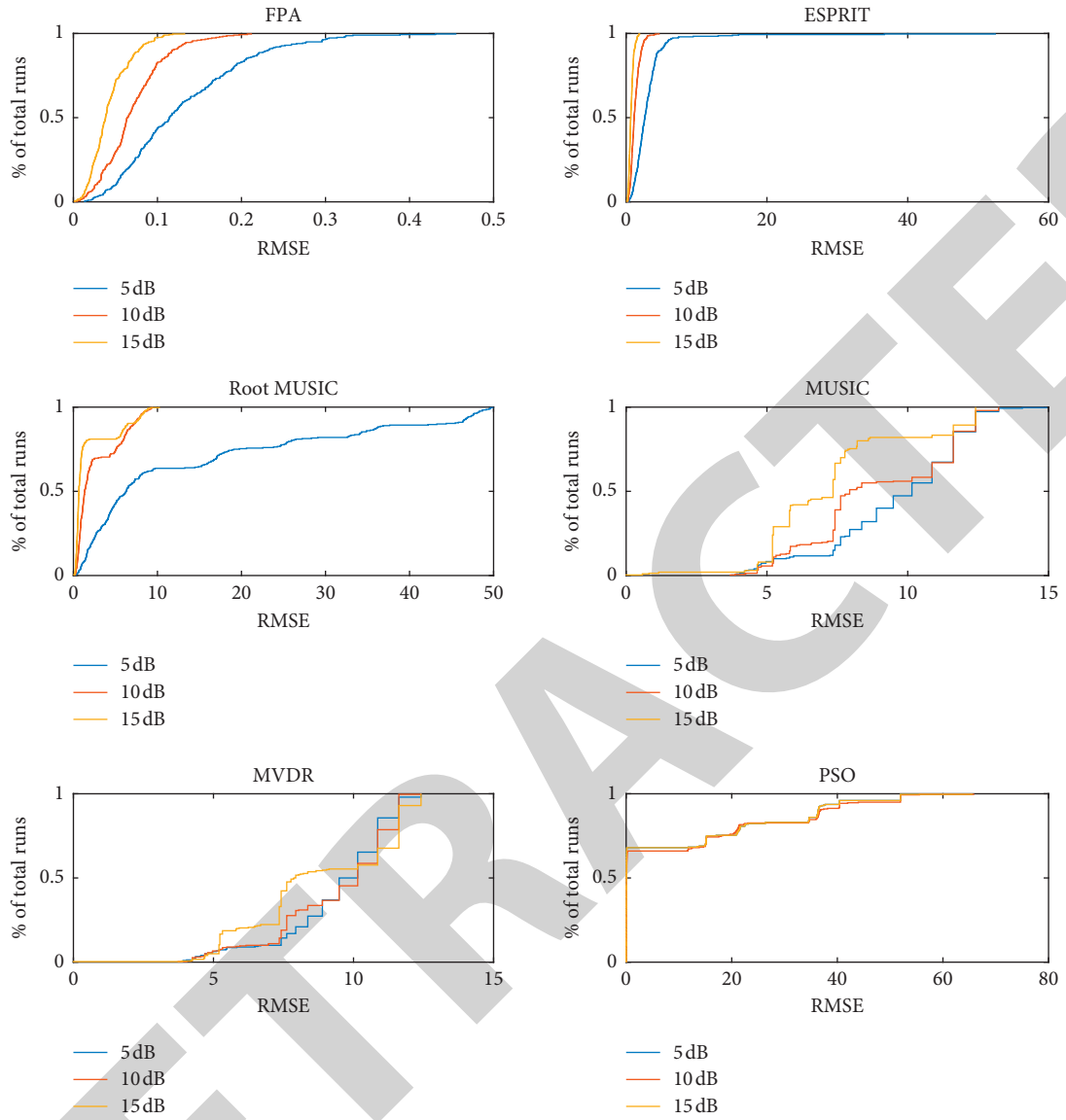

Figure 16: CDF of RMSE for three sources.

4.4. Robustness against Noise. In this section, the performance of these algorithms is measured by calculating the RMSE under varying levels of additive white noise. The convergence of RMSE also depicts performance analysis of such algorithms with the different number of signal sources having different DOAs.

We have used eight hydrophones, and the number of snapshots is 20 for two sources located at 30° and 35° and for three sources situated at 30°, 34°, and 50°. The result analysis in Figures 7 and 8 presents that the RMSE is a function of SNR. As the SNR increases, the RMSE decreases substantially. It can be seen that the FPA is robust enough to produce excellent results even in the presence of low SNR as compared to the other algorithms. CRB has also validated the performances of the algorithms.

4.5. Robustness against the Number of Hydrophones. The results in Figures 9–12 plotted the RMSE as a function of the number of hydrophones. As the number of hydrophones increases, the directivity also increases and hence RMSE decreases significantly. It can be seen that the FPA produces even for fewer hydrophones than the other algorithms in both cases of 5 and 10 dB of SNR.

4.6. Robustness against Snapshots. Another parameter to be considered is the impact of snapshots on RMSE. In this simulation, the SNR at 5 dB is fixed and the number of snapshots from 5 to 200 is varied with a step size of 5. Figures 13 and 14 show that as the number of snapshots increases, the RMSE decreases towards zero. The FPA outperforms the MVDR, MUSIC, RMUSIC, and ESPRIT algorithms. The worst performance of MUSIC and MVDR is due to low SNR, which results in a distorted spatial spectrum.

4.7. Analysis of Empirical Cumulative Distribution Function of RMSE. In this section, the observations of the RMSE are

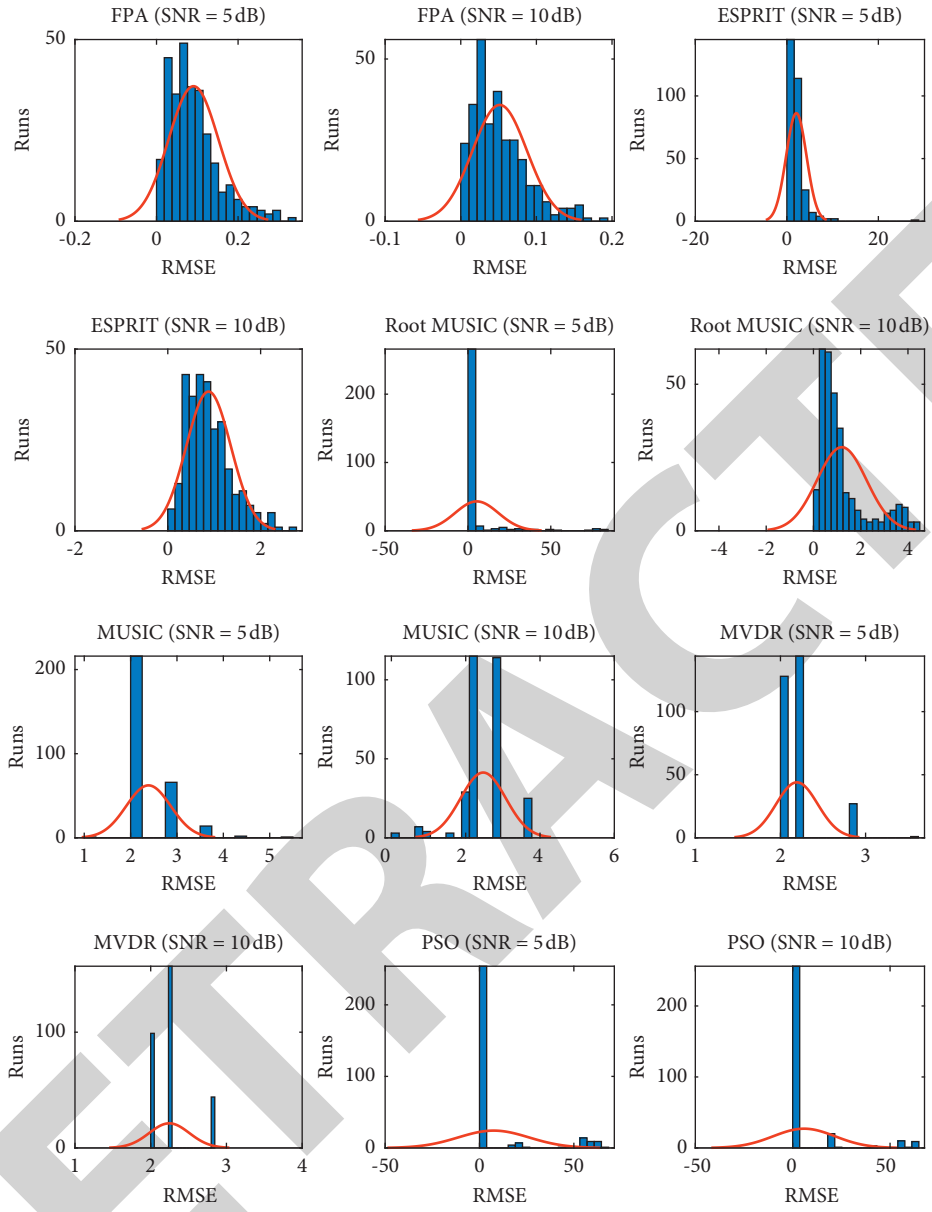

Figure 17: Histogram analysis of RMSE for two sources.

depicted in the order from least to greatest. This analysis corresponds to the survival and failure times of the algorithms over the Monte Carlo runs. It can be seen from Figures 15 and 16 that the FPA gives a significant amount of the Monte Carlo runs having the least RMSE. MVDR and MUSIC algorithms depict a colossal number of Monte Carlo trials with the most incredible value of RMSE that leads to the failure of the algorithm for DOA estimation. More specifically, the FPA and ESPRIT algorithms also give a remarkable amount of Monte Carlo trials the least RMSEs compared to PSO, MUSIC, Root MUSIC, and MVDR algorithms. Ultimately, the noteworthy performances are possessed by the FPA.

4.8. Frequency Distribution of RMSE. In this section, the histogram provides a visual interpretation of RMSE observations by showing the number of RMSE observations that fall within a specified range of RMSE values. This analysis also explains the skewness of the RMSE observations to validate the performance of the algorithms. It can be seen from Figures 17 and 18 that most of the occurrences underlie the least values of the RMSE for FPA. Furthermore, the ESPRIT algorithm gives a fair distribution of frequency of RMSE over the Monte Carlo runs compared to PSO, Root MUSIC, MUSIC, and MVDR algorithms.

4.9. Variability Analysis of the RMSE. In this section, the spread-out of the RMSE is analyzed in the five pieces of the information (minimum, first quartile, median, third quartile, and maximum) over the Monte Carlo trials. "Minimum" depicts the minimum value of the RMSE from Monte Carlo observations. In comparison, the first and

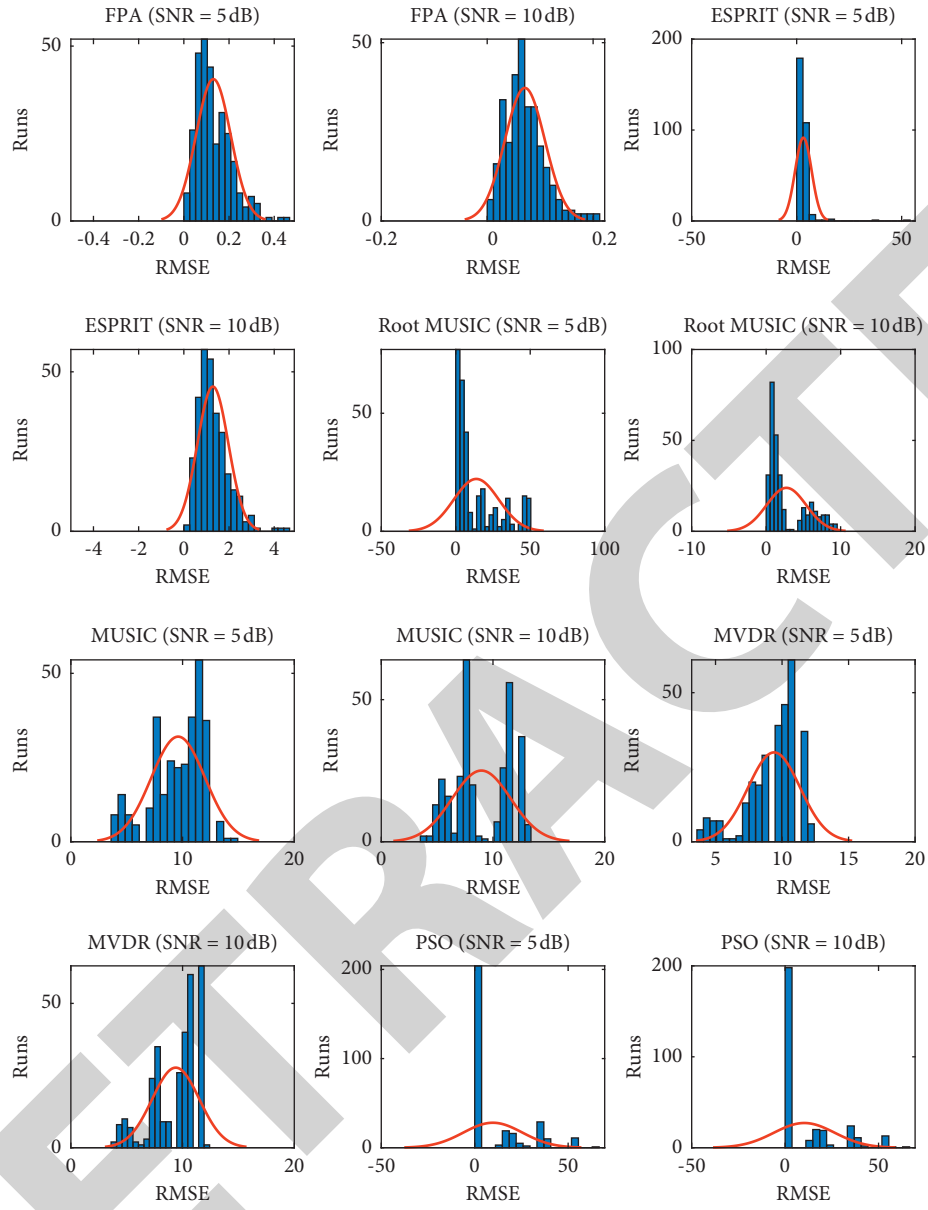

Figure 18: Histogram analysis of RMSE for three sources.

third quartiles describe 25 and 75 percent of the RMSE observations (Monte Carlo runs). This measure of the spread-out is a comprehensive description of the RMSE distribution to validate the performance of the algorithms. It can be seen from Figures 19 and 20 that FPA displays the distribution of RMSE with the least values of the RMSE, which reveals it is outperforming the other algorithms. Furthermore, the ESPRIT algorithm also gives significant performance compared to the PSO, Root MUSIC, MUSIC, and MVDR algorithms.

4.10. The Resolution Ability for Closely Spaced Targets. In this section, the simulation background is estimated for the proposed structure to check the superresolution performance. The probability of resolution is defined as

$$P_r = \text{Prob}\left[\left|\theta_e - \theta_a\right| \leq \frac{\triangle\theta}{2}\right], \tag{21}$$

where $\triangle\theta = |\theta_1 - \theta_2|$. The resolution ability of both closely spaced sources is shown in Figures 21–24. The performance is analyzed based on different DOA positions. It can be seen that the FPA outperforms the others but the PSO performs significantly too for closely spaced sources. Simulation is carried out by fixing the first source and moving the second source from 35 to 34 degrees. The resolution ability is analyzed for each separation for both sources independently.

4.11. Computational Complexity Analysis. In this, the computation loading performance is analyzed using MUSIC, MVDR, and RMUSIC algorithms, which are highly

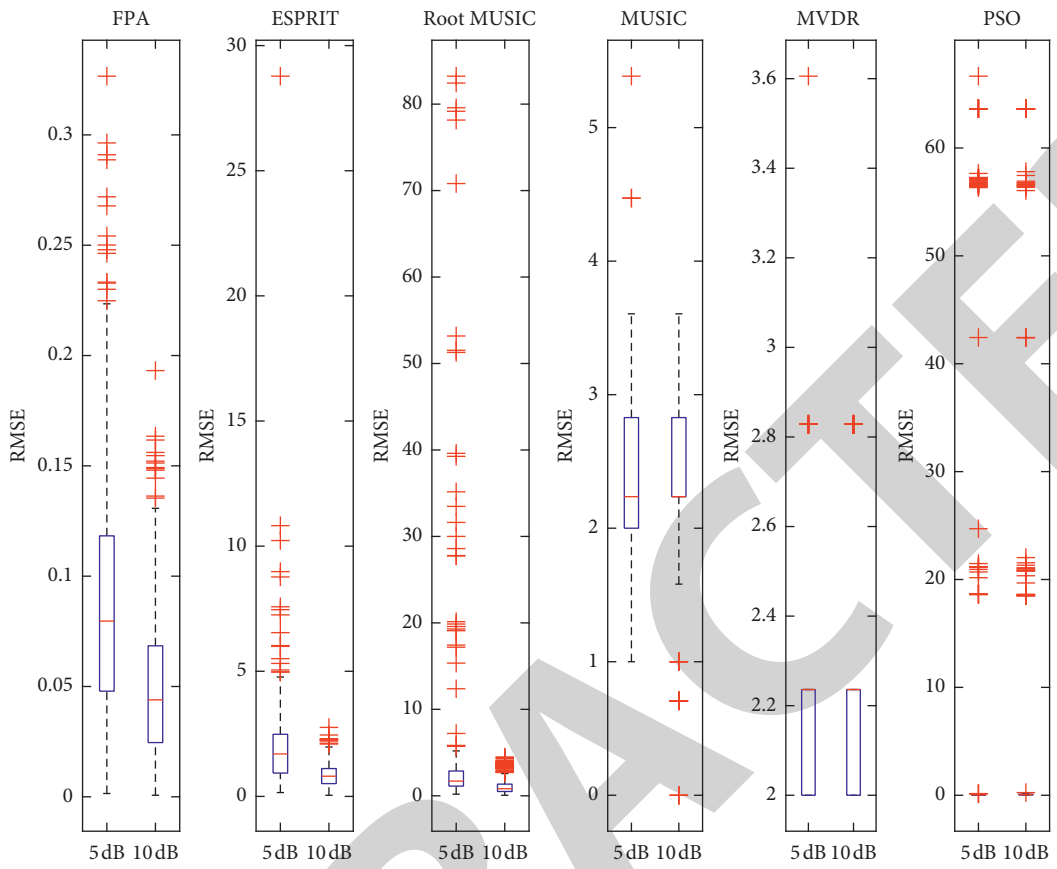

Figure 19: Variability analysis for two sources.

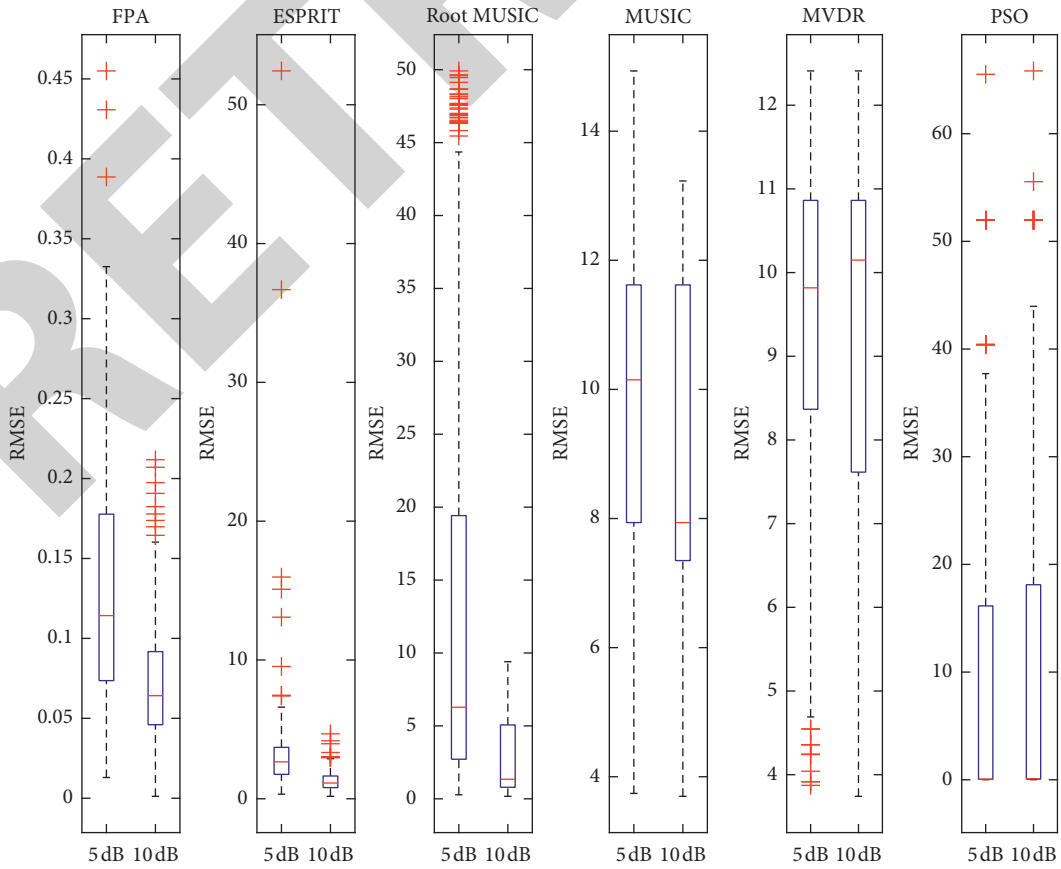

Figure 20: Variability analysis for three sources.

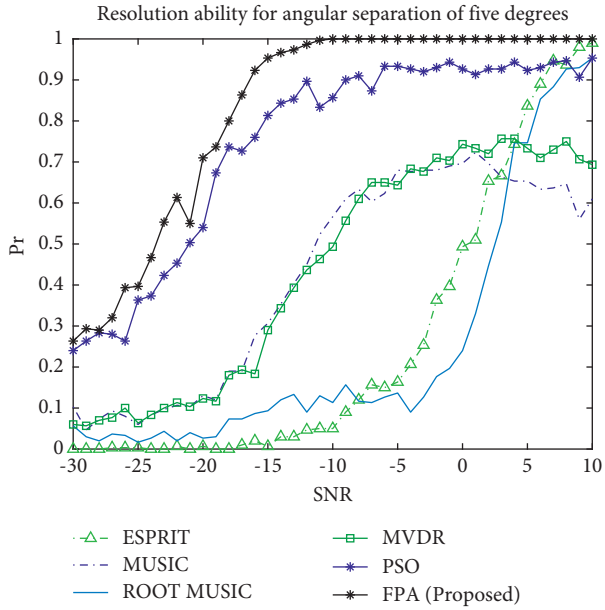

Figure 21: Probability of resolution for the source at 30 degrees.

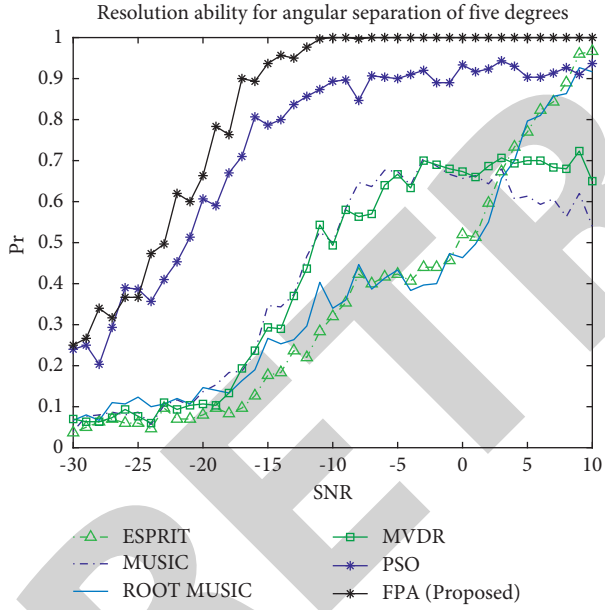

Figure 22: Probability of resolution for the source at 35 degrees.

computational practical algorithms due to their spectral search approach to estimate the DOA. Moreover, the ESPRIT algorithm neither includes the extrema search optimization nor the spectral search approach; hence, it results in better computational complexity than the other algorithms as mentioned in Table 4. The FPA also outperforms the MUSIC, MVDR, and RMUSIC algorithm but is not better than the ESPRIT algorithm due to its extrema searching approach to optimize the cost function. The extrema searching approach of FPA and PSO to optimize the cost function increases the computational complexity that sometimes restrain the application of swarming intelligent algorithms.

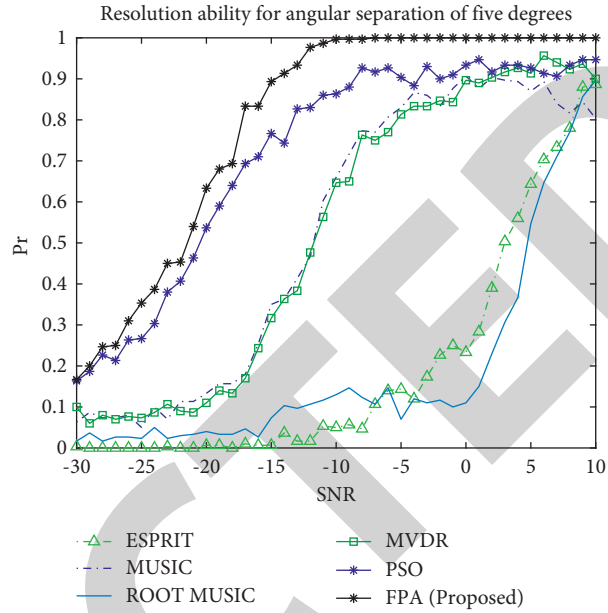

Figure 23: Probability of resolution for the source at 30 degrees.

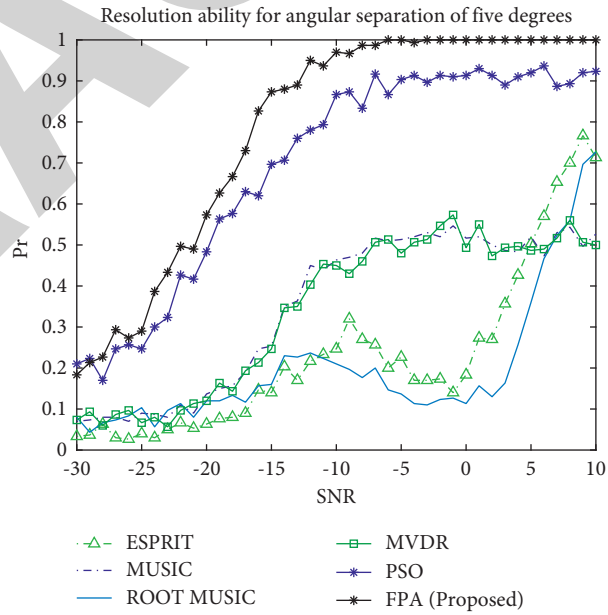

Figure 24: Probability of resolution for the source at 34 degrees.

Table 4: Computational loading analysis.

Algorithm	Complexity
MVDR	$W^2(K+6)+W+4*D*P$
MUSIC	$5/3W^3+W^2(K+1+D+W)+4*D*P$
RMUSIC	$11/3W^3+W^2(K+D-1)+2(W-1)$
ESPRIT	$W^2(K+2*W+1)+D(D+1)$
PSO	$K*T*N*W*D$
FPA	$D*T*K*N*W(1-p_s)$

5. Conclusion

The simulation results demonstrate that the FPA outperforms the conventional beamforming and conventional

subspace-based algorithms in most situations. The performance improvement is more significant when multiple signals are incident at closely spaced angles at a low signal-to-noise ratio and when a small number of snapshots are used to estimate direction of arrival (DOA). Statistical analysis of the RMSE in Monte Carlo trials, that is, ECDF of RMSE, variability analysis of RMSE, frequency distribution of RMSE, and the probability of resolution, witnesses the strength of FPA in the challenging environment of low SNR using less number of snapshots. In the future, the estimation of 2D-DOA of underwater multitargets using 2D arrays should be investigated with modern heuristic algorithms to achieve high accuracy and resolution. Moreover, the proposed flower pollination heuristics look promising to deal with the optimization problems in diversified fields.

Data Availability

No data were used to support this study.

Conflicts of Interest

The authors declare no conflicts of interest.

Acknowledgments

This work was supported in part by the Beijing Natural Science Foundation (No. 4212015), Natural Science Foundation of China (No. 61801008), China Ministry of Education-China Mobile Scientific Research Foundation (No. MCM20200102), China Postdoctoral Science Foundation (No. 2020M670074), Beijing Municipal Commission of Education Foundation (No. KM201910005025), and China National Key Research and Development Program (No. 2018YFB0803600).The authors express their gratitude to Princess Nourah bint Abdulrahman University Researchers Supporting Project (Grant no. PNURSP2022R60), Princess Nourah bint Abdulrahman University, Riyadh, Saudi Arabia.

References

[1] K. Hameed, S. Tu, N. Ahmed et al., "DOA estimation in low SNR environment through coprime antenna arrays: an innovative approach by applying flower pollination algorithm," *Applied Sciences*, vol. 11, 2021.

[2] H. Jing, H. Wang, Z. Liu, and X. Shen, "DOA estimation for underwater target by active detection on virtual time reversal using a uniform linear array," *Sensors*, vol. 18, 2018.

[3] N. Ahmed, H. Wang, M. A. Z. Raja et al., "Performance analysis of efficient computing techniques for direction of arrival estimation of underwater multi targets," *IEEE Access*, vol. 9, 2021.

[4] A. Mushtaq and G. Mahendru, "A proposed DOA estimation technique based on wavelet packet decomposition for fading channel in MIMO systems," in *Proceedings of the 6th International Conference on Signal Processing and Integrated Networks (SPIN)*, pp. 278–281, Noida, India, March 2019.

[5] Y.-F. Liang, P.-F. Jiang, J.-N. Xu, W. An, and M. Wu, "Initial alignment of compass based on genetic algorithm-particle swarm optimization," *Defence Technology*, vol. 16, no. 1, pp. 257–262, 2020.

[6] P. Wang, Y. Kong, X. He, M. Zhang, and X. Tan, "An improved squirrel search algorithm for maximum likelihood DOA estimation and application for MEMS vector hydrophone array," *IEEE Access*, vol. 7, Article ID 118343A, 2019.

[7] Y. Chen, F. Wang, J. Wan, and K. Xu, "DOA estimation for long-distance underwater acoustic sources based on signal self-nulling," in *Proceedings of the IEEE 2nd Advanced Information Technology, Electronic and Automation Control Conference (IAEAC)*, pp. 563–567, Chongqing, China, March 2017.

[8] Y. Sato, N. Kikuma, and K. Sakakibara, "Improvement of estimation accuracy by using multiple guiding sensors in DOA estimation of radio waves with VESPA algorithm," in *Proceedings of the International Symposium on Antennas and Propagation (ISAP)*, pp. 1-2, Busan, Korea (South), October 2018.

[9] X. Zhao, Y. Yang, and K.-S. Chen, "Direction-of-Arrival estimation over sea surface from radar scattering based on convolutional neural network," *Remote Sensing*, vol. 13, no. 14, 2021.

[10] Z. Zheng, W. Q. Wang, H. P. Meng, H. C. So, and H. B. Zhang, "Efficient beamspace-based algorithm for two-dimensional DOA estimation of incoherently distributed sources in massive MIMO systems," *IEEE Transactions on Vehicular Technology*, vol. 67, no. 12, Article ID 11776, 2018.

[11] A. Dixit, J. Sathyamurthy, S. Rao, S. Gurugopinath, and G. Thiagarajan, "Detection and localization of targets using millimeter wave radars: an experimental study," in *Proceedings of the IEEE International Conference on Electronics, Computing and Communication Technologies (CONECCT)*, pp. 1–6, Bangalore, India, July, 2021.

[12] V. V. Chudnikov, B. I. Shakhtarin, A. V. Bychkov, and S. M. Kazaryan, "Doa estimation in radar sensors with colocated antennas," in *Proceedings of the Systems of Signal Synchronization Generating and Processing in Telecommunications (SYNCHROINFO)*, Svetlogorsk, Russia, July 2020.

[13] X. Chen, Y. Li, Y. Li, and J. Yu, "PHD and CPHD algorithms based on a novel detection probability applied in an active sonar tracking system," *Applied Sciences*, vol. 8, no. 1, 2017.

[14] Y. Li, X. Gao, and L. Wang, "Reverse dispersion entropy: a new complexity measure for sensor signal," *Sensors*, vol. 19, no. 23, 2019.

[15] Y. Li, B. Geng, and S. Jiao, "Refined composite multi-scale reverse weighted permutation entropy and its applications in ship-radiated noise," *Entropy*, vol. 23, no. 4, 2021.

[16] S. Jeong, Y. Won, and D. Shin, "Fast doa estimation method based on music algorithm combined Newton method for fmcw radar," in *Proceedings of the IEEE MTT-S International Conference on Microwaves for Intelligent Mobility (ICMIM)*, pp. 1–5, Detroit, MI, USA, April 2019.

[17] S. Cho, H. Song, K.-J. You, and H.-C. Shin, "A new direction of arrival estimation method using automotive radar sensor arrays," *International Journal of Distributed Sensor Networks*, vol. 13, no. 6, Article ID 155014771771362, 2017.

[18] E. Schubert, F. Meinl, M. Kunert, and W. Menzel, "High resolution automotive radar measurements of vulnerable road users - pedestrians cyclists," in *Proceedings of the IEEE MTT-S International Conference on Microwaves for Intelligent Mobility (ICMIM)*, pp. 1–4, Heidelberg, Germany, April 2015.

[19] S.-H. Jeong, Y.-S. Won, and D. Shin, "Fast DOA estimation method based on MUSIC algorithm combined Newton method for FMCW radar," in *Proceedings of the IEEE MTT-S*

Hindawi
Shock and Vibration
Volume 2024, Article ID 9891849, 1 page
https://doi.org/10.1155/2024/9891849

Retraction

Retracted: Precision Analysis of Noncircular Gears Based on CNC Machining Technology under Cloud Computing Platform

Shock and Vibration

Received 23 January 2024; Accepted 23 January 2024; Published 24 January 2024

This article has been retracted by Hindawi following an investigation undertaken by the publisher [1]. This investigation has uncovered evidence of one or more of the following indicators of systematic manipulation of the publication process:

(1) Discrepancies in scope

(2) Discrepancies in the description of the research reported

(3) Discrepancies between the availability of data and the research described

(4) Inappropriate citations

(5) Incoherent, meaningless and/or irrelevant content included in the article

(6) Manipulated or compromised peer review

The presence of these indicators undermines our confidence in the integrity of the article's content and we cannot, therefore, vouch for its reliability. Please note that this notice is intended solely to alert readers that the content of this article is unreliable. We have not investigated whether authors were aware of or involved in the systematic manipulation of the publication process.

Wiley and Hindawi regrets that the usual quality checks did not identify these issues before publication and have since put additional measures in place to safeguard research integrity.

We wish to credit our own Research Integrity and Research Publishing teams and anonymous and named external researchers and research integrity experts for contributing to this investigation.

The corresponding author, as the representative of all authors, has been given the opportunity to register their agreement or disagreement to this retraction. We have kept a record of any response received.

References

[1] J. Dai, W. Xu, and F. OuYang, "Precision Analysis of Noncircular Gears Based on CNC Machining Technology under Cloud Computing Platform," *Shock and Vibration*, vol. 2022, Article ID 1359084, 12 pages, 2022.

Hindawi
Shock and Vibration
Volume 2022, Article ID 1359084, 12 pages
https://doi.org/10.1155/2022/1359084

Research Article

Precision Analysis of Noncircular Gears Based on CNC Machining Technology under Cloud Computing Platform

JianQing Dai,[1] **Wei Xu**,[2] **and FenFen OuYang**[1]

[1]*College of Mechanical and Electrical Engineering, Pingxiang University, 211 Pinganbei Ave., Pingxiang 337055, China*
[2]*Department of Engineering, Jiangxi Hongzhou Vocational College, Longjin Lake Headquarters Economic Base, Fengcheng 331100, China*

Correspondence should be addressed to JianQing Dai; 21010042@pxu.edu.cn

Received 24 May 2022; Accepted 16 June 2022; Published 28 June 2022

Academic Editor: Yuxing Li

In order to solve the problem of machining error of noncircular gears, a method based on the analysis and research of the accuracy of noncircular gears based on CNC machining technology under the cloud computing platform is proposed to further improve the technical accuracy of noncircular gears. The error and error items are analyzed mainly, and a model framework based on cloud computing platform is proposed on this basis. The architecture of the system is deeply analyzed, focusing on the dynamic integration method of gear cloud measurement system resources based on cloud platform, building a gear cloud measurement system based on cloud computing platform, and testing needs to use Hadoop to install the software that needs to be prepared: virtual machine version, VMware Workstation-14.0.0 build-6661328, Linux version. The results show that the technical support of the cloud computing platform can effectively improve the accuracy of noncircular gears.

1. Introduction

The development of industrialization and the emergence of digital industrialization are inseparable from the progress of technology. Especially for the construction and manufacturing industry, the emergence of technologies such as intelligent manufacturing and intelligent processing provides technical support for industry transformation and technological progress. Noncircular gears have been widely used in modern aviation, instrumentation, machinery, and other related fields. Throughout the development history of gear measurement technology, with the advancement of technology, from the measurement principle, measurement technical means, to the measurement results, it shows the progress and leap of technology. The noncircular gear mainly transfers the motion and power between any two shafts in the space by converting the transmission ratio. On this basis, it also has the advantages of the cam mechanism and the cylindrical gear structure, which can be better through technical optimization. It is precisely based on this advantage that noncircular gears have been widely used in many mechanical-related fields. However, from the perspective of noncircular gear processing, there are still transmission errors, rotary axis position errors, tool errors, and other errors. These errors can be summarized as systematic errors and random errors. Therefore, how to reduce the machining error of noncircular gears and improve the operation accuracy with the help of technological progress and optimization is the focus of this paper. Therefore, based on the cloud computing platform, this paper deeply analyzes the machining error of noncircular gears and proposes a gear cloud measurement technology model and data processing dynamic integration method based on the cloud computing platform.

2. Literature Review

Gear measurement is based on the theory of precision. Fan and Ye said that gear accuracy theory covers gear error dynamics theory, gear error kinematics theory, and gear error geometry theory [1]. Wei et al. said that Chinese and foreign scholars and scientific researchers have developed

nearly a hundred kinds of gear measuring instruments based on the above three theories: in the early days, the German universal involute inspection instrument and the universal helical inspection instrument, the British grating type single represented by the gear overall error measurement technology proposed by NieYi and China Chengdu Tool Research Institute, the high-precision measurement of gears, and the overall control of gear quality are realized [2]. Li and others said that in the development process of the gear measurement principle, it was first "comparative measurement," then "measuring motion measurement," and then "modeled measurement" [3]. Zheng et al. said that for the realization of the measurement principle, the early stage was "mechanical-based," followed by "electromechanical integration," and finally developed into the comprehensive integration of "optical-mechanical-electrical" and "information technology" [4]. Li et al. said that the acquisition of measurement results: from "reading from the indicator table with the naked eye" to "the recorder records the processing reading" until "the computer automatically analyzes and feeds the results back to the manufacturing system" [5]. Li et al. said that the cloud manufacturing model is an innovative application of cloud computing in the manufacturing field, and it is also the development of the network manufacturing model [6]. Fan and others said that in 2010, some scholars proposed cloud manufacturing based on the concept of cloud computing [1]. Chinese foreign research institutes and universities have systematically studied a series of issues such as the intervention and adaptation of cloud manufacturing service platforms, the perception of manufacturing equipment, the virtualization of manufacturing resources, and the establishment of cloud manufacturing systems. Research on cloud manufacturing platform for gear industry, it provides new ideas for cloud manufacturing research from the aspects of manufacturing mode, manufacturing strategy, and mode architecture. Compared with traditional measurement methods, network-based gear measurement has great advantages, but there are still some shortcomings in the current measurement methods; especially, it is difficult to achieve precise measurement, evaluation, measurement services and collaboration for machining process analysis, in-service dynamic characteristics, etc. Soyoye said that in China, the research on the measurement of noncircular gears has used the double-sided meshing method, the single-sided whistle method, and the polar coordinate method for measurement [7]. Hao et al. said that the biggest difference between the gear single-sided whistle method and the double-sided meshing method is whether the tested gear has backlash during the whistle-coupling transmission process [8]. Among them, the measurement method of gear single-sided congruence is to use two gears that are in contact with each other, one is the measured noncircular gear, and the other is an ideal and accurate standard cylindrical gear. Under the nominal center distance, only one-sided, side the meshing transmission of the gap reflects the tangential comprehensive error of the measured noncircular gear by measuring the angle error of the measured noncircular gear. Han et al. said that the noncircular gear double-sided whistle-fit measurement method is to use the above two gears, under the nominal center distance, to perform meshing transmission with both surfaces in contact and without backlash, by measuring the actual center distance of the measured gear. Corresponding changes are generated according to the change of the pole diameter of the pitch curve of the noncircular gear, reflecting the radial comprehensive error of the measured noncircular gear. The polar coordinate measurement method is a method of measuring the polar coordinates established by the polar diameter and polar angle [9]. The precision analysis and research of noncircular gears based on CNC machining technology under the cloud computing platform is shown in Figure 1.

3. Methods

According to the form of error, the machining error of noncircular gear is mainly divided into systematic error and random error, and its specific classification is shown in Figure 2.

According to the noncircular gear machining process, the nature of the coupling between the tool and the gear and the variation law are classified, as shown in Figure 3.

The process of gear hobbing processing spur noncircular gears can be regarded as the whistling of the rack and the processed noncircular gears. During the whistling process, the two pitch curves are pure rolling without sliding, and the tooth profile of the noncircular gear is the relative motion of the two is enveloped by the tooth profile of the rack, and the principle of hobbing is shown in Figure 4.

In the process of cutting with a gear hob, the movement of the hobbing is as follows: the gear hob rotates to form the cutting speed, and the tool translates along the axial direction to form the translation of the tool rack; while the teeth are still rotating, its center moves up and down in the direction perpendicular to the pitch line of the rack, changing the center distance. The whole machining process can be abstracted into the machining process of the tool rack. The schematic diagram is shown in Figure 5.

In the above figure, the pitch line of the rack is x, and it moves horizontally to the left during processing. In order to ensure the tangent pure rolling of the pitch curves of the rack and the noncircular gear, the center of the gear is 0_1 up and down while the gear is rotating. The machine tool coordinate system is P_{xy}, and the polar coordinate equation of the noncircular gear pitch curve is shown in

$$r = r(\phi). \tag{1}$$

When set at the starting position, the pitch curve of the noncircular gear and the rack is tangent at point a, and the coordinate of point a is (r_0, ϕ_0), and μ_0 is the angle between the tangent line at point a and the radius vector of the noncircular gear pitch curve $\overline{0_1 a}$. As shown in formula (2),

$$\mu_0 = \arctan \frac{r_0}{\left(\mathrm{d}r_1/\mathrm{d}\phi_1\right)_{r_0}}, \tag{2}$$

where $\mathrm{d}r/\mathrm{d}\phi$ is the value of the derivative of the r pair at r_0.

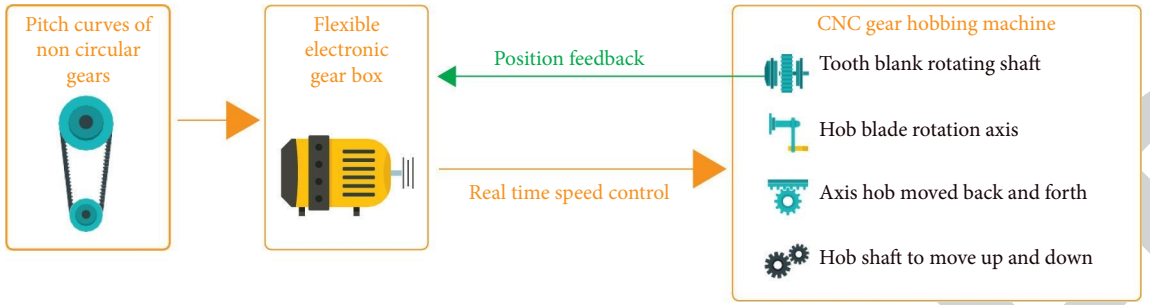

Figure 1: Analysis and research on the accuracy of noncircular gears.

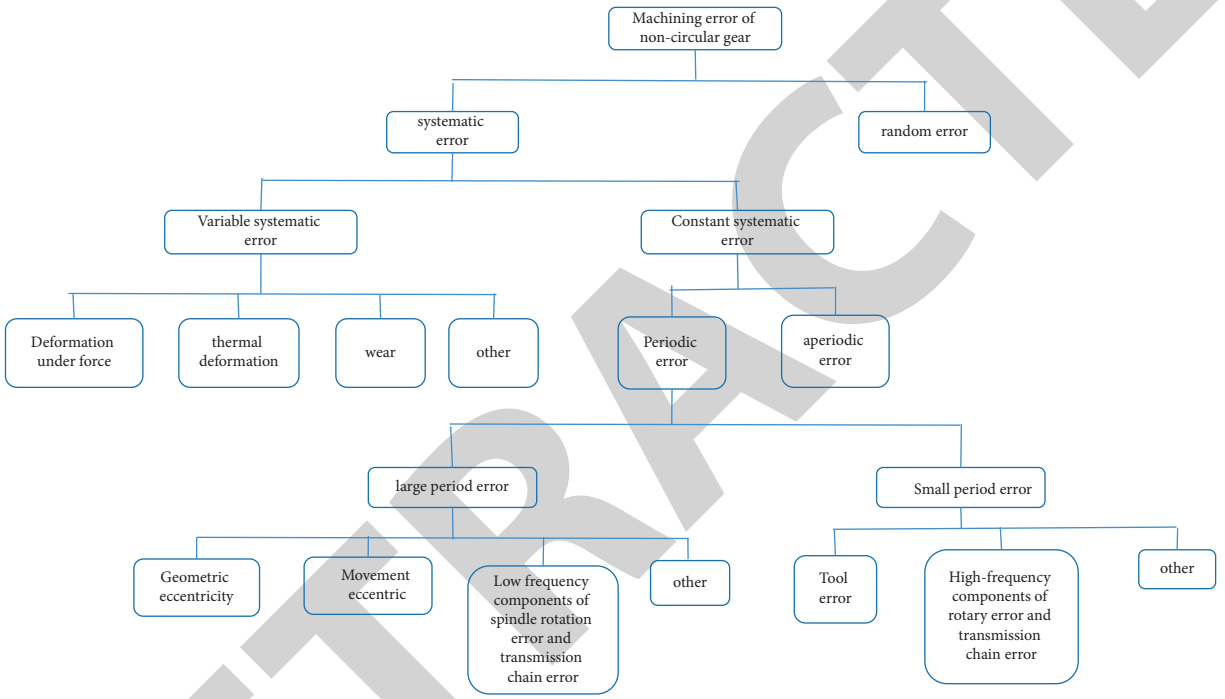

Figure 2: Classification diagram according to the manifestation of noncircular gear machining error.

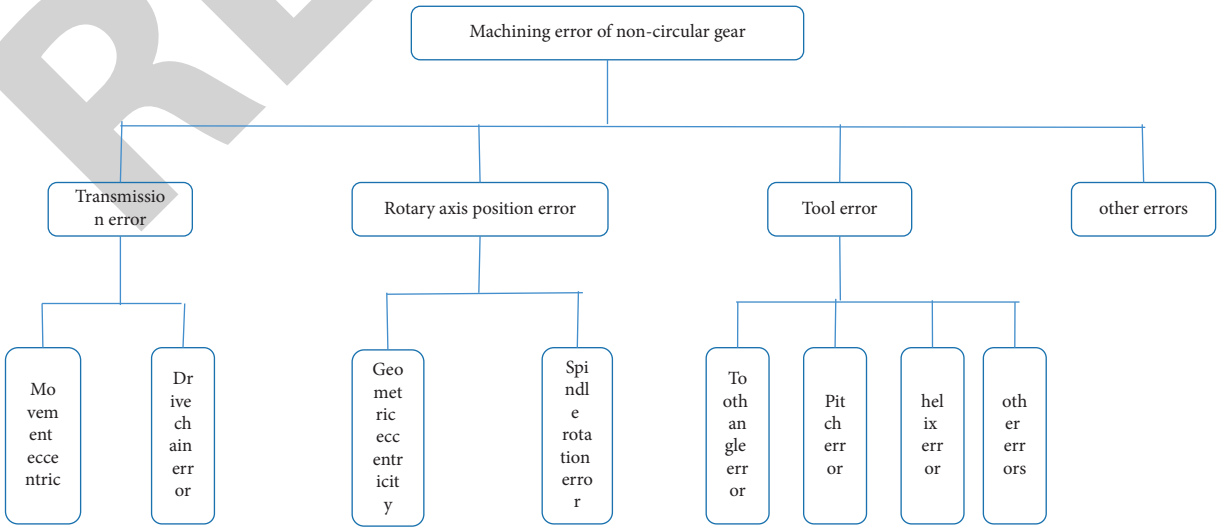

Figure 3: Classification according to the nature of the compound.

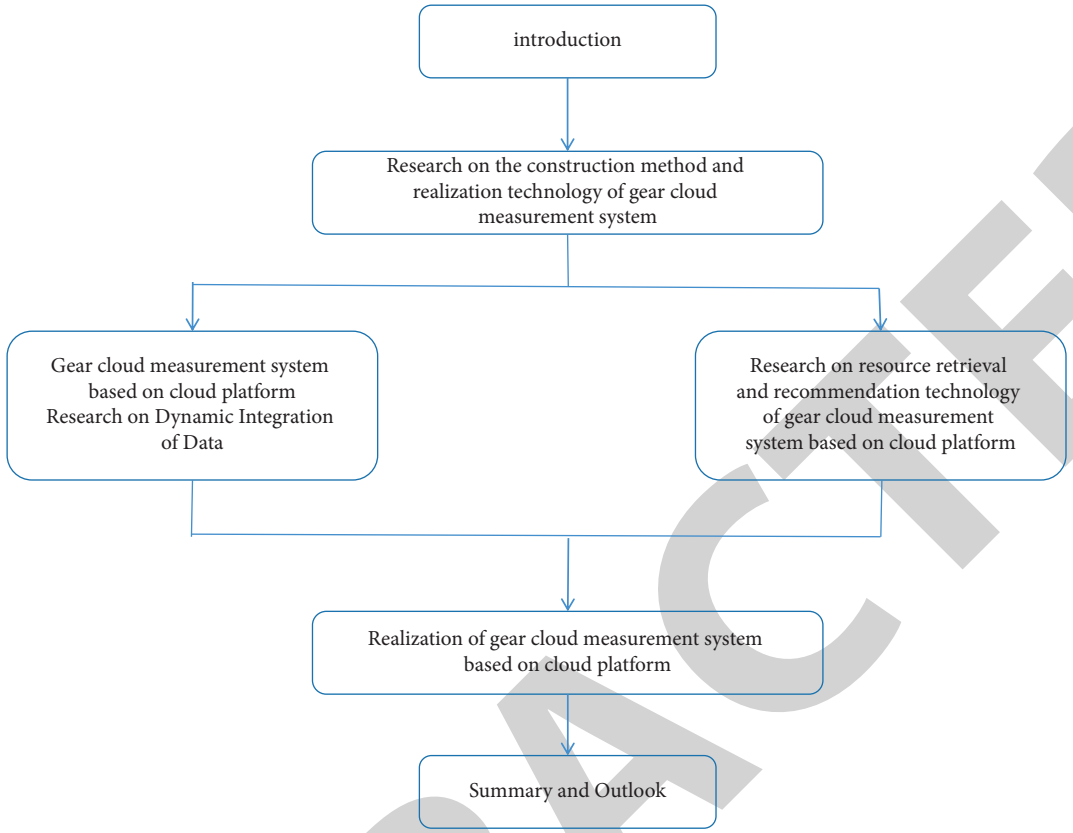

Figure 4: Schematic diagram of gear hobbing.

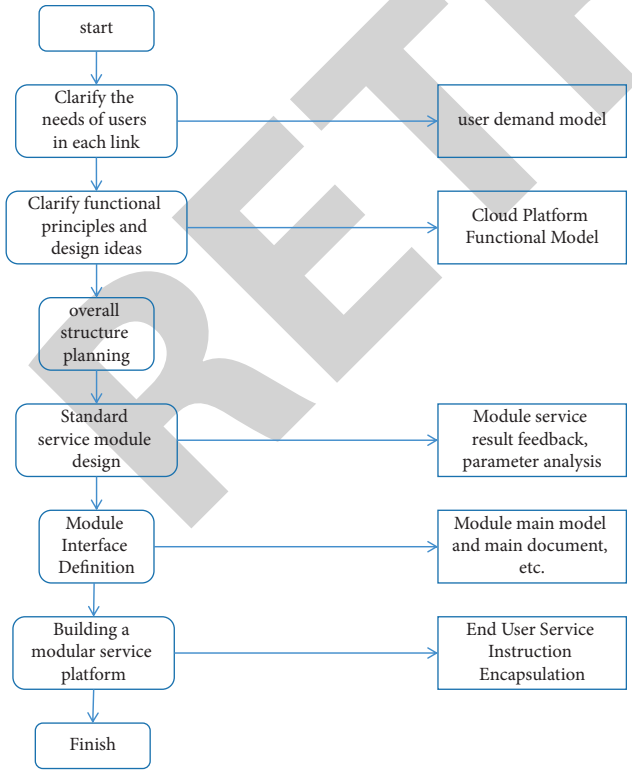

Figure 5: Schematic diagram of noncircular gear machining.

At the starting position, the tangent of point a completely coincides with the x-axis, so the distance from point a to axis y_1 is shown in

$$r_0 \cos \mu_0. \tag{3}$$

At any position, suppose the noncircular gear rotates through the angle θ_1, and the tangent point of the two curves is b, then the angle between the tangent at point b and the radial vector is shown in

$$\mu_1 = \arctan \frac{r_i}{(dr/d\phi)_{r_i}}, \tag{4}$$

$$bP = r_i \cos \mu_1. \tag{5}$$

The instantaneous center distance is shown in

$$a_i = r_i \sin \mu_i. \tag{6}$$

The arc length between a and b is shown in

$$l_i = \int_{\phi_0}^{\phi_1} \sqrt{r^2 + \left(\frac{\mathrm{d}r}{\mathrm{d}\phi}\right)^2} d\phi. \tag{7}$$

As can be seen from the figure, the rotated θ_1 angle is shown in

$$\theta_i = \phi_i + \mu_i - (\phi_0 + \mu_0). \tag{8}$$

The horizontal distance that the rack moves to the left from the starting position is shown in

$$x_i = l_i + r_0 \cos \mu_0 - r_i \cos \mu_i. \tag{9}$$

Combining formulas (8) and (9), it can be seen that the machining model of the hob machining noncircular gear is completely determined by the pitch curve of the noncircular gear.

Machining errors in noncircular gears and installation errors in transmission mechanisms mainly affects the quality of use of noncircular gears. In the process of processing noncircular gears, the combination of various errors will cause errors in the final noncircular gears manufactured. These errors include machine tool error, tool error, fixture error, tooth return error, and thermal error. Based on the reason that the processing methods of noncircular gears and cylindrical gears are basically the same, by analogy to cylindrical gears, the machining errors of noncircular gears can also be considered to be summarized from the following four aspects, as shown in Figure 6 [10, 11].

In the working state, on the circumference where O is the center of the circle, the distribution of the teeth of the gear is not as uniform as in the nonworking state, which leads to the unevenness of the rotation angle and errors [12]. The angle error can be represented by the meshing line increment of the left and right tooth surfaces of the gear. This is because the variation law between the two has a certain quantitative relationship, and the meshing line increment of the left and right tooth surfaces can be obtained by the following formula:

$$\begin{cases} \Delta_1 F_L = e \sin(\varphi + \alpha), \\ \Delta_1 F_R = -e \sin(\varphi - \alpha). \end{cases} \tag{10}$$

Among them, $\Delta_1 F_L$ is the left meshing line increment, $\Delta_1 F_R$ is the right meshing line increment, e is the geometric eccentricity, φ is the rotation angle of the gear, and α is the pressure angle of the gear.

When the measured noncircular gear meshes with the ideal gear on both sides, due to the geometric eccentricity of the measured noncircular gear, fixing the axis position of the measured noncircular gear and the ideal gear will produce radial displacement as shown in the following formula:

$$\Delta R = \frac{\Delta_1 F_L + \Delta_1 F_R}{2 \sin \alpha} = \frac{e \sin(\phi + \alpha) - e \sin(\phi - \alpha)}{2 \sin \alpha} = e \cos \phi. \tag{11}$$

When the rotated angle of the tested gear satisfies the following conditions,

$$\phi = 0^\circ, \phi = 180^\circ. \tag{12}$$

The radial runout of the gear will be generated as shown in the following equation:

$$\Delta F_r = 2e. \tag{13}$$

The resulting radial runout can be used to represent the geometric eccentricity in the radial machining error as shown in Figure 7.

The installation error on the hobbing tool is mostly reflected in the runout in a single radial direction and a certain amount of skew [13, 14]. When the hobbing cutter is processing spur gears, the installation error of the hobbing cutter usually leads to the tooth profile error. In the process of gear operation, the tooth profile error will reduce the stability of the gear transmission and also reduce the contact area of the tooth height when the gear meshes. When machining helical gears, the waviness of the contact line between the tool and the helical gear is shown in Figure 8.

The tangential machining error is for a machine tool working with the generation method. The tangential machining error is mainly caused when the generative motion of the tool and tooth is destroyed. Some tangential machining errors may also be caused by indexing errors, because some machine tools have their own indexing mechanisms [15]. The transmission error and difference of the rod in the processing process, or the error of the machine tool indexing plate, and the final error of the indexing pot and rod pair are the main sources of tangential errors in the kinematic chain of the machine tool. The tangential error is a constant value along each contact line. It is the characteristic of gear hobbing to process by means of continuous indexing motion and generating motion. In such a processing method, from the tool to the gear burr, the tangential error of gear hobbing is caused by the accumulation of errors in the entire kinematic chain [16]. The main reason for the tangential error is the pot wheel and rod pair that performs indexing motion. The error generated by the pan wheel pot rod pair causes the noncircular gear to be processed to move eccentrically. The movement eccentricity is caused by the periodic change of the speed of the tooth return and the tool during the machining process compared with the speed of the generating movement. The movement eccentricity is reflected on the tooth return as shown in Figure 9.

In the longitudinal plane, the inclination error of the tool post guide of the machine tool will mainly cause a certain taper of the machined gear, as well as the contact line error and the helical line error. The existence of the guide rail error of the tool post of the machine tool will ultimately affect the stability of the gear transmission process and the uniformity of the load distribution, as shown in Figure 10.

The contact line error of the guide rail caused by the inclination amount y in the longitudinal plane is given by

$$\Delta F_b = \frac{y}{l} b \sin \alpha_n. \tag{14}$$

The tooth orientation error caused by the inclination amount y is shown in

$$\Delta F_\beta = \frac{y}{l} b \tan \alpha_n. \tag{15}$$

The taper on the gear width caused by the inclination amount y is given by

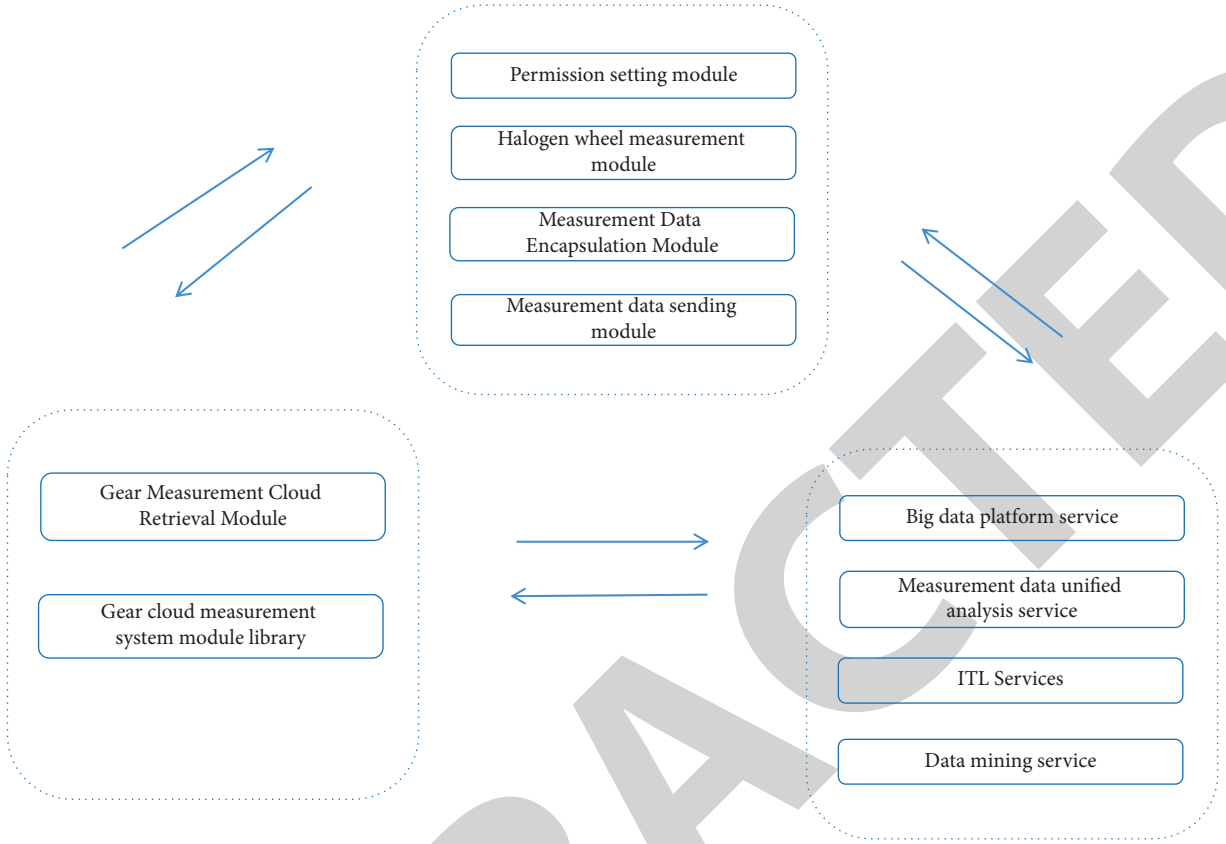

Figure 6: Four types of errors during hobbing of noncircular gears.

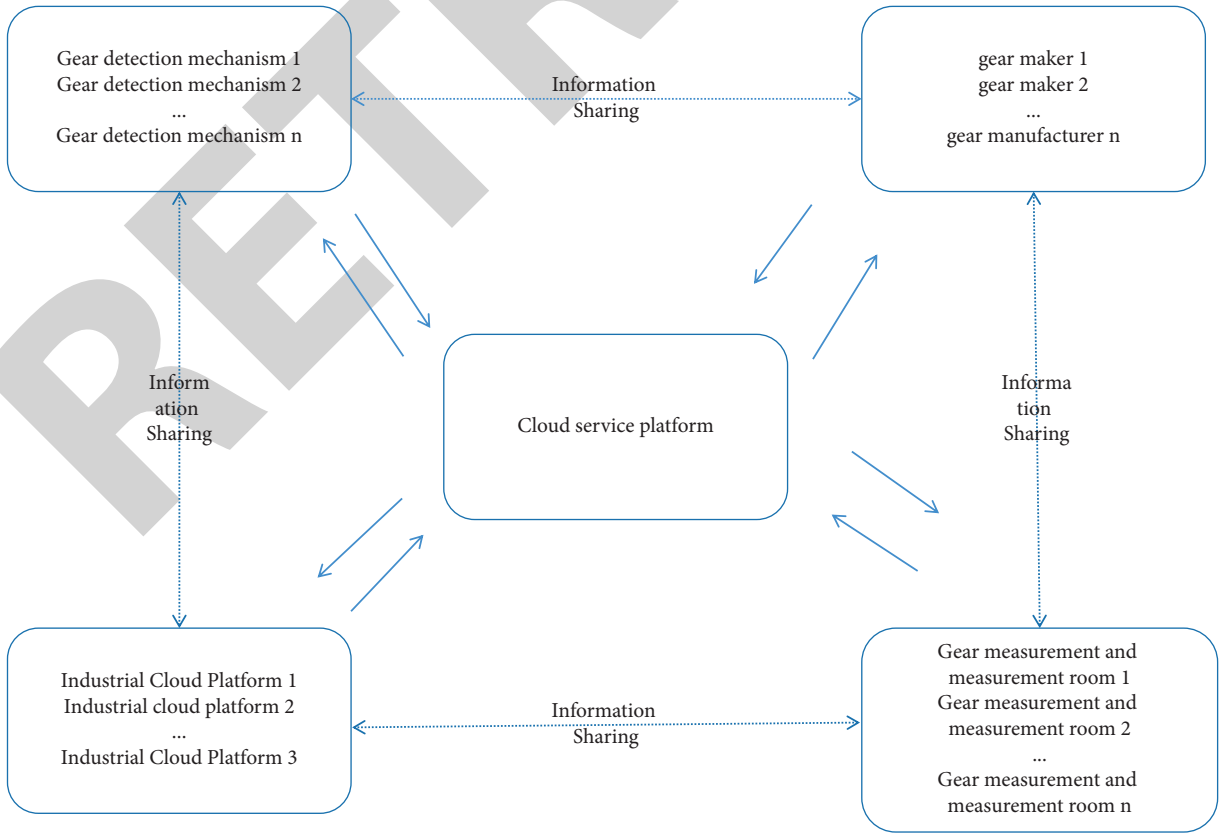

Figure 7: Geometric eccentricity.

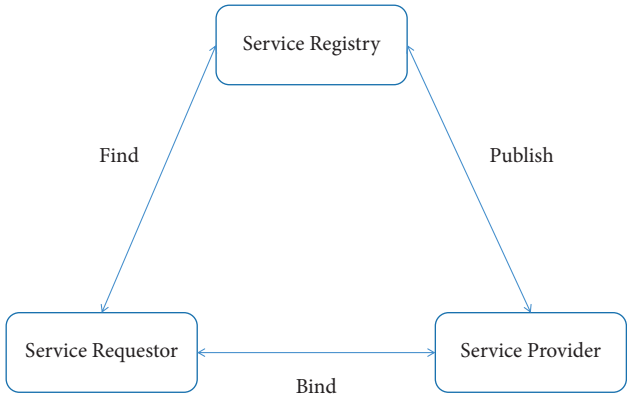

Figure 8: Tooth profile error and contact line error caused by hob installation error.

$$\Delta H = \frac{y}{l} b. \tag{16}$$

In the transverse plane of the machine tool, the error caused by the inclination of the tool holder guide rail in the direction of the contact line is shown in Figure 10, as shown in

$$\Delta F_b = \frac{x}{l} b \cos \alpha_n. \tag{17}$$

Then, the tooth direction error of the processed gear is shown in

$$\Delta F_\beta = \frac{y}{l} b. \tag{18}$$

Therefore, the expression of tooth direction error caused by inclination x and y is shown in

$$\Delta F_{\beta z} = \sqrt{\Delta F_{\beta x}^2 + \Delta F_{\beta y}^2}. \tag{19}$$

Although the tooth direction error of the gear is constant in one revolution of the gear, the errors caused by x and y can be distinguished. The tooth direction error caused by x shows that the left and right tooth surfaces are equal, and the symbols are the same; Unlike the tooth alignment error caused by x, the symbol of the tooth alignment error caused by y is no longer the same [17, 18]. Therefore, when the two appear at the same time, they are offset on one tooth surface and strengthened on the other tooth surface, as shown in Figure 11.

When the tooth reduction axis is skewed relative to the gear machine tool, the runout of the tooth reduction reference end face is generated. The runout error of the tooth reference end face will produce a variable tooth direction error of the cut gear, and the tooth direction error has a great impact on the longitudinal contact of the gear, as shown in Figure 12.

4. Experiment and Analysis

We completed the construction of the gear cloud measurement platform, in which the cloud computing platform is realized by Hadoop technology. Because the distributed operation has not been fully applied in the Windows system, the Linux system is used to provide support for platform development. Among them, the experimental network topology of Hadoop cluster fully distributed mode in cloud platform is shown in Figure 13.

According to the specific architecture of Hadoop, when building clusters, they can be divided into master and slave roles. Master mainly manages namenode nodes and jobtracker nodes, while slave mainly manages datanode and tasktracker nodes [19].

This paper uses VMware Workstation virtual machine to provide Linux environment in the Windows system, then deploys Hadoop cluster in the Linux operating system, and uses Hadoop cluster with high availability to build a small cloud computing platform. Software to be prepared for Hadoop installation: virtual machine version: VMware workstation-14.0.0 build-6661328; Linux version: centos-6.8-x86_ 64-bin-DVD1. Iso; JDK version: jdk-8u144-linux-x64.0 tar. gz; Hadoop version: hadoop-2.7.2 tar. gz; You also need to install ssh and rsync software. The cloud platform is built in the fully distributed mode of Hadoop cluster. The cluster is composed of three Linux system servers created by virtual machines. The relevant environment and configuration information of each server node are shown in Table 1.

First prepare 3 clients in the virtual machine, set static IP and host name, then install JDK and Hadoop, respectively, and configure their environment variables; finally, configure ssh, group, and test the cluster [20].

In the Linux system, after the Hadoop cluster is built, it can provide distributed storage, computing services, and corresponding resource management services. In order to realize the functions of data collection, analysis, and storage of cloud platform, it is also necessary to build other services supporting Hadoop cluster to improve the development environment. The planning of other services supporting Hadoop cluster in the three nodes is shown in Table 2.

In order to enable the cloud platform to meet the data entry requirements of as diverse data sources as possible, the cloud data acquisition module deploys Flume, Sqoop components, and custom interceptors, respectively. The biggest feature of Flume component is that it can read the data from the local disk of the server in real time and write the data to HDFS. Through the configuration of the Agent in Flume, it helps to realize the rapid entry into the cloud of the log files and sensor network port data generated by the measurement site in the data collection link of the cloud platform. Sqoop component can make data migrate back and forth between traditional relational database and HDFS, Hive, and HBase, so as to ensure safe and efficient import and export of data in different systems [21]. The user-defined interceptor is used to preprocess the collected data and prepare for subsequent data analysis. This part of the work is introduced below. The data acquisition module deploys Flume to collect multiple data sources, including text data, port monitoring data, and console data. After Flume is successfully deployed, Sqoop is used to export and store the traditional relational database My SQL and Oracle data as HDFS or data warehouse Hive. Next, test it, import the new table companydatas of My SQL database into the HDFS file

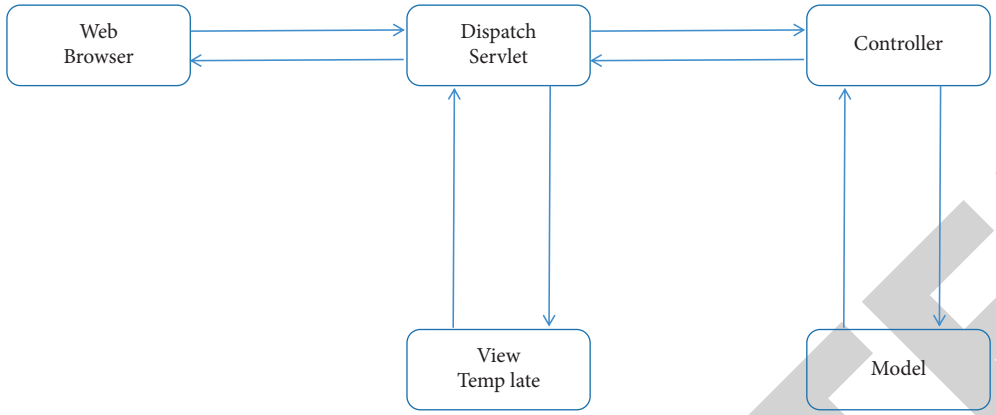

Figure 9: Motion eccentricity.

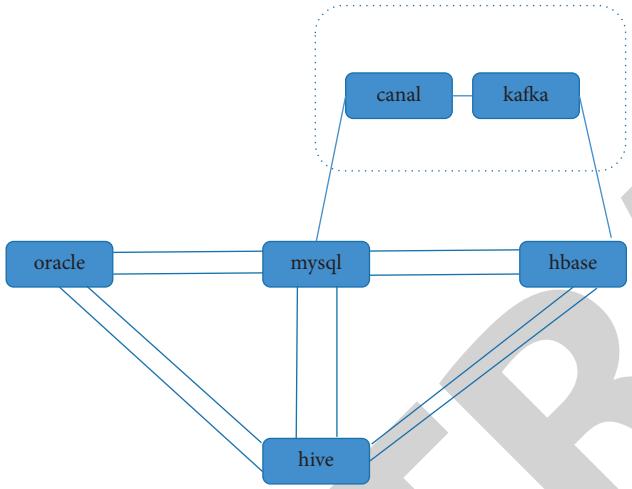

Figure 10: Inclination of the tool holder guide towards the front of the workpiece.

system, and save it in the path of/user/hpu. Hive has built a set of data warehouse based on cloud distributed storage. The data enter the distributed storage through the cloud platform data acquisition channel, and then extract and process the collected data in the data warehouse. Information about hive startup. Among them, it contains the version information of Hive and the version information of Hive running engine tez. To verify Hive's availability, perform the following tests. The data in the txt file of the distributed system are loaded into the data table of the data warehouse, and the first ten data in the table are queried through the query statement. Put the custom parsing function in cloud distributed parsing into the Java project built with maven, make a jar package, deploy it to the hive folder in the main node, add the jar package to Hive's class path through instructions, and create a temporary function to associate with the Java class developed by the user. In the cloud distributed data retrieval module, deploy and test Elasticsearch and Kibana. The Elasticsearch version is elasticsearch-7.4.2, and Kibana version is kibana-7.4.2. The distributed search engine deployed in this paper is an Elasticsearch cluster composed of three nodes. After its installation, configuration, and deployment, you can access the corresponding service port through the browser to view the health and node status of the test cluster. The configuration of the gear measuring system is mainly verified by uploading the data generated by the three probe measuring system and the gear measuring system to the cloud measuring system. The CMM system is mainly composed of measuring probe, measuring machine host, control system, and computer [22].

The gear cloud measurement system processes the measurement data in the cloud based on the cloud platform. The service process of the gear cloud measurement system is that the user logs in through the browser, controls the user's operation and access rights to the page content in the system according to the user role relationship and role menu relationship, and fills in the resource information, supplier information, measurement items, and measurement content according to the measurement resource information table provided on the terminal page, and publish resources on cloud platform [23]. Inside the enterprise, you can enter the data monitoring interface to view the measurement data in real time by clicking the corresponding data directory, or retrieve and view the historical data and the monitoring standards in international and Chinese enterprises. In addition to online verification of measurement data, when the CMM detects one or a batch of gears, it can also upload the data file. Users can view the comprehensive measurement results or single measurement indicators of a measurement item through the terminal page. The terminal system provides cloud storage service. The data generated by CMM and other gear measurement instruments are stored on the cloud platform and stored in different areas according to time or content classification, and Users can also access, use, and view data in corresponding ways through the cloud [24].

Measurement data integration management is a multi-user oriented data resource sharing service and a heterogeneous data processing service. The data processing service includes data classification and definition, source data characteristic coding, model and diagram document management service, etc. For the measuring instruments connected to the platform, users can log in to the client of the cloud platform to view the corresponding content [25, 26].

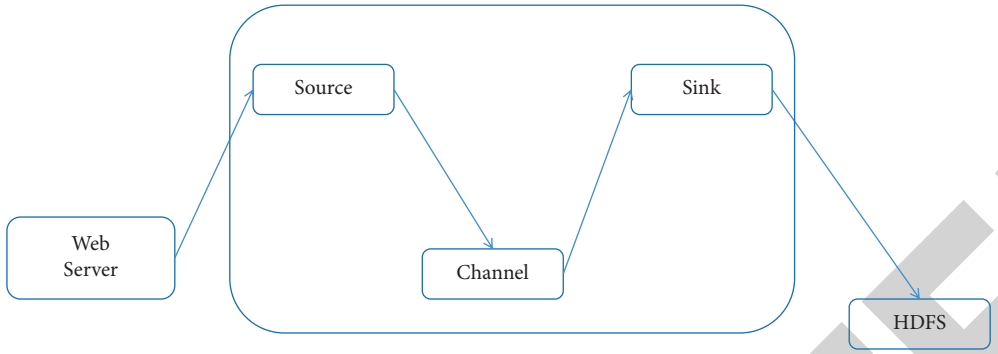

Figure 11: Inclination of tool rest guide rail to the left and right of workpiece.

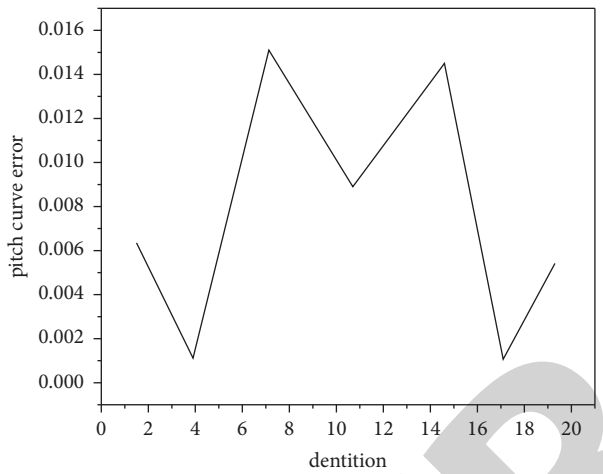

Figure 12: Tooth profile error caused by circular runout of workpiece end face.

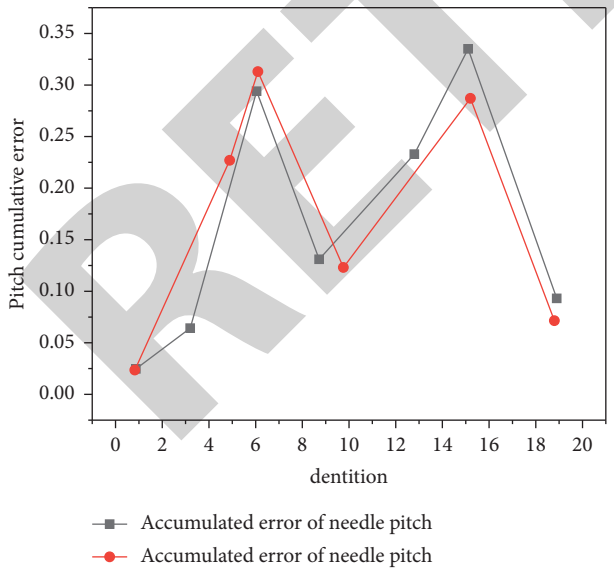

Figure 13: Experimental network topology of Hadoop cluster fully distributed mode in cloud platform.

In this section, the data collection of the laboratory CMM by the cloud platform is realized by uploading text files. The specific steps are to log in to the gear cloud measurement terminal system by using the user account and password. After logging in, click the "gear measurement data integration management" column of the navigation menu on the side bar of the page to enter the data upload directory. The measurement data generated by the CMM is uploaded to the server by dragging the file or clicking the select File button. The data acquisition channel collects the data through the monitoring of the server disk folder and then completes the data acquisition, processing, and processing in turn through the system data process designed by the cloud platform transmission and storage processes. During data transmission on the web page, the JSON format is used to define the measurement data. After processing the data uploaded by the CMM, enter the measurement index analysis directory. On this page, you can click the gear error item according to the different measurement indexes to access the error monitoring status, data, and content. The user can select the date through the date and time selector in the upper left corner of the page, by calling the error curve generation service, the measurement results of gear radial runout are obtained, with the tooth number as the abscissa and the radial distance of the stylus center as the ordinate.

Upload, analyze, and store the data collected from CMM, which provides support for the management of measurement data. The processed data information has the same data structure and standard, which can be operated and processed through the page. The data management service in the data integration of the gear cloud measurement platform manages it through a specific database according to the name, data content, and data type of the measurement

Table 1: Environment configuration information of each service node in the cluster.

Type of environment	Master node	Slave node①	Slave node②
Operating system	CentOS-6.8	CentOS-6.8	CentOS-6 8
CPU	8 Nuclear	8 Nuclear	8 Nuclear
RAM	7G	4G	4G
Disk	50 GB	50 GB	50 GB
JDK Version	1.8	1.8	1.8
IP Address	192.168.174.102	192.168.174.103	192.168.174.104
Hadoop Version	hadoop-2.7.2	hadoop-2.7.2	hadoop-2.7.2

Table 2: Construction and testing of the gear cloud measurement system based on cloud platform.

Service name	Master node	Slave node①	Slave node②
K afka	✓	✓	✓
Flume(collection)	✓		
Zo okeeper	✓	✓	✓
Flume(Consumption)			✓
Hive	✓		
MySQL	✓		
Sqoop	✓		

platform. The data obtained by the cloud platform from the CMM are placed in different data tables of the same database. The user invokes the encapsulated service instructions in the form of buttons on the page to realize the operation of data management.

When the cloud platform collects measurement data through CMM and other measurement resources, in order to ensure the integrity of the data, it also encapsulates and manages the measurement resources. In addition, the resources in the cloud platform are jointly maintained by registered users with a basic material database, such as integrated measurement data, gear part library, equipment resource information, and document information, to provide support for all stages of gear measurement [27].

In the process of gear measurement, various problems may be encountered. At this time, the retrieval module of the terminal system can be used to search for specific solutions or relevant information, such as the retrieval of gear parts information or measurement methods. The retrieval process is a process in which users actively pull data from the system. The terminal system will also provide offline recommendation service and real-time recommendation service according to different recommendation algorithms, so as to realize auxiliary decision-making and improve measurement efficiency.

Firstly, this chapter introduces the deployment of cloud platform development environment, including the hardware facilities and software configuration built by distributed cluster, and gives the operation status of each node. Then, the deployment and testing of relevant functional modules are carried out to prepare for the data acquisition, data analysis, and data retrieval of the platform. Finally, the case application of the terminal system is carried out, and the functions of the terminal system are verified according to some functional modules.

5. Conclusion

Under the background of the continuous integration and development of traditional industry services and new generation information technology, this paper studies the gear cloud measurement technology based on cloud platform. Taking the cloud platform as the carrier, this paper proposes a gear cloud measurement solution based on big data cloud computing platform, which realizes the collection, storage, and analysis of measurement data in different places, as well as the management and visual display of error parameters in measurement indicators. Firstly, from the perspective of the overall requirements of the gear cloud measurement system, the functional requirements and overall architecture of the gear cloud measurement platform are analyzed and designed. According to the corresponding functional level, the cloud platform is divided into cloud data acquisition and transmission module, cloud data analysis and conversion module, and cloud data retrieval and push module. Next, the above modules are developed, deployed, and implemented one by one. The main research contents and achievements of this paper are as follows:

(1) The architecture of the gear measurement terminal system based on cloud platform is studied

Under the traditional mode, the information exchange in gear measurement and other links in its life cycle is usually within the department and enterprise. At the same time, the traditional software development adopts the chimney system architecture, which also increases the difficulty of data sharing. Through cloud computing technology, the contradiction between the global optimization requirements of gear measurement and fragmented collection can be well solved. The service-oriented cloud architecture and cloud data center solve the problems of software system closure, data fragmentation, and data island, promote the sharing of data, the unification of system technical architecture, and the agile development and deployment of applications, and realize rapid response and service innovation through rich front-end applications.

(2) The resource dynamic integration method of the gear cloud measurement system based on cloud platform is given

In resource collaboration, application collaboration, and data collaboration, it is necessary to integrate the distributed resources of enterprises and institutions into one by some means to form a cloud data center and provide data and other services uniformly and transparently. The cloud data center gathers the resources of different enterprises and institutions to analyze and manage the received data through certain rules. Moreover, the virtualization of the cloud data center encapsulates the distributed physical resources of network, computing, and storage for the use of the cloud platform.

(3) The information retrieval technology of gear measurement terminal based on cloud platform is introduced

Firstly, this paper discusses the resource retrieval and recommendation technology of the gear cloud measurement system based on cloud platform, describes the retrieval process of surveyors on cloud platform, and analyzes several mainstream retrieval strategies and calculation methods of sorting retrieval results. Finally, the recommendation technology of the gear cloud measurement system based

on cloud platform is discussed, and the cloud platform recommendation model and collaborative filtering recommendation algorithm based on argot model are analyzed.

(4) Implementation of the gear cloud measurement system based on cloud platform

Finally, the experimental environment, deployment, and testing of the cloud platform in this paper are introduced, the functional modules and components of the gear cloud measurement system are tested, and the final effect of the gear cloud measurement platform is summarized.

Data Availability

The labeled data set used to support the findings of this study is available from the corresponding author upon request.

Conflicts of Interest

The author declares that there are no conflicts of interest.

Acknowledgments

This work was supported by the Science and Technology Project of Jiangxi Provincial Education Department (grant no. GJJ181106) and Pingxiang Science and Technology Support Project (2018C0103).

References

[1] J. Fan and Q. Ye, "Research on geometric error modeling and compensation method of cnc precision cylindrical grinding machine based on differential motion theory and jacobian matrix," *International Journal of Advanced Manufacturing Technology*, vol. 120, no. 3-4, pp. 1805–1819, 2022.

[2] C. Wei, Q. Wang, and C. Liu, "Research on construction of a cloud platform for tourism information intelligent service based on blockchain technology," *Wireless Communications and Mobile Computing*, vol. 2020, no. 2, Article ID 8877625, 2020.

[3] W. Li, B. Jiang, and W. Zhao, "Obstetric Imaging Diagnostic Platform Based on Cloud Computing Technology under the Background of Smart Medical Big Data and Deep Learning," *IEEE Access*, vol. 8, pp. 78265–78278, 2020.

[4] H. Zheng, M. Huang, L. Zhan, Y. Zhu, and P. Liu, "Research on high precision servo system of actuator based on pid parameter stability domain under mixed sensitivity constraint," *Journal of Electrical Engineering & Technology*, vol. 16, no. 3, pp. 1651–1665, 2021.

[5] B. Li, T. Wang, and P. Wang, "An analytical and optimal corner smoothing method for cnc machine tools along linear segments," *Journal of Mechanical Science and Technology*, vol. 36, no. 4, pp. 1959–1973, 2022.

[6] J. Li, D. L. Tan, F. Zhao, and X. J. Yue, "Research on Piv Image Matching Algorithm of Turbulent Velocity Field Based on Circular Projection," *IEEE Access*, vol. 9, pp. 35681–35690, 2021.

[7] B. O. Soyoye, "Development of the instrumentation unit of a motorized precision planter," *European Journal of Engineering Research and Science*, vol. 5, no. 4, pp. 403–407, 2020.

[8] T. Hao, X. Chen, and Y. Song, "A topic-based bibliometric analysis of two decades of research on the application of technology in classroom dialogue," *Journal of Educational Computing Research*, vol. 58, no. 7, pp. 1311–1341, 2020.

[9] X.-h. Han, X.-c. Zhang, F.-y. Zheng, M. Xu, and J. Tian, "Mathematic model and tooth contact analysis of a new spiral non-circular bevel gear," *Journal of Central South University*, vol. 29, no. 1, pp. 157–172, 2022.

[10] I. M. A. Ali, I. Attiaoui, R. Khalfaoui, and A. K. Tiwari, "The effect of urbanization and industrialization on income inequality: an analysis based on the method of moments quantile regression," *Social Indicators Research*, vol. 161, no. 1, pp. 29–50, 2022.

[11] P. Wang, L. Han, J. Li, and F. Liu, "Research on design and manufacturing of gear slicing cutter for circular arc tooth," *International Journal of Advanced Manufacturing Technology*, vol. 113, no. 19, pp. 1–13, 2021.

[12] X. U. Chuanbo, M. Chi, L. Dai, Y. Jiang, and Z. Guo, "Research on rubber spring model of high-speed emu based on non-hyperelastic forces," *Mechanika*, vol. 27, no. 1, pp. 12–21, 2021.

[13] B. Liu, J. Zhang, and C. Zhu, "Research on control technology of grid connected inverter based on non-ideal grid," *Telecommunications and Radio Engineering*, vol. 79, no. 15, pp. 1363–1373, 2020.

[14] H. Zhu and J. Li, "Research on the cnc incremental forming based on multidirectional real-time adjustment of the sheet posture," *International Journal of Advanced Manufacturing Technology*, vol. 110, no. 5-8, pp. 1–12, 2020.

[15] G. M. Veselov, A. P. Voiskovskii, and V. A. Yakimenko, "Control algorithm of the angular position of a quadcopter based on statistical analysis of experimental data," *Russian Engineering Research*, vol. 41, no. 8, pp. 748–751, 2021.

[16] J. Zhang, J. Cenci, V. Becue, and S. Koutra, "Analysis of spatial structure and influencing factors of the distribution of national industrial heritage sites in China based on mathematical calculations," *Environmental Science and Pollution Research*, vol. 29, no. 18, pp. 27124–27139, 2022.

[17] H. Xie, "Research and case analysis of apriori algorithm based on mining frequent item-sets," *Open Journal of Social Sciences*, vol. 09, no. 4, pp. 458–468, 2021.

[18] V. T. Do, "Empirical model for surface roughness in hard milling of aisi h13 steel under nanofluid-mql condition based on analysis of cutting parameters," *Journal of Mechanical Engineering Research and Developments*, vol. 43, no. 2, pp. 89–94, 2020.

[19] Y. He, S. Yang, C. Y. Chan, L. Chen, and C. Wu, "Visualization analysis of intelligent vehicles research field based on mapping knowledge domain," *IEEE Transactions on Intelligent Transportation Systems*, vol. 22, pp. 5721–5736, 2020.

[20] S. Gao and L. Bhagi, "Design and research on caddcam system of plane based on nc machining technology," *Computer-Aided Design and Applications*, vol. 19, pp. 64–73, 2021.

[21] Q. Guo, Z. Wu, C. Zhang et al., "Study on a new clean machining method instead of sanding technology for wood," *Alexandria Engineering Journal*, vol. 60, no. 2, pp. 2369–2380, 2021.

[22] F. Chen and C. Wang, "Image recognition technology based on cloud computing platform," *Journal of Intelligent and Fuzzy Systems*, vol. 39, no. 5, pp. 1–11, 2020.

[23] J. Leyva-Bravo, P. Chias-Sanchez, A. Hernandez-Rodriguez, and G. G. Hernandez-Alba, "Electrochemical discharge machining modeling through different soft computing

Hindawi
Shock and Vibration
Volume 2022, Article ID 6808641, 9 pages
https://doi.org/10.1155/2022/6808641

Research Article

Single Feature Extraction Method of Bearing Fault Signals Based on Slope Entropy

Erna Shi

Xi'an Traffic Engineering Institute, Xi'an, Shaanxi 710300, China

Correspondence should be addressed to Erna Shi; shierna0719@163.com

Received 5 April 2022; Revised 22 April 2022; Accepted 6 May 2022; Published 2 June 2022

Academic Editor: Yuxing Li

As an entropy representing the complexity of sequence, slope entropy (SloE) is applied to feature extraction of bearing signal for the first time. With the advantage of slope entropy in feature extraction, the effectiveness of bearing fault signal diagnosis can be verified. Five different kinds of entropy are selected to be comparative methods for experiments, and they are permutation entropy (PE), dispersion entropy (DE), a version of entropy adapted by PE, which is weighted permutation entropy (WPE), and two versions of entropy adapted by DE, which are fluctuating dispersion entropy (FDE) and reverse dispersion entropy (RDE). A method of extracting a single feature of bearing fault signals based on SloE is carried out. Firstly, the features of the bearing signals are extracted by the six kinds of entropy. Then, some relevant data are computed, and the identification ratios are calculated by the K-nearest neighbor (KNN) algorithm. The experimental result indicated that the identification ratio of SloE is the highest at 97.71% by comparing with the identification ratios of the other five kinds of entropy, which is higher by at least 13.54% than the others and 27.5% higher than the lowest one.

1. Introduction

Bearing is an indispensable part of modern mechanical equipment, and its roles in modern mechanical equipment are the support of the mechanical rotating body, the sliding part in motion, and the guarantor of rotation accuracy [1–3]. Self-aligning ball bearing is the research object of this paper, which is a kind of rolling bearing equipped with spherical balls installed between the inner race with two raceways and the outer race with a spherical raceway. Its curvature center of the outer race is consistent with the bearing center, so it has the same centering function as the automatic centering ball bearing. It can be adjusted automatically when the shaft and housing deflect, and this process will not increase the bearing burden. Self-aligning ball bearing ball bearings can bear the loads in two directions, which are radial and axial. Compared with the axial bearing capacity, the self-aligning ball bearing has a greater radial bearing capacity, so it can well deal with heavy load and impact load. The self-aligning ball bearing belongs to the bearing that has tapered holes in the inner diameter of the inner race. It can be installed directly or installed on the cylindrical shaft with a remove pipe or fastening sleeve. The cage is stamped with a steel plate and formed with polyamide. Due to its strong ability to bear heavy load and impact load, self-aligning ball bearings are used in sugar pressing, papermaking, precision instrument, petroleum, cement, metallurgy, mines, low noise motor, motorcycle, rolling mill, automobile, and such industries. Therefore, as such a widely used, fine, and important component, bearing fault diagnosis is a subject that needs to be studied carefully [4–6].

Due to the nonlinear stiffness and bearing clearance of rolling bearing [7, 8], the vibration signal generated by its operation often shows nonstationary and nonlinear. Therefore, extracting useful fault feature information from nonstationary and nonlinear signals is the focus and difficulty of rolling bearing fault diagnosis. Aiming at the problem of bearing fault, many scholars have done lots of research on the early diagnosis of bearing fault [9, 10].

Many scholars apply the methods commonly used in signal processing to bearing fault diagnosis. Many methods of nonlinear dynamic are proposed [11], such as fuzzy

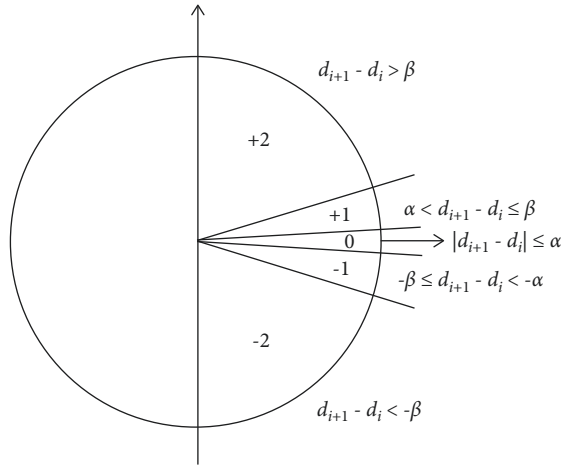

Figure 1: Symbol allotment of SloE.

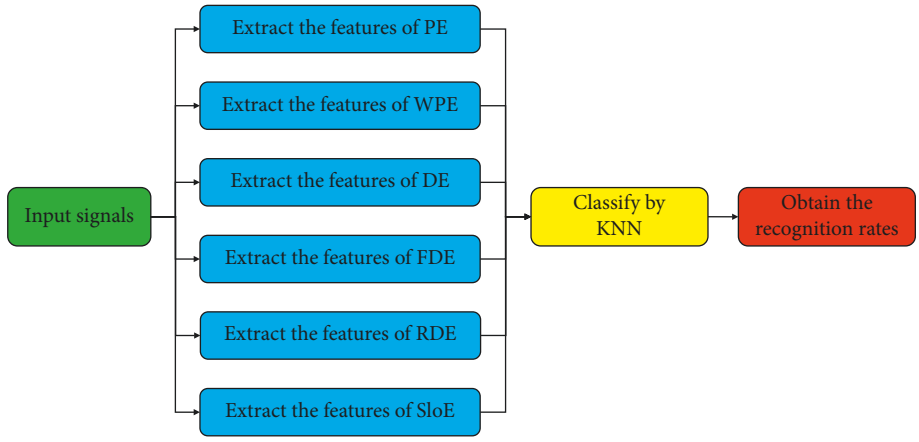

Figure 2: The flow chart of the single feature extraction method.

entropy (FE) [12], permutation entropy (PE) [13], Rényi entropy (RE) [14], dispersion entropy (DE) [15], sample entropy (SE) [16], Wiener entropy (WE) [17], and instantaneous spectral entropy (ISE) [18], which can extract the nonlinear feature of the signals and characterize the health state of the equipment. For SE, its calculation time is long, real-time performance is poor, and similarity measurement is prone to mutation [19]. PE has the advantage of simple calculation, but it ignores the amplitude information of dynamic number sequences [20–25]. Although FE is obtained by improving SE, it still has the disadvantages of slow calculation speed and so on [26–28]. DE has the advantages of small influence by burst signals and better stability, which make up for the problem of PE [29–32]. WE is very sensitive to small alterations. ISE has the relatively low computational burden and fast execution time. Reverse dispersion entropy (RDE) [33] as an improved version of DE has the advantages of both PE and DE and has stronger stability and noise robustness [34, 35]. Similarly, FDE [36] is also an improved version of DE [37], and WPE [38] is an improved version of PE [39, 40]. There are also many other kinds of entropy that are not listed here [41–44].

Slope entropy (SloE) [45] is a new entropy estimator proposed in recent years, which is based on only the vibration amplitude of dynamic number sequences and five symbol patterns. In the three years since it came out, it has been used in many fields, such as medicine and underwater acoustic signal, and achieved excellent results. SloE is applied to the field of medicine by David Cuesta-Frau in 2020 [46, 47], and it is applied to the underwater acoustic signal processing field by Li et al. in 2021 [48]. SloE has a good feature extraction effect in various fields, so it is introduced into the field of fault diagnosis for the first time in this paper.

SloE is applied to the field of bearing fault diagnosis for the first time in this paper. The remaining of the paper is structured as follows: the specific calculation steps of SloE are introduced, and an example of the algorithm is given in Section 2. Section 3 introduces the detailed steps of the experiment and gives a flow chart of the steps. In Section 4, the graphs of the six types of signals are given, the single feature extraction experiment is carried out, and KNN is used for classification. Section 5 is the summary, where the main innovations and conclusions of this paper are given.

2. Slope Entropy

2.1. Basic Principle. SloE is a new algorithm put forward in 2019, which can indicate dynamic number sequence complexity. It is founded on both the vibration amplitude of the

Table 1: Types and codes of the signals.

Type	Normal	Inner race	Ball	Outer race		
				Centered	Orthogonal	Opposite
Code	100	108	121	133	147	160

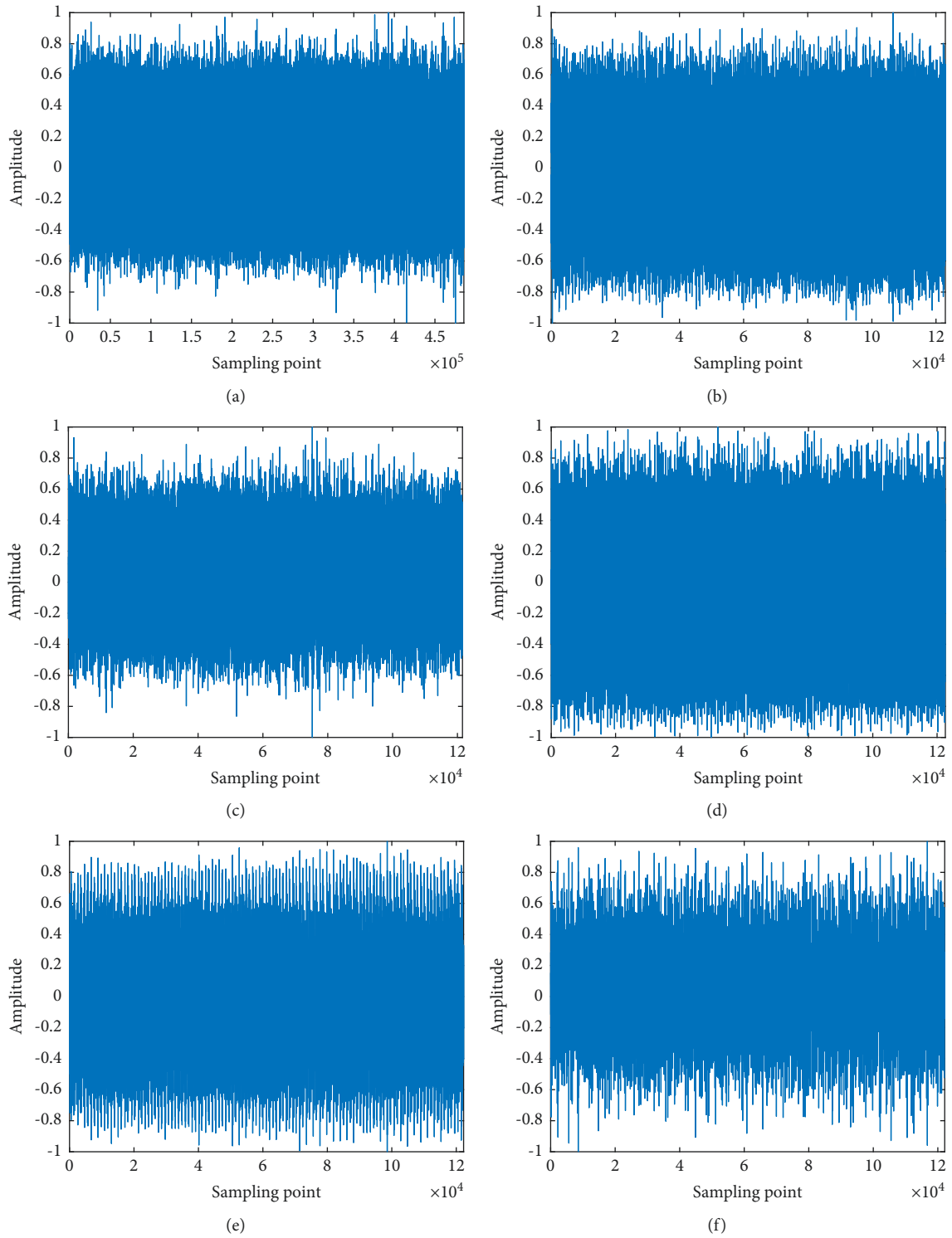

Figure 3: The normalized six types of bearing signals. (a) 100, (b) 108, (c) 121, (d) 133, (e) 147, (f) 160.

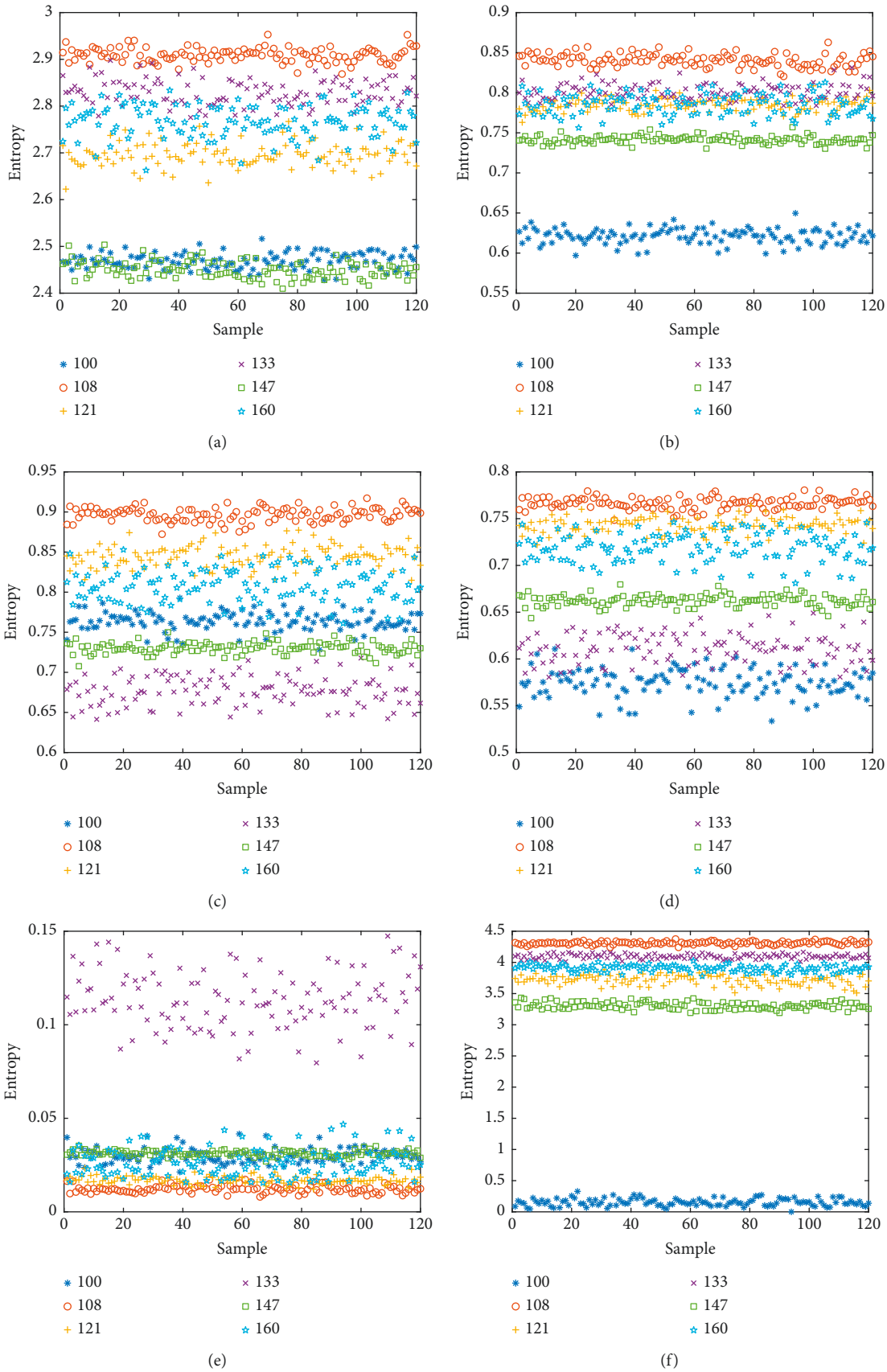

Figure 4: Feature distribution of six types of bearing signals. (a) PE, (b) WPE, (c) DE, (d) FDE, (e) RDE, (f) SlOE.

Table 2: The mean and AMMD of different features.

Entropy	Type	100	108	121	133	147	160
PE	Mean	2.4693	2.9093	2.6961	2.8296	2.4503	2.7676
	AMMD			0.019			
WPE	Mean	0.6214	0.8406	0.7852	0.8016	0.7414	0.7856
	AMMD			0.0004			
DE	Mean	0.7635	0.8968	0.8452	0.6769	0.7302	0.8086
	AMMD			0.0366			
FDE	Mean	0.5751	0.7666	0.7435	0.6117	0.6624	0.7192
	AMMD			0.0231			
RDE	Mean	0.0302	0.0122	0.0169	0.1134	0.0312	0.026
	AMMD			0.001			
SloE	Mean	0.1529	4.3098	3.7154	4.0954	3.3072	3.9055
	AMMD			0.1901			

dynamic number sequence and the five symbol patterns that have been set. Each symbol pattern is allocated according to the difference between the vibration amplitude of the input dynamic number sequences. The calculation process of the SloE algorithm is simple and easy to understand, whose main operation has only addition and subtraction calculations. SloE is calculated as follows.

(1) For given dynamic number sequences $D = \{d_i, i = 1, 2, \ldots, N\}$, the number of subsequences of D is extracted in the light of the embedding dimension m, $D_1 = \{d_1, d_2, \ldots, d_n\}$, $D_2 = \{d_2, d_3, \ldots, d_{n+1}\}$, $\ldots$, $D_k = \{d_k, d_{k+1}, \ldots, d_N\}$, where $k = N - n + 1$.

(2) Diverse symbol modes (+2, +1, 0, −1, −2) are partitioned by the positive and negative values of the two threshold parameters (β and α). Figure 1 is the symbol allotment of SloE.

The specific symbol modes of SloE are assigned in a very unequivocal way. The vertical increments of SloE are decided by β and α, and the horizontal increment between the samples of the continuous dynamic number sequence is always set up as 1. If $\beta = 0.296$, the inclination of the borderlines is 16.5° and −16.5°. And if $\alpha = 0.09$, the boundaries slope of the region of symbol "0" is 5° and -5°.

The specific distribution principles are as follows: if $d_{i+1} - d_i > \beta$, the symbol mode is +2; if $\alpha < d_{i+1} - d_i \le \beta$, the symbol mode is +1; if $|d_{i+1} - d_i| \le \alpha$, the symbol mode is 0; if $-\beta \le d_{i+1} - d_i < -\alpha$, the symbol mode is -1; if $d_{i+1} - d_i < -\beta$, the symbol mode is -2, where $\beta > \alpha > 0$.

(3) Mode sequences $M_1, M_2, \ldots, M_k$, which are corresponding to $D_1, D_2, \ldots, D_k$, are gained after symbol allotment, $M_1 = \{m_1, m_2, \ldots, m_{n-1}\}$, $M_2 = \{m_2, m_3, \ldots, m_n\}$, $\ldots$, $M_k = \{m_k, m_k, \ldots, m_{N-1}\}$, where $k = N - n + 1$, $m_1, m_2, \ldots, m_{N-1}$ are the symbol modes calculated by $d_2 - d_1$, $d_3 - d_2$, $\ldots$, $d_N - d_{N-1}$ through step (2).

(4) Mode sequences have $x = 5^{n-1}$ diverse forms. The quantity of each form is $f_1, f_2, \ldots, f_n$. The frequencies of the mode sequences are the proportions of the number of times they appear: $R_1 = f_1/f$, $R_2 = f_2/f$, $\ldots$, $R_n = f_n/f$. The calculation formula of SloE is defined as follows in view of the classical Shannon entropy:

$$E_s(m) = -\sum_{j=1}^{n} R_j \ln R_j. \quad (1)$$

2.2. Example. Here is a dynamic number sequence $D = \{9, 7, 6, 4, 2, 1, 7, 8, 6, 4, 2, 1, 6, 4, 2, 1\}$, sequence length $N = 16$. Set up the delay time $\varepsilon = 1$, the embedding dimension $m = 4$, and the two threshold parameters $\beta = 1$ and $\alpha = 0.001$. The specific steps of calculating SloE are as follows:

(1) According to D, get the subsequences $D_1 = \{9, 7, 6, 4\}$, $D_2 = \{7, 6, 4, 2\}$, $D_3 = \{6, 4, 2, 1\}$, $D_4 = \{4, 2, 1, 7\}$, $D_5 = \{2, 1, 7, 8\}$, $D_6 = \{1, 7, 8, 6\}$, $D_7 = \{7, 8, 6, 4\}$, $D_8 = \{8, 6, 4, 2\}$, $D_9 = \{6, 4, 2, 1\}$, $D_{10} = \{4, 2, 1, 6\}$, $D_{11} = \{2, 1, 6, 4\}$, $D_{12} = \{1, 6, 4, 2\}$, $D_{13} = \{6, 4, 2, 1\}$.

(2) Then, according to the subsequences, obtain the mode sequences: $M_1 = \{-2, -1, -2\}$, $M_2 = \{-1, -2, -2\}$, $M_3 = \{-2, -2, -1\}$, $M_4 = \{-2, -1, +2\}$, $M_5 = \{-1, +2, +1\}$, $M_6 = \{+2, +1, -2\}$, $M_7 = \{+1, -2, -2\}$, $M_8 = \{-2, -2, -2\}$, $M_9 = \{-2, -2, -1\}$, $M_{10} = \{-2, -1, +2\}$, $M_{11} = \{-1, +2, -2\}$, $M_{12} = \{+2, -2, -2\}$, $M_{13} = \{-2, -2, -1\}$.

(3) There are 10 types of mode sequences. The frequency of $\{-2, -2, -1\}$ is 3, the frequency of $\{-2, -1, +2\}$ is 2, and the frequency of other types is all 1. Therefore, the probabilities are $R_1 = 1/13$, $R_2 = 1/13$, $R_3 = 3/13$, $R_4 = 2/13$, $R_5 = 1/13$, $R_6 = 1/13$, $R_7 = 1/13$, $R_8 = 1/13$, $R_9 = 1/13$, $R_{10} = 1/13$.

(4) Finally, the value of SloE obtained by equation (1) is $E_s(m)$ = -(8 × 1/13 × ln 1/13 + 3/13 × ln 3/13 + 2/13 × ln 2/13) = 2.2048.

3. Proposed Method

A single feature extraction method is put forward for the six types of bearing signals in this experiment. As shown in

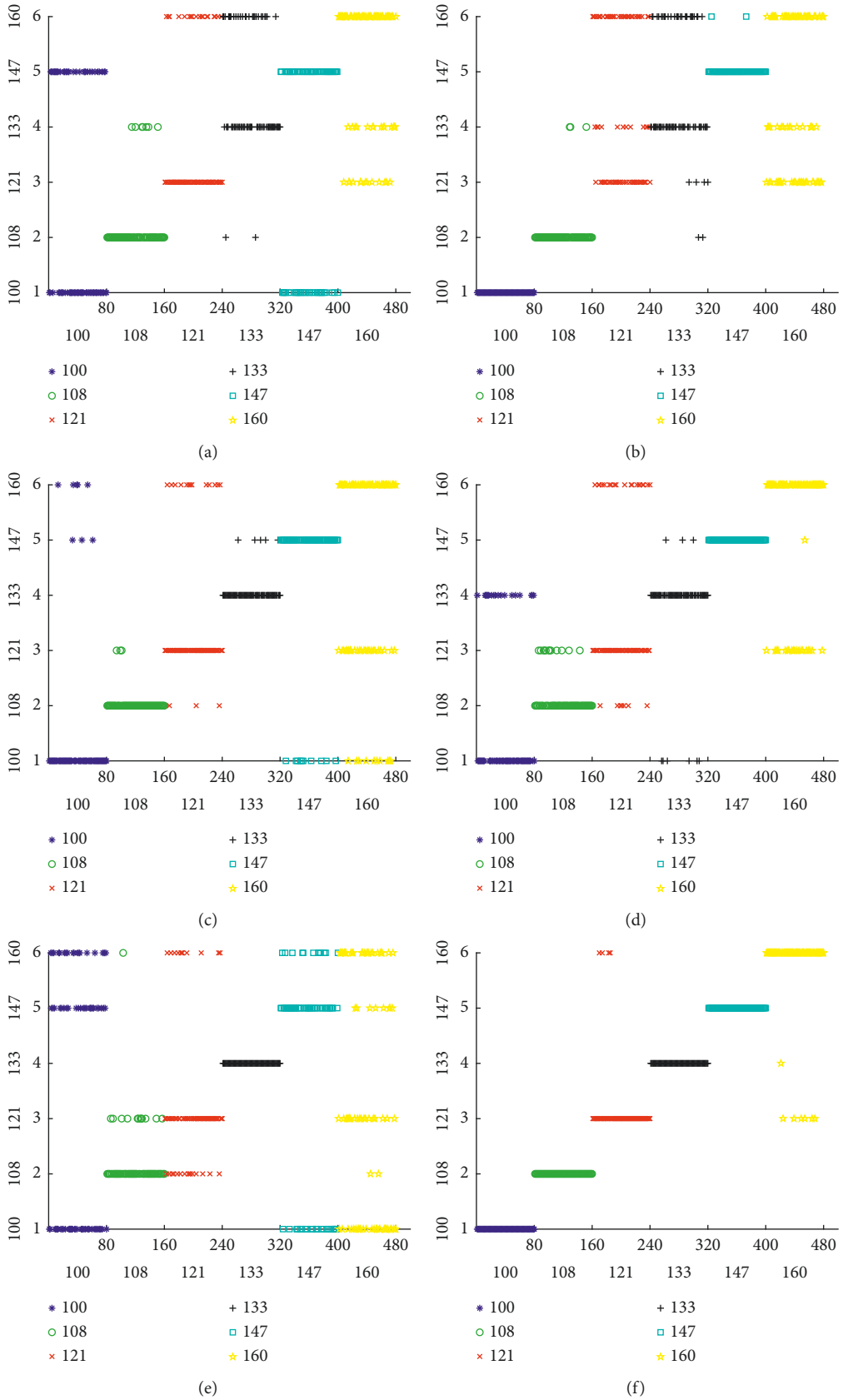

Figure 5: Feature classification and recognition distribution. (a) PE, (b) WPE, (c) DE, (d) FDE, (e) RDE, (f) SLoE.

Table 3: Identification ratios of the feature.

Signals	100 (%)	108 (%)	121 (%)	133 (%)	147 (%)	160 (%)	Average (%)
PE	60	91.25	77.5	63.75	62.5	66.25	70.21
WPE	100	96.25	43.75	58.75	97.5	48.75	74.17
DE	90	96.25	80	93.75	87.5	57.5	84.17
FDE	76.25	85	67.5	88.75	100	72.5	81.67
RDE	47.5	83.75	67.5	100	57.5	30	64.38
SloE	100	100	95	100	100	91.25	97.71

Figure 2 is the flow chart of the single feature extraction method, the particular procedures of the method are as follows.

(1) The six types of bearing signals are imported after being normalized.

(2) For the normal bearing signals or each type of bearing fault signals, which are normalized, 120 samples are selected, where each sample contains 1000 sample points. The features of PE, WPE, DE, FDE, RDE, and SloE are extracted.

(3) K-nearest neighbor (KNN) is chosen as the classifier to classify the features of six kinds of bearing signals. For each type, 40 groups of sample signals are selected as training samples, and 80 groups of sample signals are selected as test samples. The number of nearest samples is set as $k = 3$.

(4) The identification ratios are obtained by operation.

Through these steps, we can conclude that SloE is effective in single-feature classification by comparing the identification ratio calculated by SloE and the others of the five other kinds of entropy.

4. Feature Extraction

4.1. Six Types of Signals. The features of the six types of signals are extracted, which are normal signals, bearing inner race, ball, and outer race fault signals [49]. According to the position relative to the load zone, which is centered, orthogonal, and opposite, there are three types of bearing outer race faults signals. The signals come from the same website, and they are acquired under the same fault diameter, motor load, and motor speed. The names of these signals are replaced by 100, 108, 121, 133, 147, and 160 in the paper. Types and codes of the signals are shown in Table 1.

The lengths of sampling points for them are 485643, 122917, 121556, 122571, 122281, and 122136. The normalized six types of bearing signals are shown in Figure 3.

4.2. Extraction Method. In the feature extraction experiment, for normal signals or each type of bearing fault signal, 120 samples are chosen, and every sample includes 1000 sampling points. These samples almost contain all sampling points of the five bearing fault signals.

For reasonable and scientific comparison, because all kinds of entropy have the same settable parameters the embedding dimension and the delay time, set up them as $m = 4$ and $\varepsilon = 1$. The number of categories is the same settable parameters of DE and two changed versions of DE, set up it as $c = 3$. DE and FDE have the same mapping format, which is the normal cumulative distribution function (NCDF). The two threshold parameters of SloE are set up as $\beta = 0.296$ and $\alpha = 0.09$. Feature distribution of six types of bearing signals is shown in Figure 4.

It can be inferred from Figure 4, for PE distribution, the entropy points of 100 and 147 and the entropy points of 108, 121, 133, and 160 are near to each other; for WPE distribution, almost all entropy points of 121, 133, and 160 are mixed together; for DE and FDE distribution, the entropy points of all types of signals intersect in varying degrees; for RDE distribution, only the entropy points of 133 are significantly distinguished from those of the other five types of signals; for SloE distribution, only a few entropy points of 160 are close to those of 121 and 133. It indicates that SloE has better classification ability on the six types of bearing signals.

For proving the validity of SloE, the mean and the absolute minimum mean difference (AMMD) of diverse features are computed. AMMD is set to the absolute value of the minimum mean difference, and it can intuitively express the distance between the entropy points of the two types of signals, whose entropy points are the closest to each other in the six types of signals. The larger the MMD, the more reliable the interclass separability of the entropy. Table 2 shows the mean and AMMD of different features.

As Table 2 shows, with regard to the six kinds of entropy, the average value of each type of signal has diverse degrees of diversity. RDE has the minimum AMMD of 0.001, and the AMMD of SloE is the maximum, which is 0.1901. It is preliminarily judged that RDE has the worst interclass separability and SloE has the better.

4.3. Feature Classification. For proving the better effect of bearing fault signals feature extraction and classification based on SloE, KNN classification is led into this experiment. For the normal bearing signals or each type of bearing fault signals, which are normalized, 120 samples are selected, where each sample contains 1000 sample points. For each type, 40 groups of sample signals are chosen as training samples, and 80 groups of sample signals are classified as test samples. The feature classification and recognition distribution are shown in Figure 5.

As shown in Figure 5, for these six types of signals, PE and DE have diverse quantities of wrongly classified samples, where the ones of 100 and 160 are separately the largest; WPE, FDE, and RDE only correctly classify the samples of

100, 147, and 133, respectively, but a large number of samples in other signals are classified wrongly; SloE has only a few misclassified samples for 121 and 160, which are classified to 160, 121, and 133, and the other four types of signals are classified correctly; among the six feature extraction methods, 160 has the worst classification effect, while SloE has the best average classification effect. Identification ratios of the feature are shown in Table 3.

As shown in Table 3, for 100, WPE and SloE have the highest classification and identification ratio of 100%, that of DE is 90%, and those of PE, FDE, and RDE are less than 80%; for 108, the classification and identification ratios are more than 90% expect FDE and RDE, where that of SloE is 100%; for 121 and 160, only the classification and C of SloE are more than 90%, and the other kinds of entropy have the classification and identification ratios less than or equal to 80%; for 133, SloE and RDE have the highest classification and identification ratio of 100%, and WPE has the lowest one of 58.75%; for 147, SloE and FDE have the highest classification and identification ratio of 100%, and RDE has the lowest one of 57.5%; for the six types of signals, SloE has the maximum average identification ratio of 97.71%. The mean identification ratios of the other five kinds of entropy are lower than 85%.

The results show that the SloE classification of six kinds of signal samples is the most accurate, and the average identification ratio is the highest.

5. Conclusions

SloE is applied to the field of bearing fault diagnosis, and a new method of extracting features is put forward. The practicability of the proposed method is proved by the feature distribution and the recognition distribution of the six types of measured bearing signals. The main innovations and conclusions are as follows.

(1) SloE is applied to the field of bearing fault diagnosis for the first time.

(2) A new single feature extraction method based on SloE is proposed, and all methods in the paper adopt single feature extraction, which saves a lot of time.

(3) The proposed single feature extraction method based on SloE in this paper has larger AMMD than the single feature extraction method of the six signals based on PE, WPE, DE, FDE, and RDE, which proves that the interclass separability of SloE is better. Moreover, it has the highest average identification ratio of 97.71%, which is higher by at least 13.54% than the others of the other five kinds of entropy.

Data Availability

The data supporting the findings of this study are available within the reference [49].

Conflicts of Interest

The authors declare that they have no conflicts of interest.

References

[1] Z. Chen, A. Mauricio, W. Li, and K. Gryllias, "A deep learning method for bearing fault diagnosis based on cyclic spectral coherence and convolutional neural networks," *Mechanical Systems and Signal Processing*, vol. 140, Article ID 106683, 2020.

[2] K. Kaplan, K. Y. Lmaz, K. Melih, M. N. M. Recep, and E. H. Metin, "An improved feature extraction method using texture analysis with LBP for bearing fault diagnosis," *Applied Soft Computing*, vol. 87, Article ID 106019, 2020.

[3] S. Haidong, C. Junsheng, J. Hongkai, Y. Yu, and W. Zhantao, "Enhanced deep gated recurrent unit and complex wavelet packet energy moment entropy for early fault prognosis of bearing," *Knowledge-Based Systems*, vol. 188, Article ID 105022, 2020.

[4] Y. Li, S. Wang, and Z. Deng, "Intelligent fault identification of rotary machinery using refined composite multi-scale Lempel-Ziv complexity," *Journal of Manufacturing Systems*, vol. 61, pp. 725–735, 2021.

[5] B. Cai, H. Liu, and M. Xie, "A real-time fault diagnosis methodology of complex systems using object-oriented Bayesian networks," *Mechanical Systems and Signal Processing*, vol. 80, pp. 31–44, 2016.

[6] Y. Li, X. Wang, Z. Liu, X. Liang, and S. Si, "The entropy algorithm and its variants in the fault diagnosis of rotating machinery: a review," *IEEE Access*, vol. 6, Article ID 66723, 2018.

[7] T. Han, C. Liu, L. Wu, S. Sarkar, and D. Jiang, "An adaptive spatiotemporal feature learning approach for fault diagnosis in complex systems," *Mechanical Systems and Signal Processing*, vol. 117, pp. 170–187, 2019.

[8] T. Han, Y. Li, and M. Qian, "A hybrid generalization network for intelligent fault diagnosis of rotating machinery under unseen working conditions," *IEEE Transactions on Instrumentation and Measurement*, vol. 70, Article ID 3520011, 2021.

[9] A. Lempel and J. Ziv, "On the complexity of finite sequences," *IEEE Transactions on Information Theory*, vol. 22, no. 1, pp. 75–81, 1976.

[10] Z. Zhang, A. Verma, and A. Kusiak, "Fault analysis and condition monitoring of the wind turbine gearbox," *IEEE Transactions on Energy Conversion*, vol. 27, no. 2, pp. 526–535, 2012.

[11] L. Zhang, J. Lin, and R. Karim, "Adaptive kernel density-based anomaly detection for nonlinear systems," *Knowledge-Based Systems*, vol. 139, pp. 50–63, 2018.

[12] M. Zair, C. Rahmoune, and D. Benazzouz, "Multi-fault diagnosis of rolling bearing using fuzzy entropy of empirical mode decomposition, principal component analysis, and SOM neural network," *Proceedings of the Institution of Mechanical Engineers - Part C: Journal of Mechanical Engineering Science*, vol. 233, no. 9, pp. 3317–3328, 2019.

[13] C. Bandt and B. Pompe, "Permutation entropy: a natural complexity measure for time series," *Physical Review Letters*, vol. 88, Article ID 174102, 2002.

[14] Y. Yin, K. Sun, and S. He, "Multiscale permutation Rényi entropy and its application for EEG signals," *PLoS One*, vol. 13, Article ID 0202558, 2018.

[15] M. Rostaghi and H. Azami, "Dispersion entropy: a measure for time-series analysis," *IEEE Signal Processing Letters*, vol. 23, no. 5, pp. 610–614, 2016.

[16] J. S. Richman and J. R. Moorman, "Physiological time-series analysis using approximate entropy and sample entropy," *American journal of physiology. Am. J. Physiol.-Heart Circ. Physiol*, vol. 6, pp. 2039–2049, 2000.

[17] R. Ceravolo, M. Civera, E. Lenticchia, G. Miraglia, and C. Surace, "Detection and localization of multiple damages through entropy in information theory," *Applied Sciences*, vol. 13, 2021.

[18] M. Civera and C. Surace, "An application of instantaneous spectral entropy for the condition monitoring of wind turbines," *Applied Sciences*, vol. 3, 2022.

[19] Z. Jinde, C. Junsheng, and Y. Yu, "A rolling bearing fault diagnosis approach based on LCD and fuzzy entropy," *Mechanism and Machine Theory*, vol. 70, pp. 441–453, 2013.

[20] L. Tylová, J. Kukal, V. Hubata-Vacek, and O. Vyšata, "Unbiased estimation of permutation entropy in EEG analysis for Alzheimer's disease classification," *Biomedical Signal Processing and Control*, vol. 39, pp. 424–430, 2018.

[21] D. Xie, S. Hong, and C. Yao, "Optimized variational mode decomposition and permutation entropy with their application in feature extraction of ship-radiated noise," *Entropy*, vol. 23, 2021.

[22] C. Bandt, "A new kind of permutation entropy used to classify sleep stages from invisible EEG microstructure," *Entropy*, vol. 19, 2017.

[23] J. Qu, C. Shi, F. Ding, and W. Wang, "A novel aging state recognition method of a viscoelastic sandwich structure based on permutation entropy of dual-tree complex wavelet packet transform and generalized Chebyshev support vector machine," *Structural Health Monitoring*, vol. 19, no. 1, pp. 156–172, 2020.

[24] D. Li, X. Li, Z. Liang, L. J. Voss, and J. W. Sleigh, "Multiscale permutation entropy analysis of EEG recordings during sevoflurane anesthesia," *Journal of Neural Engineering*, vol. 7, Article ID 046010, 2010.

[25] H. Azami and J. Escudero, "Improved multiscale permutation entropy for biomedical signal analysis: interpretation and application to electroencephalogram recordings," *Biomedical Signal Processing and Control*, vol. 23, pp. 28–41, 2016.

[26] Z. Jinde, P. Haiyang, T. Jinyu, and L. Qingyun, *Generalized Refined Composite Multiscale Fuzzy Entropy and Multi-Cluster Feature Selection Based Intelligent Fault Diagnosis of Rolling Bearing*, ISA Trans, Beaumont de, France, 2021.

[27] J. Zheng, J. Cheng, Y. Yang, and S. Luo, "A rolling bearing fault diagnosis method based on multi-scale fuzzy entropy and variable predictive model-based class discrimination," *Mechanism and Machine Theory*, vol. 78, pp. 187–200, 2014.

[28] F. Xu and P. W. Tse, "A method combining refined composite multiscale fuzzy entropy with PSO-SVM for roller bearing fault diagnosis," *Journal of Central South University*, vol. 26, no. 9, pp. 2404–2417, 2019.

[29] J. Zheng and H. Pan, "Use of generalized refined composite multiscale fractional dispersion entropy to diagnose the faults of rolling bearing," *Nonlinear Dynamics*, vol. 101, no. 2, pp. 1417–1440, 2020.

[30] M. Rostaghi, M. R. Ashory, and H. Azami, "Application of dispersion entropy to status characterization of rotary machines," *Journal of Sound and Vibration*, vol. 438, pp. 291–308, 2019.

[31] W. Zhang and J. Zhou, "A comprehensive fault diagnosis method for rolling bearings based on refined composite multiscale dispersion entropy and fast ensemble empirical mode decomposition," *Entropy*, vol. 21, 2019.

[32] H. Azami, M. Rostaghi, D. Abasolo, and J. Escudero, "Refined composite multiscale dispersion entropy and its application to biomedical signals," *IEEE Transactions on Biomedical Engineering*, vol. 64, pp. 2872–2879, 2017.

[33] Y. Li, X. Gao, and L. Wang, "Reverse dispersion entropy: a new complexity measure for sensor signal," *Sensors*, vol. 19, 2019.

[34] Y.-x. Li, S.-b. Jiao, and X. Gao, "A novel signal feature extraction technology based on empirical wavelet transform and reverse dispersion entropy," *Defence Technology*, vol. 17, no. 5, pp. 1625–1635, 2021.

[35] Y. Li, S. Jiao, B. Geng, and Y. Zhou, "Research on feature extraction of ship-radiated noise based on multi-scale reverse dispersion entropy," *Applied Acoustics*, vol. 173, Article ID 107737, 2021.

[36] H. Azami and J. Escudero, "Amplitude- and fluctuation-based dispersion entropy," *Entropy*, vol. 20, 2018.

[37] Z. Li, Y. Li, and K. Zhang, "A feature extraction method of ship-radiated noise based on fluctuation-based dispersion entropy and intrinsic time-scale decomposition," *Entropy*, vol. 21, 2019.

[38] B. Fadlallah, B. Chen, A. Keil, and J. Príncipe, "Weighted-permutation entropy: a complexity measure for time series incorporating amplitude information," *Physical review. E, Statistical, nonlinear, and soft matter physics*, vol. 87, Article ID 022911, 2013.

[39] B. Deng, L. Cai, S. Li et al., "Multivariate multi-scale weighted permutation entropy analysis of EEG complexity for Alzheimer's disease," *Cognitive Neurodynamics*, vol. 11, no. 3, pp. 217–231, 2017.

[40] W. Zhenya, Y. Ligang, C. Gang, and D. Jiaxin, "Modified multiscale weighted permutation entropy and optimized support vector machine method for rolling bearing fault diagnosis with complex signals," *ISA Transactions*, vol. 114, pp. 470–480, 2021.

[41] Y. Li, X. Liang, Y. Wei, and X. Wang, "A method based on refined composite multi-scale symbolic dynamic entropy and ISVM-BT for rotating machinery fault diagnosis," *Neurocomputing*, vol. 315, pp. 246–260, 2018.

[42] Z. Wang, L. Yao, and Y. Cai, "Rolling bearing fault diagnosis using generalized refined composite multiscale sample entropy and optimized support vector machine," *Measurement*, vol. 156, Article ID 107574, 2020.

[43] S. Jiao, B. Geng, and Y. Li, "Fluctuation-based reverse dispersion entropy and its applications to signal classification," *Applied Acoustics*, vol. 175, no. 4, Article ID 107857, 2021.

[44] L. Yongjian, S. Hao, M. Bingrong, Z. Weihua, and X. Qing, "Improved multiscale weighted-dispersion entropy and its application in fault diagnosis of train bearing," *Measurement Science and Technology*, vol. 32, Article ID 075002, 2021.

[45] D. Cuesta-Frau, "Slope entropy: a new time series complexity estimator based on both symbolic patterns and amplitude information," *Entropy*, vol. 21, 2019.

[46] D. Cuesta-Frau, P. H. Dakappa, C. Mahabala, and A. R. Gupta, "Fever time series analysis using slope entropy. Application to early unobtrusive differential diagnosis," *Entropy*, vol. 22, 2020.

[47] D. Cuesta-Frau, J. Schneider, E. Bakštein, P. Vostatek, F. Spaniel, and D. Novák, "Classification of actigraphy records from bipolar disorder patients using slope entropy: a feasibility study," *Entropy*, vol. 22, 2020.

[48] Y. Li, P. Gao, and B. Tang, "Double feature extraction method of ship-radiated noise signal based on slope entropy and permutation entropy," *Entropy*, vol. 24, no. 1, 2022.

[49] Case Western Reserve University, "Bearing data center," 2021, https://engineering.case.edu/bearingdatacenter/pages/welcome-case-western-reserve-university-bearing-data-center-website.

Hindawi
Shock and Vibration
Volume 2022, Article ID 3238461, 10 pages
https://doi.org/10.1155/2022/3238461

Research Article

Feature Extraction of Ship-Radiated Noise Based on Hierarchical Dispersion Entropy

Leilei Xiao

Xi'an Traffic Engineering Institute, Xi'an, Shaanxi 710300, China

Correspondence should be addressed to Leilei Xiao; dierxiaoleilei1982@163.com

Received 9 April 2022; Revised 30 April 2022; Accepted 13 May 2022; Published 28 May 2022

Academic Editor: Yuxing Li

The classification and recognition of ship-radiated noise (SRN) is of great significance to the processing of underwater acoustic signals. In order to improve the stability of recognition and more accurately identify SRN, single feature extraction and dual feature extraction based on hierarchical dispersion entropy (HDE) are proposed. For single feature extraction, HDE of the best node among the eight nodes of the third layer decomposition is extracted. For dual feature extraction, HDE of the best two nodes among the 14 nodes of the first-, second-, and third-layer decompositions are required. The results show that the recognition rate of single and dual feature extraction originated from the method based on HDE reaches 85% and 100%, respectively, better than the method of hierarchical reverse dispersion entropy (HRDE) and hierarchical permutation entropy (HPE).

1. Introduction

SRN is the signal generated by engine vibration during ship navigation, which contains a lot of feature information about the ship underway [1–3]. The commonly used features are time-domain features [4], frequency-domain features [5], and auditory features [6]. However, affected by the complex marine environment, the collected SRN signals often have the characteristics of nonlinearity and nonstationary, and the traditional features cannot guarantee the separability and stability [7–12]. Therefore, it is very important to find a feature suitable for characterizing the SRN.

In recent years, the characteristics of nonlinear dynamics have attracted many scholars' attention because of their advantages in representing nonlinear signals. The commonly used nonlinear dynamics features include Lyapunov index [13], fractal dimension [14], Lempel-Ziv complexity [15, 16] and entropy algorithm [17], among which entropy algorithm can be used to represent the amount of information in a period of time, and has been widely used in many fields due to its simplicity of calculation [18, 19]. In 2002, Bandt and Pompe first proposed permutation entropy (PE) and applied it to the detection of biomedical signals [20]. Later, Li et al. improved PE and applied it to the feature extraction of SRN signals, and achieved good results in classification [8]. In 2016, Rostaghi and Azami proposed dispersion entropy (DE) to solve the defect that PE did not take into account the relationship between the amplitudes of time series [21]. Later, Jiao et al. proposed Fluctuation-based reverse dispersion entropy (FRDE) on the basis of DE, which was used in ship signal classification and achieved high recognition rate [22]. In 2019, Cuesta Frau proposed slope entropy (SlEn) based on relative frequency of simple symbol patterns [23], after that, Li combined SlEn with PE to improve the classification and recognition rate of ship signals through the double feature extraction method [24]. In conclusion, it is of great significance to further extract the features of SRN signals based on entropy.

Although these aforementioned entropies have achieved good results in feature extraction of SRN, they all ignore the hierarchical information between signals. HDE can obtain the hierarchical information of signals obtained in the full frequency band. Xue et al. applied HDE to the field of rolling bearing fault diagnosis [25], Ke et al. applied HDE to the weak fault diagnosis scheme of common rail injectors [26], and Song et al. also applied HDE to the fault diagnosis of high pressure common rail injectors [27], and all these paper have achieved good results. Influenced by that, HDE is

applied to SRN recognition in this paper, which fills the gap of HDE application in underwater acoustic field.

In this paper, HDE is introduced into the field of underwater acoustics to identify and classify SRN, hierarchical decomposition of SRN is carried out, and DE features are extracted from the obtained nodes. Section 2 introduces HDE, including hierarchical decomposition and DE. Section 3 represents the proposed method. Section 4 illustrates feature extraction of SRN. Section 5 shows some conclusions obtained from the experiment.

2. Methodology

2.1. Hierarchical Decomposition

(1) For a time series $\{u(i), i = 1, 2, \ldots, N\}$, define the two operators Q_0 and Q_1, as

$$\begin{aligned} Q_0(u) &= \frac{u(2j) + u(2j+1)}{2}, \quad j = 1, 2, \ldots, 2^{n-1}, \\ Q_1(u) &= \frac{u(2j) - u(2j+1)}{2}, \quad j = 1, 2, \ldots, 2^{n-1}, \end{aligned} \tag{1}$$

where $Q_0(u)$ and $Q_1(u)$ represent the low and high-frequency components of signal decomposition; for $j = 0, 1$ the matrix form of Q_j can be shown as

$$Q_j = \begin{pmatrix} \frac{1}{2}\left(-\frac{1}{2}\right)^j & 0 & 0 & \cdots & 0 & 0 \\ 0 & 0 & \frac{1}{2}\left(-\frac{1}{2}\right)^j & \cdots & 0 & 0 \\ 0 & 0 & 0 & 0 & \cdots & \frac{1}{2}\left(-\frac{1}{2}\right)^j \end{pmatrix}_{2^{n-1} \times 2^n}. \tag{2}$$

(2) Construct an n-dimensional vector $[\gamma_1, \gamma_2, \ldots, \gamma_n] \in \{0, 1\}$, the integer e can be expressed as

$$e = \sum_{j=1}^{n} \gamma_j 2^{n-j}. \tag{3}$$

(3) According to vector $[\gamma_1, \gamma_2 \ldots, \gamma_n]$, the decomposition nodes of each layer of the signal are

$$u_{k,e} = Q_{\gamma_n} \cdot Q_{\gamma_{n-1}} \cdot \cdots Q_{\gamma_1}(u). \tag{4}$$

2.2. Hierarchical Dispersion Entropy. DE is an index to measure the irregularity of time series. A larger value of this indicates a higher irregularity of this time series. On the contrary, a smaller value means a smaller irregularity.

For a time series $\{x(i), i = 1, 2, \ldots, N\}$, the DE was calculated as follows:

(1) Mapping time series $x(i)$ to $\{x(j), j = 1, 2, \ldots, N\}$ through a normal distribution function, $y(j) \in (0, 1)$

$$y(j) = \frac{1}{\sigma\sqrt{2\pi}} \int_{-\infty}^{x(i)} e^{\left(-(t-\mu)^2/2\sigma^2\right)} \mathrm{d}t, \tag{5}$$

where μ and σ represent the expectation and variance of x, respectively.

(2) Mapping $y(j)$ to an integer between 1 and c by the following formula:

$$z_j^c = \mathrm{Round}(c \cdot y(j) + 0.5), \tag{6}$$

where Round is an integer function and c is the number of mapped categories.

(3) Calculating embedded vector $z_i^{m,c}$,

$$z_i^{m,c} = \left\{z_i^c, z_{i+d}^c, \ldots, z_{i+(m-1)d}^c\right\}, \tag{7}$$

where m is the embedded dimension and d is the time delay constant.

(4) Calculating the dispersion pattern $\pi_{v_0 v_1 \ldots v_{m-1}}$ $(v = 1, 2, \ldots c)$ for each time series $z_i^{m,c}$, the number of dispersion patterns are c^m, $z_i^c = v_0, z_{i+d}^c = v_1, \cdots z_{i+(m-1)d}^c = v_{m-1}$.

(5) For these patterns, the probability $p(\pi_{v_0 v_1 \ldots v_{m-1}})$ of each dispersion pattern $\pi_{v_0 v_1 \ldots v_{m-1}}$ is

$$p\left(\pi_{v_0 v_1 \ldots v_{m-1}}\right) = \frac{\mathrm{Number}\left(\pi_{v_0 v_1 \ldots v_{m-1}}\right)}{N - (m-1)d}, \tag{8}$$

where $\mathrm{Number}(\pi_{v_0 v_1 \ldots v_{m-1}})$ is the number of dispersion patterns.

(6) DE of time series is defined as

$$DE(x, m, c, d) = -\sum_{\pi=1}^{c^m} p\left(\pi_{v_0 v_1 \ldots v_{m-1}}\right) \ln\left(p\left(\pi_{v_0 v_1 \ldots v_{m-1}}\right)\right). \tag{9}$$

For each node obtained by hierarchical decomposition, its DE is calculated, and all the results obtained are HDE.

3. Proposed Method

This paper recognizes SRN by extracting HDE feature of the signal, and two feature extraction methods, single feature extraction and dual feature extraction are used. The method of identifying SRN using HDE features is shown in Figure 1. The specific steps for single feature extraction are as follows:

(1) Input SRN as the signal to be identified.

(2) Hierarchical decomposition of the signal at the third level, the signal is decomposed into eight nodes.

(3) Selecting the optimal node and calculating its DE as the feature of SRN.

(4) Classify and recognize the obtained features by k-nearest neighbor (KNN) to get the recognition result of the signal.

Dual feature extraction and single feature extraction are the same except for the second and third steps; in the second

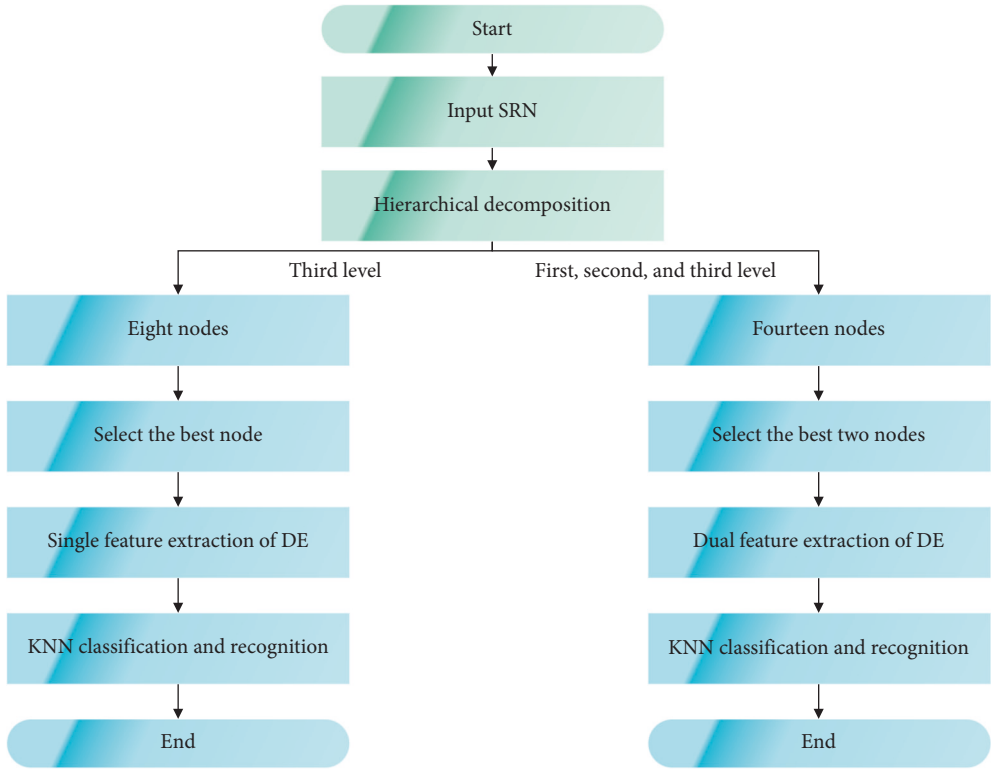

Figure 1: The method of identifying SRN using HDE features.

step, dual feature extraction requires fourteen nodes derived from the first-, second-, and third-level decomposition of the signal; in the third step, two optimal nodes are selected.

4. Feature Extraction of Ship-Radiated Noise

4.1. Ship-Radiated Noise. Feature extraction and classification recognition of four types of SRN are carried out. These four types of signals are identified as SRN1, SRN2, SRN3, and SRN4. The signal lengths of the first and second types are 1380000, the third type are 2828835, and the fourth type are 1641600, and the sampling frequency is 44.1 kHz. Take data points from 1 to 1200000 of the four types of SRN. Figure 2 presents four types of SRN after normalization.

4.2. Feature Extraction Experiment

4.2.1. Single Feature Extraction. In this section, we extract the features of four types of SRN. First, hierarchical decomposition of SRN is carried out, then take eight nodes of the third-level decomposition and extract their DE features. This is called HDE of the third-level decomposition of SRN. Then, as a comparison, we extract the reverse dispersion entropy and PE of the nodes separately, these are called HRDE and HPE of the third-level decomposition, respectively.

The HDE of eight nodes for four types of SRN is extracted, and the sample distribution is observed. The HDE of eight nodes for four types of SRN is shown in Figure 3.

It can be seen from the diagram that the HDE of the four types of SRN in the Node 1 is quite different. There are duplicate parts of the HDE of SRN1 and SRN4, and the same is true of SRN2 and SRN3; there is no significant difference in HDE between the four types of SRN in Node 2 to Node 7; HDE of SRN2 in Node 8 differs significantly from the other three types. The HRDE of eight nodes for four types of SRN can be seen in Figure 4.

The results of feature extraction show that there is no obvious difference among the four types of SRN samples under the same node; the difference of HRDE is obvious only under Node1; of the remaining seven nodes, a few samples of SRN 3 had significant differences in HRDE; in Node 2, HRDE of SRN1 is somewhat different from the other three types of SRN. Figure 5 displays the HPE of eight nodes for four types of SRN.

It can be seen from the figure that there are many differences in HPE for the four types of SRN only in the first node, but the range of entropy values for each type of SRN sample still has a large repetition; the sample entropy values of SRN2 and other SRN in the eighth node are different; the entropy values of four types of SRN from Node 2 to Node 7 differ little except for a small number of samples; differences of HPE between the four types of SRN are small, making it difficult to distinguish them effectively.

4.2.2. Results of Classification. Using k-nearest neighbor to recognize the results of feature extraction, the value of K was 1. Fifty training samples are used for each type of SRN, and the rest are used as test samples to classify and identify the four types of SRN. The validity of the feature extraction method proposed in this paper is verified by comparing the

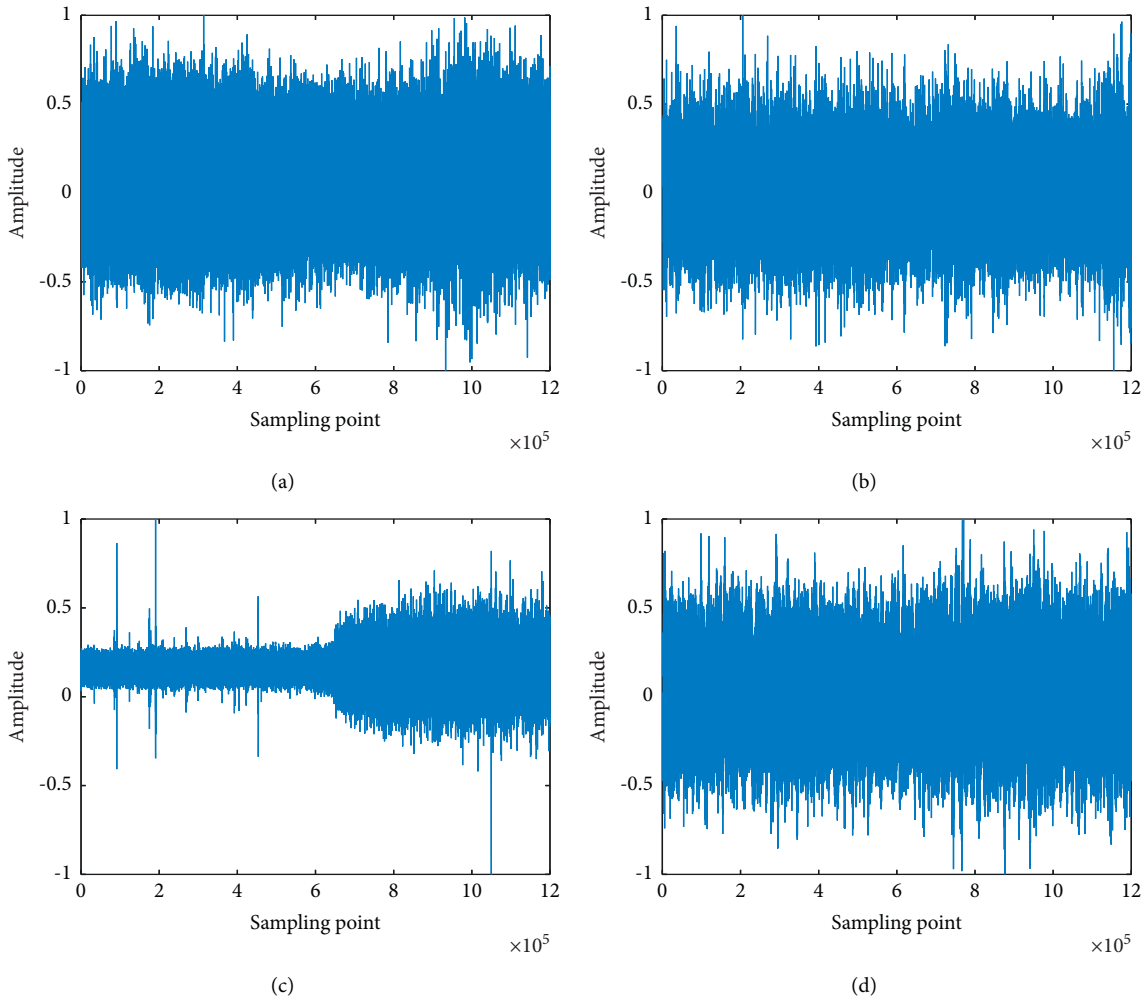

Figure 2: Four types of SRN after normalization. (a) SRN1. (b) SRN2. (c) SRN3. (d) SRN4.

recognition rates of the four feature extraction methods. The HDE recognition rate for four types of SRN is shown in Table 1.

It can be seen from Table 1 that the recognition results of four types of SRN are not good, and the highest average recognition rate is 85%; the highest recognition rate is 96% of the eight nodes for four types of SRN, and the lowest recognition rate is only 16%. The recognition rate of each node of SRN3 and SRN4 is less than 90%. Node 4 and Node 7 have recognition rates of less than 50%, and the HRDE recognition rates for four types of SRN are presented in Table 2.

As can be seen from Table 2, the HRDE of the eight nodes for four types of SRN has the highest recognition rate of 100% and the lowest recognition rate of 22%; the average recognition rate of Node 1 is 82.5%, but the average recognition rate of the remaining seven nodes is not more than 50%; the highest recognition rate of SRN2 appeared in Node 8, and the highest recognition rate of the other three types of SRN appeared in Node 1; the identification rate of all nodes in SRN3 is lower than 80%. In general, the recognition results are not good for distinguishing the four types of SRN. Table 3 shows the HPE recognition rate for four types of SRN.

According to Table 3, the results of HPE recognition of eight nodes for four types of SRN are poor, with the highest average recognition rate is only 60.5%; the recognition rate of the four types of SRN from Node 2 to Node 7 is less than 60%; in SRN2, the recognition rate of Node 1 and Node 8 is significantly higher than that of other nodes; besides SRN2, the highest recognition rate of all nodes of the three types of SRN is only 54%; it is difficult to distinguish four kinds of SRN by HPE.

Because the recognition results obtained by single feature extraction for eight nodes after three-level decomposition are not obvious, which is difficult to distinguish four types of SRN, consider adding more nodes and improving the feature extraction method. Dual feature extraction experiments are performed on fourteen nodes of the first-, second-, and third-level decomposition results.

4.3. Dual Feature Extraction Experiment. The results of hierarchical decomposition consist of fourteen nodes, third-level decomposition as the first to eight nodes, second-level decomposition as the ninth to twelfth nodes, and first-level decomposition as the thirteenth and fourteenth nodes.

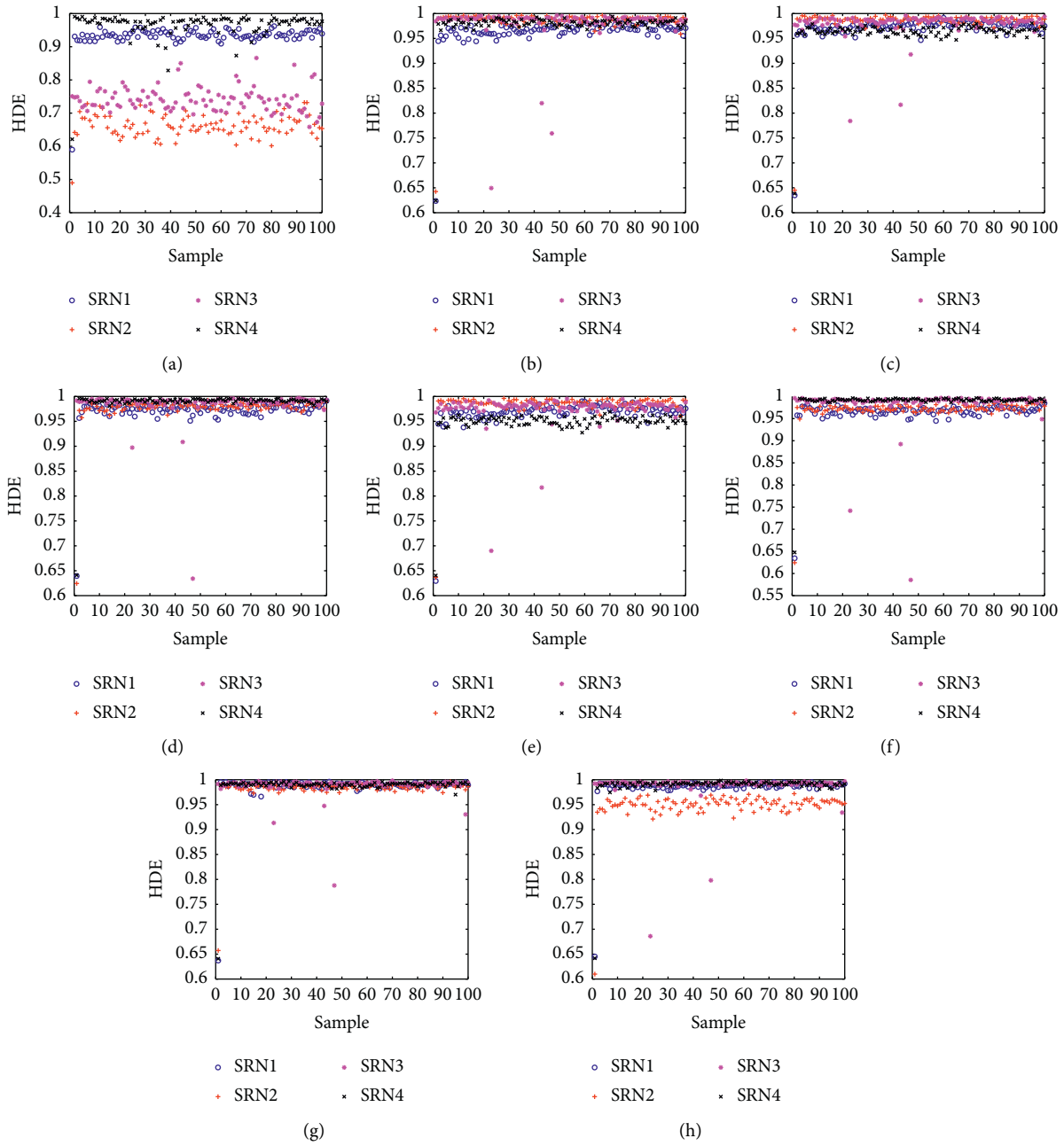

Figure 3: HDE of eight nodes for four types of SRN. (a) Node 1. (b) Node 2. (c) Node 3. (d) Node 4. (e) Node 5. (f) Node 6. (g) Node 7. (h) Node 8.

Feature distribution and recognition rate of the optimal result of dual feature recognition of four types of SRN are shown in Figure 6 and Table 4.

From Figure 6, we can see that the dual feature distribution of the same feature of the four types of SRN is significantly different, and the general distribution range of the four types of SRN can be clearly identified besides a very small number of samples.

It can be seen from Table 4 that in the dual feature extraction experiment, the recognition effect of the HDE is the best, and the highest recognition rate reaches 100%; among the three, the HPE has the worst recognition effect, and the highest recognition rate is 98.5%; the combination with the highest HDE recognition rate is Node 6 and Node 13, and the combination with the highest HRDE and HPE recognition rate is Node 1 and Node 13.

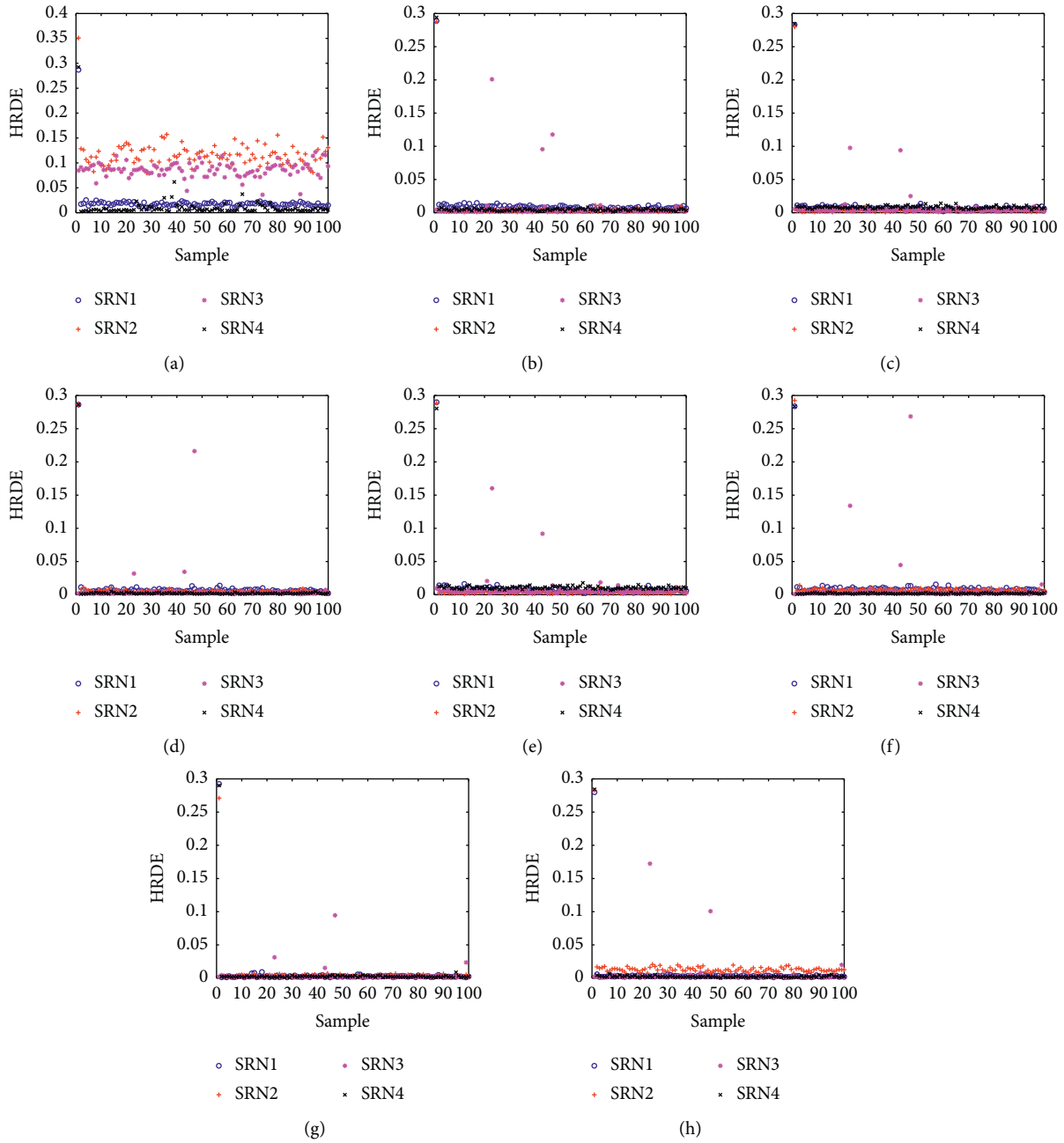

Figure 4: HRDE of eight nodes for four types of SRN. (a) Node 1. (b) Node 2. (c) Node 3. (d) Node 4. (e) Node 5. (f) Node 6. (g) Node 7. (h) Node 8.

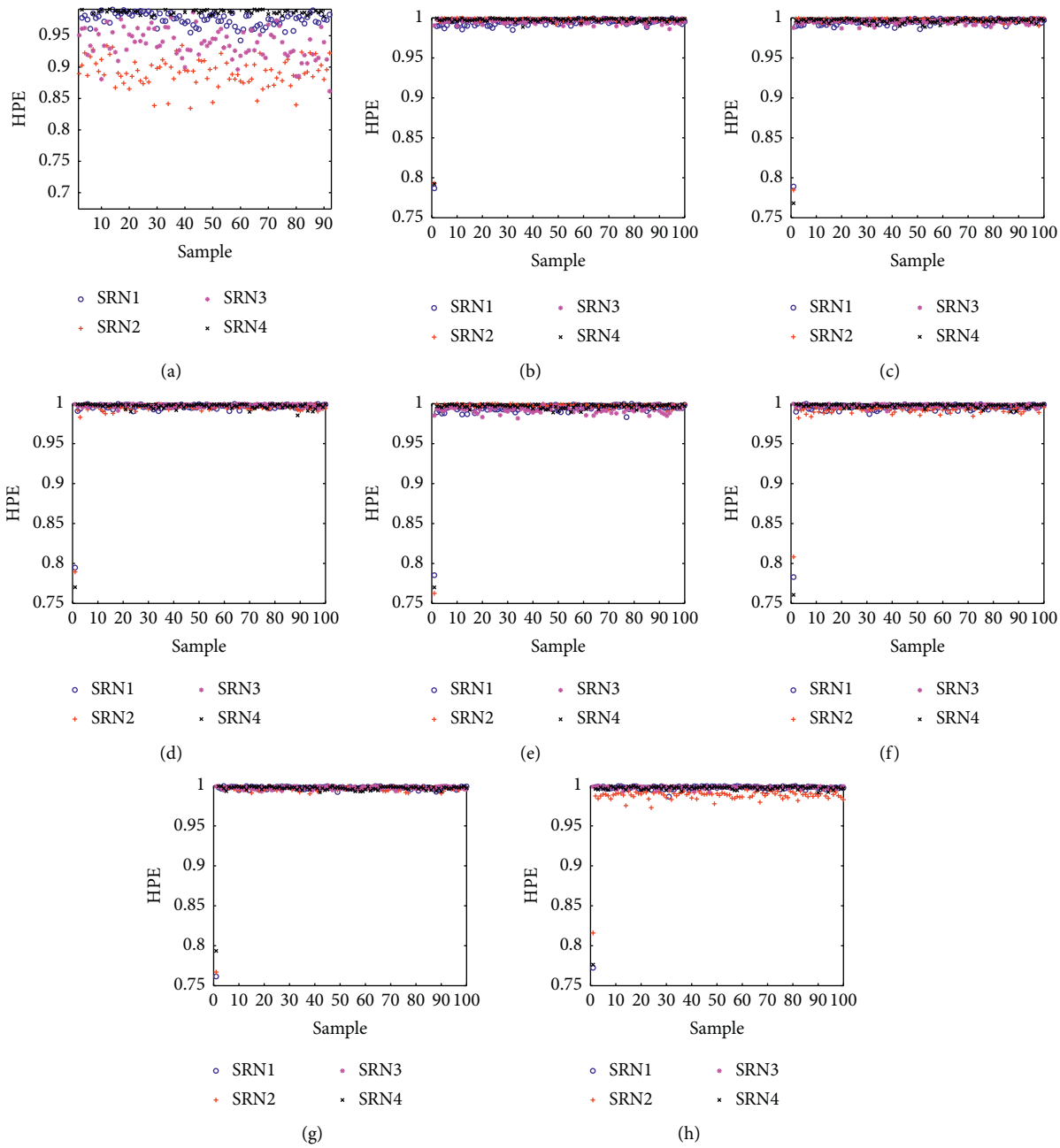

Figure 5: HPE of eight nodes for four types of SRN. (a) Node 1. (b) Node 2. (c) Node 3. (d) Node 4. (e) Node 5. (f) Node 6. (g) Node 7. (h) Node 8.

Table 1: HDE recognition rates for four types of SRN.

	SRN1 (%)	SRN2 (%)	SRN3 (%)	SRN4 (%)	Average (%)
Node 1	92	86	76	86	85
Node 2	56	42	16	52	41.5
Node 3	40	64	38	42	46
Node 4	44	36	40	38	39.5
Node 5	50	72	50	64	59
Node 6	58	34	56	52	50
Node 7	24	42	28	22	29
Node 8	48	96	38	34	54

Table 2: HRDE recognition rates for four types of SRN.

	SRN1 (%)	SRN2 (%)	SRN3 (%)	SRN4 (%)	Average (%)
Node 1	92	78	74	86	82.5
Node 2	42	40	30	46	39.5
Node 3	42	64	40	54	50
Node 4	48	26	38	56	42
Node 5	24	56	40	58	44.5
Node 6	48	48	48	56	50
Node 7	36	40	22	28	31.5
Node 8	40	100	26	32	49.5

Table 3: HPE recognition rates for four types of SRN.

	SRN1 (%)	SRN2 (%)	SRN3 (%)	SRN4 (%)	Average (%)
Node 1	54	82	54	52	60.5
Node 2	26	20	52	26	31
Node 3	26	36	18	22	25.5
Node 4	20	34	36	36	31.5
Node 5	24	56	38	22	35
Node 6	28	40	48	30	36.5
Node 7	36	24	20	24	26
Node 8	34	80	32	36	45.5

Table 4: Recognition rate of the optimal result of dual feature recognition for four types of SRN.

	HDE	HRDE	HPE
Recognition rate	100%	99%	98.5%
Node	6, 13	1, 13	1, 13

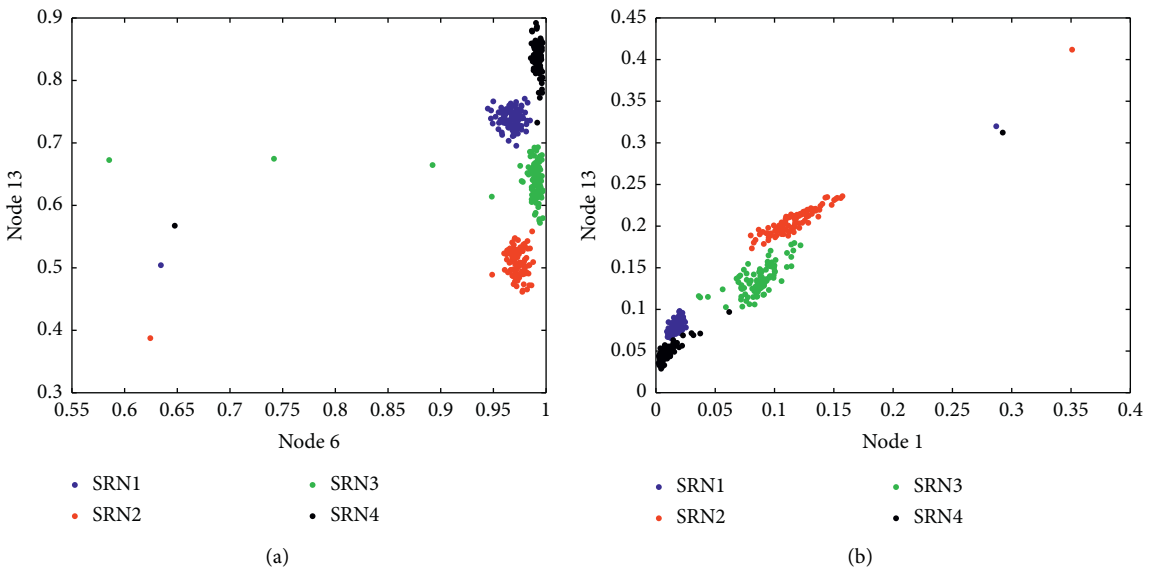

Figure 6: Continued.

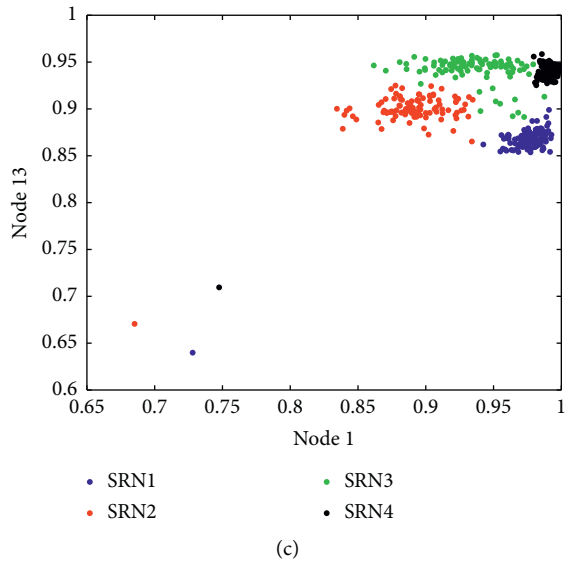

(c)

Figure 6: Feature distribution of the optimal result of dual feature recognition for four types of SRN. (a) HDE. (b) HRDE. (c) HPE.

5. Conclusions

In this paper, HDE is introduced into the feature extraction field of SRN, and single feature extraction and double feature extraction methods based on HDE are proposed. The final recognition rate reaches 100%, which verifies the effectiveness of HDE, and the main conclusions of the experiments are as follows:

(1) HDE can show the high-frequency and low-frequency feature of signals, and it is often used in fault diagnosis of rolling bearings. This paper introduces it into the field of SRN recognition as a new feature of SRN.

(2) Compared with the extractions of HRDE and HPE, the recognition result of HDE single feature recognition can better distinguish SRN.

(3) In order to further improve the performance of HDE in feature extraction, a dual feature extraction method is proposed. The recognition rate is significantly improved compared with the single feature, and the recognition effect is better than the dual feature recognition of the other two feature extraction methods.

Data Availability

The data that support the findings of this study are available on request from the corresponding author.

Conflicts of Interest

The authors declare that they have no conflicts of interest.

References

[1] S. Wang and X. Zeng, "Robust underwater noise targets classification using auditory inspired time frequency analysis," *Applied Acoustics*, vol. 78, no. 4, pp. 68–76, 2014.

[2] F. Yuan, X. Ke, and E. Cheng, "Joint representation and recognition for ship-radiated noise based on multimodal deep learning," *Journal of Marine Science and Engineering*, vol. 7, no. 11, p. 380, 2019.

[3] S. Shen, H. Yang, and M. Sheng, "Compression of a deep competitive network based on mutual information for underwater acoustic targets recognition," *Entropy*, vol. 20, no. 4, p. 243, 2018.

[4] W. Zhao, J. Yang, Z. Hu, and L. Tao, "Coupled analysis of nonlinear sloshing and ship motions," *Applied Ocean Research*, vol. 47, pp. 85–97, 2014.

[5] A. Banazadeh, M. S. Seif, M. J. Khodaei, and M. Rezaie, "Identification of the equivalent linear dynamics and controller design for an unmanned underwater vehicle," *Ocean Engineering*, vol. 139, pp. 152–168, 2017.

[6] J. Li and H. Yang, "The underwater acoustic target timbre perception and recognition based on the auditory inspired deep convolutional neural network," *Applied Acoustics*, vol. 182, Article ID 108210, 2021.

[7] Y. Li, X. Chen, and J. Yu, "A hybrid energy feature extraction approach for ship-radiated noise based on CEEMDAN combined with energy difference and energy entropy," *Processes*, vol. 7, no. 2, p. 69, 2019.

[8] Y.-X. Li, Y.-A. Li, Z. Chen, and X. Chen, "Feature extraction of ship-radiated noise based on permutation entropy of the intrinsic mode function with the highest energy," *Entropy*, vol. 18, no. 11, p. 393, 2016.

[9] D. Xie, H. Esmaiel, H. Sun, J. Qi, and Z. A. H. Qasem, "Feature extraction of ship-radiated noise based on enhanced variational mode decomposition, normalized correlation coefficient and permutation entropy," *Entropy*, vol. 22, no. 4, p. 468, 2020.

[10] Y. Li, Y. Li, X. Chen, and J. Yu, "Denoising and feature extraction algorithms using NPE combined with VMD and their applications in ship-radiated noise," *Symmetry*, vol. 9, no. 11, p. 256, 2017.

[11] Y. Li, C. Xiao, and Y. Jing, "The data-driven optimization method and its application in feature extraction of ship-radiated noise with sample entropy," *Energies*, vol. 12, no. 3, p. 356, 2019.

[12] Y. Li, X. Chen, J. Yu, and X. Yang, "A fusion frequency feature extraction method for underwater acoustic signal based on variational mode decomposition, duffing chaotic oscillator

and a kind of permutation entropy," *Electronics*, vol. 8, no. 1, p. 61, 2019.

[13] K. Tee, S. Ge, and E. Tay, "Barrier lyapunov functions for the control of output-constrained nonlinear systems," *IFAC Proceedings Volumes*, vol. 46, no. 20, pp. 449–455, 2013.

[14] R. Lopes and N. Betrouni, "Fractal and multifractal analysis: a review," *Medical Image Analysis*, vol. 13, no. 4, pp. 634–649, 2009.

[15] X. Zhang, R. Roy, and E. Jensen, "EEG complexity as a measure of depth of anesthesia for patients," *IEEE Transactions on Biomedical Engineering*, vol. 48, no. 12, pp. 1424–1433, 2001.

[16] M. Aboy, R. Hornero, D. Abasolo, and D. Alvarez, "Interpretation of the lempel-ziv complexity measure in the context of biomedical signal analysis," *IEEE Transactions on Biomedical Engineering*, vol. 53, no. 11, pp. 2282–2288, 2006.

[17] C. E. Shannon, "A mathematical theory of communication," *Bell System Technical Journal*, vol. 27, no. 4, pp. 623–656, 1948.

[18] S. M. Pincus, "Approximate entropy as a measure of system complexity," *Proceedings of the National Academy of Sciences*, vol. 88, no. 6, pp. 2297–2301, 1991.

[19] Y. Li, X. Gao, and L. Wang, "Reverse dispersion entropy: a new complexity measure for sensor signal," *Sensors*, vol. 19, no. 23, Article ID 5203, 2019.

[20] C. Bandt and B. Pompe, "Permutation entropy: a natural complexity measure for time series," *Physical Review Letters*, vol. 88, no. 17, Article ID 174102, 2002.

[21] M. Rostaghi and H. Azami, "Dispersion entropy: a measure for time-series analysis," *IEEE Signal Processing Letters*, vol. 23, no. 5, pp. 610–614, 2016.

[22] S. Jiao, B. Geng, Y. Li, Q. Zhang, and Q. Wang, "Fluctuation-based reverse dispersion entropy and its applications to signal classification," *Applied Acoustics*, vol. 175, no. 4, Article ID 107857, 2021.

[23] D. Cuesta-Frau, "Slope entropy: a new time series complexity estimator based on both symbolic patterns and amplitude information," *Entropy*, vol. 21, no. 12, p. 1167, 2019.

[24] Y. Li, P. Gao, B. Tang, Y. Yi, and J. Zhang, "Double feature extraction method of ship-radiated noise signal based on slope entropy and permutation entropy," *Entropy*, vol. 24, no. 1, p. 22, 2021.

[25] Q. Xue, B. Xu, C. He et al., "Feature extraction using hierarchical dispersion entropy for rolling bearing fault diagnosis," *IEEE Transactions on Instrumentation and Measurement*, vol. 70, pp. 1–11, 2021.

[26] Y. Ke, C. Yao, and E. Song, "A weak fault diagnosis scheme for common rail injector based on MGOA-MOMEDA and improved hierarchical dispersion entropy," *Measurement Science and Technology*, vol. 32, no. 2, Article ID 025012, 2021.

[27] E. Song, Y. Ke, C. Yao, Q. Dong, and L. Yang, "fault diagnosis method for high-pressure common rail injector based on IFOA-VMD and hierarchical dispersion entropy," *Entropy*, vol. 21, no. 10, p. 923, 2019.

Hindawi
Shock and Vibration
Volume 2022, Article ID 6266671, 34 pages
https://doi.org/10.1155/2022/6266671

Research Article

Rotating Machinery Fault Diagnosis Using HHO-RSSD and RCGmvMAAPE

Ning Zhang

School of Naval Architecture, Ocean and Energy Power Engineering, Wuhan University of Technology, Wuhan 430070, China

Correspondence should be addressed to Ning Zhang; qq081100@yandex.com

Received 22 December 2021; Revised 19 January 2022; Accepted 9 February 2022; Published 15 March 2022

Academic Editor: Yuxing Li

Rotating machinery has played an enormous role in industrial production, and its stable operation is related to whether production can proceed smoothly. At present, multichannel entropy-based methods are usually be adopted to analyze multichannel vibration signals. However, the collected signal may only have one channel in the actual situation. At this time, analyzing only a single channel signal cannot effectively utilize the advantages of multivariate analysis. For this reason, this paper presents a novel multivariate analysis approach and applies it to the fault diagnosis of machinery. Firstly, the parameter-optimized resonance sparse decomposition (RSSD) algorithm is adopted to decompose the single-channel vibration signal into high and low resonance components. Then, the two components are regarded as dual-channel vibration signals and input into the refined composite generalized multivariate multiscale amplitude aware permutation entropy (RCGmvMAAPE) method to gain fault features. Eventually, the features are input to the deep belief network (DBN) classifier to perform fault judgment. The experiments of rotating machinery are carried to verify the effectiveness of the developed approach. The results display that the proposed fault diagnosis method can achieve the classification accuracy of 100% and 98% when only a single-channel vibration signal is used, which is better than the fault diagnosis method based on a multichannel vibration signal and enjoys strong stability.

1. Introduction

Rotating machinery is the most widely adopted mechanical equipment in the industrial sector. However, since the working environment of rotating machinery is mostly harsh, various types of faults are prone to occur, resulting in serious personal and property losses [1, 2]. Therefore, it is necessary to study the general diagnostic techniques for rotating machinery. The internal structure of the rotating machinery will change if there are the faults, which exacerbate internal vibration. Consequently, the vibration signal of the rotating machinery contains information that can characterize the current state, which indicates that the signals can be used for analysis to determine the present status [3, 4].

The operating conditions of rotating machinery can be characterized by vibration during operation, but the vibration is nonlinear data [5]. In order to extract the state feature from the vibration data, effective methods must be adopted to amplify the characteristic information and eliminate the interference [6]. Signal decomposition algorithms are typical methods for processing this kind of signals. By decomposing raw signal into several components, these methods analyze the complexity of the signal on multiple time scales and reduce the interference of disturbance components such as noise on feature extraction [7]. In the current signal decomposition algorithms, the more typical ones include wavelet transform (WT) and empirical mode decomposition (EMD). Both of the above two algorithms have obvious defects, which affect the reliability of analysis. For example, WT cannot analyze the high frequency components. In addition, it lacks ability to adaptively process signals since its reliability is influenced by the wavelet basis function. EMD decomposes the signal based on the local characteristics of the signal itself, so it can realize the analysis without manually setting parameters, thereby has the advantage of adaptive analysis. However, EMD has serious modal aliasing and end effect defects, and the

physical meaning of some components is not obvious, which affects its reliability [8].

Resonance-based sparse signal decomposition (RSSD) is a signal decomposition method based on resonance properties of signals, which can realize accurate analysis and complexity measurement for nonlinear signals with complex components [9, 10]. Based on the tunable Q-factor wavelet transform (TQWT), RSSD uses the difference of quality factor Q between the continuous oscillation signal and the transient impact component to represent the complex signal sparsely with high quality factor and low quality factor [11]. Different from signal decomposition approaches based on frequency or time scale such as EMD, RSSD combines the frequency and bandwidth of the signal simultaneously, so it can perfectly separate the periodic pulse component and the transient nonoscillating component in the vibration signal [12]. Based on different quality factors, the approach divides the composition of the signal into periodic harmonics, fault impact, and noise and divides them into high resonance components and low resonance components [13]. Therefore, the RSSD algorithm has a significant advantage for analyzing the impact fault signals. Nevertheless, the excellent performance of the RSSD algorithm is influenced by the quality factor, the weight coefficient and the Lagrangian operator. The improper parameter settings will interfere with the performance of RSSD [14]. The Harris Hawk algorithm (HHO) is a novel heuristic optimization algorithm proposed by Mirjalili, which mainly simulate predation behavior of Harris Hawk in nature. Compared with several other typical optimization algorithms, the HHO algorithm performs better and has higher search efficiency [15]. Considering the excellent performance of HHO in the optimization problem, combined with the RSSD algorithm, this paper proposes an optimized RSSD based on HHO. This method not only can adaptively find the best combination of RSSD parameters, but also has high optimization efficiency and excellent generalization.

After processing the vibration signals, how to extract the highly distinguishable features is the key to the fault diagnosis of rolling bearings. With the development of nonlinear science, the feature extraction technology based on entropy theory, such as permutation entropy (PE), amplitude-aware permutation entropy (AAPE), and multiscale amplitude-aware permutation entropy (MAAPE) had been favored by a large number of researchers due to the good nonlinear data processing performance [16, 17]. Because of the good ability to extract the nonlinear fault information hidden in the vibration signal, Wu used multiscale permutation entropy (MPE) for the health detection of rolling bearings and obtained ideal results [18]. However, the permutation entropy does not consider the contribution of the amplitude of the time series to the entropy value in the calculation, which leads to inaccurate and sufficient analysis [19]. In this regard, Chen proposed multiscale AAPE (MAAPE) by replacing PE with AAPE and used it to excavate the fault characteristics of rolling bearings [20]. Although MAAPE has better feature extraction performance, there are still two shortcomings in the application process as follows: (1) the coarse-grained method adopted by MAAPE is achieved by calculating the mean value of each coarse-grained time series, which slows down the dynamic mutation trend of the original time series to some extent; (2) the stability of MAAPE will decrease significantly when the time series is short [21]. In view of the abovementioned shortcomings, this paper proposes a refined composite generalized coarse grained technology and thus proposes refined composite generalized multiscale amplitude aware permutation entropy (RCGMAAPE) method.

Although RCGMAAPE enjoys excellent performance, it is only applied to a single channel vibration data, thereby has insufficient characterization capacity for multichannel data, which reduces the quality of the fault information obtained to a certain extent [22]. Reasonable use of multiple channel fault information can achieve a more comprehensive diagnosis of rotating machinery faults. Based on the theory of multidimensional embedding reconstruction, RCGMAAPE is extended to multivariate, that is, the refined composite generalized multivariate multiscale amplitude aware permutation entropy (RCGmvMAAPE), which is adopted to realize the complexity measurement of multichannel data. At present, most of the feature extraction approaches based on vibration signals are univariate analysis techniques. These methods extract the single-entropy or multiscale entropy of multiple components to mine the fault characteristics of vibration signals, which can only effectively use the signal of a single channel. It has been proved by experiments that these methods also have good results and can achieve accurate classification of rotating machinery fault types. However, it can be noted that the features composed of multiscale entropy of multiple components usually are high-dimensional and contain more redundant information, so it is necessary to reduce the dimensionality to improve the classification efficiency and accuracy. To this end, this paper develops a new feature extraction model that can realize multivariate analysis using only a single-channel signal. The principle is to disintegrate the fault signal into a pair of high and low resonance components through the parameter optimized resonance sparse decomposition algorithm. After that, these two components are employed as multichannel data to form a multivariate signal. Finally, the proposed RCGmvMAAPE method is applied to extract the fault feature of the signal.

After obtaining the fault characteristics of rotating machinery, selecting a suitable classifier for fault identification is the very critical part. At present, the commonly used classifiers include support vector machine (SVM) and extreme learning machine (ELM), which are widely used in pattern recognition because of their good generalization and reliability. Nevertheless, the performance of SVM is easily affected by the parameters, which need to be optimized [23]. ELM has high classification efficiency and excellent performance. However, it is prone to large errors when dealing with high-dimensional nonlinear classification problems since the kernel function is not used [24]. With the continuous development of deep learning, the application of deep learning to deal with classification problems has gradually become a feasible solution. However, deep learning is mainly aimed at the classification and

identification of large batches of data, so the performance of classification problems for small samples is not as good as machine learning. Deep belief network (DBN) is an atypical structure of deep learning in the processing of small samples, which is composed of multilayer restricted Boltzmann machines [25, 26]. DBN can effectively avoid the problem of parameter selection by using pretraining and repeated fine-tuning. In addition, it can be effectively used for the pattern recognition problem of small samples, so this paper employs it for the fault recognition of rotating machinery.

In conclusion, the main contribution of this paper is to propose a new multivariate feature extraction method, RCGmvMAAPE, and apply it to the fault diagnosis of rotating machinery. In addition, considering that the vibration signal may have only one channel, it cannot effectively take advantage of the multivariate analysis method. Therefore, an optimized RSSD is proposed to convert single-channel vibration signals into dual channel signals, so as to make full use of the advantage that the multivariate analysis method can extract fault information from multichannel vibration signals synchronously. The structure of this paper is as follows: Sections 2.1 and 2.2 mainly introduce the principle of RSSD and the specific implementation process of optimized RSSD. Sections 2.3 mainly introduces the theory of RCGmvMAAPE and compares it with RCmvMPE, RCmvMSE and mvMAAPE. Sections 3 introduces the specific steps of the proposed fault diagnosis method. Sections 4 validates the effectiveness of the proposed method by using two typical rotating machinery data. Section 5 draws the conclusion of this paper.

2. Modified RSSD Method

2.1. Principle of RSSD. Resonance is a property of the signal. The larger the resonance property, the better the frequency aggregation of the signal; the smaller the resonance property, the better the time aggregation of the signal. The signal resonance sparse decomposition method sparsely decomposes a complex signal into high and low resonance components according to the different signal resonance properties. The resonance property is represented by Q, and the formula is as follows:

$$Q = \frac{f_c}{B_W}, \tag{1}$$

where f_c is the center frequency of the signal and B_W is the bandwidth.

The resonant sparse signal decomposition method combines the influence of frequency and bandwidth on the signal. It can effectively separate the signals with overlapping frequency bands and similar center frequencies using different quality factors. This method first uses the two-channel filter bank shown in Figure 1 to perform TQWT on the signal to obtain a base function library with high and low-quality factors. Here, $H_0(w)$ and $H_1(w)$ are low-pass and high-pass filters, respectively; $v_0(n)$ and $v_1(n)$ are the filtered subband signals, respectively. The low-pass scale factor α and the high-pass scale factor β can be obtained through the quality factor Q and the redundancy r, as shown in (2).

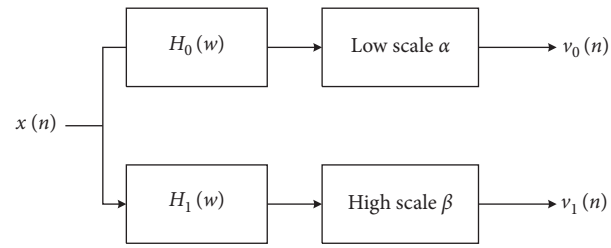

Figure 1: The two-channel filter banks.

$$\beta = \frac{2}{(Q+1)\alpha} = 1 - \frac{\beta}{r}. \tag{2}$$

Then, the corresponding coefficients were obtained by iteration, and the sparse decomposition objective function was established by morphological analysis method, as follows:

$$J(W_1, W_2) = \left\| x - S_1 W_1 - S_2 W_2 \right\|_2^2 + \lambda_1 \left\| W_1 \right\|_1 + \lambda_2 \left\| W_2 \right\|_1, \tag{3}$$

where J is the objective function; W_1 and W_2 are the transformation coefficients of the subband signals x_1 and x_2 under the frameworks S_1 and S_2, respectively; and λ_1 and λ_2 are the regularization parameters.

The different values of λ_1 and λ_2 affect the energy distribution of sparse components. If only λ_1 increases, the energy of the corresponding component of λ_1 decreases, and the same is true for λ_2. If λ_1 and λ_2 are increased at the same time, the residual component energy will increase. In equation (3), the first norm is not differentiable, making it challenging to solve. For this reason, this paper adopts the split augmented Lagrangian search algorithm. The objective function is minimized by iterative updating, and finally, the high and low resonance components are separated.

$$\begin{cases} \hat{x}_1 = S_1 W_1^*, \\ \hat{x}_2 = S_2 W_2^*, \end{cases} \tag{4}$$

where W_1^* and W_2^* are, respectively, the transformation matrix of the high and low resonance components when the objective function J is the minimum; $\hat{x}_1$ and $\hat{x}_2$ are the estimated values of high and low resonance components, respectively.

2.2. HHO-RSSD Decomposition

2.2.1. Fitness Function. Correlation kurtosis is an index used to evaluate the impact component content [27]. Compared with a single kurtosis index, correlation kurtosis introduces a correlation function based on kurtosis to perform auxiliary operations, which can characterize the transformation of shock components in a shock signal. The correlation kurtosis can be expressed as follows.

$$\mathrm{CK}_M(T) = \sum_{n=1}^{N}\left(\frac{\prod_{m=0}^{M} x_{n-MT}}{\left(\sum_{n=1}^{N} x_n^2\right)^{M+1}}\right), \tag{5}$$

where x_n represents the initial time series; N is the number of data points contained in the signal; T indicates the period of the required pulse signal; M is the number of offset periods.

The correlation kurtosis index is sensitive to the impact component in the signal, and its sensitivity is related to the settings of the parameters T and M. For a vibration signal, when the given parameter T matches the period of the initial signal, at this time, as the impact component in the signal increases, the magnitude of the correlation kurtosis also increases. In addition, in the decomposition process of RSSD, more identical components may be decomposed between high and low resonance components. To avoid this situation, the constraint condition of cross-correlation is introduced. Assuming there are two signals X and Y, the correlation coefficient between the two signals is expressed as follows:

$$C = \frac{\sum_{i=1}^{n}(x_i - \overline{x})(y_i - \overline{y})}{\sqrt{\sum_{i=1}^{n}(x_i - \overline{x}) * \sqrt{\sum_{i=1}^{n}(y_i - \overline{y})^2}}}, \tag{6}$$

where C represents the correlation coefficient of the two signals, and the value range is [−1,1]. When C is −1, the two signals are negatively correlated; when C is 0, the two signals are not correlated; when C is 1, the two signals are positively correlated, and the two signals can be considered the same signal. Therefore, combining the advantages of the correlation kurtosis and the correlation coefficient, the maximum ratio of the correlation kurtosis value of the low resonance component to the correlation coefficient of the high resonance component is used as the fitness function K, as follows:

$$K = \frac{CK_M}{C}. \tag{7}$$

2.2.2. HHO Algorithm. The Harris Hawk optimization algorithm is an intelligent optimization algorithm that simulates the predation behavior of Harris Hawk. It mainly consists of three parts: the search phase; and the conversion and development phase.

(1) Search Phase. Harris Hawks randomly roost somewhere and find their prey through two strategies:

$$X(t+1) = \begin{cases} X_{\mathrm{rand}}(t) - r_1\left|X_{\mathrm{rand}}(t) - 2r_2X(t)\right|, q \geq 0.5, \\ \left[X_{\mathrm{rabbit}}(t) - X_m(t)\right] - r_3\left[lb + r_4(ub - lb)\right], q < 0.5, \end{cases} \tag{8}$$

where $X(t)$ and $X(t+1)$ are the positions of the individuals in the current and next iteration respectively; t is number of iterations; $X_{\mathrm{rand}}(t)$ is the position of the randomly selected individual, $X_{\mathrm{rabbit}}(t)$ is the position of the prey, that is, the position of the individual with the best fitness; r_1, r_2, r_3, r_4, and q are all random numbers between [0,1]. q is used to select the strategy to be adopted, $X_m(t)$ is the average position of the individual; (ub, lb) refers to the range of the initial random position of the eagle and the expression is as follows:

$$X_m(t) = \sum_{k=1}^{M}\frac{X_k(t)}{M}, \tag{9}$$

where $X_k(t)$ is the position of the k-th individual in the population and M is the population size.

(2) Search and Development Conversion Phase. The HHO algorithm can switch between different development behaviors according to the escape energy of the prey. During the flight, the energy of the prey will be greatly reduced. In order to simulate this situation, the energy of the prey can be expressed as

$$E = 2E_0\left(1 - \frac{t}{T}\right), \tag{10}$$

where E_0 is the initial energy of the prey, which is a random number between [−1,1], which is automatically updated at each iteration, t is the number of iterations, and T is the maximum number of iterations.

(3) Development Phase. Define r as a random number between [0,1], used to select different development strategies. When $0.5 \leq |E| < 1$ and $r \geq 0.5$, the soft siege strategy is adopted for position update:

$$X(t+1) = \Delta X(t) - E\left|JX_{\mathrm{rabbit}}(t) - X(t)\right|, \tag{11}$$

where $\Delta X(t) = X_{\mathrm{rabbit}}(t) - X(t)$ represents the difference between the position of the prey and the current position of the individual, and J is a random number between [0, 2].

When $|E| < 0.5$ and $r \geq 0.5$, a hard siege strategy is adopted to update the position:

$$X(t+1) = X_{\mathrm{rabbit}}(t) - E|\Delta X(t)|. \tag{12}$$

When $0.5 \leq |E| < 1$ and $r < 0.5$, the asymptotic fast swooping soft siege strategy is adopted for position update:

$$X(t+1) = \begin{cases} Y, f(Y) < f(X(t)), \\ Z, f(Z) < f(X(t)), \end{cases} \tag{13}$$

$$Y = X_{\mathrm{rabbit}}(t) - E\left|JX_{\mathrm{rabbit}}(t) - X(t)\right|, \tag{14}$$

$$Z = Y + S * \mathrm{LF}(2), \tag{15}$$

where f is the fitness function, S is a two-dimensional random vector, the elements are random numbers between [0,1], and LF is the mathematical expression of Levi flight.

When $|E| < 0.5$ and $r < 0.5$, the position is updated by the hard encircling strategy of asymptotic fast swooping:

$$X(t+1) = \begin{cases} Y, f(Y) < f(X(t)), \\ Z, f(Z) < f(X(t)), \end{cases} \tag{16}$$

$$Y = X_{\mathrm{rabbit}}(t) - E\left|JX_{\mathrm{rabbit}}(t) - X_m(t)\right|, \tag{17}$$

$$Z = Y + S * LF(2). \tag{18}$$

Algorithm steps:

Step 1: population initialization. According to the upper and lower bounds of each dimension of the search space, initialize each individual.

Step 2: calculate the initial fitness. Set the position of the individual with the best fitness as the current prey position.

Step 3: location update. First, update the escape energy of the prey, and then execute the corresponding location update strategy in the search or development behavior according to the escape energy and the generated random number.

Step 4: calculate fitness. Calculate the fitness of the individual after the location update, and compare it with the fitness value of the prey. If the fitness value of the individual after the location update is better than the prey, the individual location with the better fitness value is used as the new prey location.

Repeat Steps 3 and 4, when the number of iterations of the algorithm reaches the maximum number of iterations. Output the current position of the prey as the estimated position of the target.

2.2.3. HHO-Optimized RSSD Algorithm Steps. The technical flowchart of the proposed HHO optimization RSSD is shown in Figure 2 , and the specific optimization steps are as follows:

(1) The random position of the eagle was initialized, the number of iterations $T = 50$, the population size $N = 20$, and the three parameters were set between 0.001 and 200, and determine the fitness evaluation function K.

(2) Preset the value range of the parameters to be optimized, such as the quality factor Q, the weight coefficient A, and the Lagrangian multiplier u, and give an initial value randomly.

(3) The RSSD is used to decompose the vibration signal, and the three parameters of the RSSD are optimized through the HHO algorithm. After iteration, the local optimal parameters are retained.

(4) HHO updates the position of the eagle through different strategies, introduces it into the RSSD, obtains the fitness function value, compares it with the optimal fitness function value obtained in the previous iteration, and obtains the optimal parameters corresponding to this optimal fitness function.

(5) When the number of algorithm iterations reaches the maximum number of iterations, the global optimal fitness function value and the optimal parameter value are output.

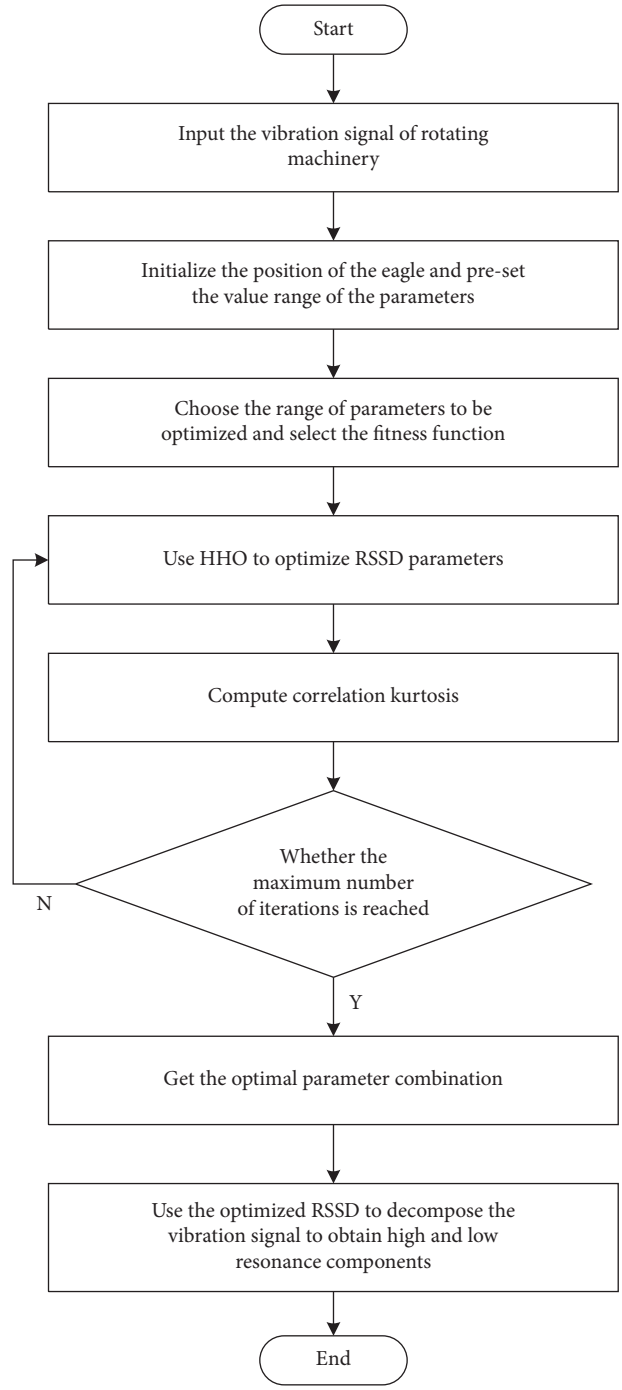

Figure 2: The technical flowchart of the proposed HHO optimization RSSD.

(6) Substitute the optimal parameter combination into the RSSD to realize the decomposition of the vibration signal.

2.3. RCGmvMAAPE

2.3.1. AAPE. AAPE is based on PE [28]. Therefore, its theory is very similar to PE similarity, and it is necessary to explain the specific improvement method of AAPE after describing

the theory of PE. The foundation principle of PE is as follows:

(1) For a one-dimensional time series $x = \{x_1, x_2, \ldots x_i, \ldots x_N\}$ of length N, at any time point t, the reconstruction vector of m dimension can be generated by the reconstruction of x

$$X_t^{m,d} = \left\{x_t, x_{t+d}, \ldots, x_{t+(m-2)d}, x_{t+(m-1)d}\right\} \quad t = 1, 2, \ldots, N-(m-1)d, \tag{19}$$

where m indicates the embedding dimension and d indicates the time delay.

(2) In each reconstruction vector, according to the size of each element, in ascending order, the permutation of $\pi_{r_0, r_1, \cdots, r_{m-1}}$ can be obtained, which fulfills:

$$\left\{x_{t+(j_1-1)d}, x_{t+(j_2-1)d}, \ldots, x_{t+(j_{m-1}-2)d}, x_{t+(j_m-1)d}\right\}, \tag{20}$$

where j_* denote the index of the column of each element in the reconstructed component. Thus, when the embedding dimension is m, there are $m!$ possible ordinal patterns, of which the ith permutation is marked as π_i.

(3) The relative frequency of occurrence of π_i in each permutation pattern is described as

$$p(\pi_i) = \frac{g(\pi_i)}{N-(m-1)d}, \tag{21}$$

where $g(\pi_i)$ indicate a function that counts the number of occurrences of π_i in $X_t^{m,d}$. Whenever the permutation order of the internal elements of $X_t^{m,d}$ is π_i, the value of $g(\pi_i)$ linearly increases by 1.

(4) Therefore, according to the definition of entropy, PE can be described as

$$PE(x, m, d) = -\sum_{\pi_i=1}^{\pi_i=m!} p(\pi_i) \ln\, p(\pi_i). \tag{22}$$

Although PE has excellent performance, it is still found to have more serious defects, which makes it less reliable in quantifying the complexity of time series. First of all, based on the above description, PE only considers the contribution of the ordering structure of the time series to the complexity when calculating the probability, while the influence of the amplitude information of each data point in the time series on the entropy value is not calculated. Secondly, when there are components with equal amplitude in the time series, the influence of this group of elements on the entropy value is not clearly stated. For this reason, by enhancing the sensitivity to the amplitude and frequency of the time series, AAPE is more comprehensive and accurate in measuring the complexity of the time series. The principle of AAPE is reviewed as follows:

Supposing that the starting value of $p(\pi_i^{m,d})$ is 0, for the reconstruction vector $X_t^{m,d}$, when the time t adds from 1 to N-m+1 increasingly, the value of $p(\pi_i^{m,d})$ is updated when the permutation $\pi_i^{m,d}$ changed.

$$p^{\text{update}}\left(\pi_i^{m,d}\right) = p\left(\pi_i^{m,d}\right) + \left(\frac{\alpha}{m}\sum_{k=1}^{m}\left|x_{t+(k-1)d}\right| + \frac{1-\alpha}{m-1}\sum_{k=2}^{d}\left|x_{t+(k-1)d} - x_{t+(k-2)d}\right|\right), \tag{23}$$

where $\alpha \in [0, 1]$ denotes the adjustment coefficient, which is used to adjust the weight of the time series amplitude mean and the deviation between the amplitudes. Thus, the probability of $p(\pi_i^{m,d})$ occurring in the whole time series is $\pi_i^{m,d}$.

$$p\left(\pi_i^{m,d}\right) = \frac{p^{\text{update}}\left(\pi_i^{m,d}\right)}{\sum_{t=1}^{N-m+1}\left(\alpha/m\sum_{k=1}^{m}\left|x_{t+(k-1)d}\right| + 1 - \alpha/m - 1\sum_{k=2}^{m}\left|x_{t+(k-1)d} - x_{t+(k-2)d}\right|\right)}. \tag{24}$$

The AAPE of time series can be computed as follows:

$$\text{AAPE}(x, m, d, \alpha) = -\sum_{\pi_k=1}^{\pi_k=m!} p(\pi_k) \ln\, p(\pi_k). \tag{25}$$

2.3.2. mvAAPE. In this part, the multivariate amplitude perception permutation entropy is developed to quantify the complexity of multichannel time series. The principle of mvAAPE can be expressed as follows [29]:

(1) Given the multivariate data $X = \left\{X_{c,1}, X_{c,2}, \ldots, X_{c,i}, \ldots, X_{c,L}\right\} c = 1, 2, \ldots, q$ of q channels of length L to be analyzed. Perform phase space reconstruction on each sample, and the resulting matrix is as follows:

$$Z = \left\{X_{c,i}, X_{c,i+d}, \ldots, X_{c,i+(m-2)d}, X_{c,i+(m-1)d}\right\}. \quad (26)$$

(2) Rearrange the reconstruction vector Z into $\{x_{c,i+(j_1-1)d} \le x_{c,i+(j_2-1)d} \le \cdots \le x_{c,i+(j_{m-1}-1)d} \le x_{c,i+(j_m-1)d}\}$ in ascending order. At this time, the possible sorting mode π_i exists $m!$

(3) Assume that the starting value of $p(\pi_{c,i}^{m,d})$ is zero. For the reconstruction vector Z, when the time i gradually increases from 1 to $L-m+1$, the value of $p(\pi_{c,i}^{m,d})$ is updated every time $\pi_{c,i}^{m,d}$ appears.

$$p^{\text{update}}\left(\pi_{c,i}^{m,d}\right) = p\left(\pi_{c,i}^{m,d}\right) + \left(\frac{\alpha}{m}\sum_{k=1}^{m}\left|x_{c,t+(k-1)d}\right| + \frac{1-\alpha}{m-1}\sum_{k=2}^{m}\left|x_{c,t+(k-1)d} - x_{c,t+(k-2)d}\right|\right). \quad (27)$$

(4) Compute the probability of i-th sorting pattern $\pi_i\,(1 \le i \le m!)$ in c-th channel as

$$p\left(\pi_{c,i}^{m,d}\right) = \frac{p^{\text{update}}\left(\pi_{c,i}^{m,d}\right)}{\sum_{t=1}^{N-m+1}\left(\alpha/m\sum_{k=1}^{m}\left|x_{c,t+(k-1)d}\right| + 1 - \alpha/m - 1\sum_{k=2}^{m}\left|x_{c,t+(k-1)d} - x_{c,t+(k-2)d}\right|\right)}. \quad (28)$$

For q-channel time series, $p(\pi_{c,i})$ satisfies $\sum_{c=1}^{q}\sum_{i=1}^{m!}p(\pi_{c,i}) = 1$.

(5) The probability of the i-th pattern π_i in q-channel time series can be computed as follows:

$$p(\pi_i) = \sum_{c=1}^{q} p\left(\pi_{c,i}\right). \quad (29)$$

(6) According to the definition, mvAAPE can be expressed as

$$\text{mvAAPE}(X, m, d, \alpha) = -\sum_{i=1}^{m!} p(\pi_i)\ln\, p(\pi_i). \quad (30)$$

mvAAPE mainly integrates data from multiple channels so that AAPE can extract more features, making the analysis more comprehensive and accurate. However, mvAAPE can only extract the features of the signal on a single scale. But, the effective information contained in the actual vibration signal is often presented on multiple scales, and it is difficult to fully extract the fault characteristics in the vibration signal by only carrying out a single-scale analysis. Therefore, in order to mine the fault information of the vibration signal from multiple scales and enhance the robustness of the analysis, the multivariate multiscale amplitude aware permutation entropy was developed.

2.3.3. mvMAAPE. The realization principle of mvMAAPE is to obtain multiple coarse-grained time series by performing coarse-grained processing on the multichannel time series. These coarse-grained time series respectively represent the vibration information of the original multichannel signal at various scales. Subsequently, based on mvAAPE to mine the fault information in these coarse-grained time series to realize mvMAAPE analysis. The basic implementation principle of mvMAAPE is described as follows.

(1) For q channel time series $U = \{u_{k,1}, u_{k,2}, \ldots, u_{k,i}, \ldots, u_{k,L}\}$ with data points L. The multivariate coarse-grained time series at scale factor τ is computed as

$$y_{k,j}^{\tau} = \frac{1}{\tau}\sum_{i=(j-1)\tau+1}^{j\tau} u_{k,i} \quad 1 \le j \le \frac{L}{\tau}, 1 \le k \le p, \quad (31)$$

Where τ is the scale factor, the coarse grained time series is the raw time series when $\tau = 1$.When $\tau > 1$, the original time series is divided into coarse-grained time series of length L/τ.

(2) Compute the mvAAPE of each multivariate coarse-grained time series, and get the mvMAAPE of U as follows:

$$\text{mvMAAPE} = \text{mvAAPE}\left(y_{k,j}^{\tau}, m, d, \alpha\right). \quad (32)$$

By extending mvAAPE from single-scale analysis to multiscale, more information can be obtained from multivariate coarse-grained time series of different scales, which is called multivariate multiscale amplitude aware permutation entropy analysis. However, in the abovementioned multivariate coarse-grained time series with a scale factor of τ, only the information of the multivariate coarse-grained time series starting from $u_{k,1}$ is considered, and the information of the remaining $\tau - 1$ multivariate time series is not used. mvMAAPE does not consider the relationship between adjacent coarse-grained time series, resulting in a lack of statistical information.

2.3.4. RCGmvMAAPE. To overcome the shortcomings of mvMAAPE, a new entropy method is proposed, which is called RCGmvMAAPE. Compared with mvMAAPE, RCGmvMAAPE mainly made two improvements. Firstly, to reduce the large variance of mvFE when the scale factor is large, this paper adopts refined composite analysis to achieve coarse graining of time series, which can reduce the dependence of entropy value on the length of time series data and achieve stable results even when the length of time series to be analyzed is short. Secondly, in order to accurately describe the dynamic changes of the time series, the second-order moment (root mean square) is used to replace the first-order moment (mean) used in the traditional coarse-graining method, so that it has a stronger fault feature extraction ability. The principle of RCGmvMAAPE is as follows:

(1) For the n-channel multivariate time series $X = \{x_{k,b}\}_{b=1}^{L}$, $k = 1, 2, \ldots, n$ with data point L, the multivariate coarse grained time series is calculated by using root mean square instead of mean value at scale factor τ. The elements in the a-th coarse-grained time series $Y_a^\tau = \{y_{k,i,1}^\tau, y_{k,i,2}^\tau, \ldots\}$ are expressed as follows:

$$y_{k,i,a}^\tau = \sqrt{\frac{1}{\tau}\sum_{b=a+\tau(i-1)}^{a+i\tau-1} x_{k,b}^2} \quad 1 \le i \le \frac{L}{\tau},\ 1 \le k \le n,\ 1 \le a \le \tau. \tag{33}$$

For a scale factor τ, there will be τ diverse coarse-grained multivariate time series, as present in Figure 3.

(2) For each coarse-grained multivariate time series, calculate the marginal relative frequencies $p(\pi_j)$.Then the average relative frequency $\overline{p(\pi_j)}$ can be calculated as follows

$$\overline{p(\pi_j)} = \frac{1}{\tau}\sum_{a=1}^{\tau} p_a(\pi_j). \tag{34}$$

(3) Therefore, the RCGmvMAAPE of the multichannel time series can be described as follows:

$$\text{RCGmvMAAPE} = -\sum_{\pi_j=1}^{\pi_j=m!} \overline{p(\pi_j)} \ln \overline{p(\pi_j)}. \tag{35}$$

2.3.5. Parameter Selection and Performance Analysis. In the RCGmvMAAPE algorithm, there are five parameters that need to be set in advance, namely the embedding dimension m, the time delay d, the adjustment coefficient a, the length of the time series N and the scale factor S. For the embedding dimension m, too small value will result in too few states contained in the reconstruction vector, and the algorithm losses its effectiveness, making it impossible to detect dynamic mutations in the time series. Conversely, if m is too large, the reconstruction of the phase space will homogenize the time series, which not only increases the amount of calculation but also fails to highlight subtle changes in the time series. Therefore, consider setting the embedding dimension m as 5. The time delay has little effect on the performance of the algorithm, so set it as $d = 1$. The value of the adjustment coefficient is usually $a = 0.5$. In addition, the scale factor S cannot be set too large; otherwise, it will produce more redundant information and affect the efficiency of the analysis. On the contrary, too small value will make the information extraction insufficient and affect the effectiveness of the analysis, so this article is set as $S = 20$. The length of the time series also has a certain degree of influence on the performance of the algorithm. Without loss of generality, three-channel Gaussian white noise signals are used for analysis, the lengths are respectively $N = 256, 512, 1024, 2048, 4096, 8192$, and their RCGmvMAAPE is calculated under the condition that other parameters are the same. Figure 4 shows the entropy values under different lengths. From Figure 1, when the length $N \ge 2048$, the entropy curve is smoother and the fluctuation is small. At this time, the RCGmvMAAPE of the white noise signals of different lengths has a small difference and the performance is relatively stable, so $N = 2048$ is selected.

This part is mainly based on simulation signals to verify the excellent performance of RCGmvMAAPE in measuring the complexity of multichannel vibration signals. The RCGmvMAAPE method is compared with other typical multivariate analysis methods through four different multichannel signals. White Gaussian noise (WGN) and $1/f$ noise are two time series used to construct multichannel simulation signals. The irregularity of WGN is higher than $1/f$. Compared with WGN, the power spectrum of $1/f$ noise is more complex, so more mode information is integrated. The generation of WGN is random, so the probability of its state transition matrix is approximately equal. On the contrary, $1/f$ is a long-range correlation signal, and the irregularity of $1/f$ noise is low than that of WGN. Therefore, $1/f$ noise is more complicated than WGN.

Without loss of generality, multichannel signals with three different channels are generated based on WGN and $1/f$ noise, which are (a) three channel WGN; (b) two channel WGN and one channel $1/f$; (c) one channel WGN and two channel $1/f$; (d) three channel $1/f$. RCGmvMAAPE, RCmvMPE, RCmvMSE and mvMAAPE were studied, respectively. The data length of each channel is $N = 2\,048$. The mean and standard deviation curves of RCGmvMAAPE, RCmvMPE, RCmvMSE and mvMAAPE of the four synthetic signals are shown in Figure 3. It can be seen from Figure 5 that compared with the other three methods, the standard deviation of RCGmvMAAPE is significantly smaller, which shows that RCGmvMAAPE is more stable when measuring the complexity of multichannel time series. In addition, RCGmvMAAPE and RCmvMPE methods can clearly distinguish four kinds of multichannel synthetic signals, while mvMAAPE method cannot effectively separate (a), (b), and (c), which indicates that the coarse grainization method based on refined composite generalized processing can obtain more accurate results, thus effectively measuring the complexity

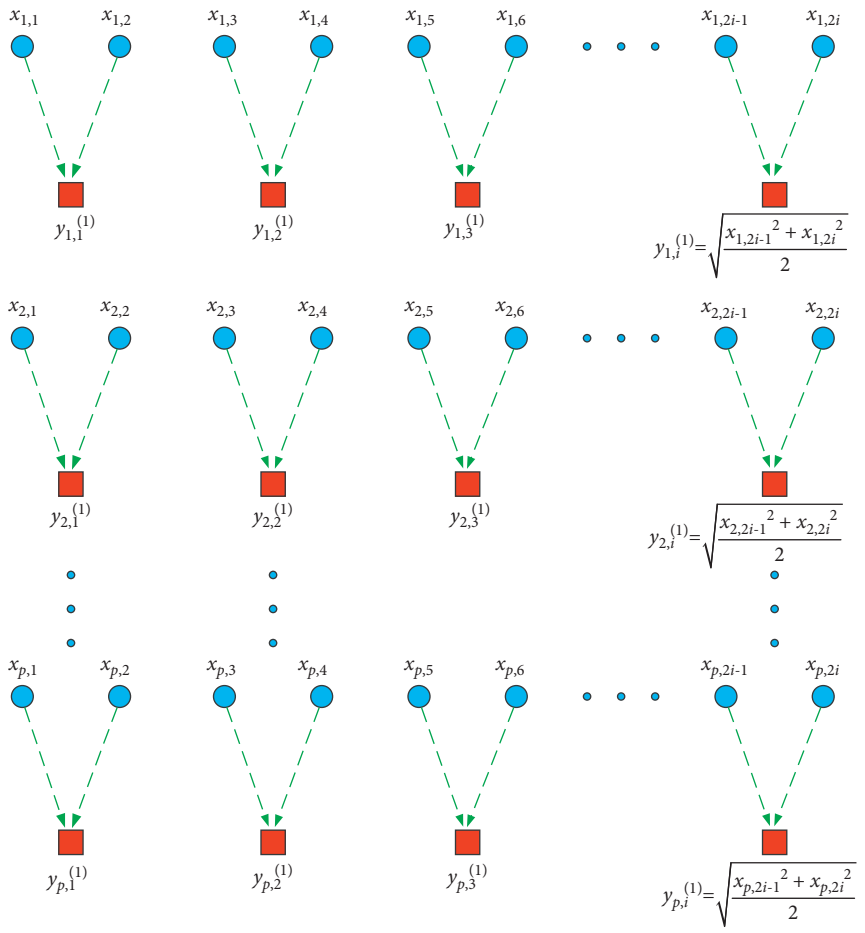

(a)

Figure 3: Continued.

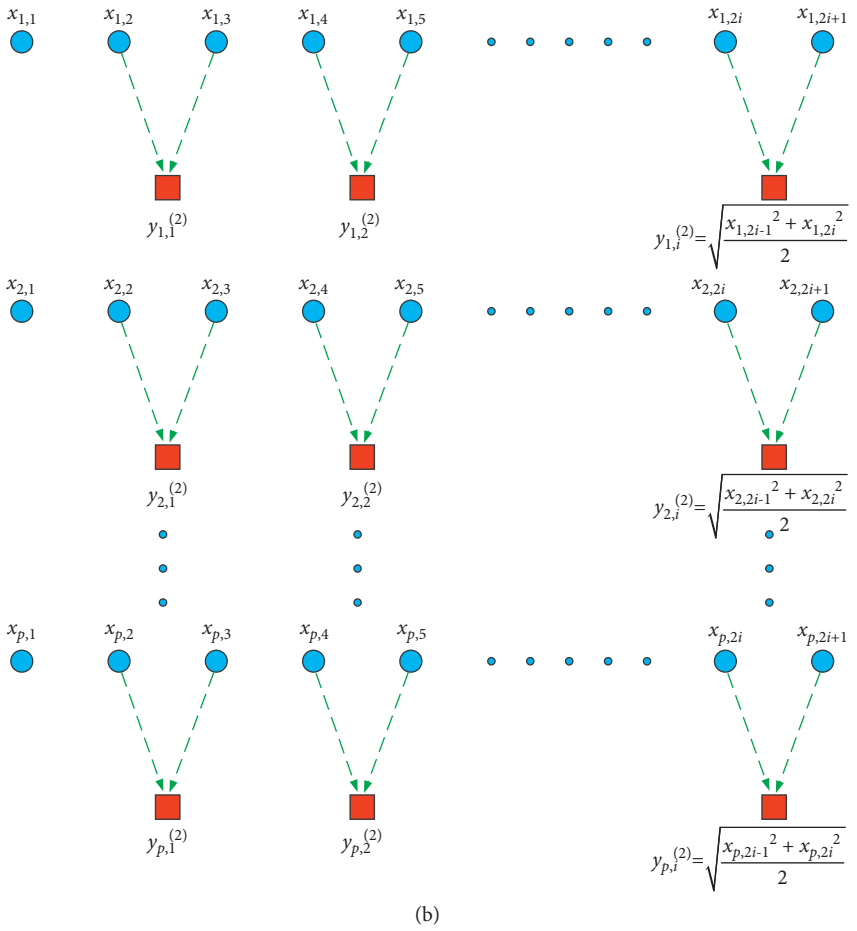

Figure 3: Illustration of refined composite coarse-grained approach for multivariate time series with scale factor 2. (a) First coarse-grained time series; (b) second coarse-grained time series. Figure is reproduced from Fuming Zhou 2020.

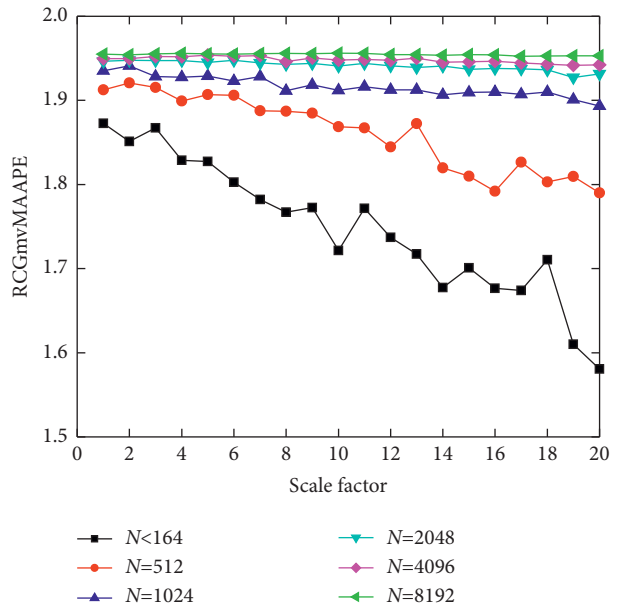

Figure 4: RCGmvMAAPE of three channel white noises under diverse lengths.

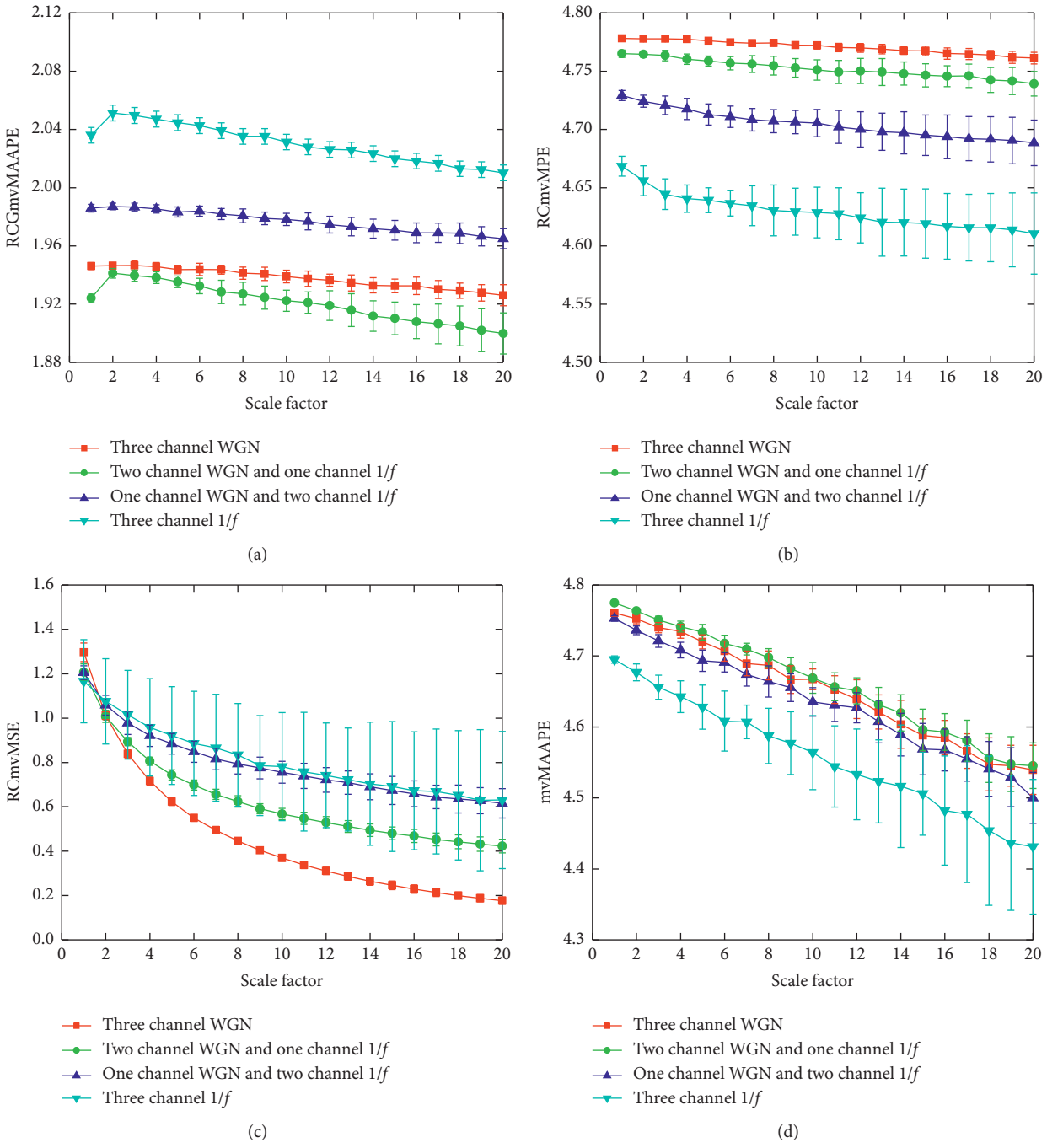

Figure 5: RCGmvMAAPE, RCmvMPE, RCmvMSE, and mvMAAPE of four multichannel synthetic signal.

of time series. Besides, RCmvMSE has a poor distinction between (c) and (d), which is mainly because the method is mainly based on multivariate sample entropy to realize its function, and sample entropy has many defects when processing time series, so RCmvMSE has a poor performance. In conclusion, compared with the other three multivariate analysis methods, RCGmvMAPE improves its ability to extract feature information from multichannel vibration signals by adopting refined generalized composite coarsing processing, so it can better measure the complexity of multichannel signals.

3. The Proposed Fault Diagnosis Model

According to the previous analysis, RCGmvMAAPE can effectively measure the complexity of multichannel time series. The HHO-RSSD can adaptively decompose the vibration signal into high and low resonance components, and has excellent time-frequency analysis performance. Therefore, a new fault diagnosis technology for rotating machinery was developed. First, HHO-RSSD and RCGmvMAAPE are adopted to extract high-quality features that characterize the fault state from the signals of rotating machinery.

Subsequently, a deep belief network classifier with excellent generalization performance is used to identify the types of faults. The technical implementation process is shown in Figure 6. The detailed steps are as follows:

(1) Under a given sampling frequency, the vibration data of the rotating machinery in different fault states are collected through the accelerometer and divided into training samples and test samples.

(2) HHO algorithm is used to optimize the key parameters of RSSD and find the best combination of parameters. Subsequently, the optimized RSSD is used to decompose the vibration signal to obtain high and low resonance components containing rich vibration information to highlight the fault components.

(3) The high and low resonance components are used as multichannel data to construct a multivariate time series, and then the RCGmvMAAPE of the multivariate time series is calculated to generate fault features.

(4) The deep belief network classifier is trained through the training data set to obtain the best classifier model.

(5) The remaining test data set is input to the trained DBN classifier model for fault identification. According to the output result of the DBN classifier, the fault type of the rotating machinery is judged.

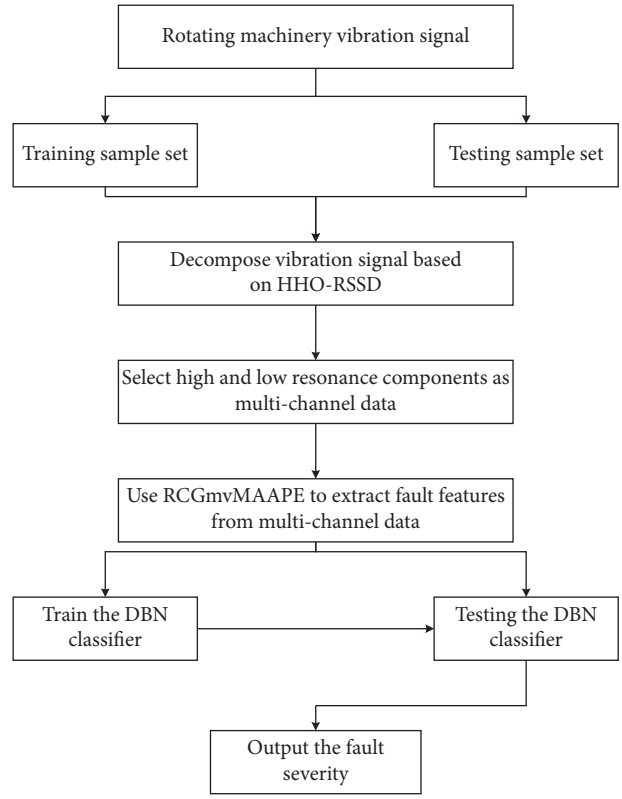

Figure 6: The technical implementation process.

4. Experimental Verification

To validate the validity and reliability of the approach raised in this paper for the health recognition of general rotating machinery, experiments were carried out using two typical rotating machinery vibration data, rolling bearings and gears. The rolling bearing data is offered by the public data set, and the gear vibration data is collected on the QPZZ-II vibration test platform.

4.1. Case 1

4.1.1. Data Collection. To test the effectiveness of the raised approach of fault diagnosis for rotating machinery, firstly, experiments are carried out adopting rolling bearing data. The experimental data used the typical vibration data set of rolling bearings offered by the Electrical Laboratory of Case Western Reserve University [30]. The structure of the platform is shown in Figure 7. Seen from Figure 7, the vibration acquisition platform is composed of components such as a motor, a drive end bearing, a fan end bearing, and an accelerometer. The bearing model adopted in the experiment is 6205-2RS-JEM SKF. The running power of the motor is 0 horsepower and the rotating speed is 1797 rpm. The vibration data is collected by sensors installed at the drive end and the fan end. The sampling frequency is 12 kHz, and the sampling time for each working condition is 10 s. Different types of single-point faults are set up on the rolling bearings by EDM. The fault diameters are 0.1778 mm, 0.3556 mm and 0.5334 mm, and the fault depth is 0.2794 mm. The fault diameter represents the severity of the fault of the rolling bearing. Experiments were performed for both fan and drive end bearings with outer race faults located at 6 o'clock. The fault data used in this experiment includes four types of normal, inner race fault, outer race fault, and ball fault. Each fault type contains three different severity, so a total of ten types of vibration data are included. The vibration data of each working condition is divided into 58 groups of nonoverlapping samples, and the number of data points contained in each sample is 2048. Randomly select 28 groups of samples as the training set, and the remaining 30 groups as the test set. The brief information of the data used is displayed in Table 1.

4.1.2. Analysis and Feature Extraction. Figure 8 presents the waveform of the vibration data adopted in the experiment. The waveform is a nonlinear modulation signal with complex components and contains a large number of irregular impact components. Therefore, it is hard to easily judge the status of fault of the rolling bearing by observing the waveform of the vibration signal, and further processing of the vibration signal is required to obtain more failure information.

This part mainly studies how to obtain the best RSSD algorithm. First input the rolling bearing vibration signal to HHO-RSSD to perform signal decomposition. Taking the normal state as an example, the iterative process ends when the value of the correlation kurtosis is the smallest.

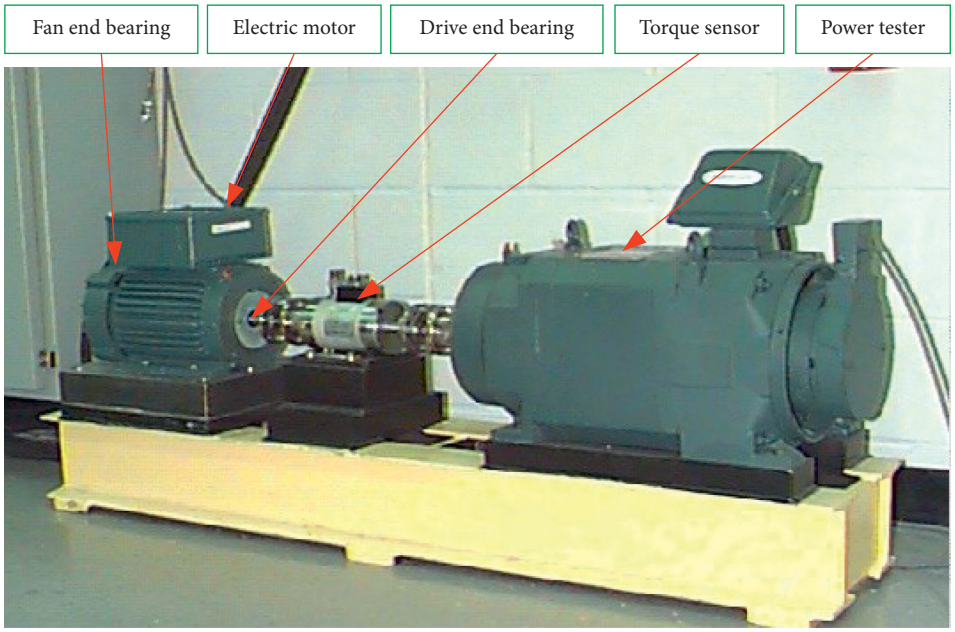

Figure 7: The fault simulation test platform of rolling bearing.

Table 1: The brief information of the data.

Working condition	Fault Diameter (mm)	Abbreviation	Training Sample	Testing Sample	Label
Normal		Nor	28	30	1
Inner race fault	0.1778	IRF1	28	30	2
	0.3556	IRF2	28	30	3
	0.5334	IRF3	28	30	4
	0.1778	ORF1	28	30	5
Outer race fault	0.3556	ORF2	28	30	6
	0.5334	ORF3	28	30	7
	0.1778	BF1	28	30	8
Ball fault	0.3556	BF2	28	30	9
	0.5334	BF3	28	30	10

Subsequently, after HHO optimized RSSD, a set of best parameter combinations were obtained, which are $Q_1 = 11.206$, $Q_2 = 0.958$, $A_1 = 0.92$, $A_2 = 0.16$, $u = 0.456$. Figure 9 is the evolution curve of fitness value in the optimization process of HHO. Seen from Figure 9, HHO can reach the local optimum relatively quickly, and then jump out quickly and reach the global optimum, and the final convergence value is also small, which shows that HHO has higher optimization performance. Then, the optimal parameter combination obtained by optimization is input into the RSSD, and the vibration signal is decomposed to acquire the high and low resonance components. The RSSD decomposition result of Nor is shown in Figure 10.

The high and low resonance components are taken as a multichannel time series, and then RCGmvMAAPE is adopted to excavate the fault features of the constructed multivariable data to construct the fault samples. In addition, to validate the effectiveness of the raised RCGmvMAAPE approach, it is compared with RCmvMPE, RCmvMSE, mvMAAPE and RCGMAAPE. The entropy results of seven methods are displayed in Figures 11(a)~ Figures 11(g). Here, Figures 11(a)–11(d) are the analysis results of four multivariate analysis methods on multivariate data composed of high resonance components and low resonance components; Figure 11(e) and Figure 11(f) are the results of using the univariate analysis method RCGMAAPE to analyze the high and low resonance components, respectively; Figure 11(g) is the analysis result of RCGmvMAAPE on the multivariate data composed of the vibration signals of the drive end bearing and the fan end bearing. By comparing Figures 11(a)–11(d), the advantages of RCGmvMAAPE in measuring the complexity of multichannel data over the other three methods can be validated. By comparing Figure 11(a) and Figures 11(e) and 11(f), it can be proved that using RCGmvMAAPE to analyze multichannel data is better than RCGMAAPE to analyze single-channel data. In addition, the comparison between Figure 11(a) and Figure 11(g) can prove that after proper processing, only a single-channel vibration signal can also achieve good results. Seen from Figure 11, compared with several other feature extraction models, the standard deviation of the entropy value of Figure 11(a) is smaller and the performance is more stable. On most scales, the ability of Figure 11(b) to distinguish between bearing faults is not

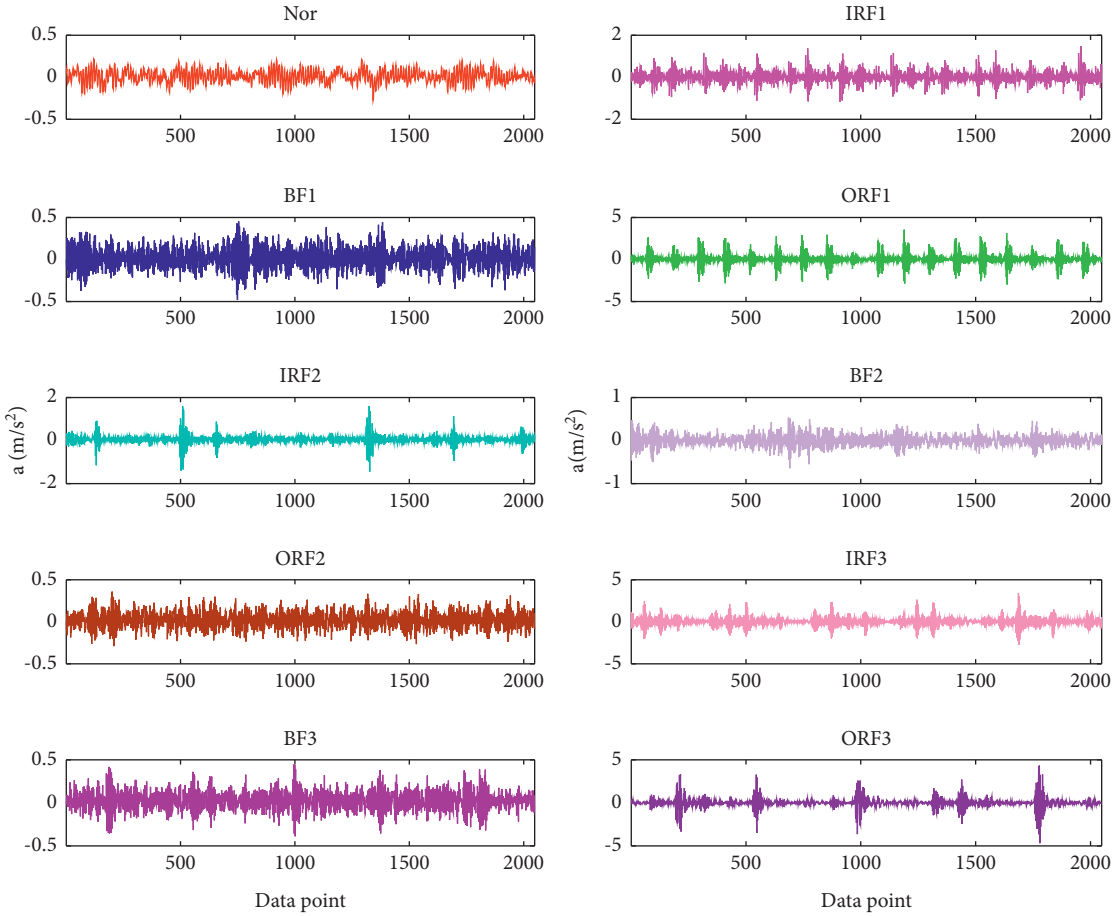

Figure 8: The vibration waveform of rolling bearing under ten fault conditions.

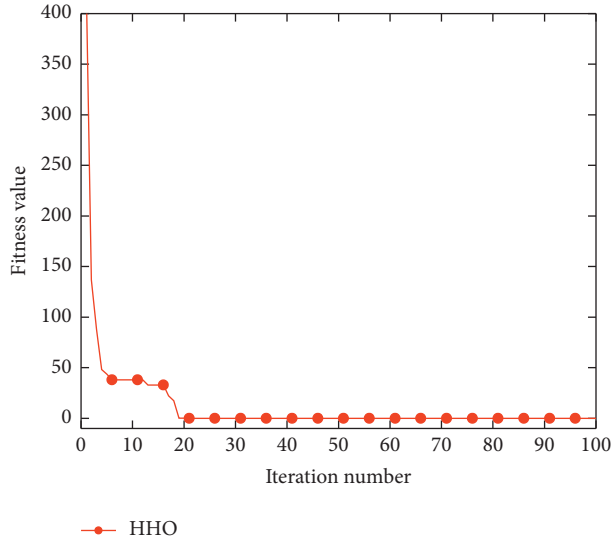

Figure 9: The evolution curve of fitness value.

satisfactory. Especially for IRF1 and BF1 samples, the curves of these two samples have obvious aliasing, so it is difficult to distinguish these two fault states. Figure 11(c) has a relatively obvious degree of discrimination, but its entropy deviation is obviously larger, that is, the error is larger. Compared with Figure 11(a), Figure 11(d) has significantly worse ability to distinguish samples from each state, and the entropy deviation is also larger, which indicates that its performance is

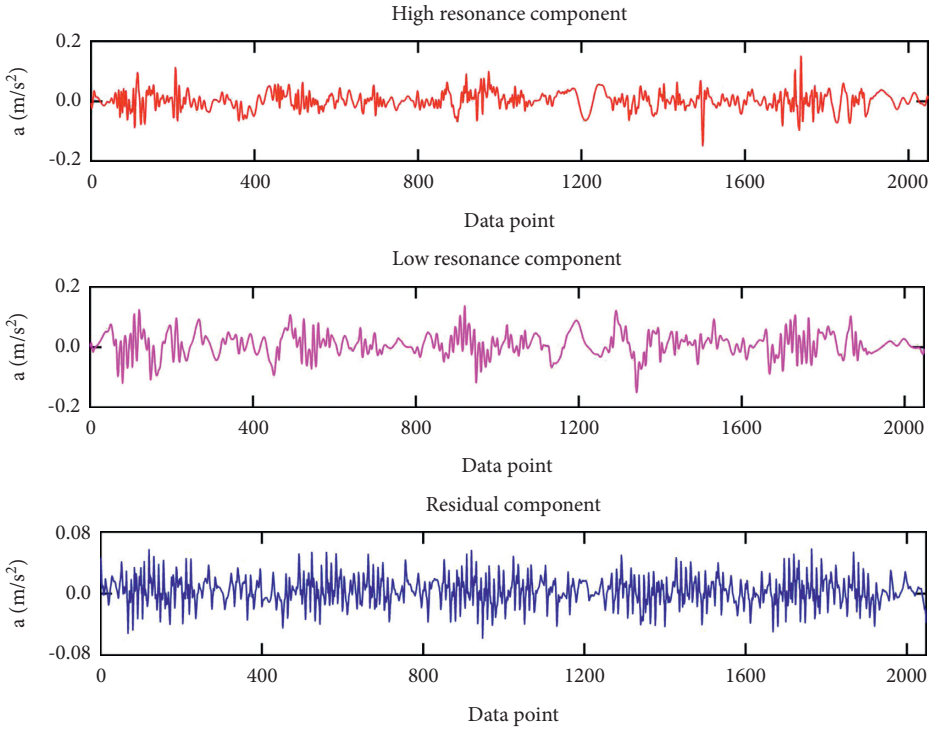

Figure 10: The RSSD decomposition result of vibration signal nor.

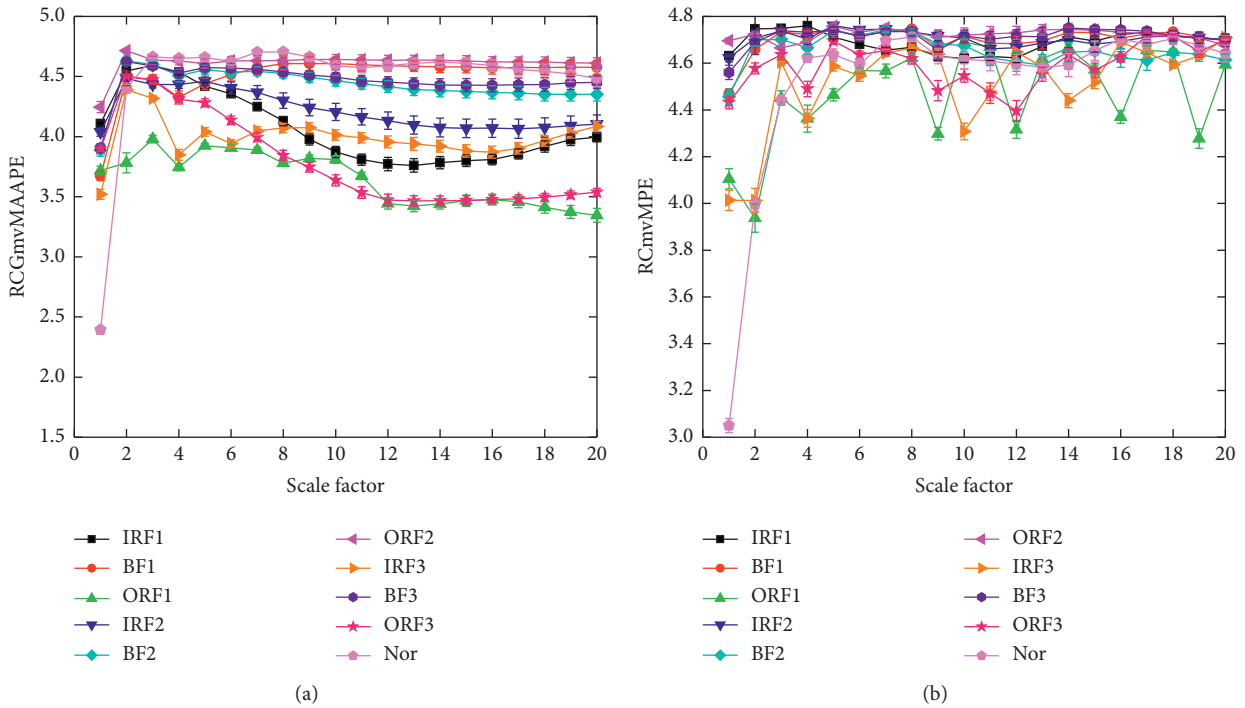

Figure 11: Continued.

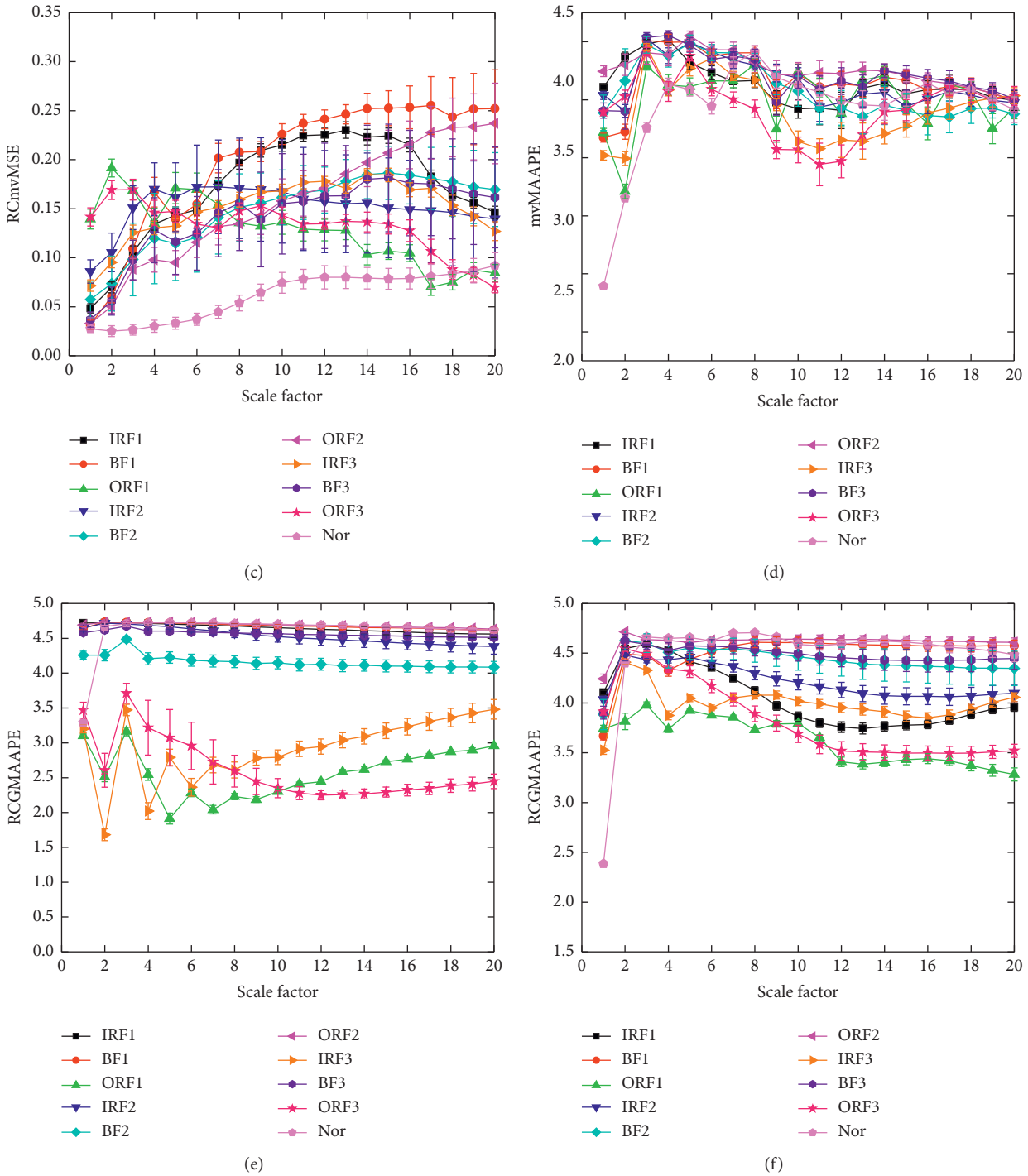

Figure 11: Continued.

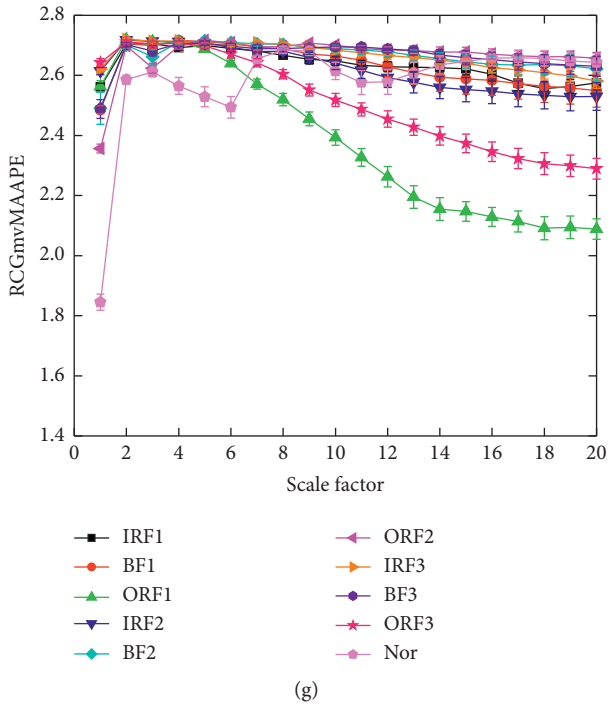

Figure 11: The entropy results of rolling bearing data analyzed by using seven methods.

unstable and its reliability is low. The entropy curves of the six samples in Figure 11(e) are obviously aliased, and the ability to distinguish these samples is very poor. Figure 11(f) has excellent performance, but it can be found that its entropy deviation is slightly larger than that of Figure 11(a), and the stability is insufficient, so its performance is weaker than Figure 11(a). Figure 11(g) can effectively distinguish between ORF1 and ORF3 samples, while the ability to distinguish other samples is weaker than Figure 11(a). But it can be found that the entropy deviation of Figure 11(g) is smaller, that is, the stability and reliability are better. This is mainly because the vibration signal of the fan end also contains the vibration information of the bearing during operation. As the Figure 11(g) integrates the information of two bearings, it has a relatively excellent effect. In summary, using RCGmvMAAPE to analyze multichannel data composed of high and low resonance components can achieve very excellent results, and the effect is even better than that of data composed of vibration signals from the drive end and the fan end.

To compare the performance of the abovementioned seven feature extraction models from a more intuitive perspective, the t-stochastic neighbor embedding (t-SNE) method is used for auxiliary analysis. The t-SNE approach is adopted to project the original features into a two-dimensional space. The visualization of the features extracted by the seven methods is 1 in Figure 12. Observed from Figure 12, the features of the same category in Figure 12(a) are accurately clustered, and samples of different categories are separated from each other, that is, the features are highly distinguishable. However, the distinguishability of features extracted based on other six models is weak, and some samples are aliased with each other, which makes it difficult to distinguish their categories. Comparing Figures 12(e) and 12(f), It can be observed that the visualization effect of Figure 12(f) is better than Figure 12(e), which shows that the low resonance component contains more fault information, so the extracted quality is higher. In addition, by comparing Figures 12(a) and 12(g), it can be found that the visualization effect of Figure 12(a) is better, while the BF2 and BF3 samples in Figure 12(g) show obvious aliasing, and the distribution of samples in the same category is relatively scattered, without obvious clustering center. Therefore, by visualizing the features, it can be proved that using RCGmvMAAPE to extract features from multivariate data composed of high resonance components and low resonance components has a better effect, which proves the reliability and effectiveness of the raised approach.

4.1.3. Fault Recognition. To quantify the performance of the above seven feature extraction models on rolling bearing fault diagnosis, the state features excavated by the seven approaches are input into the DBN recognizer for fault classification. The confusion matrix is a tool for describing the performance of a classification model. It contains information about the actual and predicted classifications completed by the classification model, which can be used to evaluate the performance of the classification model. By observing the confusion matrix, the detailed classification results of each category can be clear. The confusion matrix of the seven feature extraction models is displayed in Figure 13. Observed from Figure 13, the proposed fault diagnosis method achieves the best fault recognition rate, and samples

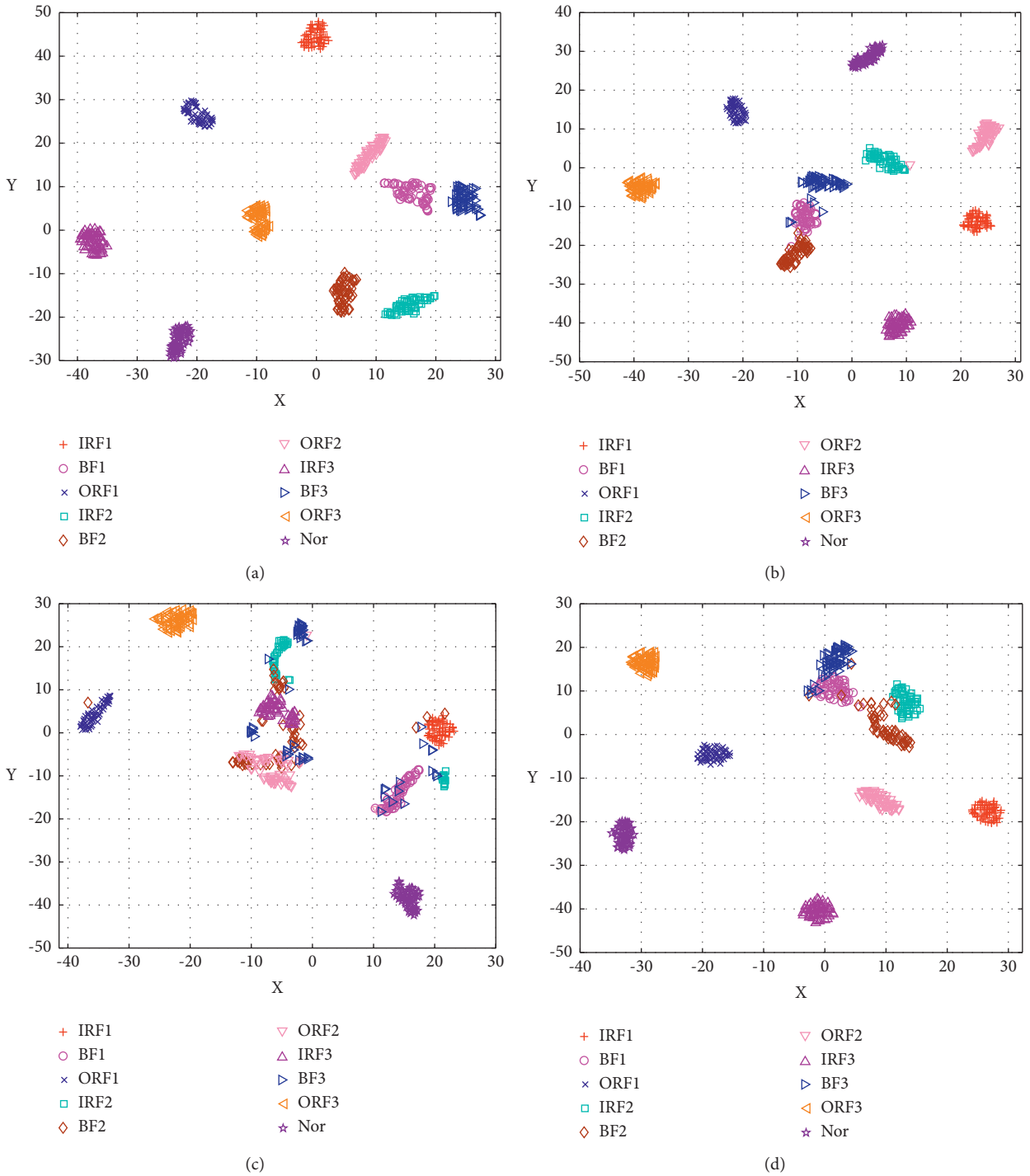

Figure 12: Continued.

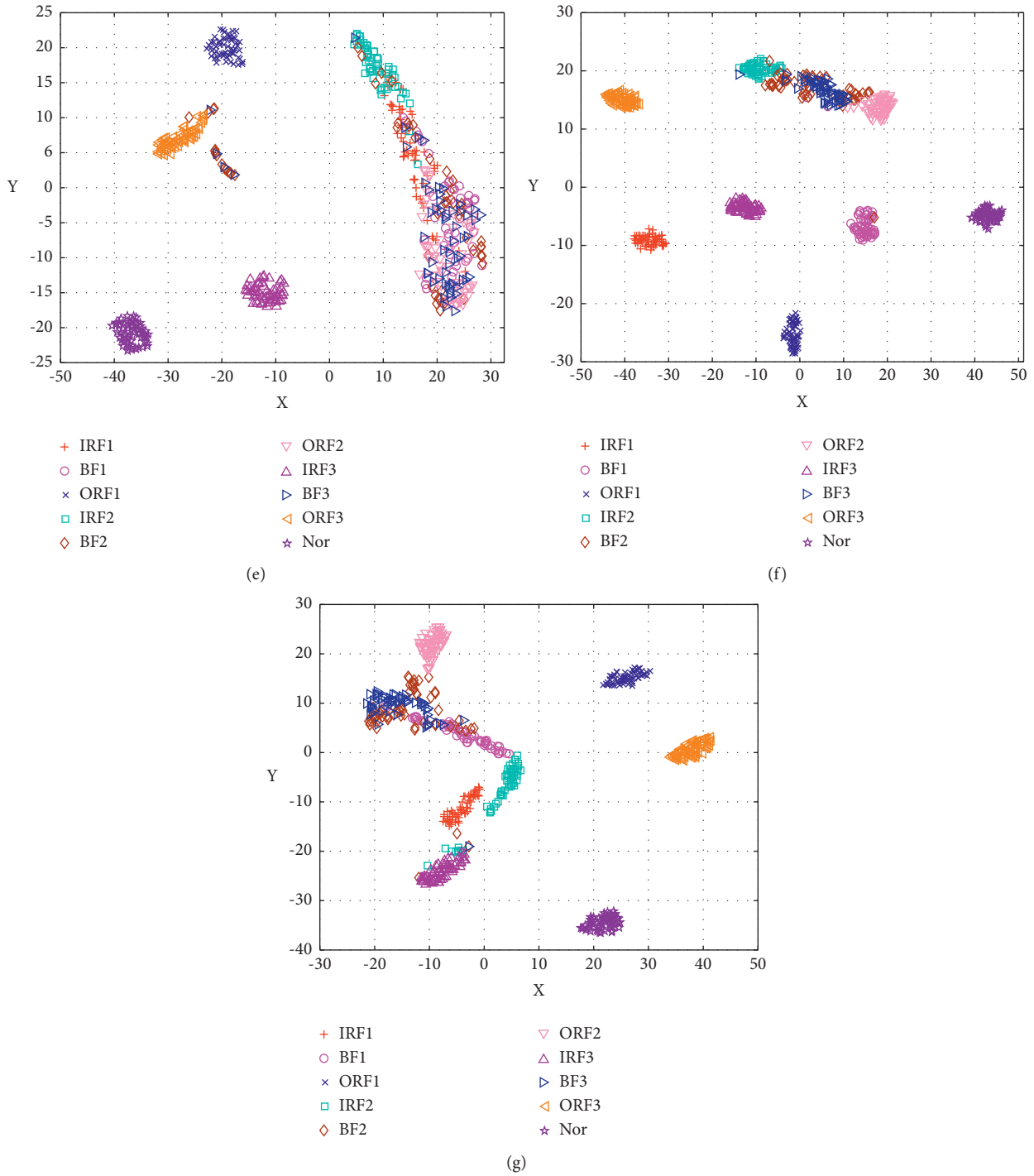

Figure 12: The two-dimensional feature visualization map obtained by t-SNE.

of all categories are accurately classified. However, the classification accuracy of several other feature extraction models is lower than the proposed method. Corresponding to the previous analysis, the classification accuracy of Figure 13(e) is poor, and only a fault recognition rate of 90.33% has been achieved. Except for the Nor, IRF3 and ORF1 samples, the fault recognition rates of the other categories of samples are all lower than 100%. This is because after RSSD decomposes the vibration signal, most of the vibration information is concentrated in the low resonance component, and the high resonance component contains less fault information, so the features extracted from the high resonance component have lower quality. In addition, by comparing Figures 13(a) and 13(g), it can be noticed that the multichannel data composed of vibration signals from the driver end and fan end does not achieve the best recognition

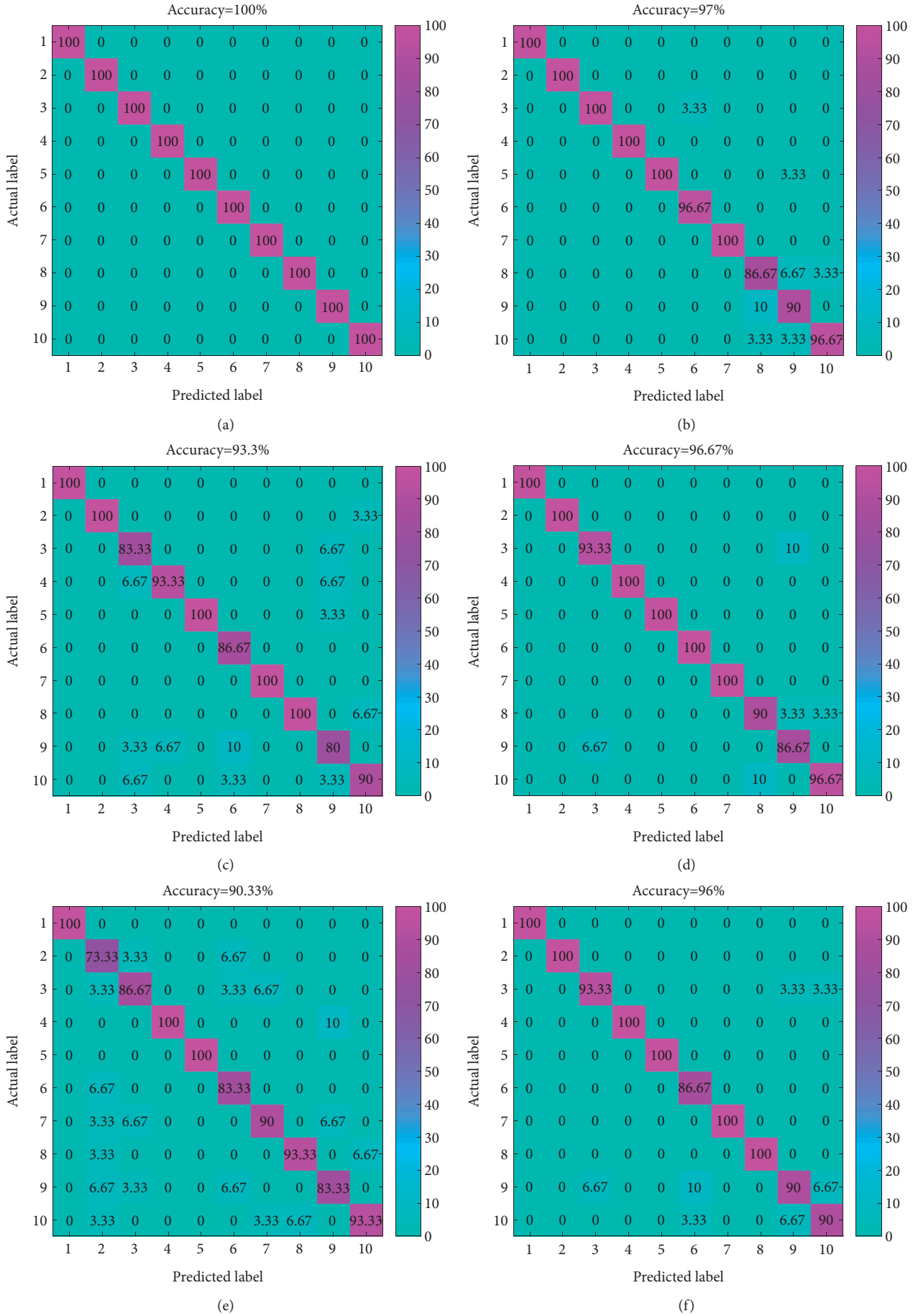

Figure 13: Continued.

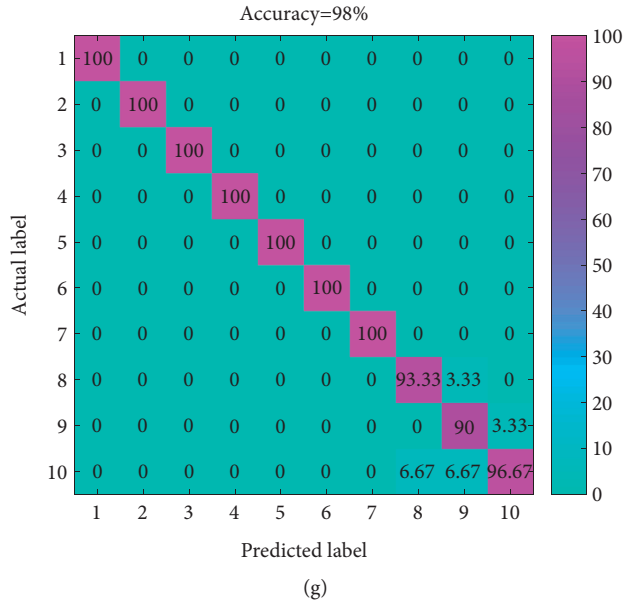

(g)

Figure 13: The confusion matrix of the seven feature extraction models.

effect, and its performance is weaker than the multichannel data composed of high resonance components and low resonance components. This proves that the RSSD decomposition can eliminate the interference in the signal. In summary, the proposed feature extraction model has excellent performance and can accurately identify various types of faults.

There may be errors in performing only a single classification experiment, and the performance of the proposed method cannot be reliably evaluated. Therefore, 20 trials was repeated to reduce the deviation caused by randomness and other factors. The results of seven feature extraction models in 20 trials are shown in Figure 14 and Table 2. Seen from Figure 14 and Table 2, the raised approach has the highest accuracy rate, and the average accuracy rate is 100%, that is, there are no misclassified samples in each classification. However, the classification accuracy of the other methods fluctuates, and the effect of each classification cannot be accurately estimated, that is, the stability is poor. Besides, comparing the feature extraction methods based on RCmvMSE and mvMAAPE, it can be found that the performance of the latter is better than the former. This shows that although the former adopts a fine composite coarse-graining process with excellent performance, mvAAPE has a stronger feature extraction performance than mvSE, so it can make up for the shortcomings of the traditional coarse-graining process. In addition, the diagnostic performance of each model is consistent with the previous visual analysis, that is, the performance of the model can be roughly judged by observing the distribution of each feature. In general, the proposed feature extraction model still has the best performance after many experiments, which proves its reliability.

This part mainly verifies the advantages of using RSSD to preprocess the signal. Typical signal decomposition techniques such as EEMD, LMD, and LCD are used to process vibration signals. Here, the first two components decomposed by each method are regarded as the components containing the main fault information to construct a multivariate signal. The subsequent processing steps are same with the presented approach. The diagnostic results of the four signal decomposition approaches under 20 trials are shown in Figure 15. Seen from Figure 15, the signal decomposition method based on HHO-RSSD achieves the best results, proving that the parameter-optimized RSSD has great application potential. The accuracy of the other three methods fluctuates, and the possibility of misclassification appears in each trial. The reason for this phenomenon is that the components decomposed by these three methods are of low quality, which affects the quality of extracted features. In short, as long as the parameters of the RSSD are reasonably selected, it can achieve very excellent results.

To explore the superiority of the DBN over other typical classifiers, the state features excavated by the proposed method are input into the typical recognizer. The selected classifiers are SVM, ELM, and Back Propagation Neural Network (BP). For convenience, the previous seven feature extraction models are marked as (a)–(g). The number of training samples and test samples remains the same. The results of these seven feature extraction models using different classifiers are shown in Table 3. Seen from Table 3, the DBN recognizer used is the best. The average recognition accuracy of DBN for the seven feature extraction models is 96.38%, which is higher than the other three classifiers, which proves its effectiveness and advantages. In addition, no matter what classifier is used, the recognition rate of the feature extraction model (a) is also the highest, with an average accuracy rate of 99.34%, which proves the advantages of this model over other models once again.

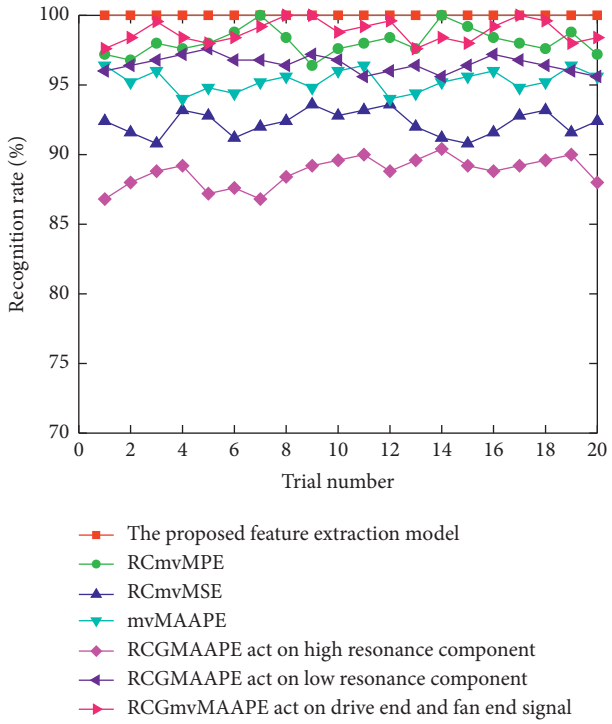

Figure 14: The diagnostic result of the seven feature extraction models in 20 trials.

Table 2: Recognition result of seven methods in 20 trials.

Methods	Accuracy obtained using diverse approaches (%)			SD
	Max	Min	Mean	
The presented approach	100	100	100	0
RCmvMPE	100	97	98.42	0.786
RCmvMSE	94.67	92.33	93.55	0.744
mvMAAPE	97	95	96.08	0.639
RCGMAAPE_High	92	89	90.63	0.885
RCGMAAPE_Low	98	96.33	97.08	0.483
RCGmvMAAPE_Drive_Fan	100	98	99.02	0.669

4.2. Case 2

4.2.1. Data Acquisition. The gearbox vibration data was collected on the QPZZ experimental platform [31]. The appearance and structure of the gearbox platform are displayed in Figure 16. The platform is made up of gearboxes, motors, bases and sensors. The sensor is arranged directly above the gear box. The rotating speed of the motor is set to 880 rpm. Five operating states were set up in the experiment: normal, gear pitting fault, gear broken tooth fault, gear wearing fault, gear pitting fault coupling with wearing fault. The brief information of the experimental data is displayed in Table 4. The sampling frequency of the sensor is set to 5.12 kHz, and the sampling time is 6 s. Due to the small amount of data, to ensure the accuracy of analysis, a sliding sampling method is adopted to select samples. The signal of the bearing Y on the motor side of the input shaft is used for analysis. In the subsequent multichannel analysis, the

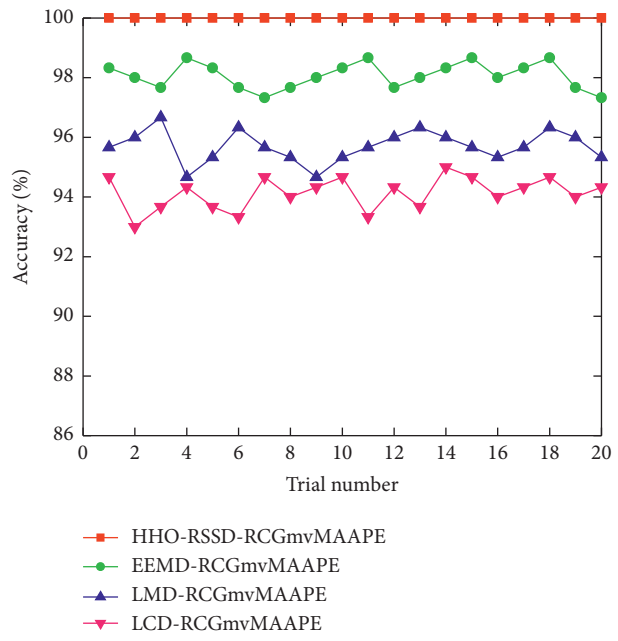

Figure 15: The diagnostic result of four signal decomposition methods.

vibration signals of the input shaft motor side bearing Y and the output shaft load side bearing Y are selected for analysis. The collected vibration signals are divided into 52 groups of samples after sliding sampling. Each group contains 2048 data points, of which 22 groups are adopted as the training data, and the remaining samples are adopted as the test data.

Table 3: The diagnostic results obtained by combining seven models with four classifiers.

Classifier model	The accuracy of test sample with different feature extraction model (%)							Average accuracy
	(a)	(b)	(c)	(b)	(e)	(f)	(g)	
DBN	100	98.67	93.33	96	91.33	96.67	98.67	96.38
SVM	100	97.67	94.67	93.33	90	95.33	97.33	95.48
ELM	99.67	95.33	91	95.33	88.67	94.67	97	94.52
BP	97.67	92	89.33	92.67	90.67	93.33	96	93.10
Average accuracy	99.34	95.92	92.08	94.33	90.18	95	97.25	_

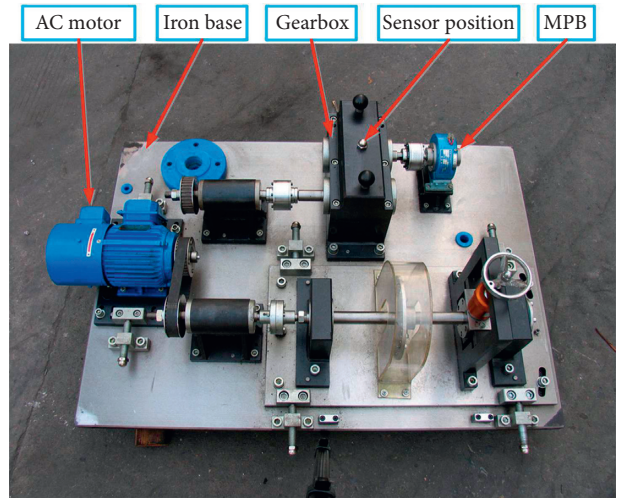

Figure 16: The gearbox test platform.

Table 4: The brief information of gear vibration data.

Fault state	Abbreviation	Training sample	Testing sample	Label
Normal	Nor	22	30	1
Gear wearing fault	WF	22	30	2
Gear pitting fault	PF	22	30	3
Gear tooth breaking fault	TBF	22	30	4
Gear pitting & wearing fault	PWF	22	30	5

4.2.2. Feature Excavation. Figure 17 shows the waveforms of vibration data in five states of the gearbox. Similarly, due to the lack of obvious rules and characteristics of the waveform, it is hard to easily judge the fault status. Therefore, it is necessary to carry out subsequent processing on the data to acquire more and more distinguishable features.

Similarly, this part first studies how to obtain the best parameters of RSSD. First, input the gear vibration signal into HHO-RSSD for decomposition, and execute the parameter optimization process. Taking the Nor signal as an example, the optimization process ends when the correlation kurtosis value is the smallest. Then, after parameter optimization, a set of optimal parameters was obtained, $Q_1 = 9.336$, $Q_2 = 1.319$, $A_1 = 1.23$, $A_2 = 0.11$, and $u = 0.377$,respectively. Figure 18 is the evolution curve of fitness value in the optimization procedure of HHO. Seen from Figure 18, HHO could quickly reach a local optimal value, and this value is finally determined to be the global optimal value. Therefore, this shows that HHO can optimize the target from the global scope, so as to find an optimal solution. Then, the optimal parameter combination obtained by optimization is input into the RSSD, and the vibration signal is decomposed to acquire the high and low resonance components. The RSSD decomposition result of Nor is shown in Figure 19.

The high and low resonance components are taken as a multichannel time series. Then, RCGmvMAAPE is adopted to excavate the fault features of the constructed multivariable data to construct the fault samples. Moreover, to validate the superiority of the raised RCGmvMAAPE approach, it is compared with RCmvMPE, RCmvMSE, mvMAAPE, and RCGMAAPE. The entropy results of seven methods are displayed in Figures 20(a)~20(g). Here, the method used in each figure is consistent with the previous experiment. Seen from Figure 20, compared with several other feature extraction models, the standard deviation of the entropy value of Figure 20(a) is smaller and the performance is more stable. The distinguishability of several other features is also very strong, but the entropy deviation is generally large, and the error bar has obvious aliasing. This phenomenon proves that

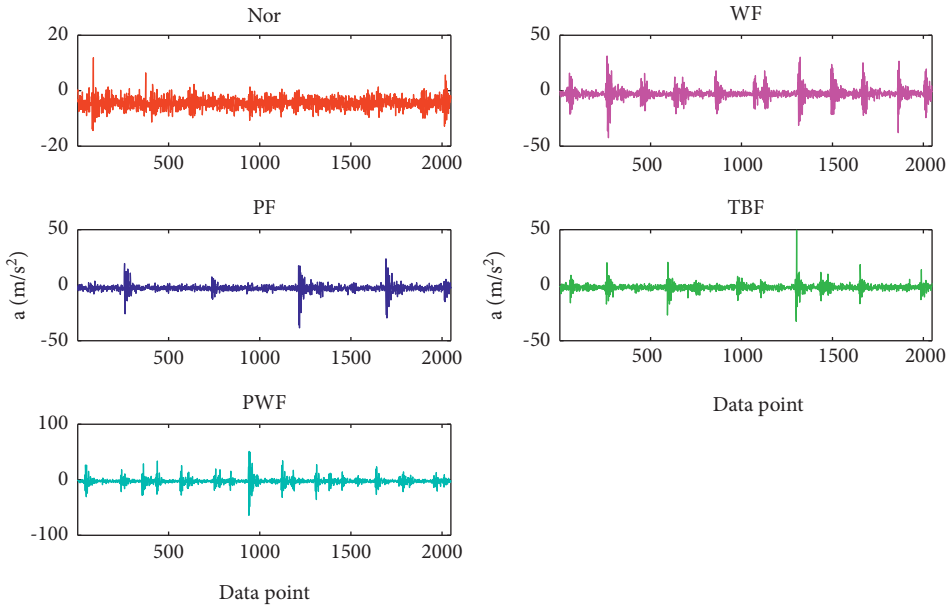

Figure 17: The vibration waveform of gearbox under five fault conditions.

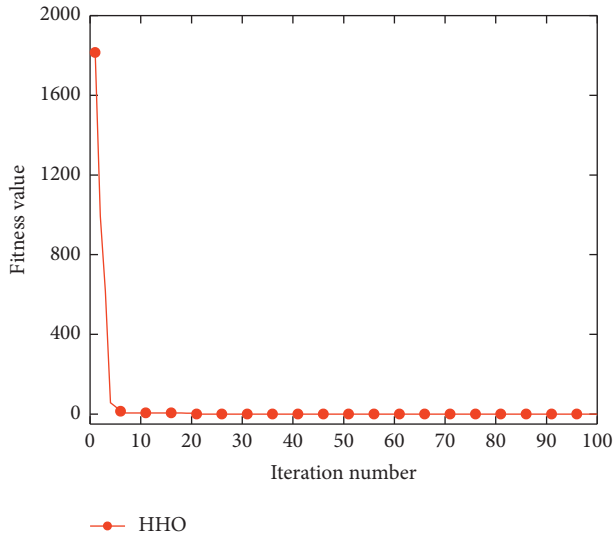

Figure 18: The evolution curve of fitness value.

although the features have obvious discrimination, the performance fluctuates greatly, which is not conducive to subsequent classification. The proposed model can distinguish each fault state better, and has a small entropy deviation on most scales, so it has not only strong separability, but also has stable performance.

Similarly, t-SNE is used for auxiliary analysis to intuitively compare the performance of the above seven feature extraction models. The visualization of the features extracted by the seven methods is displayed in Figure 21. Observed from Figure 21, the WF sample and the TBF sample in Figure 21(a) are partially aliased, and the distribution of these two categories is relatively scattered, that is, the samples of these two categories have poor separability. The distinguishability of features extracted based on other feature extraction models is worse, and some samples do not even have cluster centers. Comparing Figures 21(a) and 21(g), Figure 12(g) has a better visualization effect. The clusters of the five categories are relatively scattered, but the distribution of samples of the same category is relatively scattered, and there is no obvious cluster center. By visualizing the features, the quality of the features extracted by each model can be roughly judged, and then the performance of the model can be judged. Therefore, it can be verified that the features of Figure 21(a) have better quality, which proves the superiority of the presented approach.

4.2.3. Fault Recognition. For the sake of quantifying the performance of the above seven fault feature extraction

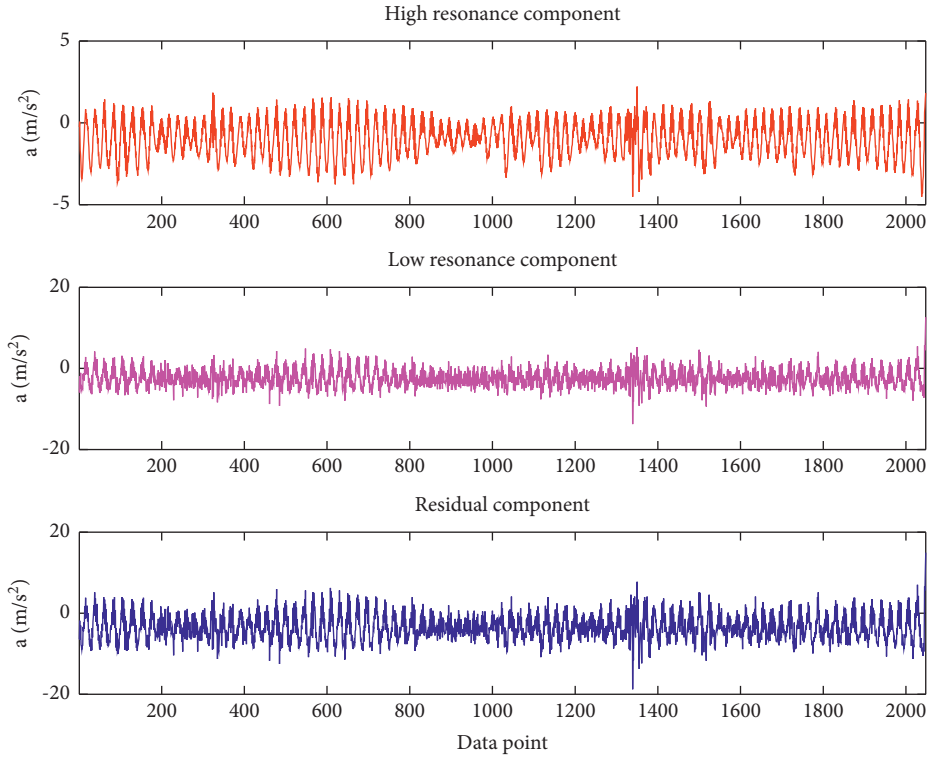

Figure 19: The RSSD decomposition result of vibration signal nor.

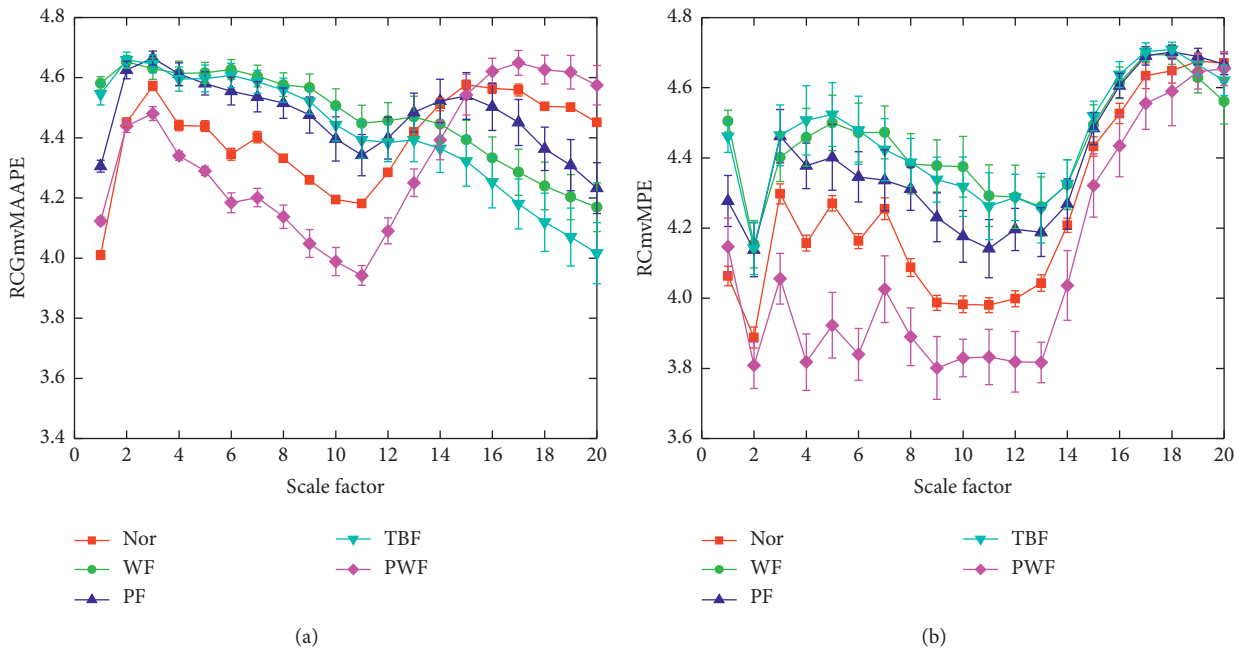

Figure 20: Continued.

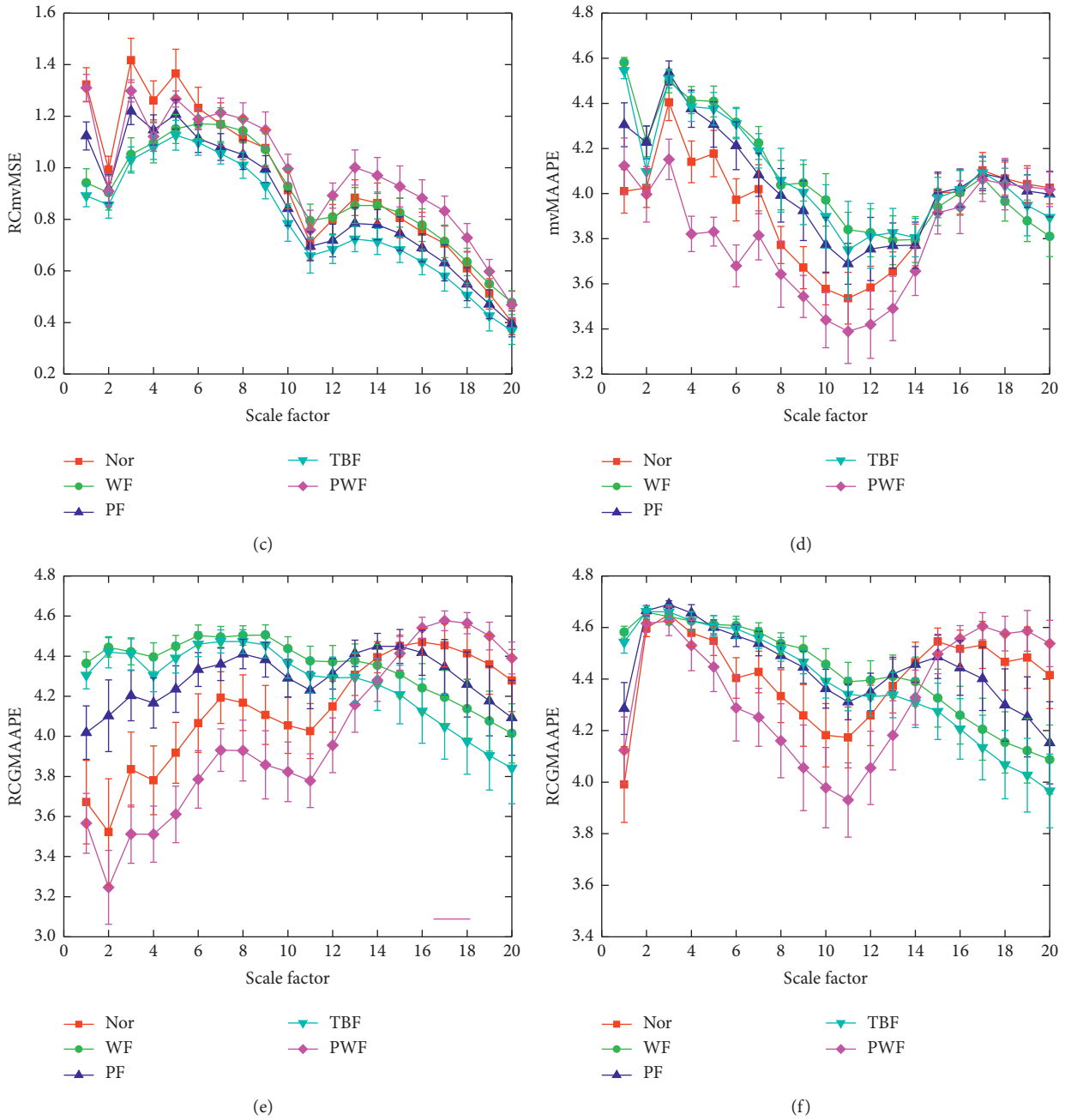

Figure 20: Continued.

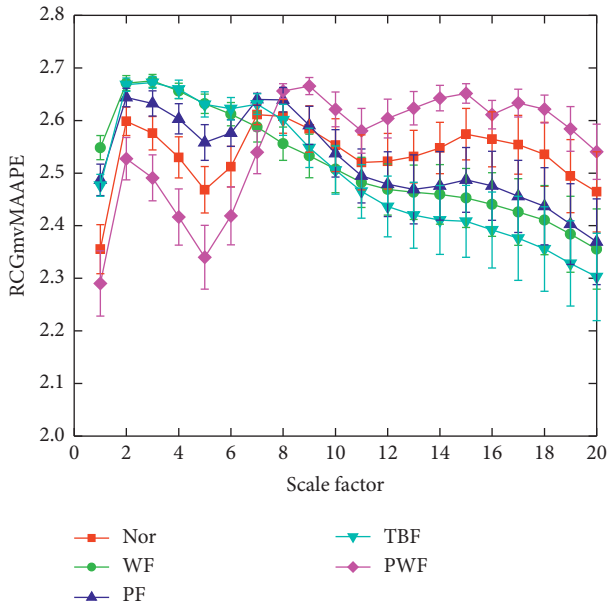

(g)

Figure 20: The entropy results of gearbox data analyzed by adopting seven approaches.

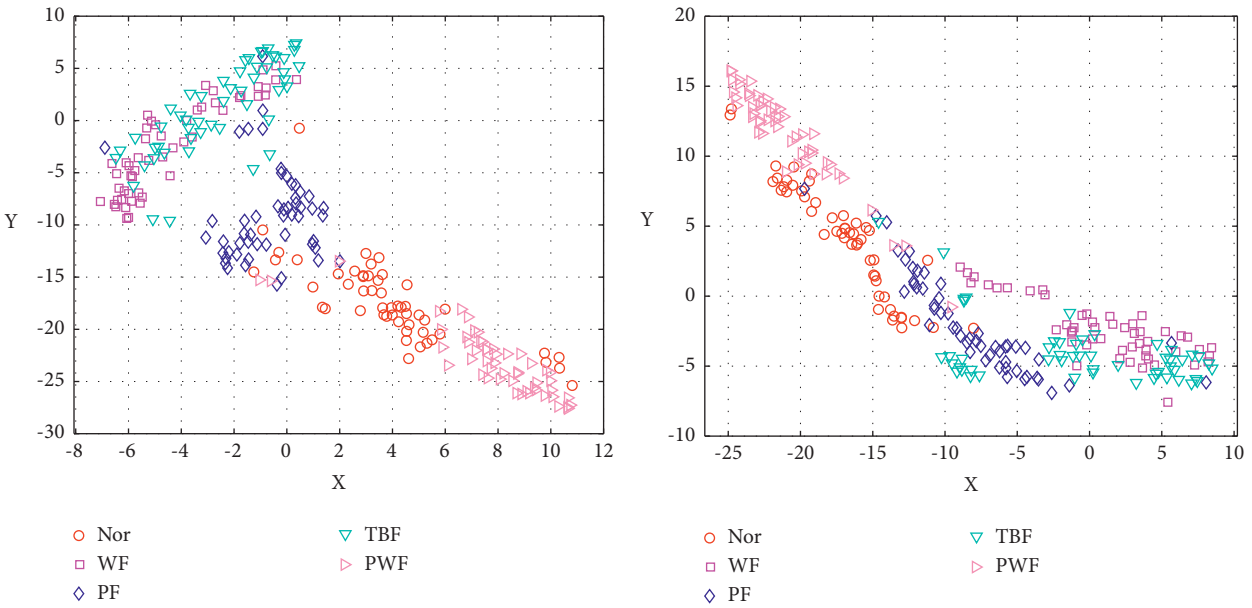

(a) (b)

Figure 21: Continued.

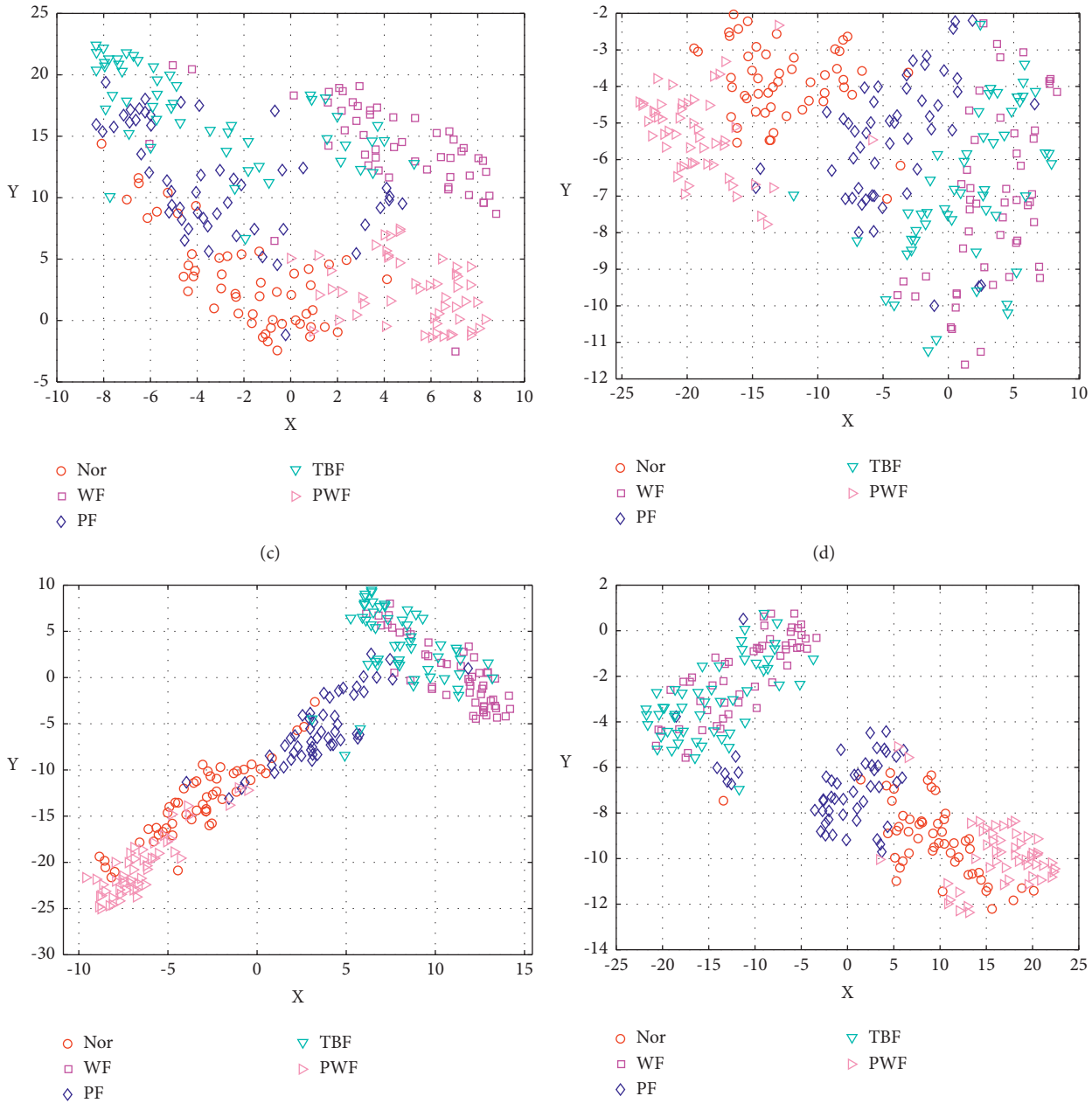

Figure 21: Continued.

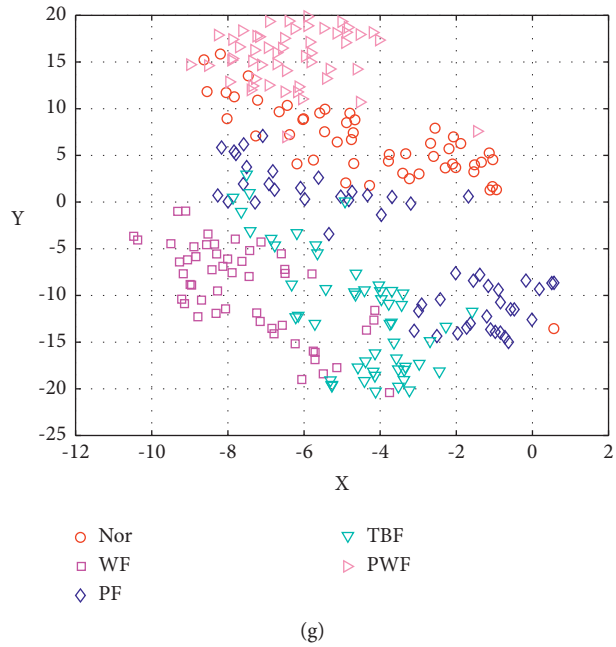

(g)

Figure 21: The two-dimensional feature visualization map obtained by t-SNE.

models on rolling bearing fault diagnosis, the features excavated by the seven approaches are input into the DBN recognizer for fault classification. The confusion matrix of the seven feature extraction models is presented in Figure 22. Observed from Figure 22, some WF samples and TBF samples were misclassified. One WF sample was misclassified to TBF, and two TBF samples were misclassified to WF. The accuracy of a single classification is 98%, which is still reliable. The performance of several other feature extraction models is weaker than the proposed model, which is also consistent with the previous t-SNE analysis. In addition, the fault recognition rate of Figure 22(g) is better than Figure 21(a), reaching 98.67%. This is mainly because the gear vibration data usually includes multiple channels, and its operating information is distributed in multiple directions. Key feature will inevitably be missed when the signal of a single channel is used for analysis. Although Figure 22(g) only analyzes the original multichannel vibration signal without corresponding processing, the rich vibration information contained in the multichannel signal can provide enough features for judging the fault state. The proposed feature extraction model only uses a single-channel vibration signal, but can achieve a fault recognition rate of 98%, which is satisfactory to a certain extent. Comparing Figure 22(e) and Figure 22(f), the analysis of low resonance components has achieved better results, which is also consistent with the results of the previous experiment. This shows that the main fault information after RSSD decomposition is concentrated on the low resonance component, while the high resonance component contains less fault information.

By comparing Figures 22(a) and 22(f), it can be found that only a single experiment may not be able to estimate the effectiveness of the approach reliably, that is, a single experiment has strong randomness. Therefore, 20 trials was repeated to reduce the deviation caused by randomness and other factors. The results of seven feature extraction models in 20 trials are shown in Figure 23 and Table 5. Seen from Figure 23 and Table 5, the proposed model achieves the best classification results, with an average accuracy rate of 98.10%, of which the highest is 100% and the lowest is 96%. Although the recognition rate has obvious fluctuations, it is generally reliable. The other six methods fluctuate sharply, especially the fifth feature extraction model, with a standard deviation as high as 2.191. Such a high deviation proves that the performance of the method is quite unstable, and the classification result is not very reliable. In addition, it can be found that the performance of the method proposed in this paper is better than that of the seventh model, which is consistent with the previous analysis, that is, a single experiment is not convincing. As the number of classifications increases, the proposed model has higher stability and performance. Therefore, it can be guaranteed that it is reliable in most classifications, while the performance stability of the seventh model is weaker than the proposed model, so the overall performance of the proposed method is excellent.

This part mainly verifies the advantages of using RSSD to preprocess the signal. Typical signal decomposition techniques such as EEMD, LMD, and LCD are used to process vibration signals. Here, the first two components decomposed by each method are regarded as the components containing the main fault information to construct a multivariate signal. The subsequent processing steps are same with the presented approach. The diagnostic results of the four signal decomposition approaches under 20 trials are shown in Figure 24. Seen from Figure 24, the signal decomposition method based on HHO-RSSD achieves the best results, proving that the parameter-optimized RSSD has

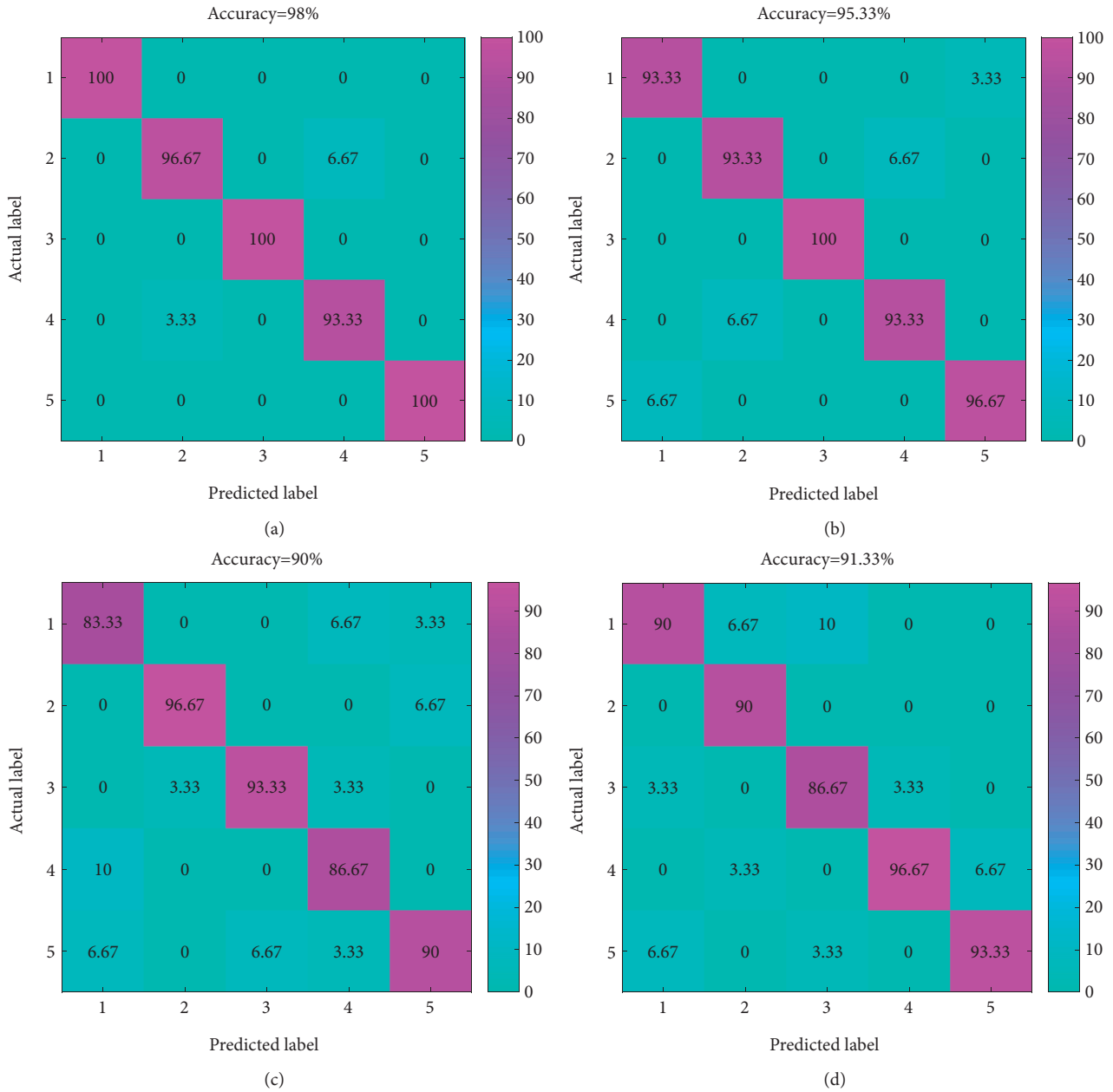

Figure 22: Continued.

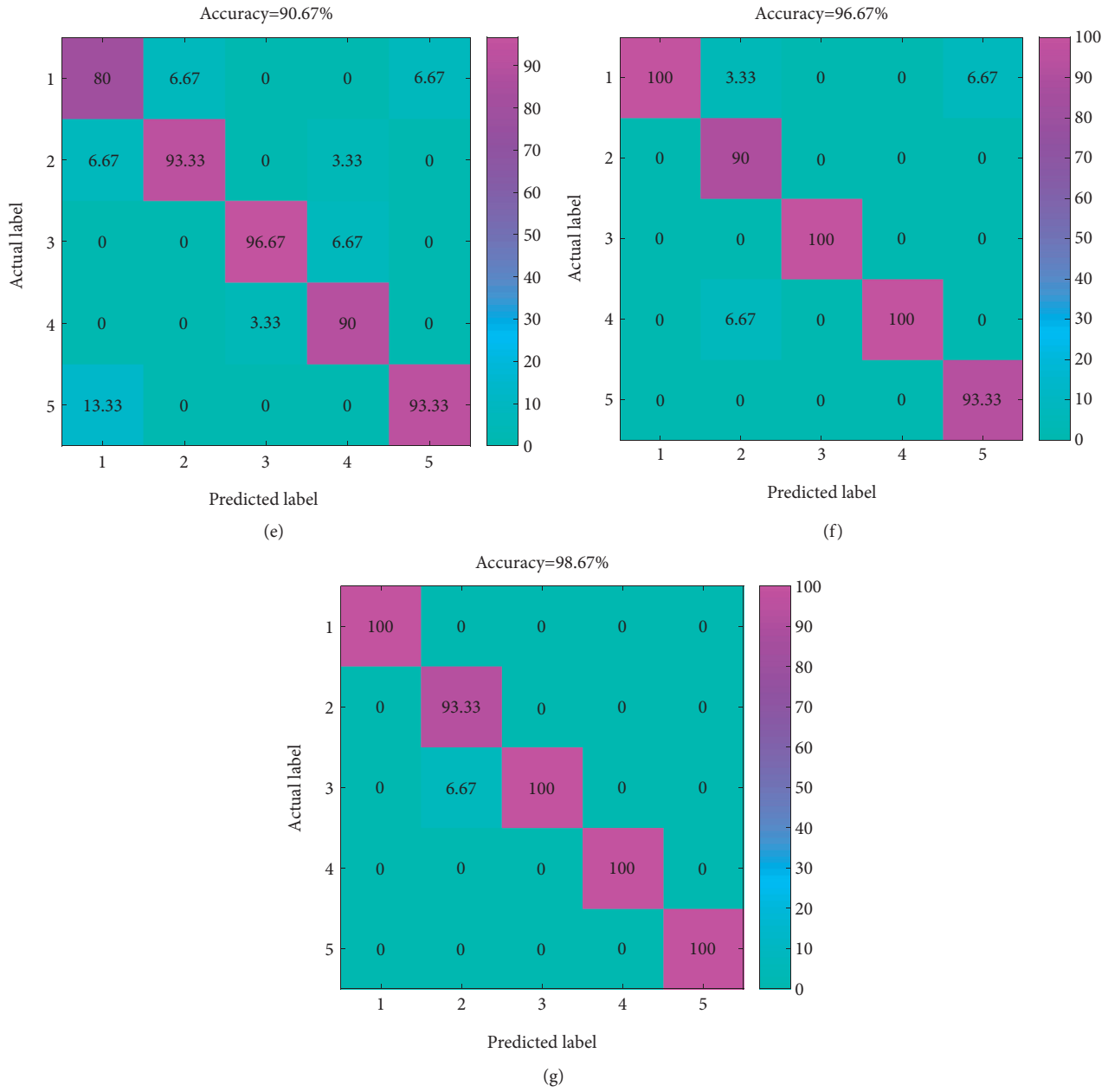

Figure 22: The confusion matrix of the seven feature extraction models.

great application potential. The accuracy of the other three methods fluctuates, and the possibility of misclassification appears in each trial. This proves that HHO-RSSD has excellent signal analysis performance. By decomposing the signal, it can reduce the influence of interference components in the signal on feature extraction. Therefore, it is necessary and effective to use HH0-RSSD to process the signal.

Similarly, this part is used to study the advantages of choosing DBN as a classifier, so three typical classifiers are also selected for comparison. Here, the ratio of the test and training samples remains the same. Similarly, for convenience, the previous seven feature extraction models are marked as (a)–(g). The results of these seven feature extraction models using different classifiers are shown in Table 6. Seen from Table 6, the DBN recognizers obtain the highest recognition rate. The average recognition accuracy of DBN for the seven feature extraction models is 93.71%, which is higher than the other three classifiers, which proves its effectiveness and advantages. In addition, no matter what classifier is used, the recognition rate of the feature extraction model (a) is also the highest, with an average accuracy rate of 99%, which proves the advantages of this model over other models once again.

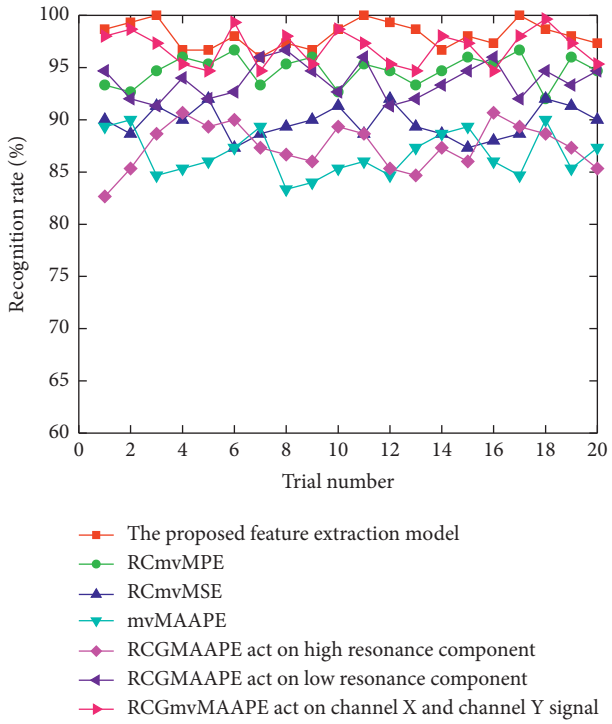

Figure 23: The diagnostic result of the seven feature extraction models in 20 trials.

Table 5: Recognition result of seven methods in 20 trials.

Methods	Accuracy obtained using diverse approaches (%)			SD
	Max	Min	Mean	
The presented approach	100	96	98.10	1.247
RCmvMPE	96.67	92	94.73	1.400
RCmvMSE	92	87.33	89.73	1.520
mvMAAPE	90	83.33	86.70	2.124
RCGMAAPE_High	90.67	82.67	87.47	2.191
RCGMAAPE_Low	96.67	91.33	93.73	1.696
RCGmvMAAPE_Drive_Fan	99.63	94.67	96.88	1.701

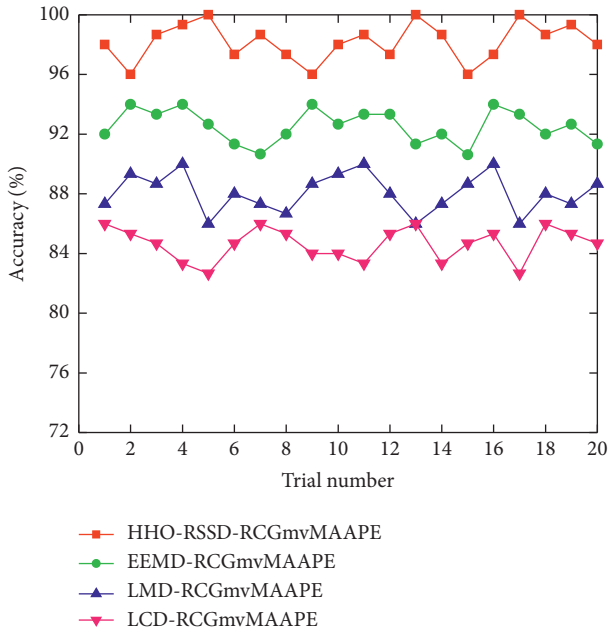

Figure 24: The diagnostic result of four signal decomposition methods.

Table 6: The recognition results of seven models with four recognizers (%).

Classifier model	The recognition rate of the test sample with different feature extraction model							Average accuracy
	(a)	(b)	(c)	(b)	(e)	(f)	(g)	
DBN	99.33	94.67	92	89.33	88.67	94	98	93.71
SVM	100	93.33	92.67	86.67	87.33	92	96	92.57
ELM	98	95.33	90.67	88	84.67	94	96.67	92.48
BP	98.67	92.67	88.67	86	88.67	91.33	94	91.43
Average accuracy	99	94	91	87.5	87.34	92.83	96.17	_

5. Conclusion

At present, typical health detection approach on the basis of signal processing and entropy are usually as follows: (1) Multiscale entropy of a single component; (2) Single entropy of multiple components; (3) Multiscale entropy of multiple components; These three types have some defects that can be improved. For example, the fault features extracted by the first two approaches are not comprehensive and sufficient, which may cause information omission. Although the third method can extract very comprehensive features, it may cause the dimensionality to be too large, and usually requires dimensionality reduction. Thus, a novel multiscale feature extraction method is proposed. First, the RSSD algorithm optimized by HHO is adopted to decompose the single-channel signal into high and low resonance components. Then use these two components as multichannel data and perform RCGmvMAAPE analysis to extract fault features. Eventually, the features are input to the DBN classifier for identification. Based on two rotating machinery vibration data sets, six different feature extraction models are utilized to compare with the presented approach. Experimental results show that the raised model can obtain a higher fault recognition rate and a higher utilization rate of information when only using a single channel vibration signal. Subsequently, to prove the superiority of the RSSD, three classic signal decomposition algorithms were used for comparative analysis, and the results proved that HHO-RSSD has satisfactory performance.

Data Availability

The data used to support the findings of this study are available from the corresponding author upon request.

Conflicts of Interest

The author declares no conflicts of interest.

References

[1] R. Liu, B. Yang, E. Zio, and X. Chen, "Artificial intelligence for fault diagnosis of rotating machinery: A review," *Mechanical Systems and Signal Processing*, vol. 108, pp. 33–47, 2018.

[2] K. Li, L. Su, J. Wu, H. Wang, and P. Chen, "A rolling bearing fault diagnosis method based on variational mode decomposition and an improved kernel extreme learning machine," *Applied Sciences*, vol. 7, no. 10, 2017.

[3] Z. Feng and M. J. Zuo, "Vibration signal models for fault diagnosis of planetary gearboxes," *Journal of Sound and Vibration*, vol. 331, no. 22, pp. 4919–4939, 2012.

[4] L. You, W. Fan, Z. Li, Y. Liang, M. Fang, and J. Wang, "A fault diagnosis model for rotating machinery using VWC and MSFLA-SVM based on vibration signal analysis," *Shock and Vibration*, vol. 2019, 2019.

[5] X. Yang, J. Yan, H. Zhu, Y. Cao, and L. Shao, "Research on fault diagnosis of hydraulic pump using convolutional neural network," *Journal of Vibroengineering*, vol. 18, no. 8, pp. 5141–5152, 2016.

[6] W. Zhang and J. Zhou, "A comprehensive fault diagnosis method for rolling bearings based on refined composite multiscale dispersion entropy and fast ensemble empirical mode decomposition," *Entropy*, vol. 21, no. 7, p. 680, 2019.

[7] Y. Lei, J. Lin, Z. He, and M. J. Zuo, "A review on empirical mode decomposition in fault diagnosis of rotating machinery," *Mechanical Systems and Signal Processing*, vol. 35, pp. 108–126, 2013.

[8] W. Y. Liu, Q. W. Gao, G. Ye, R. Ma, X. N. Lu, and J. G. Han, "A novel wind turbine bearing fault diagnosis method based on Integral Extension LMD," *Measurement*, vol. 74, pp. 70–77, 2015.

[9] I. W. Selesnick, "Resonance-based signal decomposition: A new sparsity-enabled signal analysis method," *Signal Processing*, vol. 91, no. 12, pp. 2793–2809, 2011.

[10] B. Chen, B. Shen, F. Chen et al., "Fault diagnosis method based on integration of RSSD and wavelet transform to rolling bearing," *Measurement*, vol. 131, pp. 400–411, 2019.

[11] P. Ma, H. Zhang, W. Fan, and C. Wang, "Early fault diagnosis of bearing based on frequency band extraction and improved tunable Q-factor wavelet transform," *Measurement*, vol. 137, pp. 189–202, 2019.

[12] W. Huang, H. Sun, and W. Wang, "Resonance-based sparse signal decomposition and its application in mechanical fault diagnosis: A review," *Sensors*, vol. 17, no. 6, p. 1279, 2017.

[13] N. Chai, M. Yang, Q. Ni, and D. Xu, "Gear fault diagnosis based on dual parameter optimized resonance-based sparse signal decomposition of motor current," *IEEE Transactions on Industry Applications*, vol. 54, no. 4, pp. 3782–3792, 2018.

[14] Y. Lu, J. Du, and X. Tao, "Fault diagnosis of rolling bearing based on resonance-based sparse signal decomposition with optimal Q-factor," *Measurement and Control*, vol. 52, pp. 1111–1121, 2019.

[15] A. A. Heidari, S. Mirjalili, H. Faris, I. Aljarah, M. Mafarja, and H. Chen, "Harris hawks optimization: Algorithm and applications," *Future Generation Computer Systems*, vol. 97, pp. 849–872, 2019.

[16] Y. Li, X. Wang, Z. Liu, X. Liang, and S. Si, "The entropy algorithm and its variants in the fault diagnosis of rotating machinery: review," *Ieee Access*, vol. 6, pp. 66723–66741, 2018.

[17] Z. Huo, M. Martinez-Garcia, Y. Zhang, R. Yan, and L. Shu, "Entropy measures in machine fault diagnosis: Insights and applications," *IEEE Transactions on Instrumentation and Measurement*, vol. 69, no. 6, pp. 2607–2620, 2020.

[18] S.-D. Wu, P.-H. Wu, C.-W. Wu, J.-J. Ding, and C.-C. Wang, "Bearing fault diagnosis based on multiscale permutation

entropy and support vector machine," *Entropy*, vol. 14, pp. 1343–1356, 2012.

[19] B. Fadlallah, B Chen, A Keil, and J Príncipe, "Weighted-permutation entropy: complexity measure for time series incorporating amplitude information," *Physical review. E, Statistical, nonlinear, and soft matter physics*, vol. 87, no. 2, p. 022911, 2013.

[20] Y. Chen, Zhang, Zhao, Luo, and Sun, "Fault diagnosis of rolling bearing using multiscale Amplitude-aware permutation entropy and random forest," *Algorithms*, vol. 12, no. 9, p. 184, 2019.

[21] J. Zheng, H. Pan, J. Tong, and Q. Liu, "Generalized refined composite multiscale fuzzy entropy and multicluster feature selection based intelligent fault diagnosis of rolling bearing," *ISA Transactions*, 2021.

[22] C. Li, J. Zheng, H. Pan, J. Tong, and Y. Zhang, "Refined composite multivariate multiscale dispersion entropy and its application to fault diagnosis of rolling bearing," *IEEE Access*, vol. 7, pp. 47663–47673, 2019.

[23] A. Subasi, "Classification of EMG signals using PSO optimized SVM for diagnosis of neuromuscular disorders," *Computers in Biology and Medicine*, vol. 43, no. 5, pp. 576–586, 2013.

[24] A. Iosifidis, A. Tefas, and I. Pitas, "On the kernel extreme learning machine classifier," *Pattern Recognition Letters*, vol. 54, pp. 11–17, 2015.

[25] G. E. Hinton, S. Osindero, and Y.-W. Teh, "A fast learning algorithm for deep belief nets," *Neural Computation*, vol. 18, no. 7, pp. 1527–1554, 2006.

[26] G. Hinton, "Deep belief networks," *Scholarpedia*, vol. 4, no. 5, p. 5947, 2009.

[27] M. Sedlaček, P. Bojan, and J. Vižintin, "Correlation between standard roughness parameters skewness and kurtosis and tribological behaviour of contact surfaces," *Tribology International*, vol. 48, pp. 102–112, 2012.

[28] H. Azami and J. Escudero, "Amplitude-aware permutation entropy: Illustration in spike detection and signal segmentation," *Computer Methods and Programs in Biomedicine*, vol. 128, pp. 40–51, 2016.

[29] F. Zhou, "An integrated health condition detection method for rotating machinery using refined composite multivariate multiscale Amplitude-aware permutation entropy," *Mathematical Problems in Engineering*, vol. 2020, 2020.

[30] "Case western Reserve university bearing data center website," 2018, http://csegroups.case.edu/bearingdatacenter/home.

[31] Y. Chen, Zhang, Zhao, Luo, and Lin, "Rotating machinery fault diagnosis based on improved multiscale amplitude-aware permutation entropy and multiclass relevance vector machine," *Sensors*, vol. 19, no. 20, p. 4542, 2019.